UNIVERSITAT POLITÈCNICA
DE CATALUNYA
BARCELONATECH

Galileo broadcast ephemeris and clock errors, and observed fault probabilities for ARAIM

María Teresa Alonso Alonso

Ph.D. Thesis
Doctoral Program in Aerospace Science and Technology

Galileo Broadcast Ephemeris and Clock Errors, and Observed Fault Probabilities for ARAIM

Doctoral Thesis by:

María Teresa Alonso Alonso

Advisors:

Dr. Jaume Sanz Subirana
Dr. Adrià Rovira Garcia

Research group of Astronomy and Geomatics (gAGE)
Department of Mathematics and Department of Physics
Universitat Politècnica de Catalunya (UPC)
Barcelona, Spain

October 2022

Abstract

Galileo is the European Global Navigation Satellite System (GNSS). Similar to the other GNSSs (GPS, GLONASS, and BeiDou), it provides positioning, navigation, and timing services for worldwide users.

Galileo Initial Service Open Service (IS OS) was declared by the European Commission on 15 December 2016. After the re-profiling of Galileo Safety-of-Life (SoL) in the early 2010s, Galileo is meant to support augmentation for SoL services through a Dual-Frequency Multi-constellation (DFMC) Satellite-Based Augmentation System (SBAS) and Advanced Receiver Autonomous Integrity Monitoring (Advanced RAIM or ARAIM). Integrity denotes the measure of trust that can be placed in the information supplied by the navigation system.

The characterization of Clock and Ephemeris errors of the GNSSs is a key element to validate the assumptions for the integrity analysis of GNSS SoL augmentation systems. Specifically, the performance metrics of SoL applications require the characterization of the nominal User Range Errors (UREs) as well as the knowledge of the probability of a satellite, P_{sat}, or a constellation fault, P_{const}, i.e. when one or more satellites are not in the nominal mode.

Preliminary results of Galileo broadcast Ephemeris and Clock characterization were published in Alonso MT et al. (2020), based in 43 months of data collected after Galileo IS OS was declared. In this PhD dissertation, this study is extended to two years more. The total period of more than five years, from 1 January 2017 to 31 July 2022, starts to become statistically significant for these studies.

The present dissertation carries-out an end-to-end characterization and analysis of Galileo and GPS satellites for ARAIM. It involves two main targets. First, the characterization of Galileo and GPS broadcast ephemeris and clock, to determine the fault probabilities P_{sat} and P_{const}, and the determination of an upper bound of User Range Accuracy (URA). Second, using these experimental results, to assess the performance of the ARAIM at user level.

As in the previous work of Alonso MT et al. (2020), the Not-to-Exceed (NTE) thresholds from Galileo commitments have been used to identify the satellite faults and to estimate the observed probabilities P_{sat} and P_{const}. Using the NTE = 39.78 m, when excluding the first six-month period of Galileo IS OS, the analysis over the last five-year window, from 1 August 2017 to 31 July 2022, shows very promising results. Only two satellite faults have been found, the In-Orbit-Validation (IOV) satellite E101 on 29 October 2019, lasting for 30 min, and the Full-Operation-Capability (FOC) satellite E210 on 29 April 2022, lasting for 10 min. These two faults over this five-year period result in a fault probability P_{sat} = 3.0 × 10^{-6}/sat, which is far below the 1 × 10^{-5}/sat commitment. Moreover, P_{sat} has been also estimated using the NTE = 25.04 m threshold, a value steaming from the International Civil Aviation Organization (ICAO) Navigation Systems Panel (NSP) of April 2020. In this case, two additional satellite faults are

included in the statistics, experienced by the IOV satellites E101, on 26 December 2017, lasting for 6 h and 25 min, and E102, on 21 January 2021, lasting for 25 min, which leads to P_{sat} = 5.3× 10^{-6}/sat when considering the last five-year time window, being again, a result compliant with the commitment.

The dissertation includes a sensitivity analysis of ARAIM algorithm as a function of the Integrity Support Message (ISM). The conclusions are in full agreement with those of the previous authors. The σ_{URA} value is the dominant parameter, while the bias b_{nom} has a low impact on performances. The P_{cons} has a higher impact on the availability coverage than the P_{sat}, being, in general, the results quite similar for $P_{sat} = 10^{-5}/sat$ to $P_{sat} = 10^{-7}/sat$. Then, $P_{sat} = 10^{-5}/sat$ can be enough to use. Finally, as expected, performances are strongly degraded when considering only the single frequency E5 (Galileo) and/or L5 (GPS) or its degraded constellations.

Then, based in the experimental results of previous characterization of σ_{URA}, P_{sat}, and P_{cons}, the global coverage for H-ARAIM is assessed for different configurations with Galileo alone or Galileo plus GPS. The metric for such H-ARAIM examination is the 99.5th percentile of availability for the Required Navigation Performance (RNP) with lateral accuracy of 0.1 Nautical Miles (RNP-0.1). The results show almost 100% global coverage for all analysed configurations, except with single-frequency Galileo with E1 or E5, or Galileo plus GPS with E5 and L5. This is when the basic-constellation, with 24 satellites per constellation, or the optimistic-constellation with 27 satellites per constellation, are used. With a degraded-constellation (depleted-constellation of 23 satellites per constellation), RNP-0.1 is only achieved with multi-constellation and dual frequency [Galileo E1/E5 plus GPS L1/L5].

Resumen

Galileo es el Sistema Global de Navegación por Satélite Europeo (GNSS). Al igual que los otros GNSS (GPS, GLONASS y BeiDou), proporciona servicios de posicionamiento, navegación y tiempo para usuarios en todo el planeta.

Galileo Initial Service Open Service (IS OS) fue declarado el 15 de diciembre de 2016 por la Comisión Europea. Después del rediseño de Galileo *Safety-of-Life* (SoL) a principios de la década de 2010, Galileo está destinado a respaldar la aumentación de los servicios SoL a través de un sistema de aumentación basado en satélites (SBAS) con múltiple constelación y doble frecuencia (DFMC), y de técnicas avanzadas para la monitorización autónoma de la integridad de receptor (Advanced RAIM o ARAIM). La integridad denota la medida de confianza que se puede depositar en la información proporcionada por el sistema de navegación.

La caracterización de los errores de Reloj y Efemérides de los satélites GNSS es un elemento clave para validar los supuestos para el análisis de integridad de los sistemas de aumentación GNSS SoL. Específicamente, las métricas de rendimiento de las aplicaciones SoL requieren la caracterización de los errores nominales de rango de usuario (URE), así como el conocimiento de la probabilidad de fallo de los satélites, P_{sat}, o constelaciones, P_{const}, es decir, cuando uno o más los satélites no están en el modo nominal.

Los resultados preliminares del análisis y caracterización de las efemérides y los relojes transmitidos por los satélites Galileo se publicaron en Alonso MT et al. (2020) basados en 43 meses de datos recopilados después de que se declarara el servicio abierto de Galileo (IS OS). En esta tesis, se extiende el estudio dos años más. Este periodo total de más de cinco años, desde el 1 de enero de 2017 hasta el 31 de julio de 2022, empieza a ser estadísticamente significativo para estos estudios.

En esta tesis se realiza una caracterización y un análisis *end-to-end* de los satélites Galileo y GPS, para evaluar la monitorización autónoma de la integridad de receptor mediante ARAIM. Ello supone dos objetivos principales: 1) La caracterización de las efemérides y el reloj transmitidos por los satélites, para determinar la probabilidades de fallo P_{sat} y P_{const}, y la determinación de un límite superior para la *User Range Accuracy* (URA). 2) La utilización de estos resultados experimentales, para la evaluación del ARAIM a nivel de usuario.

Del mismo modo que en el trabajo previo Alonso MT et al. (2020), los umbrales *Not-to-Exceed* (NTE) de los compromisos de Galileo se han utilizado para indentificar los fallos del satélite y estimar la probabilidades observadas P_{sat} y P_{const}. Usando el NTE = 39.78 m, después de excluir el primer período de seis meses de Galileo IS OS, el análisis durante la última ventana de cinco años, desde el 1 de agosto de 2017 hasta el 31 de julio de 2022, muestra resultados muy prometedores. Sólo se han encontrado dos fallos de satélite, el satélite *In-Orbit-Validation* (IOV) E101 el 29 de octubre de 2019, con una duración de 30 minutos, y el satélite *Full-Operation-Capability* (FOC) E210 el 29 abril 2022,

de sólo 10 minutos. Estos dos únicos fallos durante este período de cinco años dan como resultado una probabilidad de fallo P_{sat}= 3.0 × 10^{-6}/sat, que está muy por debajo del compromiso de 1 × 10^{-5}/sat. Además, también se ha estimado P_{sat} utilizando el umbral NTE = 25,04 m, de la *International Civil Aviation Organization* (ICAO) *Navigation Systems Panel* (NSP) de abril de 2020. En este caso, se incluyen dos fallos de satélites más en la estadística, los experimentados por los satélites IOV E101, el 26 de diciembre de 2017, con una duración de 6 horas y 25 minutos, y E102, el 21 enero de 2021, con una duración de 25 minutos, que dan lugar a una valor de P_{sat} = 5.3 × 10^{-6}/sat al considerar la ventana de tiempo de los últimos cinco años, siendo, nuevamente, un resultado que satisface los requerimientos establecidos.

La tesis incluye un análisis de la sensibilidad del algoritmo ARAIM en función del Mensaje de Soporte de Integridad (ISM). Las conclusiones concuerdan plenamente con las de otros autores previos. El valor σ_{URA} es el parámetro dominante, mientras que el sesgo b_{nom} tiene un impacto bajo en los resultados. El P_{cons} tiene un mayor impacto en la cobertura de disponibilidad que el P_{sat}, siendo, en general, los resultados bastante similares para $P_{sat} = 10^{-5}/sat$ o $P_{sat} = 10^{-7}/sat$. Entonces, $P_{sat} = 10^{-5}/sat$ puede ser suficiente para usar. Finalmente, como era de esperar, los resultados se degradan mucho cuando se consideran solo las frecuencias únicas E5 (Galileo) y/o L5 (GPS) o sus constelaciones degradadas.

A continuación, con base a los resultados experimentals obtenidos previamente para σ_{URA}, P_{sat}, y P_{cons}, se evalúa la cobertura global para H-ARAIM para diferentes configuraciones con Galileo solo o Galileo más GPS. La métrica para dicha evaluación de H-ARAIM es el percentil 99.5 de disponibilidad para la Performance de Navegación Requerida (RNP) con precisión lateral de 0.1 Millas Náuticas (RNP-0.1). Los resultados muestran una cobertura global de casi el 100 % para todas las configuraciones analizadas, excepto para la navegación una sola frecuencia con Galileo usando E1 o E5, o con Galileo más GPS con E5 y L5. Ello cuando se utiliza la constelación básica, con 24 satélites por constelación, o la optimista, con 27 satélites por constelación. Con una constelación degradada, de 23 satélites por constelación, la RNP-0.1 únicamente se alcanza con multi-constelación y doble frecuencia [Galileo E1/E5 más GPS L1/L5].

Resum

Galileo és el Sistema Global de Navegació per Satèl·lit Europeu (GNSS). Igual que els altres GNSS (GPS, GLONASS i BeiDou), proporciona serveis de posicionament, navegació i temps per a usuaris arreu del planeta.

Galileo Initial Service Open Service (IS OS) va ser declarat el 15 de desembre del 2016 per la Comissió Europea. Després del redisseny de Galileo *Safety-of-Life* (SoL) a principis de la dècada del 2010, Galileo està destinat a donar suport a l'augmentació dels serveis SoL a través d'un sistema d'augmentació basat en satèl·lits (SBAS) amb múltiple constel·lació i doble freqüència (DFMC), i de tècniques avançades per a la monitorització autònoma de la integritat pel receptor (Advanced RAIM o ARAIM). La integritat denota la mesura de confiança que es pot dipositar a la informació proporcionada pel sistema de navegació.

La caracterització dels errors de Rellotge i Efemèrides dels satèl·lits GNSS és un element clau per validar els supòsits per al anàlisi d'integritat dels sistemes d'augmentació GNSS SoL. Específicament, les mètriques de rendiment de les aplicacions SoL requereixen la caracterització dels errors nominals de rang d'usuari (URE), així com el coneixement de la probabilitat de fallada dels satèl·lits, P_{sat}, o de constel·lacions, P_{const}, és a dir, quan un o més els satèl·lits no estan en el mode nominal.

Els resultats preliminars de l'anàlisi i caracterització de les efemèrides i els rellotges transmesos pels satèl·lits Galileo es van publicar a Alonso MT et al. (2020) basats en 43 mesos de dades recopilades després de que es declarés el servei obert de Galileo (IS OS). En aquesta tesis s'estén l'estudi dos anys més, des de l'1 de gener de 2017 fins al 31 de juliol de 2022. Aquest període total de més de cinc anys comença a ser estadísticament significatiu per a aquests estudis.

En aquesta tesi es fa una caracterització i una anàlisi *end-to-end* dels satèl·lits Galileo i GPS per avaluar la monitorització autònoma de la integritat pel receptor mitjançant ARAIM. Això comporta dos objectius principals: 1) La caracterització de les efemèrides i el rellotge transmeses pels satèl·lits, per tal de determinar les probabilitats de falla P_{sat} i P_{const}, i la determinació d'un límit superior pel *User Range Accuracy* (URA). 2) La utilització d'aquests resultats experimentals, per a l'avaluació de l'ARAIM a nivell d'usuari.

De la mateixa manera que el treball previ Alonso MT et al. (2020), els llindars *Not-to-Exceed* (NTE) dels compromisos de Galileo s'han utilitzat per identificar les fallades del satèl·lit i estimar les probabilitats observades P_{sat} i P_{const}. Usant el NTE = 39.78 m, després d'excloure el primer període de sis mesos de Galileo IS OS, l'anàlisi durant l'última finestra de cinc anys, des de l'1 d'agost del 2017 fins al 31 de juliol del 2022, mostra resultats molt prometedors. Només s'han trobat dues fallades de satèl·lit, el satèl·lit *In-Orbit-Validation* (IOV) E101 el 29 d'octubre de 2019, amb una durada de 30 minuts i el satèl·lit *Full-Operation-Capability* (FOC) E210 el 29 d'abril 2022, de sols 10 minuts. Aquestes dues úniques fallides durant aquest període de cinc anys donen com

a resultat una probabilitat de fallada P_{sat}= 3.0×10⁻⁶/sat, que està molt per sota del compromís de 1×10⁻⁵/sat. A més, P_{sat} també s'ha estimat utilitzant el llindar NTE = 25.04 m, de la *International Civil Aviation Organization* (ICAO) *Navigation Systems Panel* (NSP) d'abril de 2020. En aquest cas, s'inclouen dos falles satèl·lits addicionals a les estadístiques, les experimentades pels satèl·lits IOV E101, el 26 de desembre 2017, amb una durada de 6 hores y 25 minuts, i E102, el 21 gener de 2021, amb una durada de 25 minuts, que donen lloc a un valor de P_{sat} = 5.3 × 10⁻⁶/sat en considerar la finestra de temps dels últims cinc anys, sent novament un resultat que satisfà els requeriments establerts

La tesi inclou una anàlisi de la sensibilitat de l'algorisme ARAIM en funció del Missatge de Suport d'Integritat (ISM). Les conclusions concorden plenament amb les d'altres autors previs. El valor σ_{URA} es el paràmetre dominant, mentre que el biaix b_{nom} té un impacte baix en els resultats. El P_{cons} té un major impacte en la cobertura de disponibilitat que el P_{sat}, sent, en general, els resultats força similars per a $P_{sat} = 10^{-5}/sat$ o $P_{sat} = 10^{-7}/sat$. Aleshores, $P_{sat} = 10^{-5}/sat$ pot ser suficient per utilitzar. Finalment, com es podia esperar, els resultats es degraden molt quan es consideren només les freqüències úniques E5 (Galileu) i/o L5 (GPS) o les seves constel·lacions degradades.

A continuació, en base als resultats experimentals obtinguts prèviament per σ_{URA}, P_{sat}, i P_{cons}, s'avalua la cobertura global per a H-ARAIM per a diferents configuracions amb Galileu sol o Galileu més GPS. La mètrica per a aquesta avaluació de H-ARAIM és el percentil 99.5 de disponibilitat per a la Performance de Navegació Requerida (RNP) amb precisió lateral de 0.1 Milles Nàutiques (RNP-0.1). Els resultats mostren una cobertura global de gairebé el 100% per a totes les configuracions analitzades, excepte per a la navegació una sola freqüència amb Galileu usant E1 o E5, o amb Galileu més GPS amb E5 i L5. Això quan es fa servir la constel·lació bàsica, amb 24 satèl·lits per constel·lació, o l'optimista, amb 27 satèl·lits per constel·lació. Amb una constel·lació degradada, de 23 satèl·lits per constel·lació, la RNP-0.1 únicament s'assoleix amb multi-constel·lació i doble freqüència [Galileu E1/E5 més GPS L1/L5].

Acknowledgements

I want to acknowledge to all people that made this dissertation possible, my PhD advisors Jaume and Adrià who propose me this topic and have been continuously ready to help me and to receive good news, and to my family, especially my mom, for her love and patient (*especialmente á miña nai, polo seu amor e paciencia*). Also to all my colleagues in the gAGE group who become part of my family as well.

My sweetest and most loving thoughts to my little baby Iria, who came to me in the last two years of this job. She has given me the strength to move on, although she has sometimes made it impossible for me. This is for you!

I would like to thank Carlos López Echazarreta from ESA EGNOS Project Office, Stefan Wallner from ESA Galileo Project Office, and Phillip Brieden from Airbus Defence and Space GmbH for their valuable comments and suggestions for the characterization of broadcast navigation data for ARAIM. I also thank the Stanford GPS Laboratory for making available the MATLAB Algorithm Availability Simulation Tool (MAAST) to the GNSS community, and Professor Thomas Pany and his team at the Institute of Space Technology and Space Applications (ISTA), for granting the access to the Integrity Support Tool for Advanced RAIM (ISTAR). These tools have been very useful to better understand the algorithms and crosscheck results. Finally, to the International GNSS Service for the availability of GNSS broadcast and precise products.

Table of Contents

Acronyms

ABAS	Aircraft Based Augmentation System
AL	Alert Limit
AoE	Age of Ephemeris
ANTEX	Antenna Exchange Format
ARNSS	Aero-nautical Radio Navigation Service
APC	Antenna Phase Centre
APV	Approach Procedures with Vertical guidance
ARAIM	Advanced RAIM
ASQF	Application Specific Qualification Facility
BGD	Broadcast Group Delay
C/A	Clear Acquisition
CDDISA	Crustal Dynamics Data Information System
CNES	Centre National D'Etudes Spatiales
CODE	Centre for Orbit Determination in Europe
CRAIM	Classical RAIM
CPF	Central Processing Facility
CSP	Constellation Service Provider
DCB	Differential Code Bias
DC	Dual Constellation
DF	Dual Frequency
DFMC	Dual-Frequency Multi-constellation
DOP	Dilution of Precision
DoY	Day-of-Year
DVS	Data Validity Status
EC	European Commission
ECEF	Earth Centred Earth Fixed
EGNOS	European Geostationary Navigation Overlay Service
EMT	Effective Monitor Threshold
ENU	East, North, Up
ESA	European Space Agency
ESSP	European Satellite Service Provider
EU	European Union
EUREF	European Reference Organisation for Quality Assured
EWAN	EGNOS Wide Area Network
FA	False Alert
FC	Fast Correction
FD	Fault Detection
FDE	Fault Detection and Exclusion
FE	Fault Exclusion
FF	Fault Free
FI	Fit Interval
F/NAV	Freely- accessible Navigation Message (Galileo)
FM	Fault Mode

FOC	Full Operational Capability
F-PPP	Fast Precise Point Positioning
gAGE	research Group of Astronomy and Geomatics
gLAB	GNSS Laboratory Tool Suite
gNAV	gAGE Navigation Tool
GBAS	Ground Based Augmentation System
GAGAN	GPS Aided GEO Augmented Navigation
GEO	Geostationary satellite
GECCO	Galileo Ephemeris Consolidation and Control Analysis
GFZ	Deutsches GeoForschungs Zentrum
GIM	Global Ionospheric Map
GLONASS	Globalnaya Navigatsionnaya Sputnikovaya Sistema
GNSS	Global Navigation Satellite System
GPS	Global Positioning System
GSA	European GNSS Agency
HAL	Horizontal Alert Limit
HMI	Hazardously Misleading Information
HPL	Horizontal Protection Level
HAS	High Accuracy Service
HMI	Hazardous Misleading Information
HUL	Horizontal Uncertainty Level
HPE	Horizontal Positioning Error
HS	Health Status
IAURA	Integrity Assured User Range Accuracy
ICAO	International Civil Aviation Organization
ICD	Interface Control Document
IF	Ionosphere Free
IFB	Inter-Frequency Bias
IGP	Ionospheric Grid Point
IGS	International GNSS Service
IOD	Issue-Of-Data
IODC	Issue of Data Clock
IODE	Issue of Data Ephemeris
IOV	In Orbit Validation
IPP	Ionospheric Pierce Point
IR	Integrity Risk
ISM	Integrity Support Message
ISTA	Institute of Space Technology and Space Applications
ISTAR	Integrity Support Tool for Advanced RAIM
IURE	Instantaneous SIS URE
ITU	International Telecommunications Union
IVD	Ionosphere Vertical Delay
KASS	Korea Augmentation Satellite System
LoS	Line-of-Sight
LPV	Localizer performance with vertical guidance
LPV-200	Localizer Performance with Vertical guidance down to 200 feet

LPV-250	Localizer Performance with Vertical guidance down to 250 feet
LBS	Location Based Services
LNAV	Legacy Navigation Message (GPS)
LS	Least Squares
LSB	Least-Significant Bit
LTC	Long Term Corrections
MA	Missed Alert
MAAST	MATLAB Algorithm Availability Simulation Tool
MC	Multi-Constellation
MCC	Mission Control Centre
MD	Missed Detection
MEO	Medium Earth Orbit
MGEX or MGX	Multi-GNSS Experiment
MHSS	Multiple Hypothesis Solution Separation
MI	Misleading Information
MSAS	MTSAT Satellite based Augmentation System
MT	Message Type
MTSAT	Multi-functional Transport Satellites
MTTN	Mean Time To Notify
NLES	Navigation Land Earth Stations
NM	Nautic Mile
NAGU	Notice Advisory to Galileo Users
NAPA	No Prediction Accuracy Available
NGA	National Geospatial-Intelligence Agency
NPA	Non-Precision Approach
NSE	Navigation System Error
NSP	Navigation Systems Panel
NTE	Not-To-Exceed
PA	Precision Approach
PACF	Performance Assessment and Checkout Facility
PL	Protection Level
PNT	Positioning Navigation and Timing
RAIM	Receiver Autonomous Integrity Monitoring
RD	Reference Document
RINEX	Receiver Independent Exchange Format
RNP-0.1	Required Navigation Performance (with lateral accuracy of 0.1 NM)
RNP-0.3	Required Navigation Performance (with lateral accuracy of 0.3 NM)
RNSS	Radio Navigation Satellite Service
OS	Open Service
PHMI	Probability of Hazardously Misleading Information
PRN	Pseudo Random Noise
PRS	Public Regulated Service
PS	Performance Standard
RIMS	Ranging Integrity Monitoring Stations
RMS	Root Mean Square
SBAS	Satellite Based Augmentation System

SA	Selective Availability
SAR	Search and Rescue
SC	Single Constellation
SDCM	System of Differential Correction and Monitoring
SDD	Service Definition Document
SF	Single Frequency
SFSC	Single Frequency and Single Constellation
SIS	Signal in Space
SISA	Signal In Space Accuracy
SISE	Signal In Space Error
SISRE	Signal In Space Range Error
SoL	Safety of Life
SPS	Standard Positioning Service
SR	Sampling Rate
STAN	Standalone
STEC	Slant Total Electron Content
SU	Soviet Union
SV	Satellite Vehicle
SVN	Satellite Vehicle Number
SW	Software
TBC	To Be Confirmed
TBD	To Be Determined
TBW	To Be Written
TGD	Total Group Delay
TEC	Total Electron Content
TN	Technical Note
TOC	Time of Clock
TOE	Time of Ephemeris
TP	Type (index)
TTA	Time To Alert
TTOM	Transmission Time of Message
UEE	User Equipment Error
UERE	User Equivalent Range Error
UIRE	User Ionosphere Range Error
UPC	Universitat Politècnica de Catalunya
URA	User Range Accuracy
URE	User Range Error
UK	United Kingdom
US	United States
UTC	Universal Time Coordinated
VAL	Vertical Alert Limit
VD	Validity Duration
VPE	Vertical Positioning Error
VPL	Vertical Protection Level
VUL	Vertical Uncertainty Level
WAD	Wide Area Differential Corrections (index)

WAAS	Wide Area Augmentation System
WC URE	Worst Case URE
WLS	Weighted Least Squares
WSSE	Weighted Sum of the Squared Errors
XPL	Horizontal/Vertical Protection Level

Nomenclature

Measurements and measurement errors

Symbol	Description	Unit
P	Pseudorange (referred also as code) measurement	m
L	Carrier-phase measurement	m
ρ	Geometric range	m
T_{rcv}	Receiver clock bias	m
T^{sat}	Satellite clock bias	m
$Trop$	Tropospheric error	m
I	Ionospheric error	m
D_{rcv}	Receiver code instrumental delay	m
D^{sat}	Satellite code instrumental delay	m
δ_{rcv}	Receiver carrier instrumental delay	m
δ^{sat}	Satellite carrier instrumental delay	m
σ_{URA}	Standard deviation of satellite pseudorange measurement	m
σ_{UIRE}	Standard deviation of residual user ionospheric range error	m
σ_{tropo}	Standard deviation of residual user tropospheric range error	m
σ_{air}	Standard deviation of the airborne (receiver) residual error	m
σ_{UERE}	Standard deviation of the pseudorange Effective accuracy	m
λ	Signal wavelength	m
N	Integer ambiguity	m
ε	Thermal noise and multipath	m
$\boldsymbol{x}$	Parameters vector (E,N,U,dt)	m
$\boldsymbol{y}$	Prefit-residuals vector	m
$\boldsymbol{G}$	Geometry matrix	-
$\boldsymbol{W}$	Weighting matrix	1/m²
$\boldsymbol{y_w}$	Weighted prefit-residuals: $\boldsymbol{y_w} = \sqrt{\boldsymbol{W}}\boldsymbol{y}$	-
$\boldsymbol{G_w}$	Weighted Geometry matrix: $\boldsymbol{G_w} = \sqrt{\boldsymbol{W}}\boldsymbol{G}$	1/m
$\boldsymbol{r_w}$	Weighted postfit-residuals: $\boldsymbol{r_w} = \boldsymbol{y_w} - \boldsymbol{G_w}\,\hat{\boldsymbol{x}}$	-
$\boldsymbol{A_w}$	Weighted Projection matrix: $\boldsymbol{A_w} \equiv \left(\boldsymbol{G_w^T}\,\boldsymbol{G_w}\right)^{-1}\boldsymbol{G_w^T}$	m
$\boldsymbol{S_w}$	Weighted Projection matrix: $\boldsymbol{S_w} \equiv \boldsymbol{I_n} - \boldsymbol{G_w}\,\boldsymbol{A_w}$	-
$\hat{\boldsymbol{x}}$	Weighted Less Square solution: $\hat{\boldsymbol{x}} = \left(\boldsymbol{G_w^T}\,\boldsymbol{G_w}\right)^{-1}\boldsymbol{G_w^T}\,\boldsymbol{y_w} = \boldsymbol{A_w}\,\boldsymbol{y_w}$	m
$\boldsymbol{r_w}$	Weighted postfit-residuals: $\boldsymbol{r_w} = \boldsymbol{y_w} - \boldsymbol{G_w}\,\hat{\boldsymbol{x}} = \boldsymbol{S_w}\,\boldsymbol{y_w}$	-
$WSSE$	Weighted Sum of the Squared Errors	m

For a given measurement, e.g. $P_{i\,rcv}^{sat}(t)$, the indexes refer to the satellite sat, recorded by receiver rcv on frequency band i at time t.

RAIM parameters

Symbol	Description	Unit
P_{FA}	False alert probability	/h
P_{MA}	Missed alert probability	-
P_{FD}	False detection probability	/sample
P_{MD}	Missed detection probability	-
T_{FD}	False detection decision threshold: $T_{FD} = T(n, P_{FD})$	-
$HSLOPE\ (i)$	Horizontal slope for satellite i	m
$VSLOPE\ (i)$	Vertical slope for satellite i	m
$k(P_{MD})$	Number of standard deviations used for the P_{MD}	-
$HRMS$	horizontal confidence	m
σ_V	Vertical confidence	m
HAL	Horizontal Alert Limit.	m
VAL	Vertical Alert Limit.	m

ARAIM parameters

Symbol	Description	Unit
$\sigma_{URA,i}$	Standard deviation of the clock and ephemeris error of satellite *i* used for integrity.	m
$\sigma_{URE,i}$	Standard deviation of the clock and ephemeris error of satellite *i* used for accuracy and continuity.	m
$b_{nom,i}$	Maximum nominal bias for satellite *i* used for integrity.	m
$P_{sat,i}$	Prior probability of fault in satellite *i* per approach.	/sat
$P_{const,j}$	Prior probability of a fault affecting more than one satellite in constellation *j* per approach.	-
P_{EMT}	Probability used for the calculation of the Effective Monitor Threshold.	/app
VAL	Vertical Alert Limit.	m
HAL	Horizontal Alert Limit.	m
HUL	Horizontal Uncertainty Level	m
VUL	Vertical Uncertainty Level	m
EMT	Effective Monitor Threshold	m
$\sigma_{V\ acc}$	Standard deviation of the vertical position	m
$N_{fault\ max}$	Maximum number of simultaneous faults to monitor	-
$P_{ap\ subset,k}$	A priory fault probability of subset *k*	-
$P_{fault,k}$	A priory probability of fault mode *k*	-
$P_{fault\ not\ monitored}$	Probability of not monitored faults	-
$T_{k,q}$	Solution Separation Test Detection Thresholds	m
χ^2	Chi-squared statistic	m
$\boldsymbol{W_{int}}$	Weighting matrix for integrity	m
$\hat{x}_q^{(k)}$	WLS solution of subset *k* (*k=0* is for all-in-view), (*q=1,2,3*)	m

$\sigma_q^{(k)}$	Standard deviation solution $\hat{x}_q^{(k)}$	m
$b_q^{(k)}$	Worst-case impact of $b_{nom,i}$ on the position solution	m
$\sigma_{ss,q}^{(k)}$	Standard deviation for the difference between the all-in-view $\hat{x}_q^{(0)}$ and the fault-tolerant position solutions $\hat{x}_q^{(k)}$.	m
$\sigma_{V\ acc}$	Standard deviation of the vertical position	m

ARAIM configuration parameters

Symbol	Description	Unit
$EMTL$	Effective Monitor Threshold Limit.	m
K_{ACC}	Number of standard deviations used for the accuracy formula.	-
K_{FF}	Number of standard deviations used for the 10^{-7} fault free vertical position error.	-
$PHMI_{VERT}$	Integrity budget for the vertical component.	/app
$PHMI_{HOR}$	Integrity budget for the horizontal component.	/app or /h
P_{Alert}	Continuity budget allocated to disruptions due to false alert and failed exclusions.	/h
P_{FA_VERT}	Probability of false alert allocated to the vertical mode.	/app
P_{FA_HOR}	Probability of false alert allocated to the horizontal mode.	/app or /h
P_{THRES}	Threshold for the integrity risk coming from unmonitored faults.	/app or /h
σ_{V,acc_max}	Required vertical (V) accuracy	m
σ_{H1,acc_max}	Required horizontal (H1) accuracy	m
σ_{H2,acc_max}	Required horizontal (H2) accuracy	m
F_C	Threshold used for fault consolidation.	-
$N_{ITER,MAX}$	Maximum number of iterations to compute the PL.	-
TOL_{PL}	Tolerance for the computation of the Protection Level.	m

Vectors are expressed in bold lowercase letters and matrices are expressed in bold uppercase letters. The product between two scalars is expressed with a dot (·). The scalar product between two vectors is expressed with a dot (·). The product between two matrices is expressed without a dot and without a space.

1 Introduction

The characterization of Clock and Ephemeris error of the Global Navigation Satellite Systems (GNSSs) is a key element to validate the assumptions for the integrity analysis of GNSS Safety of Life (SoL) augmentation systems. Specifically, the performance metrics of SoL applications require the characterization of the nominal Signal-in-Space (SIS) User Range Errors (UREs) as well as the knowledge of the probability of a satellite, P_{sat}, or a constellation fault, P_{const}, i.e. when one or more satellites simultaneously perform not in the nominal mode [1].

Global Positioning System (GPS) satellites broadcast in their navigation message the User Range Accuracy (URA) value that provides a conservative Root Mean Square (RMS) estimate of the URE. Indeed, a zero-mean Gaussian distribution typically characterizes the SIS URE with a standard deviation represented by the URA, i.e. σ_{URA}. Galileo satellites broadcast the Signal-in-Space Accuracy (SISA) index, but as provided today in Galileo SIS, it is not equivalent to the GPS URA. An evolution of the SISA algorithm is being developed to compute a Galileo URA [2]. The Galileo SISA is expected to be equivalent to the GPS URA as both are operated jointly in the Advanced Receiver Autonomous Integrity Monitoring (Advanced RAIM or ARAIM).

The EU-US GNSS Working Group C provided guidelines on how the GNSS Constellation Service Providers (CSPs) commitments on ARAIM should be specified [3]. In short, it establishes that in the information broadcast, the SIS ranging error is bounded by a normal distribution with a near-zero mean and standard deviation of less than or equal to σ_{URA} during fault-free operations.

According to the Global Positioning System Standard Positioning Service Performance Standard (GPS SPS PS) [4], a satellite is considered to be faulty (major service failure) when the Line-of-Sight (LoS) projected error is greater than a Not-to-Exceed (NTE) threshold. This NTE is defined as NTE = 4.42 × IAURA, where 4.42 corresponds to a k-factor of a Gaussian distribution with a probability of 1×10^{-5}, and IAURA stands for Integrity Assured URA, which is equal to the upper bound on the σ_{URA} value, corresponding to the URA index broadcast by the GPS satellites. Indeed, the commitments of [4] state an upper bound of 1×10^{-5}/sat/hour probability of satellite fault, per satellite, per hour. In addition, [4] states that major service faults will be flagged or removed with an average alarm delay of one hour (Mean Fault Duration) and a worst case of alarm delay of six hours. This implies an extreme upper bound $P_{sat} \leq 6 \times 10^{-5}$/sat of probability that at any given time a GPS satellite observation is faulty.

In the case of Galileo, the Open Service Service Definition Document (OS SDD) [5] establishes that the expected value of the Galileo probability of Signal-in-Space (SIS) fault for future configurations of Galileo during the Full Operational Capability (FOC) service provision is $P_{sat} = 6 \times 10^{-5}$/sat, with NTE = 40 m. More recently, the Galileo program established a dedicated process involving the main actors, the European Commission (EC), European Space Agency (ESA), and European GNSS Agency (GSA), which is analysing the Galileo performance to support the definition of the ARAIM concept and relative standards. The

conclusions presented in the International Civil Aviation Organization (ICAO) Navigation Systems Panel (NSP) on April 2020 proposed a Galileo URA value that shall not exceed 6 m with P_{sat} lower than 3×10^{-5}/sat, which leads to NTE = 4.17 × 6 = 25.04 m (where k = 4.17 is the factor corresponding to a 3×10^{-5} probability for the Gaussian distribution). Moreover, the Galileo constellation fault is considered with a probability P_{const} lower than 1×10^{-4} meaning that, at any given time, two or more Galileo satellites are faulty due to the same root cause [6].

Preliminary results of Galileo broadcast Ephemeris and clock characterization were published in Alonso MT, et al (2020), based in 43 months of data collected after Galileo Initial Service Open Service (IS OS) was declared by the EC on 15 December 2016. In the present dissertation, I have extended this study to two more years, being the selected period from 1 January 2017 to 31 July 2022. This total period of five years and a half starts to become statistically significant for this research.

Once the probabilities the fault probabilities P_{sat}, P_{const} and σ_{URA} values are experimentally determined for Galileo and GPS constellations, the global performance of ARAIM is assessed with multi-constellation (Galileo and GPS) and with single-constellation (Galileo alone or GPS alone). As detailed in the user algorithm described in section 3, ARAIM can detect narrow faults (single satellite faults) and wide faults (constellation faults) by monitoring a set of fault modes that depend on the P_{sat} and P_{const} parameters that will be broadcast in the Integrity Support Message (ISM), together with the σ_{URA} and nominal bias (b_{nom}). In this study, the ISM parameters are assumed as static parameters overbounding the actual distributions.

1.1 Research Objectives

The aim of the present PhD dissertation is to provide an end-to-end characterization and analysis of Galileo and GPS constellations for ARAIM studies. It involves two main goals: 1) The characterization of broadcast ephemeris and clocks, in particular, to determine the probability of a satellite or a constellation fault (P_{sat}, P_{const}) and to determine an upper bound of the User Range Accuracy (σ_{URA}). 2) Using these experimental results, to assess the performance of the ARAIM.

For the first goal, I have contributed to the development of a set of tools to monitor the ephemeris and clocks of satellites belonging to the GNSS constellations Galileo and GPS, that allow to determine the necessary information to carry out integrity studies with ARAIM. Indeed, I have contributed to set up an automatic monitoring system that works on a daily basis and generates results with aggregated monthly statistics.

For the second goal, I have contributed to the upgrade of the in-home navigation tool, gNAV, with classical RAIM and ARAIM algorithms, so that it can carry out studies completely autonomously and with a full control of the algorithm implementation. Although the ephemeris and clocks monitors have been designated to work only with Galileo and GPS data, the RAIM and ARAIM implementations support all constellations and signals in single- and multi-constellation and single- and dual-frequency.

1.2 Thesis Context

This thesis has been developed in the context of two ESA projects: The "Engineering Support for Signal in Space Feared Event Analysis and IONO Synthetic Scenarios Generation" project, ESA Contract No. 4000118045/16/NL/WE", and the "gLAB Extension" project, ESA Contract No. 4000133662/20/NL/CRS/hh. In those projects, I have contributed to the development of tools and methodologies for an end-to-end characterization and analysis of Galileo and GPS satellites for ARAIM studies.

The characterization of broadcast ephemeris and clock, to determine the probability of a satellite or a constellation fault, P_{sat}, P_{const}, and an upper bound of σ_{URA}, was one of the main activities in the first contract, where the algorithms and tools to conduct this study were developed.

The implementation of Classical RAIM and Advanced RAIM algorithms in the navigation tool gNAV, in FORTRAN, was one of the main activities of the second contract. Once these algorithms where consolidated in the gNAV tool, they were exported to the gLAB tool suite, in ANSI C, as the final target of the project.

1.3 Thesis Outline

The present dissertation is organized in six chapters as follows:

Chapter 1, the chapter you are reading, contains the introduction, thesis outline and the list of publications related with this dissertation. The later include papers in peer-reviewed journals and contributions in meeting proceedings.

Chapter 2 provides an overview of GNSS to introduce the main concepts used in this dissertation. The first part of the chapter describes the GNSS signals, GNSS measurements and error budget. Then, after a brief description of the Galileo system, the integrity concept is introduced together with the performance requirements for civil aviation. The last part of this chapter is an introduction to the Augmentation Systems, i.e. satellite-based, ground-based and aircraft-based.

Chapter 3 focuses on Classical-RAIM and Advanced-RAIM, providing a detailed description of the algorithms involved and their associated parameters. In particular, the performance requirements, protection levels derivation and test statistics are discussed. These algorithms are the ones implemented in the gNAV tool, in FORTRAN. In the case of ARAIM, the algorithms implementation and the main concepts involved are illustrated with a driving example.

Chapter 4 constitutes the core of this research, containing the methodology developed for the characterization of Galileo broadcast ephemeris and clock, and the experimental determination of satellite and constellation fault probabilities (P_{sat}, P_{const}) and an upper bound for σ_{URA}. Although the target, and the novelty, is for Galileo satellites, the GPS constellation is also analysed to have a self-contained study.

Chapter 5 evaluates the sensitivity of ARAIM and its performance based in the experimental results found in Chapter 4. The first part of this chapter provides a sensitivity analysis of the global ARAIM performance against the parameters of its ISM. It considers vertical and horizontal guidance, with single- and multi-constellation and with single- and dual-frequency signals. The second part evaluates the global Horizontal ARAIM (H-ARAIM) performance using the experimental values found for P_{sat}, P_{const} and σ_{URA} in Chapter 4. Different scenarios are considered with Galileo plus GPS and with Galileo alone, both with single- or multi-frequency signals.

Chapter 6 contains the conclusions of this thesis and ends with suggestions for further research.

1.4 Thesis Publications

Papers in peer-reviewed journals

1. **Alonso MT,** Ferigato C, Ibáñez-Segura D, Perrotta D, Rovira-Garcia A, Sordini E (2021) "*Analysis of 'Pre-Fit' Datasets of gLAB by Robust Statistical Techniques*" Stats 4(2):400-418. DOI 10.3390/stats4020026.

2. **Alonso MT**, Sanz J, Juan JM, Rovira-Garcia A, González-Casado G (2020) "*Galileo Broadcast Ephemeris and Clock Errors Analysis: 1 January 2017 to 31 July 2020*" Sensors 20(23):A6832:1-30 DOI 10.3390/s20236832.

3. Ibáñez D, Rovira-Garcia A, **Alonso MT**, Sanz J, Juan JM, González-Casado G, Lopez-Martínez M (2020) "*EGNOS 1046 Maritime Service Assessment*" Sensors 20(1):A276:1-16 DOI 10.3390/s20010276.

Contributions in Meeting Proceedings

1. Rovira-Garcia A, Ibáñez-Segura D, Li M, **Alonso MT**, Sanz J, Juan JM, González-Casado G (2022) "*gLAB hands-on education on satellite navigation*". Proceedings of the 4th Symposium on Space Educational Activities, Barcelona, Spain 27-29 April 2022. pp. 48-53, DOI 10.5821/conference-9788419184405.010

2. Ibañez D, Rovira-Garcia A, Sanz J, Juan J, Gonzalez-Casado G, **Alonso MT**, López-Salcedo JA, Jia H, Pancorbo FJ, García C, Martín I, Abadía SR (2019) "*A kinematic campaign to evaluate EGNOS 1046 maritime service*". Proceedings of the 32nd International Technical Meeting of the Satellite Division of The Institute of Navigation (ION GNSS+ 2019), Miami, Florida, USA: September 16-20, 2019. pp. 840-854. ISBN/ISSN: 9781510895850. DOI 10.33012/2019.16941.

3. Brieden P, Wallner S, Sanz J, Rovira-Garcia A, **Alonso MT**, Baur O, Lauria D, Kirchner M, Cosson F, Spinelli E, Martini I, Canestri E, Joly D (2019) "*Galileo characterization as Input to H-ARAIM and SBAS DFMC*". Proceedings of the 32nd International Technical Meeting of the Satellite Division of The Institute of Navigation (ION GNSS+ 2019), Miami, Florida, USA: September 16-20, 2019. pp. 2819-2841. ISBN/ISSN: 9781510895850. DOI 10.33012/2019.16922

4. Brieden P, Francois R, Baur O, Nuckelt A, Lauria D, Kirchner M, Wallner S, Cosson F, Spinelli E, Martini I, **Alonso MT** (2018) "*Galileo characterisation as input to safety-of-life applications*." 9th ESA Workshop on Satellite Navigation Technologies. Noordwijk, Netherlands, December 5-7, 2018. URL

5. Sanz J, Juan JM, López C, Gonzalez-Casado G, Rovira-Garcia A, **Alonso MT,** Ibañez D, (2018) *"Automated GPS Signal-in-Space anomalies monitoring over more than 11 years"*. Proceedings of the 31st International Technical Meeting of The Satellite Division of the Institute of Navigation (ION GNSS+ 2018), Miami, Florida, USA: September 24-28, 2018. pp. 2172-2185. ISBN: 0-936406-10-0 DOI 10.33012/2018.15853

2 Overview of GNSS

Global Navigation Satellite System (GNSS) is a generic term denoting a satellite navigation system (e.g. GPS, GLONASS, Galileo and BeiDou) that provides continuous positioning and timing (PNT) over the globe.

A GNSS basically consists of three main segments: the space segment, which comprises the satellites; the control segment, which is responsible for the proper operation of the system; and the user segment, which includes the GNSS receivers providing positioning, velocity and precise timing to users, see Figure 1.

The space segment is in charge of generating and transmitting carrier phase and code signals, and storing and transmitting the navigation message loaded by the control segment. These transmissions are controlled by highly stable atomic clocks on board the satellites.

The space segments of the different GNSSs are formed by satellite constellations with enough satellites to ensure that users will have at least four satellites in view simultaneously from any point on Earth's surface at any time.

The control segment (also referred to as the ground segment) is responsible for the proper operation of the GNSS. Its basic functions are:

- to control and maintain the status and configuration of the satellite constellation;
- to predict ephemeris and satellite clock evolution;
- to keep the corresponding GNSS time scale (through atomic clocks); and
- to update the navigation messages for all the satellites.

The user segment is composed of GNSS receivers. Their main function is to receive GNSS signals, determine pseudoranges (and other observables) and solve the navigation equations in order to obtain the coordinates and a very accurate time.

The basic elements of a generic GNSS receiver are: an antenna with pre-amplification, a radio frequency section, a microprocessor, an intermediate-precision oscillator, a feeding source, some memory for data storage and an interface with the user. The calculated position is referred to the antenna phase centre.

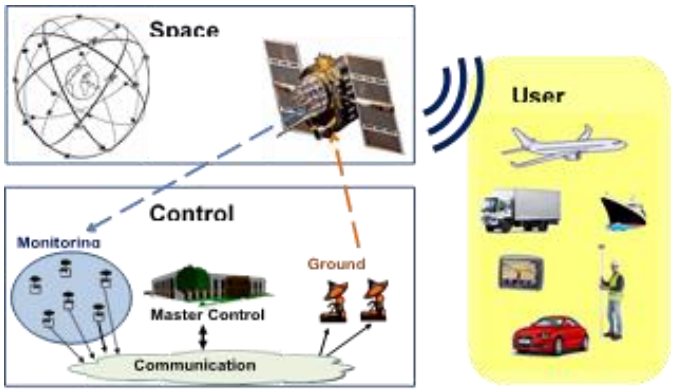

Figure 1. The GNSS architecture (this figure is from [7])

2.1 GNSS signals

GNSS satellites continuously transmit navigation signals at two or more frequencies in L band. These signals contain ranging codes and navigation data to allow users to compute both the travel time from the satellite to the receiver and the satellite coordinates at any epoch. The main signal components are described as follows:

- *Carrier:* Radio frequency sinusoidal signal at a given frequency.
- *Ranging code:* Sequences of zeros and ones which allow the receiver to determine the travel time of the radio signal from the satellite to the receiver. They are called Pseudo Random Noise (PRN) sequences or PRN codes.
- *Navigation data:* A binary-coded message providing information on the satellite ephemeris (pseudo-Keplerian elements or satellite position and velocity), clock bias parameters, almanac (with a reduced-accuracy ephemeris data set), satellite health status and other complementary information.

The allocation of frequency bands is a complex process because multiple services and users can fall within the same range. That is, the same frequencies can be allocated for different purposes in different countries. The International Telecommunications Union (ITU) is a United Nations agency coordinating the shared global use of the radio spectrum. It involves, for instance, television, radio, cell (mobile) phone, radar satellite broadcasting, etc., and even microwave ovens. The ITU divides the electromagnetic spectrum into frequency bands, with different radio services assigned to particular bands.

Figure 2 shows the frequency bands for the Radionavigation Satellite Service (RNSS). There are two bands in the region allocated to the Aeronautical Radio Navigation Service (ARNS) on a primary basis worldwide. These bands are especially suitable for Safety-of-Life (SoL) applications because no other user of this band is allowed to interfere with the GNSS signals. These correspond to the upper L band (1559–1610 MHz), containing the GPS L1, Galileo E1, GLONASS G1 and BeiDou B1 bands, and to the bottom of the lower L band (1151–1214 MHz) where the GPS L5, GLONASS G3, Galileo E5 and BeiDou B2 bands are located.

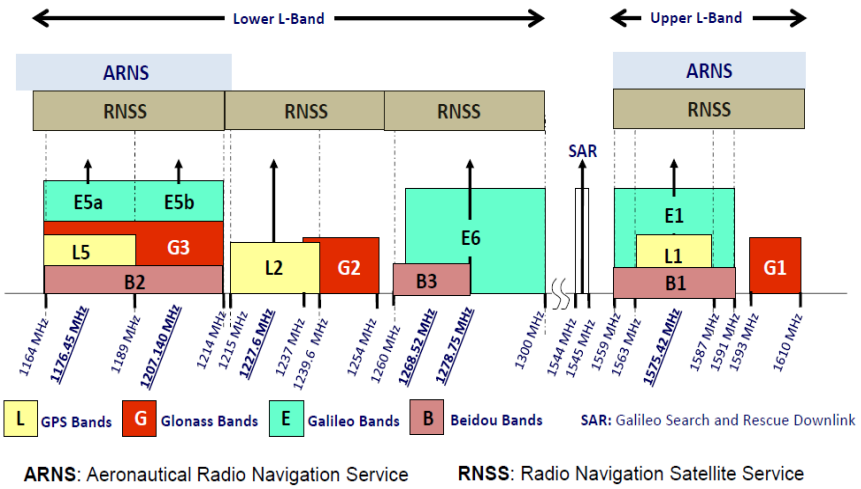

Figure 2. GPS, GLONASS, Galileo and BeiDou navigational frequency bands (from [7]).

The remaining GPS L2, GLONASS G2, Galileo E6 and BeiDou B3 signals are in the 1215.6–1350 MHz bands. These bands were allocated to radiolocation services (ground radars) and RNSS on a primary basis, so the signals in these bands are more vulnerable to interference than the previous ones.

2.2 GNSS measurements

The basic GNSS observable is the travel time ΔT of the signal to propagate from the phase centre of the satellite antenna (at the emission time) to the phase centre of the receiver antenna (at the reception time).

As mentioned before, the GNSS signals contain ranging codes to allow users to compute the travel time ΔT. This value multiplied by the speed of light gives the apparent range $P = c\ \Delta T$ between them.

The measurement P is what is known as the pseudorange. It is called pseudorange, because it is an 'apparent range' between the satellite and the receiver which does not match its geometric distance because of, among other factors, synchronisation errors between receiver and satellite clocks. Taking explicitly into account possible synchronisation errors between such clocks, the travel time between transmission and reception is obtained as the difference in time measured on two different clocks or time scales: the satellite (t^{sat}) and the receiver (t_{rcv}).

Besides the code, the carrier phase itself is also used to obtain a measure of the apparent distance between satellite and receiver. These carrier phase measurements are much more precise than the code measurements (typically two orders of magnitude more precise), but they are ambiguous by an unknown bias. Indeed, this ambiguity changes by an arbitrary integer number of wavelengths (λN) every time the receiver loses the lock on the signal, producing jumps or range discontinuities.

For instance, for a receiver (*rcv*) and a satellite (*sat*), the code and carrier phase measurements at a frequency f_i, can be modelled as:

$$P_{i}{}_{rcv}^{sat} = \rho_{rcv}^{sat} + c \cdot (T_{rcv} - T^{sat}) + M_{rcv}^{sat} \cdot Trop_{rcv} + \alpha_i \cdot I_{rcv}^{sat} + D_{rcv,i} + D_i^{sat} + \varepsilon_{P_i}$$

$$L_{i}{}_{rcv}^{sat} = \rho_{rcv}^{sat} + c \cdot (T_{rcv} - T^{sat}) + M_{rcv}^{sat} \cdot Trop_{rcv} - \alpha_i \cdot I_{rcv}^{sat} + \lambda_i \cdot \omega + \lambda_i \cdot \left(N_{i}{}_{rcv}^{sat} + \delta_{\,rcv,i} + \delta_i^{sat}\right) + \varepsilon_{L_i}$$

where, ρ is the Euclidean distance between the *sat* and *rcv* antenna phase centres, c is the speed of light in a vacuum, T_{rcv} and T^{sat} are the receiver clock and satellite clock offsets with respect to GNSS time, $Trop_{rcv}$ is the zenith tropospheric delay at the receiver position, M_{rcv}^{sat} is an obliquity factor which depends on the elevation, I_{rcv}^{sat} is the ionospheric delay, in TECU, experienced by the signal, and $\alpha_i = \frac{40.3}{f_i^2} 10^{16}$ is a factor which converts the ionospheric delay, in TECU, to metres of L_i, ω is the wind-up term, $D_{rcv,i} + D_i^{sat}$ are the code instrumental delays, λ_i is the wavelength of the L_i signal, $\left(N_{1}{}_{rcv}^{sat} + \delta_{rcv,i} + \delta_i^{sat}\right)$ is the carrier phase ambiguity that can be split into an integer part plus two real-valued instrumental delays. Finally, ε_{P_i} and ε_{L_i} are the code and carrier receiver noise and multipath.

2.2.1 Error Budget

GNSS error sources are allocated into the three afore mentioned categories: the space segment, the control segment, and the user segment:

- **Space and Control segment errors,** termed as Signal-in Space Range Error (SISRE), or SiS URE, or just URE, are pseudorange inaccuracies due to satellite ephemeris errors, satellite clock errors, satellite antenna variations, signals imperfections, etc.
  The effective accuracy of both the Space and Control segments is typically characterized by a zero-mean Gaussian distribution with a standard deviation represented by σ_{URA}.

- **User segment errors,** termed as User Equipment Error (UEE)**,** are split in
  - Propagation errors: pseudorange inaccuracies due to the atmospheric (ionosphere and troposphere) propagation modelling.
  - Measurement errors: pseudorange inaccuracies due to receiver and environment, including multipath and receiver noise (some authors refer to UEE only for measurement errors).

  The effective accuracy of the user segment errors is typically characterized by the root sum square of the individual error components, represented by their variances as:

$$\sigma_{i,iono}^2 + \sigma_{i,tropo}^2 + \sigma_{i,user}^2$$

  where σ_{iono}, σ_{tropo} and σ_{user} are, respectively, the standard deviations of satellite i residual ionospheric range error, residual tropospheric range error and the receiver residual error.

The effective accuracy of the pseudorange value is termed as the User-Equivalent Range Error (UERE). The system UERE, which can be used for σ_i in the error model, see Annex A, is characterized by the root sum square of the individual error components, represented by their variances as:

$$\sigma_i^2 = \sigma_{i,URA}^2 + \sigma_{i,iono}^2 + \sigma_{i,tropo}^2 + \sigma_{i,user}^2$$

To illustrate the concept, Table 1 from [8] depicts representative magnitudes of individual contributions to the GNSS user equivalent range error. The observed satellite ephemeris and clock nominal accuracies for Galileo and GPS are estimated in Chapter 4.

Table 1. GNSS Pseudorange Error Budget (Table from [8])

Source	Error source	Contribution 1σ (m)
Space and Control segments	**SiS User Range Error (URE)**	
	Broadcast satellite orbit	0.2-1.0
	Broadcast satellite clock	0.3-1.9
	Broadcast group delays	0.0-0.2
User segment	**User Equipment Error (UEE)**	
	Unmodeled Ionospheric delay	0-5
	Unmodeled Tropospheric Delay	0.2
	Receiver Noise and Resolution	0.2 -1
	Multipath	0.1-1
Total	**User Equivalent Range Error (UERE)**	**0.5-6**

2.3 Galileo System

Galileo is the European GNSS. Similar to the other constellations (GPS, GLONASS, and BeiDou), it provides positioning, navigation, and timing services for worldwide users.

The first phase of Galileo deployment started with a reduced constellation of four operational In-Orbit Validation (IOV) satellites launched in 2011 and 2012. After the successful completion of this initial phase, the Galileo program is currently moving towards Full Operational Capability (FOC). The first pair of Galileo FOC satellites, E201 and E202, was launched in August 2014. Unfortunately, due to an orbit injection anomaly, these satellites were placed into erroneous eccentric orbits. After these two eccentric satellites, 22 FOC satellites were successfully launched between 2015 and 2021. Sadly, due to Russian invasion of Ukraine, the launch of two additional Galileo satellites foreseen for 6 of April 2022 by Soyuz launcher was postponed and probably the other launch planned by the end of 2022 with other two additional satellites, will be also postponed. As of August 2022, the Galileo constellation comprises 28 satellites, 4 IOV (3 usable), and 24 FOC (19 usable), transmitting on five frequencies, i.e. E1, E5a, E5b, E5, and E6 [9].

The planned Galileo constellation in FOC phase consists of a total of 30 satellites (24 active and 6 spares) Medium Earth Orbit (MEO) satellites [9] at an altitude of 23222 km and with an orbit eccentricity of 0.002. Ten satellites will occupy each of three orbital planes inclined at an angle of 56° with respect to the equator. The satellites will be spread around each plane and will take about 14 hours, 4 minutes and 45 seconds to orbit Earth, repeating the geometry each 17 revolutions, which involves 10 sidereal days. This constellation guarantees, under nominal operation, a minimum of six satellites in view from any point on Earth surface at any time, with an elevation angle above the horizon of more than 10 deg.

In FOC phase, each Galileo satellite will transmit navigation signals in the frequency bands E1, E6, E5a and E5b, each right-hand circularly polarised. These signals are designed to support the different services that will be offered based on various user needs as follows:

OS: The Open Service (OS) is free of charge to users worldwide. Up to three separate signal frequencies are offered within it. Single-frequency receivers will provide performances similar to GPS C/A. In general, OS applications will use a combination of Galileo and GPS signals, which will improve performance in severe environments such as urban areas.

PRS: The Public Regulated Service (PRS) is intended for the security authorities (police, military, etc.) who require a high continuity of service with controlled access. It is under governmental control. Enhanced signal modulation/encryption is introduced to provide robustness against jamming and spoofing.

HAS: The High Accuracy Service (HAS) is free access service complementing the OS by delivering high accuracy data and providing better ranging accuracy, enabling users to achieve few decimetres level positioning accuracy.

SAR: This service contributes to the international COSPAS-SARSAT system or Search and Rescue (SAR). A distress signal will be relayed to the Rescue Coordination Centre and Galileo will inform users that their situation has been detected.

Galileo Initial Service OS was declared by the EC on 15 December 2016. After the re-profiling of Galileo SoL in the early 2010s, Galileo is meant to support augmentation for SoL services through a Dual-Frequency Multi-constellation (DFMC) Satellite Based Augmentation System (SBAS) and ARAIM [10].

2.4 Integrity Concept

Integrity denotes the measure of trust that can be placed in the information supplied by the navigation system for a specific operation. It involves to send timely alarms in case of GNSS signal failure and to provide information to users to compute the level of trust, as confidence bounds, that can be applied to the GNSS signals. These confidence bounds are the so called Protection Levels (PLs), Horizontal and Vertical Protection Levels (HPLs and VPLs), which represent an upper bound on the position error.

For each operational mode, Alert Limits (ALs) against which the user has to compare its PL are defined in the ICAO GNSS standards and recommended practices, and the system is declared as unavailable when the PL is greater than the AL. If the system is available and the position error is not bounded by the protection level, thence the event is considered as a HPL or VPL failure, because the PL is always supposed to be an upper bound on the position error. In such a case, the event is declared as Hazardously Misleading Information (HMI) if the position error exceeds the AL (which suppose an integrity risk), or as Misleading Information (MI) if the AL is not exceeded.

All these concepts are clearly depicted by the Stanford Plot that has become the reference representation technique in the position domain, providing a quick and clear view of system performances, highlighting its capability to clearly show the integrity margins offered by the integrity system.

Together with PL and AL, the integrity assessment involves two additional parameters: Integrity Risk (IR) and Time to Alert (TTA):

- *Integrity Risk*, or the Probability of Hazardously Misleading Information (PHMI), may be defined as the probability of providing a signal that is out of tolerance without warning the user in a given period of time. That is, an undetected failure that leads to an HMI event.

- *Time to Alert*: The maximum allowable time elapsed from the onset of the navigation system being out of tolerance until the equipment enunciates the alert.

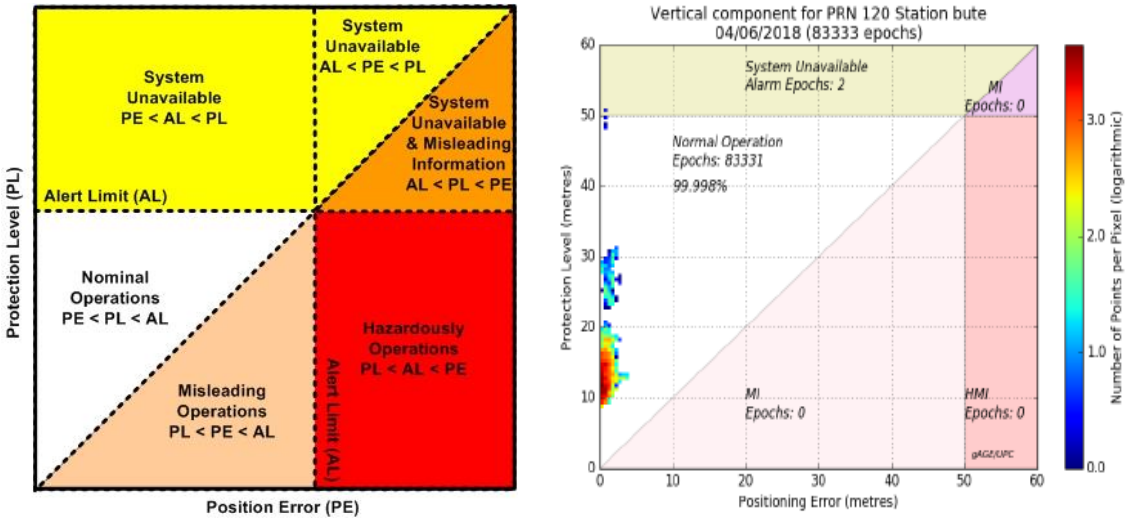

Figure 3. Stanford plot. Left figure is a layout of the Stanford plot (this figure is from [11]). Right figure shows and actual Stanford plot for a SBAS. The horizontal axis is the Horizontal (or Vertical) Positioning Error (HPE or VPE) and the vertical axis is the Horizontal (or Vertical) Protection Level (HPL or VPL). Each bin indicates (in a logarithmic colour scale) the number of occurrences of a specific (HPE, HPL) or (VPE, VPL) pair.

2.5 Navigation Performance Requirements

The International Civil Aviation Organization (ICAO) defines the performance requirements that navigation systems must meet for different flight phases of a civil aircraft (see Figure 4). These navigation performance requirements are established from the four evaluation parameters defined as follows:

- *Accuracy:* Difference between the computed position at any given time to the actual or true position. The position error should be within the accuracy requirements under nominal fault-free conditions at least 95% of the time.

- *Integrity:* Ability of a system to provide timely warnings to users or to shut itself down when it should not be used for navigation.

- *Continuity:* Ability of a system to perform its function without (unpredicted) interruptions during the intended operation, expressed as a probability. For example, there should be a high probability that guidance will remain available throughout an entire instrumental approach procedure.

- *Availability:* Ability of a system to perform its function at initiation of intended operation. System availability is the percentage of time that accuracy, integrity and continuity requirements are met.

The navigation performance requirements for each Approach Service Types are summarised in Table 2. Here, "lateral" refers to "cross-track" or perpendicular to the approach direction of the aircraft. This information has been extracted from [12,13].

Table 2. Performance requirements

Approach Service	Accuracy (95%)		Integrity				Continuity	Availability
	Hor./Lat.	Vert.	Int. Risk	TTA	HAL/LAL	VAL		
NPA RNP 0.3	220 m	N/A	$1 \times 10^{-7}/h$	10 s	556 m	N/A	$10^{-8}/h$ to $10^{-4}/h$	10^{-5} to 10^{-2}
NPA RNP 0.1	72 m	N/A	$1 \times 10^{-7}/h$	10 s	85 m	N/A	$10^{-8}/h$ to $10^{-4}/h$	10^{-5} to 10^{-2}
APV-I / LPV-250	16 m	20 m	$2 \times 10^{-7}/150s$	10 s	40 m	50 m	$8 \times 10^{-6}/15s$	10^{-5} to 10^{-2}
APV-II	16 m	8 m	$2 \times 10^{-7}/150s$	6 s	40 m	20 m	$8 \times 10^{-6}/15s$	10^{-5} to 10^{-2}
CAT-I	16 m	6-4 m	$2 \times 10^{-7}/150s$	6 s	40 m	35-10 m	$8 \times 10^{-6}/15s$	10^{-5} to 10^{-2}
LPV-200	16 m	4 m	$2 \times 10^{-7}/150s$	6.2 s	40 m	35 m	$8 \times 10^{-6}/15s$	10^{-5} to 10^{-2}

Figure 4 illustrates the different flight phases of a civil aircraft as defined by ICAO, with indication of the augmentation system/s supporting the navigation mode (ABAS, SBAS or GBAS). These augmentation systems are described in the next section.

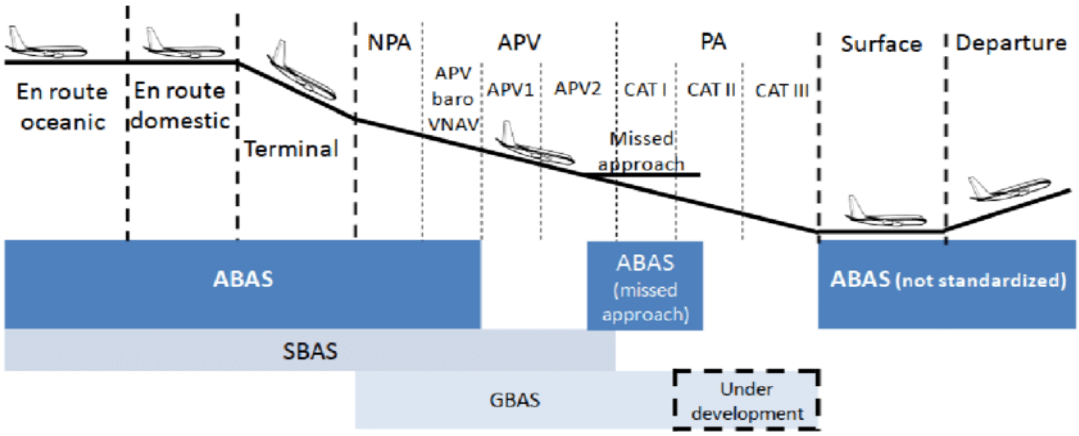

Figure 4. Flight phases of a civil aircraft as defined by ICAO (this figure is from [14])

2.6 Augmentation Systems

Current GNSSs cannot met the ICAO requirements for all phases of flight. Then, to enhance its performance, the GNSS signals are augmented with additional information to:

- Improve integrity via real-time monitoring.
- Improve Accuracy via differential corrections.
- Improve Availability and Continuity.

There are three main approaches to perform such augmentation: Satellite Based Augmentation System (SBAS), Ground Based Augmentation System (GBAS) and Aircraft Based Augmentation (ABAS).

2.6.1 Satellite-Based Augmentation Systems

The Satellite Based Augmentation Systems (SBASs) broadcast through Geostationary Satellites (GEOs) GPS-like navigation signals containing differential corrections and integrity data to enhance the GNSS positioning and making it suitable for safety critical applications such as civil aviation.

In order to cover a wide area, like a continent, SBAS treats errors affecting GNSS SiS taking into account the nature of the error [18,19]. The SBAS corrections are organized into two categories: clock-ephemeris corrections and ionospheric corrections. These corrections are computed by a Central Processing Facility (CPF) from the range measurements of a monitor stations network with baselines ranging from several hundred up to thousands of kilometres.

The SBAS data, even for individual satellites, is distributed across several individual messages types (MTs), MT0 to MT28, which are coordinated through Issues-Of-Data (IOD):

Fast Corrections (FCs) are scalar values common to all SBAS users, primarily removing satellite clock errors. In contrast, *Long Term Corrections* (LTCs) are given as a vector and affect users in a different way at different locations. LTCs primarily remove ephemeris errors and also account for the slow-varying clock trend.

FC and LTC have associated confidence intervals (i.e. sigmas) to weight the satellite data properly in the navigation filter when SBAS users compute both the PVT solution and its associated confidence bounds (i.e. the protection levels). FCs are broadcasted in MT2 to MT5, while MT25 is devoted to long term corrections. MT24 is a mixed message where both FC and LTC are broadcasted. MT25 allows saving bandwidth in case there are few satellites remaining to broadcast FC and LTC at a given time. Finally, the delay at the upper layer of the atmosphere (i.e. the ionosphere) is corrected with MT26.

Real-time applications entail delays and message losses. This is accounted for in MT7, which provides FCs degradation parameters to add uncertainty to the estimated range corrections, as well as time-outs to avoid using the FC going beyond its validity period. Finally, MT10 provides degradation factors mainly for the LTCs and ionosphere.

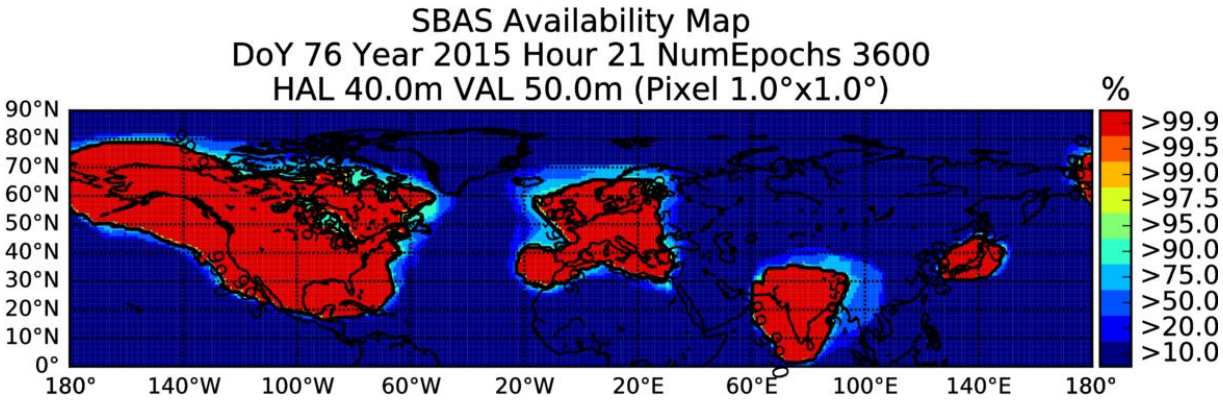

Figure 5. Example of Availability maps for different SBASs: WAAS (USA), EGNOS (Europe), GAGAN (India) and MSAS (Japan). This figure has been generated with the gLAB tool [17,18].

Different SBASs following the same standard RTCA-MOPS [19] have been deployed by US (Wide Area Augmentation System – WAAS), European Union (EGNOS), Japan (MTSAT Satellite based Augmentation System – MSAS) and India (GPS Aided GEO Augmented Navigation – GAGAN in India). Analogous systems are under deployment in other regions of the world (e.g. System of Differential Correction and Monitoring – SDCM in Russia) or under investigation (e.g. Korea Augmentation Satellite System – KASS in South Korea). Figure 5 shows an example of availability map for the commissioned SBASs on 17 March 2015.

2.6.1.1 EGNOS

The European Geostationary Navigation Overlay Service (EGNOS) is the European SBAS. Similar to any other SBAS, the EGNOS architecture is basically composed by four elements [20], see Figure 6.

- **Ground segment:** comprises a network of 39 Ranging Integrity Monitoring Stations (RIMS), 2 Mission Control Centres (MCCs), 2 Navigation Land Earth Stations (NLES) per GEO, and the EGNOS Wide Area Network (EWAN), which provides the communication network for all the components of the ground segment.

- **Support segment:** In addition to the above-mentioned stations/centres, the system has other ground support installations involved in system operations planning and performance assessment, namely the Performance Assessment and Checkout Facility (PACF) and the Application Specific Qualification Facility (ASQF) which are operated by the EGNOS Service Provider.

- **Space Segment:** composed of at least three geostationary satellites broadcasting corrections and integrity information for GPS satellites in the L1 frequency band (1575.42 MHz). This space segment configuration provides a high level of redundancy over the whole service area in the event of a failure in the geostationary satellite link. EGNOS operations are handled in such a way that, at any point in time, at least two GEOs broadcast the SBAS operational signal.

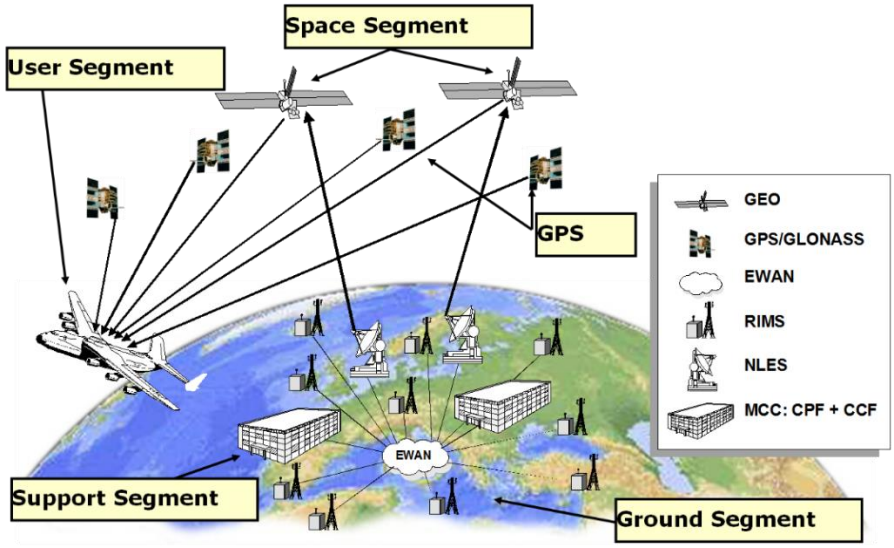

Figure 6. EGNOS architecture (this figure is from GNSS Science Support Centre)

- **User Segment:** the EGNOS user segment is comprised of EGNOS receivers that enable their users to accurately compute their positions with integrity. To receive EGNOS signals, the end user must use an EGNOS-compatible receiver. Currently, EGNOS compatible receivers are available for such market segments as agriculture, aviation, maritime, rail, mapping/surveying, road and Location Based Services (LBS).

Current EGNOS version named EGNOS-V2 augments only GPS L1 signal, that is, a Single Frequency and Single Constellation (SFSC) SBAS. The next version EGNOS-V3, currently under development, is a Dual Frequency and Multi-constellation (DFMC) SBAS that will operate with GPS and Galileo signals (L1/L5, E1/E5) and embedding security protection against cyber-attacks.

2.6.2 Ground-Based Augmentation Systems

The Ground Based Augmentation System (GBAS) is a development of local-area differential GNSS for augmenting airport applications, whose main purpose is to provide precision approach guidance for aircraft.

The system consists of three elements [21], shown in Figure 7:

- **The GNSS Space Segment** provides ranging signals and broadcasts navigation data (orbit and clock parameters, satellite health status, and other complementary information) to the ground facility and users. Current GBAS is based on GPS C/A signals transmitted on the L1 frequency band (1575.42 MHz).

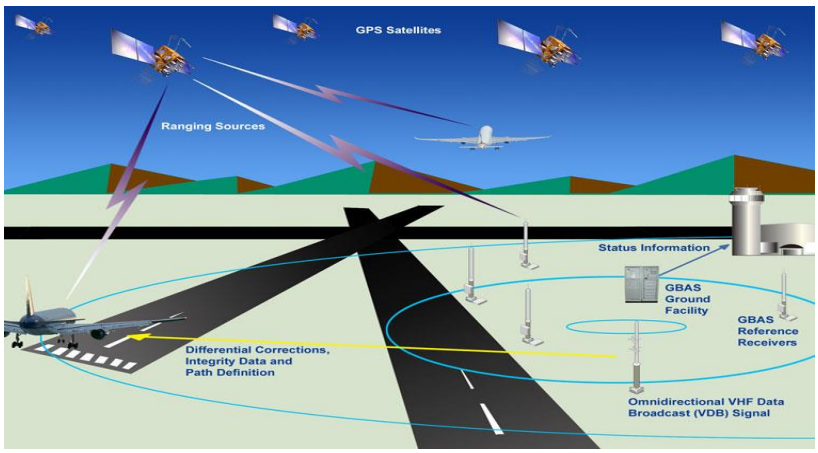

Figure 7. GBAS architecture (this figure is from https://www.faa.gov)

- **The GBAS Ground Subsystem** typically has three or more reference receivers with antennas installed at the airport area. The information generated by the receivers is sent to a central processor that calculates carrier-smoothed pseudorange differential corrections and integrity data. The processor also includes fault detection monitoring to ensure integrity in non-nominal conditions by excluding the affected measurements from the correction and integrity messages. As the service area is a local area, i.e. on the airport, the differential corrections and integrity data are transmitted to users as scalar values common for all GBAS users, on the contrary to the above mentioned SBAS. These differential corrections, the integrity parameters and the data on the precision approach trajectory points, are transmitted through of a Very High Frequency Data Transmission.

- **The GBAS equipment** in the aircraft uses the GPS signals collected by the GNSS receivers on board the aircraft and the differential pseudorange corrections transmitted by the GBAS ground station to determine its position relative to the approach path very accurately. Furthermore, it uses the integrity parameters received from the ground station to calculate conservative bounds of the residual position errors and ensure safety of the operation.

2.6.3 Aircraft-Based Augmentation System

While SBAS and GBAS provides integrity monitoring at the system level, in the Aircraft-Base Augmentation System (ABAS), the GNSS augmentation is fully performed on the aircraft, which is entirely responsible for the integrity monitoring.

There are two main approaches for ABAS: Range-domain approach and Position-domain approach:

Range-domain approach is what corresponds to the Classical RAIM (CRAIM or RAIM). It uses redundant range measurements from satellites in order to detect faulty signals and alert the pilot. It requires at least five satellites in view to detect a faulty satellite and six satellites

for Fault Detection and Exclusion (FDE). Its main drawback is that only can guarantee a reliable single-fault detection.

A barometric altimeter can be used as an additional measurement so that the number of ranging sources required for RAIM and FDE can be reduced by one.

Position-domain approach is what corresponds to the Advanced RAIM (ARAIM). It uses the Multiple Hypotheses Solution Separation (MHSS) approach, where the consistency test is performed in the position domain. ARAIM algorithm is able to provide reliable multiple-faults detection capabilities, but it requires higher computation load.

These two approaches CRAM and ARAIM are explained in detail in the next section.

3 Classical and Advanced RAIM User Algorithms

3.1 Classical RAIM (CRAIM)

This section describes the RAIM Fault Detection and Exclusion Algorithm implemented in the context of this dissertation.

3.1.1 Overview of CRAIM

Receiver Autonomous Integrity Monitoring (RAIM) is a receiver processing scheme that autonomously provides integrity monitoring for the position solution, using redundant range measurements. It is based on a FDE scheme that consists of two functions: Fault Detection (FD) and Fault Exclusion (FE). The fault detection part detects the presence of an unacceptably large position error for a given mode of flight. Upon detection of a large position error, FE follows and excludes the source of the error, thereby allowing the receiver to continue using GNSS without interruption.

Any FDE algorithm may be briefly outlined as follows. The receiver has to estimate p parameters (3 coordinates and 1 or more clocks, depending on single or multi-constellation measurements) and chooses n satellites in view, with ($n \geq p + 1$) for detection and ($n \geq p + 2$) for both detection and exclusion, where n is the number of satellite range measurements used in the position solution, and it performs a Weighted Least Squares (WLS) solution of position and clock offset(s) based on pseudorange measurements to the chosen n satellites. The range residual for each satellite is then obtained, which is the difference between its measured pseudorange and the pseudorange computed on the basis of the position and clock offset estimate using the chosen set of satellites. A test statistic for FD is then derived as a function of the range residuals. How to form a test statistic from the range residuals depends on the particular FDE scheme.

If the test statistic is within a predetermined threshold, the decision is *no failure* and CRAIM navigation continues. If the test statistic exceeds the threshold, a *failure* is declared internally and an attempt to exclude the faulty satellite is made. In order to understand the events that occur upon an exclusion attempt, one must make a distinction between a *detection* and an *alert*. A detection is declared internally upon detection of a fault by the FDE algorithm, whereas an *alert is an indication given externally to the user* (or to an integrated navigation system) that navigation cannot continue with an assurance that system integrity is provided. If exclusion succeeds, navigation may continue without raising an alert; otherwise, an alert is declared externally to the receiver.

In the following, FDE algorithm performance requirements are first described. This is then followed by a detailed procedure for calculation of FDE parameters. Finally, an FDE procedure is described.

3.1.2 FDE Algorithm Performance Requirements

Operational requirements for the receiver involve *False Alert probability* (P_{FA}), *Missed Alert probability* (P_{MA}) and Horizontal Protection Level (HPL). The Vertical Protection Level (VPL) can be also defined, depending on the navigation mode. The false alert rate must be controlled since it is directly related to availability and continuity. P_{MA} must be low enough to provide protection with sufficient confidence when large errors occur. The PLs are those values for which there will be an extremely low probability (i.e. P_{MA} times the probability of the occurrence of an abnormally large satellite range error) that the user position error will exceed this limit without a warning. For a primary means operation, the requirement for P_{FA} is $1 \times 10^{-5}/hr$ and that for P_{MA} is 1×10^{-3}.

From the above receiver operational requirements, the requirements for the operation of the FDE algorithm must be derived: Missed Detection probability (P_{MD}) and False Detection probability (P_{FD}). This conversion, however, requires knowledge of the fraction of time that exclusion is possible, which, in turn, requires knowledge about the operating satellite constellation, which varies as a function of time.

In the algorithm proposed in [22], P_{FD} and P_{MD} are selected as follows. For P_{FD}, a conservative approach is taken in which the false detection rate is equal to the false alert rate of $1 \times 10^{-5}/hr$. Indeed, since an alert will not be raised externally in case the faulty satellite can be excluded upon detection, the false alert rate would never be greater than $1 \times 10^{-5}/hr$.

When Selective Availability was enabled on GPS satellites, it was the most likely cause of false alerts and its effects were assumed to have a correlation time of two minutes. This corresponds a false alert rate of 0.333×10^{-6} per sample [22]. In the current conditions, without SA, the ionosphere becomes the largest error source, and the same value of two-minute correlation time can be assumed, due to its time correlation [23]. Then, on a per sample basis, a $P_{FD} = 0.333 \times 10^{-6}/sample$ value can be taken.

On the other hand, a P_{MD} of 1×10^{-3} equal to the P_{MA} requirement is chosen. Initially, a missed alert may occur not only upon occurrence of a failure but also after a wrong exclusion of the failed satellite. For this reason, P_{MA} could be slightly larger than P_{MD}. However, this increase is usually negligible. In addition, the probability of failure to detect an error much larger than XPL will be much lower than P_{MD}.

3.1.3 FDE Algorithm Parameters

Fault detection procedure involves three quantities: the test statistic, decision threshold, and Protection Levels (HPL, or HPL and VPL). The following subsections details how these three metrics are derived and used for fault detection.

3.1.3.1 Test statistic

While there currently exist a few different detection schemes, they are basically equivalent with no clear advantage of one over the other. The WLS scheme is used in the selected algorithm for the present PhD dissertation, which is described as follows.

A linearized equation can be derived relating changes in the measurements to the corresponding change in the user state vector in the following form:

$$\boldsymbol{y} = \boldsymbol{G}\,\boldsymbol{x} \tag{1}$$

where:

$\boldsymbol{y}$ is the prefit-residuals n-vector, containing the pseudorange measurements of n sources.

$\boldsymbol{x}$ is the unknown-parameters p-vector, containing the change in the user position state vector and clock unknowns.

$\boldsymbol{G}$ is the Geometry Matrix, $n \times p$, the linear connection matrix between $\boldsymbol{x}$ and $\boldsymbol{y}$.

Introducing the weighting matrix:

$$\boldsymbol{W} = \boldsymbol{C^{-1}} = \begin{bmatrix} \boldsymbol{\sigma_1^{-2}} & \cdots & \boldsymbol{0} \\ \vdots & \ddots & \vdots \\ \boldsymbol{0} & \cdots & \boldsymbol{\sigma_n^{-2}} \end{bmatrix}$$

Being $\boldsymbol{C}$ the covariance matrix of the measurements, assumed as diagonal, and σ_i the a priori standard deviation of error in the range measurement associated with the i^{th} ranging source (see Annex A.1.1).

Defining the vector $\boldsymbol{y_w}$ and matrix $\boldsymbol{G_w}$

$$\boldsymbol{y_w} = \sqrt{\boldsymbol{W}}\boldsymbol{y}$$

$$\boldsymbol{G_w} = \sqrt{\boldsymbol{W}}\boldsymbol{G},$$

the Eq. (1) left-multiplied vector and matrix by the squared-weighting matrix $\boldsymbol{W}$ becomes:

$$\boldsymbol{y_w} = \boldsymbol{G_w}\,\boldsymbol{x} \tag{2}$$

and the WLS solution is given by:

$$\hat{\boldsymbol{x}} = \left(\boldsymbol{G_w^T}\,\boldsymbol{G_w}\right)^{-1}\boldsymbol{G_w^T}\,\boldsymbol{y_w} = \boldsymbol{A_w}\,\boldsymbol{y_w} \tag{3}$$

where

$$\boldsymbol{A_w} \equiv \left(\boldsymbol{G_w^T}\,\boldsymbol{G_w}\right)^{-1}\boldsymbol{G_w^T} \qquad (p \times n \text{ matrix})$$

From the WLS solution, it follows the residual:

$$\boldsymbol{r_w} = \boldsymbol{y_w} - \boldsymbol{G_w}\,\hat{\boldsymbol{x}} = \boldsymbol{S_w}\,\boldsymbol{y_w} \tag{4}$$

where

$$\boldsymbol{S_w} \equiv \boldsymbol{I_n} - \boldsymbol{G_w}\,\boldsymbol{A_w} \qquad (n \times n \text{ matrix})$$

And the test statistic:

$$WSSE = \sqrt{\boldsymbol{r_w^T}\,\boldsymbol{r_w}} = \sqrt{(\boldsymbol{S_w}\,\boldsymbol{y_w})^T(\boldsymbol{S_w}\,\boldsymbol{y_w})}$$

The Weighted Sum of the Squared Errors ($WSSE$) test statistic has a Chi-distribution with $(n - p)$ degrees of freedom [22]. (Note: SSE^2 has a Chi-square-distribution). This statistic may also be obtained from other FDE schemes called parity space scheme of pbias, see [1] and [24] for more details.

3.1.3.2 Decision thresholds for fault detection

A detection threshold is typically set so that the P_{FD} requirement can be met in a no-failure condition. Since the test statistic in the WLS scheme has a central chi distribution with $(n-p)$ degrees of freedom (where n is the number of satellites used and p the number of parameters to estimate) in the absence of any signal source (satellite) failure, one can determine a threshold that would give precisely the P_{FD}. A set of thresholds is given next Table 3, as a function of the degrees of freedom, which is related to the number of satellites and constellations used.

Table 3. Fault detection decision thresholds (T_{FD})

Degrees of freedom for $WSSE$	T_{FD}: Decision threshold for s $P_{FD} = 0.333 \times 10^{-6}$
1	5.1045
2	5.4616
3	5.7391
4	5.9750
5	6.1858
6	6.3789
7	6.5576
8	6.7251
9	6.8834
10	7.0338

3.1.3.3 Example of Horizontal and Vertical Protection Levels (HPL, VPL)

The HPL is the radius of circle in the horizontal plane, with its center being at the true position, which describes the region that is assured to contain the indicated (i.e. estimated) horizontal position with the required P_{MD} and P_{FD}. The VPL is half the length of a segment on the vertical axis (perpendicular to the horizontal plane), with its centre being at the true position, which describes the region which is assured to contain the indicated (i.e. estimated) vertical position with the required P_{MD} and P_{FD}.

In general, different FDE algorithms may calculate PLs differently and could give somewhat different values of XPL_{FD} for the same user-to-satellite geometry. An PL_{FD} for use in the proposed algorithm is calculated following [25]:

$$HPL_{FD} = \max_i\{HSLOPE\ (i)\}\, T(n, P_{FD}) + k(P_{MD})\, HRMS\,,\ \ i = 1,2,\ldots,n$$

$$VPL_{FD} = \max_i\{VSLOPE\ (i)\}\, T(n, P_{FD}) + k(P_{MD})\, \sigma_V\,,\ \ i = 1,2,\ldots,n$$

where:

$$HSLOPE\ (i) = \frac{\sqrt{\boldsymbol{A}_{w1i}^2 + \boldsymbol{A}_{w2i}^2}}{\sqrt{\boldsymbol{S}_{wii}}}\ ,\ \ i = 1,2,\ldots,n$$

$$VSLOPE\ (i) = \frac{\left| \boldsymbol{A}_{w_{3i}} \right|}{\sqrt{\boldsymbol{S}_{w_{ii}}}}\ ,\ \ i = 1,2,\dots,n$$

with:

$$HRMS = \sqrt{[(\boldsymbol{G}_{\boldsymbol{w}}^{\boldsymbol{T}}\ \boldsymbol{G}_{\boldsymbol{w}}\ )^{-\mathbf{1}}]_{11} + [(\boldsymbol{G}_{\boldsymbol{w}}^{\boldsymbol{T}}\ \boldsymbol{G}_{\boldsymbol{w}}\ )^{-\mathbf{1}}]_{22}} = \sqrt{[\boldsymbol{A}_{\boldsymbol{w}}\ \boldsymbol{A}_{\boldsymbol{w}}^{\boldsymbol{T}}]_{11} + [\boldsymbol{A}_{\boldsymbol{w}}\ \boldsymbol{A}_{\boldsymbol{w}}^{\boldsymbol{T}}]_{22}}$$

$$\sigma_V = \sqrt{[(\boldsymbol{G}_{\boldsymbol{w}}^{\boldsymbol{T}}\ \boldsymbol{G}_{\boldsymbol{w}}\ )^{-\mathbf{1}}]_{33}} = \sqrt{[\boldsymbol{A}_{\boldsymbol{w}}\ \boldsymbol{A}_{\boldsymbol{w}}^{\boldsymbol{T}}]_{33}}$$

It is noted that only those geometries with PLs less than the horizontal/vertical Alert Limits (ALs) for a given mode of flight are considered to provide fault detection function in that mode of flight.

3.1.4 FD Protection Levels derivation

Let's consider the system, where the error term $\boldsymbol{\varepsilon}$ has been added to the equation (2)

$$\boldsymbol{y}_{\boldsymbol{w}} = \boldsymbol{G}_{\boldsymbol{w}}\ \boldsymbol{x} + \boldsymbol{\varepsilon} \tag{5}$$

where $\boldsymbol{\varepsilon}$ is the n-vector containing the pseudorange error to n satellites.

The WLS solution and residuals are given by equations (3) and (4):

$$\hat{\boldsymbol{x}} = \left(\boldsymbol{G}_{\boldsymbol{w}}^{\boldsymbol{T}}\ \boldsymbol{G}_{\boldsymbol{w}}\right)^{-\mathbf{1}} \boldsymbol{G}_{\boldsymbol{w}}^{\boldsymbol{T}}\ \boldsymbol{y}_{\boldsymbol{w}} = \ \boldsymbol{A}_{\boldsymbol{w}}\ \boldsymbol{y}_{\boldsymbol{w}} \tag{6}$$

$$\boldsymbol{r}_{\boldsymbol{w}} = \boldsymbol{y}_{\boldsymbol{w}} - \boldsymbol{G}_{\boldsymbol{w}}\ \hat{\boldsymbol{x}} = \boldsymbol{S}_{\boldsymbol{w}}\ \boldsymbol{y}_{\boldsymbol{w}} \tag{7}$$

Let $\boldsymbol{x}$ be the true receiver position, then from (5) and (6), the effect of a range error $\boldsymbol{\varepsilon}$ on the positioning error $\boldsymbol{e}$ is given by:

$$\boldsymbol{e} = \boldsymbol{x} - \hat{\boldsymbol{x}} = \left(\boldsymbol{G}_{\boldsymbol{w}}^{\boldsymbol{T}}\ \boldsymbol{G}_{\boldsymbol{w}}\right)^{-\mathbf{1}} \boldsymbol{G}_{\boldsymbol{w}}^{\boldsymbol{T}}\ \boldsymbol{\varepsilon} = \ \boldsymbol{A}_{\boldsymbol{w}}\ \boldsymbol{\varepsilon}$$

In the same way, substituting (5) in (7), the effect of $\boldsymbol{\varepsilon}$ in the residual it follows:

$$\boldsymbol{r}_{\boldsymbol{w}} = \boldsymbol{y}_{\boldsymbol{w}} - \boldsymbol{G}_{\boldsymbol{w}}\ \hat{\boldsymbol{x}} = \boldsymbol{S}_{\boldsymbol{w}}\ \boldsymbol{\varepsilon}$$

Assuming that error vector $\boldsymbol{\varepsilon}$ contains a bias b_i affecting to a single satellite $\boldsymbol{\varepsilon} = (0, \dots, b_i, \dots, 0)$

$$\boldsymbol{e} = \boldsymbol{A}_{\boldsymbol{w}}\ \boldsymbol{\varepsilon} = \begin{bmatrix} A_{w_{1,1}} \cdots & A_{w_{1,i}} & \cdots A_{w_{1,n}} \\ \vdots & \ddots \ \vdots & \\ \vdots & \cdots A_{w_{k,i}} \cdots & \vdots \\ & \vdots \ \ddots & \\ A_{w_{p,1}} \cdots & A_{w_{n,i}} & \cdots A_{w_{p,n}} \end{bmatrix} \begin{bmatrix} 0 \\ \vdots \\ b_i \\ \vdots \\ 0 \end{bmatrix} = b_i \begin{bmatrix} A_{w_{1,i}} \\ \vdots \\ A_{w_{k,i}} \\ \vdots \\ A_{w_{n,i}} \end{bmatrix}$$

Then, it can be taken:

$$\|\boldsymbol{e}_H\| = b_i \sqrt{\boldsymbol{A}_{\boldsymbol{w}_{1i}}^{\mathbf{2}} + \ \boldsymbol{A}_{\boldsymbol{w}_{2i}}^{\mathbf{2}}} \tag{8}$$

$$\|\boldsymbol{e}_V\| = b_i \left| \boldsymbol{A}_{\boldsymbol{w}_{3i}} \right| \tag{9}$$

In the same way:

$$\boldsymbol{r_w} = \boldsymbol{S_w}\,\boldsymbol{\varepsilon} = \begin{bmatrix} S_{w_{1,1}} & S_{w_{1,i}} & S_{w_{1,n}} \\ & \vdots & \\ \vdots & S_{w_{k,i}} & \vdots \\ & \vdots & \\ S_{w_{n,1}} & S_{w_{n,i}} & S_{w_{n,n}} \end{bmatrix} \begin{bmatrix} 0 \\ \vdots \\ b_i \\ \vdots \\ 0 \end{bmatrix} = b_i \begin{bmatrix} S_{w_{1,i}} \\ \vdots \\ S_{w_{k,i}} \\ \vdots \\ S_{w_{n,i}} \end{bmatrix}$$

$$\|\boldsymbol{r_w}\| = b_i \sqrt{(\boldsymbol{S_w^T}\,\boldsymbol{S_w})_{\boldsymbol{ii}}} = b_i \sqrt{S_{w_{i,i}}} \tag{10}$$

Notice that matrix $\boldsymbol{S_w}$ is a symmetrical ($\boldsymbol{S_w^T} = \boldsymbol{S_w}$) and idempotent ($\boldsymbol{S_w^2} = \boldsymbol{S_w}$) matrix, as it is a Projection Matrix.

From (8), to (10), the positioning errors $\|\boldsymbol{e}_H\|$ and $\|\boldsymbol{e}_V\|$ can be estimated from the residual $\|\boldsymbol{r_w}\|$ and the satellite geometry for any bias term b_i affecting only to a single satellite by:

$$\|\boldsymbol{e}_H\| = HSLOPE\ (i)\ \|\boldsymbol{r_w}\|$$

$$\|\boldsymbol{e}_V\| = VSLOPE\ (i)\ \|\boldsymbol{r_w}\|$$

where:

$$HSLOPE\ (i) = \frac{\sqrt{\boldsymbol{A}_{\boldsymbol{w}1i}^{\,2} + \boldsymbol{A}_{\boldsymbol{w}2i}^{\,2}}}{\sqrt{\boldsymbol{S}_{\boldsymbol{w}_{ii}}}}\ ,\ \ i = 1,2,\ldots,n$$

$$VSLOPE\ (i) = \frac{|\boldsymbol{A}_{\boldsymbol{w}_{3i}}|}{\sqrt{\boldsymbol{S}_{\boldsymbol{w}_{ii}}}}\ ,\ \ i = 1,2,\ldots,n$$

and

$$\|\boldsymbol{r_w}\| = \sqrt{\boldsymbol{r_w^T}\,\boldsymbol{r_w}}$$

3.1.4.1 Statistic test

In nominal conditions, $\boldsymbol{\varepsilon}$ is assumed to follow a zero mean (unbiased) Normal distribution $N(0,\sigma)$, and thence, the WLS residual is assumed to follow a Chi-distribution (χ) with $(n-p)$ degrees of freedom, where n is the number of ranging sources (satellites) and p the number of parameters to estimate.

Thus a threshold $T_{FD} = T(n, P_{FD})$ can be chosen for a given probability of false detection for χ, as a function of the $n-p$ degrees of freedom; that is, the probability that, having no any bias in $\boldsymbol{\varepsilon}$, the residual exceeds the threshold T_{FD}.

Then, a Fault Detection event can be declared, with a false detection probability (P_{FD}), when the residual $WSSE = \|\boldsymbol{r_w}\|$ exceeds the threshold T_{FD}, $WSSE \geq T_{FD}$. Or, what is the same, the no fault detection condition (i.e. nominal case) is given by:

$$WSSE < T_{FD}$$

3.1.4.2 Protection Levels

From (6) and (7), the effect of a bias $b_i = T_{FD}$ in the Horizontal and Vertical positioning errors is mapped by the geometric slope factors, $SLOPE\ (i)$.

Then, taking the worst geometries, i.e. $\max_i\{SLOPE\ (i)\}$, the larger error produced by a bias $b_i = T_{FD}$ will be less than $\max_i\{SLOPE\ (i)\}\ T(n, P_{FD})$.

So, the next protection levels can be defined:

$$HPL_{FD} = \max_i\{HSLOPE\ (i)\}\ T(n, P_{FD}) + k(P_{MD})\ HRMS\,,\quad i = 1,2,\ldots,n$$

$$VPL_{FD} = \max_i\{VSLOPE\ (i)\}\ T(n, P_{FD}) + k(P_{MD})\ \sigma_V\,,\quad i = 1,2,\ldots,n$$

where the additional terms $k(P_{MD})\ HRMS$ and $k(P_{MD})\ \sigma_V$ have been added to the protection levels to account for the measurement noise, being $k(P_{MD})$ the number of standard deviations corresponding to a given probability of miss detection (P_{MD}), i.e. due to the measurement noise.

Figure 8, based in [25], illustrates the concept.

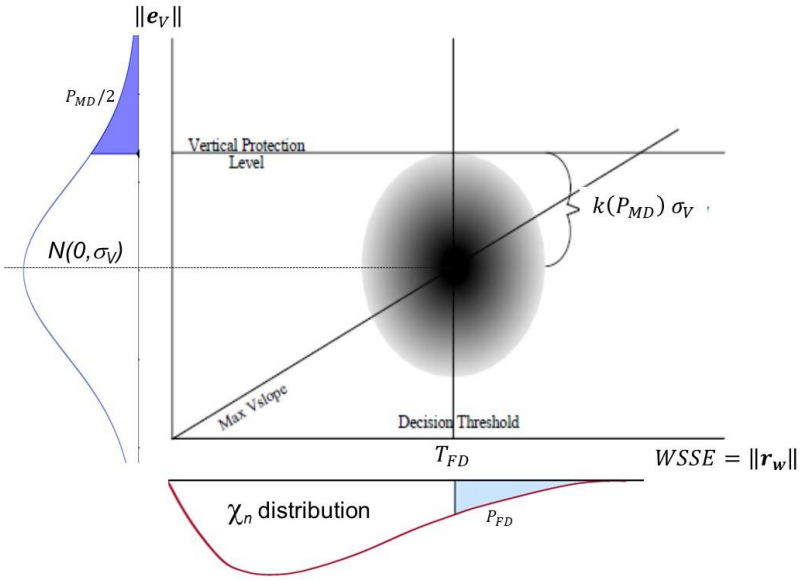

Figure 8. The distribution of vertical errors (vertical axis) and the RAIM statistic (horizontal axis) is shown for a given failed satellite.

3.2 Advanced RAIM (ARAIM)

One strong disadvantage of the Classical RAIM algorithms is that they do not provide reliable multiple-faults detection capabilities. Faults on more than one pseudorange tend to cancel out each other. This makes very hard to detect multiple simultaneous faults. Indeed, outliers need to be very significant for detecting them.

With the deployment of new GNSS constellations and new signals, there is a great interest in extending the role of RAIM in the navigation of aircrafts. However, more constellations and satellites increase the probability of multiple simultaneous faults. This challenge has led to the development of the Advanced Receiver Autonomous Integrity Monitoring (ARAIM).

ARAIM is an integrity algorithm based on Multiple Hypothesis Solution Separation (MHSS). It forms many solutions from different subsets of GNSS measurements and can detect and mitigate a wide variety of different faults, including situations where multiple faults or failures occur simultaneously. One of the drawbacks of ARAIM is that it is potentially computationally expensive, demanding the calculation of many subset navigation solutions. However, recent research has found ways to greatly reduce this computational cost [26].

ARAIM typically makes use of the dual-frequency ionosphere-free combination of smoothed pseudoranges. Additionally, unlike any SBAS, ARAIM does not use differential corrections; the accuracy depends on the large number of satellites in view due to the multi-constellation. The integrity information is provided to ARAIM users by the Integrity Support Message (ISM), which characterises the GNSS performance with respect to integrity and accuracy. The ISM contains two sets of parameters: the a priori satellite and constellation fault probabilities, P_{sat} and P_{const}, and the un-faulted error bounds (σ_{URA}, σ_{URE} and b_{nom}), to overbound satellite range errors. The σ_{URA} is used for integrity and σ_{URE} for accuracy. The bias parameter b_{nom} is the maximum nominal bias of a satellite.

I have contributed to the implementation of the ARAIM algorithms defined in [27, 28] in the in-home navigation tool gNAV, in FORTRAN-77. These algorithms are also codded, in MATLAB, in the Algorithm Availability Simulation Tool (MAAST) provided by Stanford GPS Lab [29], and in the Integrity Support Tool for Advanced RAIM (ISTAR) [28], from the Institute of Space Technology and Space Applications (ISTA). These tools have been very useful not only to crosscheck results, but also to clarify the ARAIM algorithms.

The Fault Exclusion function, not available in the public version of MAAST or in ISTAR, has also been implemented in gNAV.

3.2.1 Overview of ARAIM

The ARAIM user algorithm generates a list of $N_{fault\ modes}$ (subsets of all-in-view satellites, see section 3.2.2.2) that shall be monitored for a pre-defined fraction of the total integrity budged P_{THRES}, and assigns an a priory probability of being faulty to each fault mode ($P_{fault,m}$). This probability is calculated based on the P_{sat} and P_{const} of the ISM.

The target is to make sure that the sum of the probabilities of the un-selected modes, i.e. those that are not monitored, does not exceed the probability threshold P_{THRES}. That is, the Risk of Not Monitoring more than $N_{fault\ modes}$ is less than P_{THRES}.

The monitor chosen to protect against the list of fault modes is the Multiple Hypothesis Solution Separation (MHSS). Indeed, for each fault mode, the subset solution is computed. Then, the differences between the all-in-view and the subsets solutions, for each error component (E,N,U) separately, are used as a statistic test to perform real-time detection and to compute the position error bounds that satisfy the system requirements, see Figure 9.

$$\left| \hat{x}_q^{(k)} - \hat{x}_q^{(0)} \right| \leq T_{k,q}, \qquad k = 1, \dots, N_{fault\ modes}, \ \ q = 1,2,3$$

where $\hat{x}_q^{(0)}$ corresponds to the all-in-view solution and q to each error component (E,N,U).

The thresholds $T_{k,q}$ are given by $T_{k,q} = K_{fa_q}\, \sigma_{ss_q}^{(k)}$, where $\sigma_{ss_q}^{(k)}$ is the standard deviation of the difference between the all-in-view position solution $\hat{x}_q^{(0)}$ and the fault-tolerant position solution $\hat{x}_q^{(k)}$.

If any of these MHSS tests fails for any of the error components ($q = 1,2,3$), the all-in-view solution is declared not valid and exclusion must be attempted.

A second test based on the χ^2 statistic is applied for the all-in-view solution. This test is a sanity check not computationally expensive and can detect faults that are outside the thread model considered in ARAIM.

$$Chi2^{(0)} \leq T_{\chi^2}^{(0)}$$

Protection levels can only be computed when all MHSS tests and the χ^2 test for the all-in-view solution ($Chi2^{(0)}$), are both valid. Indeed, if none of the MHSS tests has failed, but the chi-square statistic is larger than expected, the PLs cannot be considered valid and neither exclusion cannot be attempted.

Protection Levels (PL_q), are determined by the integrity requirement ($PHMI$) where it must be guaranteed that the integrity risk contributions from all fault modes is below the total integrity risk $PHMI$. The PL_q are calculated separately for each error component (see next section).

$$\sum_{q=1}^{3} \left[2\bar{Q}\left(\frac{PL_q - b_q^{(0)}}{\sigma_q^{(0)}} \right) + \sum_{k=1}^{Nfaut\ modes} P_{fault,k}\, \bar{Q}\left(\frac{PL_q - b_q^{(k)} - T_{k,q}}{\sigma_q^{(k)}} \right) \right] \leq PHMI$$

where $\bar{Q}$ is the modified Q function, $\bar{Q}(z) = \begin{cases} Q(z); & z > 0 \\ 1 & ; z \leq 0 \end{cases}$, and Q is the zero-mean, unit variance Gaussian distribution $Q(z) = \frac{1}{\sqrt{2\pi}} \int_z^{\infty} e^{-\frac{t^2}{2}}\, dt$, i.e. $Q(z) =$ normcdf(−z) in MATLAB.

The first item in the summation, at left, is the Fault Free (FF) case and the factor is 2 because both tails of the error distribution need to be accounted for. The second item is the sum of every fault mode (FM), weighted by the corresponding fault probability $P_{fault,k}$. In the case of FMs, only one side needs to be considered.

For the navigation mode denoted localizer performance with vertical guidance down to 200 feet (LPV-200) defined in the ICAO technical report [13], two additional monitors are considered:

- The Effective Monitor Threshold (EMT), defined as the maximum of the detection thresholds that have a prior probability equal or above P_{EMT}.

$$EMT = \max_{k|P_{fault,k} \geq P_{EMT}} \{T_{k,3}\}$$

- The standard deviation of the vertical position of the user solution $\sigma_{V,acc}$.

3.2.1.1 Continuity and Integrity

The continuity risk (P_{FA}) and integrity budget ($PHMI$) are allocated between the fault modes and position components as follows:

Continuity risk: Detection Thresholds

The False Alert (FA), or Fault Free (FF) detection risk, is typically referred to as continuity risk in avionics, since the false alerts are the major source of service interruptions.

The Detection Thresholds $T_{k,q}$ of the MHSS test are determined from the continuity risk allocation:

$$\sum_{q=1}^{3} 2\, N_{fault\ modes}\ Q\left(K_{fa_q}\right) \leq P_{FA}$$

As already commented in PL equation, the factor 2 is necessary because the two tails of error distribution must be accounted for the FF case, see Figure 9.

The continuity risk (P_{FA}) is split in the horizontal and vertical components, see section 3.2.2.8:

$$T_{k,q} = K_{fa_q} \sigma_{ss_q}^{(k)}$$

$$K_{fa,1} = K_{fa,2} = Q^{-1}\left(\frac{P_{FA_{HOR}}}{4\, N_{fault\ mode}}\right) \quad ; \quad K_{fa,3} = Q^{-1}\left(\frac{P_{FA_{VER}}}{2 N_{fault\ mode}}\right)$$

where $\sigma_{ss_3}^{(k)}$ reflects the difference between the all-in-view position solution and the fault-tolerant position, and being K_{fa_q} the number of standard deviations used for the continuity/availability risk (fault free) position error in the q-th component.

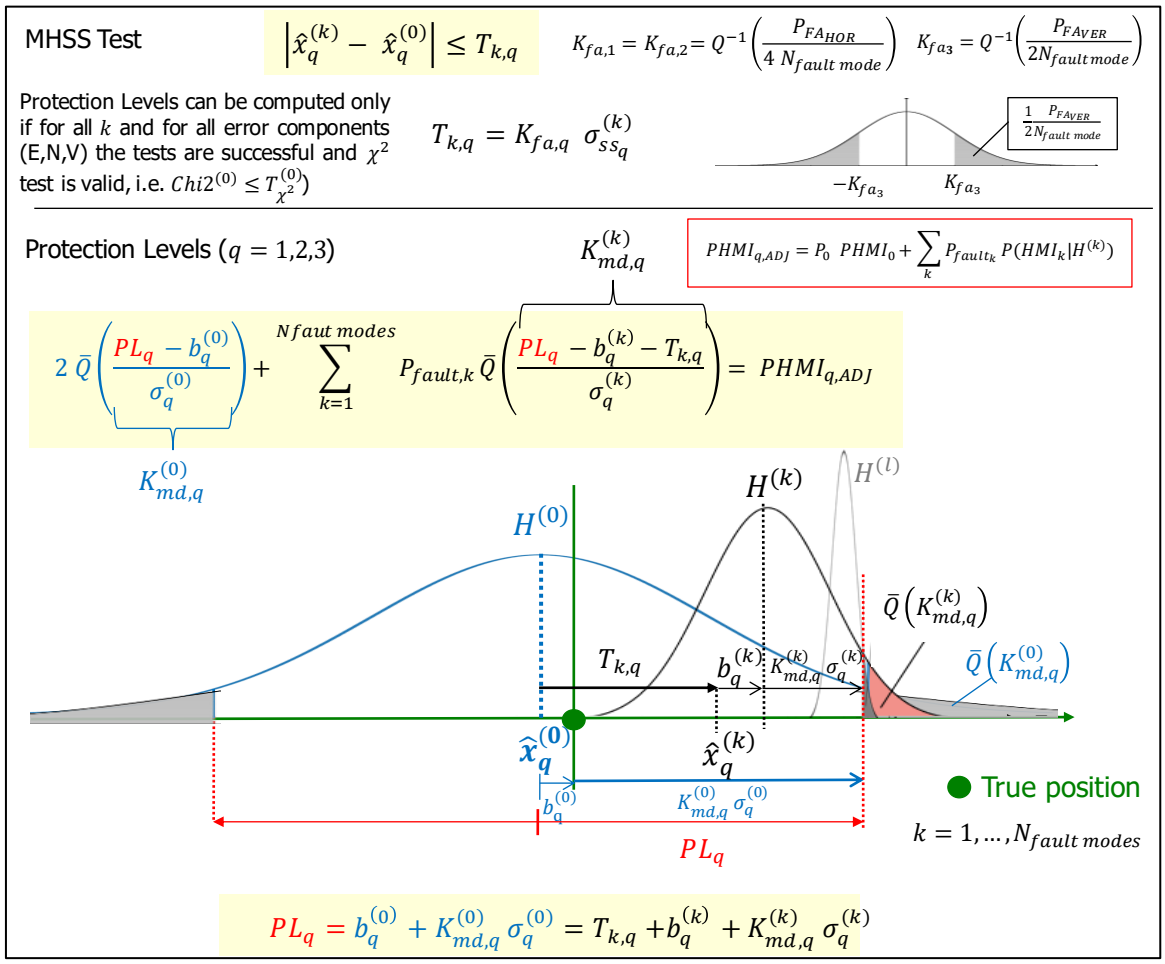

Figure 9. Layout of the MHSS test and Protection Levels equation. For each error component ($q = 1,2,3$) the PL is determined by the integrity requirement ($PHMI_{q,ADJ}$), which is distributed across the all-in-view mode and the different fault modes. Each term in the PL equation is an upper bound of the contribution of each mode to the integrity risk.

Integrity budget: Protection Levels

As commented before, a protection level (PL_q, $q = 1,2,3$) is calculated separately for each error component q.

The following equation provides the Protection Levels that meet the required integrity allocations ($PHMI = PHMI_{HOR} + PHMI_{VER}$).

$$2\,\bar{Q}\left(\frac{PL_q - b_q^{(0)}}{\sigma_q^{(0)}}\right) + \sum_{k=1}^{Nfaut\ modes} P_{fault,\,k}\,\bar{Q}\left(\frac{PL_q - b_q^{(k)} - T_{k,q}}{\sigma_q^{(k)}}\right) = PHMI_{q,\,ADJ}\ ; \quad q = 1,2,3$$

where $PHMI_{q,ADJ}$ is the total allocated integrity budged for each error component, adjusted by the residual probabilities not covered by the threat model considered ($P_{not\ monitored}$).

$$PHMI_{1,ADJ} = PHMI_{2,ADJ} = \frac{PHMI_{HOR}}{2}\left(1 - \frac{P_{not\ monitored}}{PHMI_{HOR} + PHMI_{VER}}\right)$$

$$PHMI_{3,ADJ} = PHMI_{VER}\left(1 - \frac{P_{not\ monitored}}{PHMI_{HOR} + PHMI_{VER}}\right)$$

Figure 9 illustrates the Protection Levels equation. The first term at the left hand side, in blue, corresponds to the all in view solution and the sum is extended to all monitored fault modes, in black, which are weighted by their associated probabilities $P_{fault,m}$. The graphic at the bottom depicts the biased probability distributions for the different modes and their allocated probabilities $\bar{Q}\left(K_{md,q}^{(k)}\right)$ after the protection level threshold.

Optimal allocation of integrity risk between fault modes, provides lower protections levels and leads to higher algorithm performance.

Finally, it is worth to say that PL also depend on the Continuity Risk through the thresholds $T_{k,q}$, defined for the MHSS test.

Remarks:

1. Classical RAIM and ARAIM Protection levels estimation are based on next equations (e.g. VPL):

   CRAIM: $VPL_{FD} = \max_{i=1,\ldots,Nsat}\{VSLOPE\ (i)\}\, T(n, P_{FD}) + k(P_{md})\,\sigma_V$

   ARAIM: $VPL = T_{k,3} + K_{md,3}^{(k)}\ \sigma_3^{(k)} + b_3^{(k)}$ (see more details above)

   Then, the main differences of PL estimation in ARAIM regarding to the CRAIM concepts are:
   - The determination of $K_{md,3}$ accounts for the a priori probability of the fault modes.
   - The worst-case bias impacting on the position solution is considered as:

$$b_3^{(k)} = \sum_{i=1}^{Nsat} \left|A_3^{(k)}\right| b_{nom_i}$$

2. In the classical RAIM it is assumed that the constellation fault probability is zero, and satellite fault probability is 10^{-5}, and there are rarely more than 14 satellites in view. That is, it assumes that the probability of two or more simultaneous satellite faults is negligible ($< 10^{-8}$), see [16].

3.2.2 Algorithm Description

Figure 10 shows a layout of the ARAIM algorithm implemented in the gNAV FORTRAN tool.

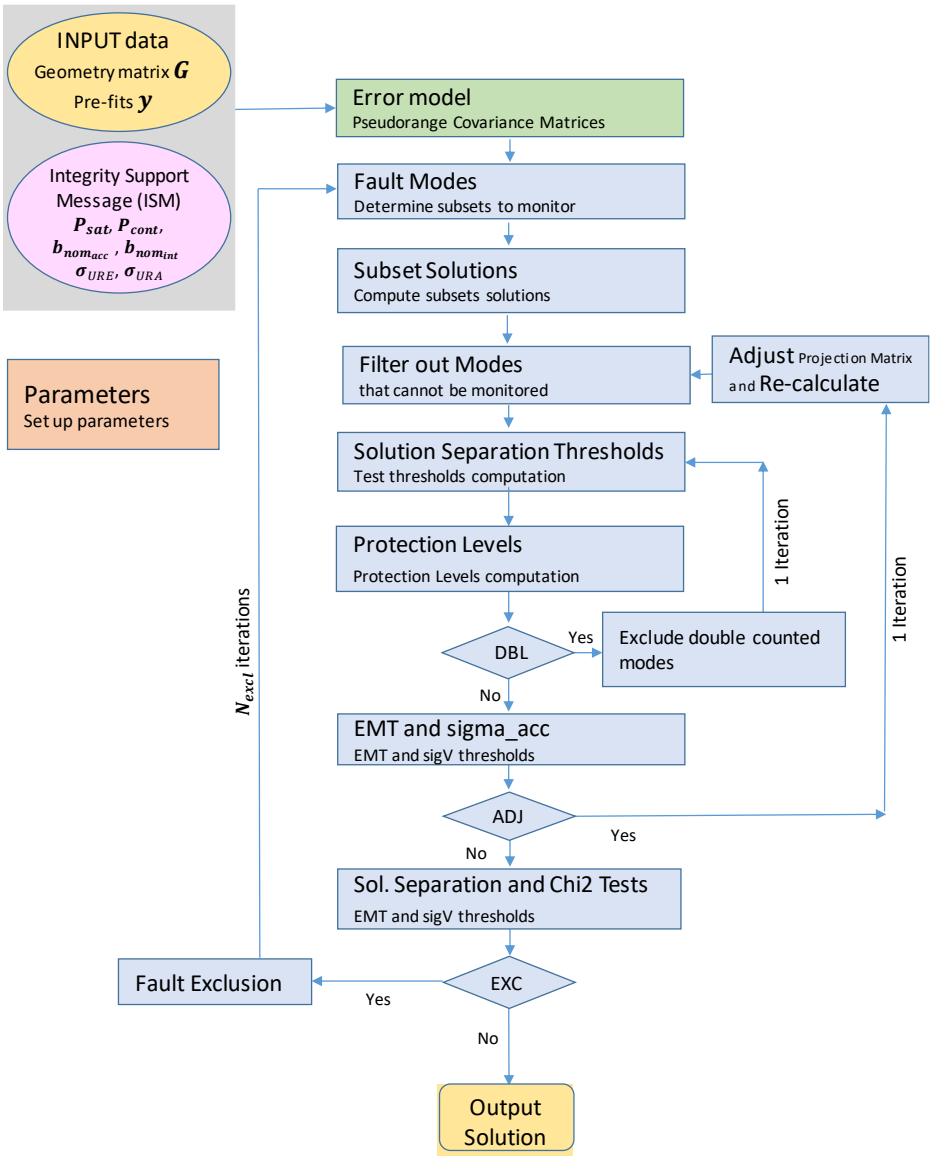

Figure 10. Layout of the ARAIM algorithm implemented in the gNAV FORTRAN tool.

The different elements of the algorithms are described in Annex E with a driving example to illustrate the main concepts.

3.2.2.1 Error Model

To simplify the reading of the dissertation, the error model is left to Annex A.

3.2.2.2 Fault Modes

There are many possible different causes of faults on the GNSS satellites. The probability $P_{sat,i}$ describes independent satellite faults (i.e. Narrow Faults) in such a way that the probability of having two satellites affected simultaneously by such independent fault modes is not greater than $P_{sat,i} \times P_{sat,j}$ [1]. These are faults that may occur on board one satellite and have no effect on the other satellites. On the other hand, P_{const} is the probability of constellation faults (i.e. Wide Faults), which are when two or more satellites of a given constellation are in fault mode due to a common cause, e.g. due to control segment or design errors [30].

The determination of faults modes (or subsets) that need to be monitored and their associated probabilities involves two steps:

1. *Preselection of subsets to monitor:*
   a) Starting with $n = 0$, generate subsets with n failures in an array of $Nsat + Nconst$ elements, i.e. combinations with "n" ones and "$Nsat + Nconst - n$" zeroes.
   b) After sorting the combinations by decreasing probability, a set of combinations is selected in such a way that the probability of not monitoring the non-selected combinations is less than the P_{THRES} threshold.
   c) If all combinations with n failures are selected, the algorithm is iterated for $n + 1$.

   As a result, a set of preselected combinations (or subsets) to monitor "$N_{fault\ modes}$" is defined, together with an updated value of $P_{not\ monitored}$. The maximum number of faults to monitor is then $N_{fault\ max} = n$.

   See more details and the selected fault modes in Figure 39 and Figure 40 in Annex E.

2. *Subsets consolidation*: Two different cases are considered:
   a. *Unique subset assimilation*: As a result of the process used to generate the fault modes, several identical combinations can appear. When this happens, identical combinations must be assimilated to a "unique subset fault" with probability equal to the added probability of all such combinations.

   b. *Two or more satellite faults within the same constellation assimilation:*
   In this case, the multiple satellite faults are assimilated to the wide-fault and their probabilities ($P_{fault,k}$) added to the wide-fault and probability (P_{fault,k_j}), provided that their added probability is under the threshold $\mathrm{FC_{THRES}}$ P_{fault,k_j}. See [31].

   The purpose of this step involving the parameter $\mathrm{FC_{THRES}}$ is to consolidate low probability faults within a constellation into the constellation wide fault. This allows to reduce the number of subsets to monitor, where the $\mathrm{FC_{THRES}}$ parameter regulates for which size parameter the faults are consolidated or not.

   See the consolidated fault modes and the associated satellite combinations in Figure 41 and Figure 42 in Annex F.

Table 4. Maximum number of simultaneous satellite faults to be monitored by user algorithm (this table is from [28])

P_{sat}/N_{sat}	10	15	20	25	30	35	40
10^{-3}	3	3	3	3	3	3	4
10^{-4}	2	2	2	2	2	2	2
10^{-5}	1	1	1	1	1	1	1
10^{-6}	1	1	1	1	1	1	1

Table 5. Maximum number of simultaneous constellation faults to be monitored by user algorithm (this table is from [28])

N_{cons}/P_{const}	10^{-4}	10^{-5}	10^{-6}	10^{-7}	10^{-8}
2	1	1	1	1	0
3	2	2	2	2	0

The maximum number of simultaneous satellite and constellation faults to be monitored, as a function of P_{sat} or P_{const} and the number of satellites N_{sat} or constellations N_{const} are given in Table 4 and Table 5.

3.2.2.3 Subsets Solutions

The solutions $\hat{\boldsymbol{x}}^{(k)}$ for the different combinations (subsets) $k = 0, \dots, N_{fault\ modes}$ are calculated, together with their formal accuracy (i.e. standard deviation) and worst-case impact of nominal biases, and the differences between the subsets solutions $\hat{\boldsymbol{x}}^{(k)}$ and all-in-view solution $\hat{\boldsymbol{x}}^{(0)}$ are obtained. The χ^2 statistic and associated threshold for each combination is also calculated.

3.2.2.3.1 Defining matrices and vectors

Pre-fits vector $\boldsymbol{y}$ and Geometry Matrix $\boldsymbol{G}$ are first normalised by the square-root of covariance matrix for integrity (see Annex A.1.2):

$$\boldsymbol{y_w} = \sqrt{\boldsymbol{W_{int}}}\,\boldsymbol{y} \quad ; \quad \boldsymbol{G_w} = \sqrt{\boldsymbol{W_{int}}}\,\boldsymbol{G}$$

where

$$\boldsymbol{W_{int}} = \begin{bmatrix} \sigma_1^{-2} & \cdots & 0 \\ \vdots & \ddots & \vdots \\ 0 & \cdots & \sigma_n^{-2} \end{bmatrix} \text{ , with } \sigma_i^2 = \boldsymbol{C_{int}}(i,i)$$

The symmetric matrix $\boldsymbol{G_w^T}\,\boldsymbol{G_w}$ is calculated and the indices of its columns having all entries as zero are identified. These columns are removed in matrices $\boldsymbol{G_w^T}\,\boldsymbol{G_w}$ in the $\boldsymbol{G_w}$.

3.2.2.3.2 Calculating subsets solutions

For each combination (satellites subset) $k = 0, \dots, N_{fault\ modes}$:

1. *Calculate* $\boldsymbol{A_w^{(k)}}$ *the weighted projection matrix for each satellite subset* k.

   a. Matrix $\boldsymbol{G_w^{(k)T}}\,\boldsymbol{G_w^{(k)}}$ is calculated and columns of with zeroes in $\boldsymbol{G_w^{(k)T}}\,\boldsymbol{G_w^{(k)}}$ are removed in $\boldsymbol{G_w^{(k)}}$ and $\boldsymbol{G_w^{(k)T}}\,\boldsymbol{G_w^{(k)}}$ matrices.

Calculate $\boldsymbol{A_w^{(k)} = \left(G_w^{(k)T}\, G_w^{(k)}\right)^{-1} G_w^{(k)T}}$ for the given subset k.

2. *Calculate $\sigma_q^{(k)}$, $b_q^{(k)}$, navigation solution $\hat{\boldsymbol{x}}^{(k)}$ and residuals $\boldsymbol{r_w^{(k)}}$ for each subset k.*

Taking: $\boldsymbol{A^{(k)} = \sqrt{W_{int}}\, A_w^{(k)}}$ (i.e. the unweighted matrix $\boldsymbol{A^{(k)}}$).

$$\sigma_q^{(k)} = \sqrt{\left(A^{(k)}\, C_{int}\, A^{(k)T}\right)_{qq}} = \sqrt{\left[A_w^{(k)}\, A_w^{(k)T}\right]_{qq}} = \sqrt{\left[\left(G_w^{(k)T}\, G_w^{(k)}\right)^{-1}\right]_{qq}} \quad ;\ q = 1,2,3$$

$$b_q^{(k)} = \sum_{i=1}^{Nsat} \left|A_{q_i}^{(k)}\right| b_{nom,i} = \sum_{i=1}^{Nsat} \sqrt{(W_{int})_{ii}}\, \left|A_{w_{q_i}}^{(k)}\right| b_{nom,i} \quad ;\quad q = 1,2,3$$

$$\hat{\boldsymbol{x}}^{(k)} = A_w^{(k)}\, y_w = \left(G_w^{(k)T}\, G_w^{(k)}\right)^{-1} G_w^{(k)T}\, y_w$$

$$\boldsymbol{r_w^{(k)} = y_w - G_w^{(k)}\, \hat{x}^{(k)}}$$

$$Chi2^{(k)} = \boldsymbol{r_w^{(k)T}\, D\, r_w^{(k)}}$$

$$\boldsymbol{D} = \begin{bmatrix} \delta_1 & \cdots & 0 \\ \vdots & \ddots & \vdots \\ 0 & \cdots & \delta_{Nsat} \end{bmatrix} \qquad \delta_i = \begin{cases} 1\ satellite\ in\ subset \\ 0\ excluded\ satellite \end{cases}$$

3. Calculate σ_{ss} for each satellite subset k.

$$\boldsymbol{\Delta A^{(k)} = A^{(k)} - A^{(0)} = \sqrt{W_{int}}\left(A_w^{(k)} - A_w^{(0)}\right)}$$

$$\sigma_{ss,q}^{(k)} = \sqrt{\left(\boldsymbol{\Delta A^{(k)}\, C_{acc}\, \Delta A^{(k)T}}\right)_{qq}} \ ;\ q = 1,2,3$$

$$\boldsymbol{C_{acc}} = \begin{bmatrix} \sigma_1^2 & \cdots & 0 \\ \vdots & \ddots & \vdots \\ 0 & \cdots & \sigma_{Nsat}^2 \end{bmatrix} \qquad \text{with} \quad \sigma_i^2 = \boldsymbol{C_{acc}}(i,i)$$

Notice that matrix $\boldsymbol{A_w^{(k)}}$ was previously weighted with the covariance matrix for integrity $\boldsymbol{W_{int}}$.

Note: Matrices $\boldsymbol{A^{(0)}}$ or $\boldsymbol{A_w^{(0)}}$ correspond to the all-in-view satellites set.

See Figure 43 and Figure 44 in Annex E.

3.2.2.4 Filter out modes that cannot be monitored

Among the subsets determined before, there could be some that cannot be monitored, because the remaining satellites do not allow the receiver to compute the position. In this case, these events must be removed from the list of faults, and their integrity risk must be subtracted from the available budget. This happens when the number of satellites is less than the number of parameters to estimate.

The next procedure has been applied:

1. Find subsets that cannot be monitored:
   These not monitored subsets are excluded form list.

2. Update the monitored subsets (k) and vectors $P_{fault,k}$, $\sigma_q^{(k)}$, $b_q^{(k)}$, $\sigma_{ss}^{(k)}$, $\boldsymbol{A}^{(k)}$, $\boldsymbol{\Delta A}^{(k)}$ solution $\hat{\boldsymbol{x}}^{(k)}$, residuals $\boldsymbol{r}_{\boldsymbol{w}}^{(k)}$ and $Chi2^{(k)}$.

3. Update the probability $P_{not\ monitored}$ by adding the $P_{fault,k}$ of the excluded subsets

$$P_{fault\ not\ monitored\ ,updated} = P_{fault\ not\ monitored} + \sum_{k \in I_{excl}} P_{fault,k}$$

In the driving example of Annex E, no modes are necessary to filter out.

3.2.2.5 Solution Separation Thresholds

For each fault mode, there are three solution separation threshold tests, one for each coordinate (E,N,U). This module, determines these thresholds as follows [27]:

$$T_{k,q} = K_{fa_q} \sigma_{ss_q}^{(k)}$$

$$K_{fa_1} = K_{fa_2} = Q^{-1}\left(\frac{P_{FA_{HOR}}}{4\ N_{fault\ modes}}\right); \quad K_{fa_3} = Q^{-1}\left(\frac{P_{FA_{VER}}}{2N_{fault\ modes}}\right)$$

where $Q^{-1}(p)$ is the inverse of function Q, defined above.
Note: $Q^{-1}(p) = -$ norminv(p) *in MATLAB.*

Comment: Protection Levels can be computed only if for all k and q is:

$$\left| \hat{x}_q^{(k)} - \hat{x}_q^{(0)} \right| \leq T_{k,q}$$

If any of these tests fails, exclusion must be attempted.

See results for the driving example in Figure 47 in Annex E.

3.2.2.6 Protection Levels

Protection Levels are determined by the integrity requirement $PHMI$. For each PL, the integrity risk (which is the sum of the contributions of each fault mode) must be below the integrity risk allocated in the associated position component.

The solutions of the following equations provide the protection levels that meets the required integrity allocation:

For the horizontal components $q = 1,2$:

$$2\,\bar{Q}\left(\frac{PL_q - b_q^{(0)}}{\sigma_q^{(0)}}\right) + \sum_{k=1}^{Nfaut\ modes} P_{fault,k}\,\bar{Q}\left(\frac{PL_q - b_q^{(k)} - T_{k,q}}{\sigma_q^{(k)}}\right) = \rho_j\,\frac{PHMI_{HOR}}{2}\left(1 - \frac{P_{not\ monitored}}{PHMI_{HOR} + PHMI_{VER}}\right)$$

For the vertical component: $q = 3$

$$2\,\bar{Q}\left(\frac{PL_3 - b_3^{(0)}}{\sigma_3^{(0)}}\right) + \sum_{k=1}^{Nfaut\ modes} P_{fault,k}\,\bar{Q}\left(\frac{PL_3 - b_3^{(k)} - T_{k,3}}{\sigma_3^{(k)}}\right) = \rho_j\,PHMI_{VER}\left(1 - \frac{P_{not\ monitored}}{PHMI_{HOR} + PHMI_{VER}}\right)$$

where ρ_j is the fraction of the integrity budget given to exclusion mode, $\bar{Q}(z)$ is the modified Q function defined above. Each term of the left-hand side of previous equations is an upper bound of the contribution of each fault to the integrity risk.

The algorithm to solve previous Protection Level equations is described in Annex D. See results for the driving example in Figure 45 in Annex E.

3.2.2.7 Exclude modes that are double counted

Due the pre-allocation of the integrity budget of the coordinates, there is the possibility that the computed distribution of integrity risk of a fault mode might exceed the probability of the fault mode.

Let us consider the mode k. The upper bound on the contribution to mode k is given by

$$IR_k = P_{fault,k}\left(\bar{Q}\left(\frac{PL_1 - b_1^{(k)} - T_1^{(k)}}{\sigma_1^{(k)}}\right) + \bar{Q}\left(\frac{PL_2 - b_2^{(k)} - T_2^{(k)}}{\sigma_2^{(k)}}\right) + \bar{Q}\left(\frac{PL_3 - b_3^{(k)} - T_3^{(k)}}{\sigma_3^{(k)}}\right)\right)$$

If the term between parentheses exceeds one, then IR_k exceeds $P_{fault,k}$. However, if chosen not to monitor mode k, IR_k would have been exactly $P_{fault,k}$ (i.e. the value of sum of parentheses equals to 1), which would have resulted in a smaller Protection Level.

The possible loss of performance can be mitigated by:

- Identifying the modes for which the integrity risk is being overestimated.
- Excluding them from the list of monitored faults.
- Re-computing thresholds and Protection Levels with the new list.

Specifically, the k faults to exclude are those such that:

$$\bar{Q}\left(\frac{PL_1 - b_1^{(k)} - T_1^{(k)}}{\sigma_1^{(k)}}\right) + \bar{Q}\left(\frac{PL_2 - b_2^{(k)} - T_2^{(k)}}{\sigma_2^{(k)}}\right) + \bar{Q}\left(\frac{PL_1 - b_3^{(k)} - T_3^{(k)}}{\sigma_3^{(k)}}\right) \geq 1$$

Let us to call I_{excl} the set of modes to exclude. Since the set is excluded from the list of monitored modes, their integrity risk contribution must be account in the $P_{fault\ not\ monitored}$. Thence,

$$P_{fault\ not\ monitored\ ,updated} = P_{fault\ not\ monitored} + \sum_{k \in I_{remove}} P_{fault,k}$$

and the new number of monitored fault modes is then:

$$N_{fault\ modes\ ,updated} = N_{fault\ modes} - |I_{remove}|$$

where $|I_{remove}|$ indicates the "cardinal" or number of elements in set I_{remove}

See results for the driving example in Figure 46 in Annex E.

3.2.2.8 Effective Monitor Threshold and Sigma of Vertical Position accuracy

Among the Alert Limits for the protection levels, three additional criteria are established for the vertical positioning performance LPV-200:

- 4 m 95% accuracy.
- 10 m, 99.99999% fault-free accuracy.
- 15 m 99.999% effective monitor Threshold.

The standard deviation of the vertical position used for the first two criteria is given by

$$\sigma_{V\ acc} = \sqrt{\left[\boldsymbol{A^{(0)}\ C_{acc}\ A^{(0)^T} A^{(0)}}\right]_{33}}$$

being the thresholds:

$$accuracy\ (95\%) = K_{ACC}\ \sigma_{Vacc}\ ;\quad (K_{ACC} = 1.96)$$

$$fault\ free\ (10^{-7}) = K_{FF}\ \sigma_{V,acc}\ ;\ \ (K_{FF} = 5.33)$$

Because 10 m/K_{FF} is smaller than 4 m/K_{ACC}, the 10 m, 99.99999% fault-free accuracy test is the only one that needs to be evaluated by the receiver. Therefore, we have only to test:

$$\sigma_{V,acc} \leq \frac{10\ m}{K_{FF}} = 1.87\ m$$

On the other hand, the Effective Monitor Threshold (EMT) is defined as the maximum of the detection thresholds of faults that have a prior probability equal or above P_{EMT}. Thence, this monitor is calculated as follows:

$$EMT = \max_{k | P_{fault,k} \geq P_{EMT}} \{T_{k,3}\}$$

3.2.2.9 Adjust Projection Matrix for weak geometries

Weak geometries, i.e. geometries with a large Dilution of Precision (DOP), such as subsets that monitor wide faults (constellation faults), lead to large detection thresholds. This increases the protection levels and reduces overall availability of the ARAIM algorithm.

The WLS solution that minimises the position estimation error under nominal conditions is not, in general, the one that minimises the integrity error bounds, i.e. PLs. It is therefore possible to reduce the PLs, while maintaining integrity, by choosing a different position solution (and therefore degrading the accuracy of such position solution).

The algorithm to deal with weak geometries proposed in [31] is based on adjusting the all-in-view projection matrix $\boldsymbol{A}^{(\mathbf{0})}$, by an affine-combination of the all-in-view least squares estimator $\boldsymbol{A}^{(\mathbf{0})}$ and the fault-tolerant estimator $\boldsymbol{A}^{\boldsymbol{max}}$, associated to the fault mode with the largest contribution to the integrity risk ($k = max$). See more details in Annex C.

The algorithm is applied to each position error component, independently:

$$\left[\boldsymbol{A}^{(\mathbf{0})^{adj}}\right]_q = \left[\boldsymbol{A}^{(\mathbf{0})}\right]_q + t_q\left(\left[\boldsymbol{A}^{\boldsymbol{max}}\right]_q - \left[\boldsymbol{A}^{(\mathbf{0})}\right]_q\right) \quad ; \; q = 1,2,3$$

Because it degrades accuracy, this approach should only be applied when a target protection level is not achieved, for instance, for LPV-200 mode when HPL exceeds 40 m or VPL exceeds 35 m or EMT exceeds 15 m, being $\sigma_{acc,Vert} \leq 1.87\ m$.

3.2.2.10 Solution Separation and Chi2 Tests

The Solution Separation and Chi-Square (χ^2) tests are applied to decide whether the all-in-view solution is accepted or Fault Exclusion must be attempted. Also it decides whether to declare the Protection Levels as valid or not.

The tests are defined as follows:

1.- Solution separation test:

This test shall be applied for each fault mode k:

$$\left|\hat{x}_q^{(k)} - \hat{x}_q^{(0)}\right| \leq T_q^{(k)}$$

Protection Levels can be computed only if this test is successful for all k modes and position components $q = 1,2,3$. If any of these tests fails, ARAIM is not available without successful exclusion.

2.- Chi2 test.

This test is applied only for the all-in-view satellites set:

$$Chi2^{(0)} \leq T_{\chi^2}^{(0)}$$

where the threshold T_{χ^2} is defined by $F\left(T_{\chi^2}, N_{sat} - 3 - N_{const}\right) = 1 - P_{FA\_CHI2}$ being $F(t, n)$ the cumulative distribution function of χ^2 distribution with n degrees of freedom.

3.- Tests decision:

If both, Solution Separation (for all subsets and all positioning components) and the all-in-view χ^2 test PASS, then the all-in-view navigation solution and its associated protection levels, EMT and $\sigma_{V,acc}$ are output to the ARAIM user.

If Solution Separation FAILS for any positioning component of any subset, then the algorithm attempts exclusion, whatever the χ^2 test results.

If the χ^2 test fails (i.e. $Chi2^{(0)} > T_{\chi^2}^{(0)}$), although being the solution separation test successful (i.e. $\left|\hat{x}_q^{(k)} - \hat{x}_q^{(0)}\right| \leq T_{k,q}$, $\forall k$ and $\forall q$) the protection levels cannot be considered valid and exclusion cannot be attempted. In this case, the χ^2 statistic is larger than expected, but none of the solution separation test have failed, which suggest that the fault is outside the threat model. In this case, the algorithm will keep the all-in-view solution, and output the so-called "Uncertainty Levels", HUL and VUL, see section 3.2.2.11.

In fact, while the χ^2 test is not linked to the threat model, it makes the algorithm more robust to violations of the threat model with no performance computation penalty. See results for the driving example in Figure 47 and Figure 48 in Annex E.

3.2.2.11 Horizontal and Vertical Uncertainty Levels

In some cases, it may be advantageous to keep using the all-in-view solution position after a fault detection, as it can provide lower error bounds. In this case the user computes a position error bound (termed the Uncertainty Level) that meets the integrity requirement but it is directly dependent on the measurement residuals. An acceptable formula for horizontal and vertical Uncertainty Levels is as follows (see equations (59) to (61) of [31]):

Horizontal and Vertical Uncertainty Levels (HUL, VUL) are defined as:

$$HUL = \sqrt{UL_1^2 + UL_2^2}$$

$$VUL = UL_3$$

where

$$UL_q = \max_{\substack{k\in[0,N_{fault\ modes}] \\ PL_q - T_{k,q} - b_q^{(k)} > 0}} \left\{ \left|\hat{x}_q^{(k)} - \hat{x}_q^{(0)}\right| + K_{md,q}^{(k)}\, \sigma_q^{(k)} \right\} \; ; \quad q = 1,2,3$$

$$K_{md,q}^{(k)} = \frac{PL_q - T_{k,q} - b_q^{(k)}}{\sigma_q^{(k)}}$$

See the conceptual layout of the Uncertainty Level in Figure 11.

These Uncertainty Levels are output when no exclusion can be attempted due to the fail of χ^2 test indicated before (while none of the solution separation test fail).

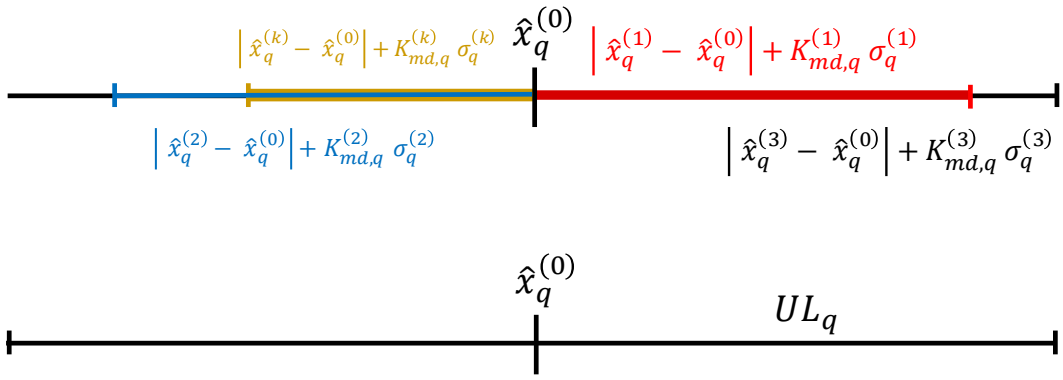

$$UL_q = \max_{\substack{k\in[0,N_{fault\ modes}] \\ PLq - T_{k,q} - b_q^{(k)} > 0}} \left\{ \left| \hat{x}_q^{(k)} - \hat{x}_q^{(0)} \right| + K_{md,q}^{(k)}\,\sigma_q^{(k)} \right\}$$

$$K_{md,q}^{(k)} = \frac{PL_q - T_{k,q} - b_q^{(k)}}{\sigma_q^{(k)}}$$

Figure 11. Conceptual layout of the Uncertainty Level for the q error component, $q = 1,2,3$

3.2.2.12 Fault exclusion

As $Chi2$ is an upper bound of the maximum separation statistic, the algorithm can avoid testing all possible subsets by checking the $Chi2$. Then, the subset with smallest $Chi2$ is very likely to be consistent, and thus, a good candidate for exclusion.

In the implementation of this PhD, the candidate subsets are explored, starting with the subsets with larger size (i.e. number of satellites), and for each size, the search starts with the subset with smaller $Chi2^{(k)} < T_{\chi^2}^{(k)}$, and increasing value of $Chi2^{(k)}$. The search (and hence, the Fault Exclusion) ends when having the first valid subset.

In case of not having any valid solution, the Fault Exclusion is declared Unavailable and the all in view solution is output.

See in Figure 49 in Annex E the subsets candidates for exclusion from the driving example.

4 Characterization of broadcast navigation data for ARAIM

4.1 Introduction

As commented in the introduction, the characterization of Clock and Ephemeris error of the GNSSs is a key element to validate the assumptions for the integrity analysis of GNSS SoL augmentation systems. Specifically, the performance metrics of SoL applications require the characterization of the nominal UREs as well as the knowledge of the probability of a satellite or a constellation fault (P_{sat}, P_{const}), i.e. when one or more satellites do not perform in the nominal mode [1].

The main target of this chapter is to characterize the performance of broadcast navigation data during the first years of initial Galileo OS.

Previous similar studies have been conducted for GPS in [32,33]. In the present PhD dissertation, the methodology developed in such papers is applied to Galileo satellites, taking into account the specificities of the Galileo system.

The general approach to perform such studies consists of identifying potentially broadcast erroneous navigation data by comparing "consolidated" Receiver Independent Exchange (RINEX) format [34] broadcast navigation files with precise orbit and clock reference products that are considered the truth. Potential anomalies are then verified using measurements collected by a network of GNSS receivers at permanent stations. The consolidated RINEX navigation files are built by cross-checking messages from a large set of individual receivers to ensure that they are valid. This helps preventing the case where a receiver on a permanent station has missing data or generates incorrect values.

The present research investigates 67 months of Galileo broadcast navigation data, i.e. from 1 January 2017 to 31 July 2022. The observed error distribution is analysed and the nominal ranging accuracy is characterised for each satellite. The probabilities of satellite failure, P_{sat}, and constellation failure, P_{const}, are then estimated from the study of the detected satellite failure events. The GPS performance is also evaluated over the same period and over the last 10 years, i.e. from 1 January 2012 to 31 July 2022, in order to compare the Galileo results with a fully deployed and consolidated constellation.

This chapter is organized as follows. Section 4.2 provides an overview of the methodology, discussing particular details related to the upgrade of the Data Cleansing developed in [33] for GPS to process Galileo navigation data. Section 4.3 describes the data sets used and identifies some issues related to data processing. Section 4.4 analyses the observed error distribution, its Gaussian overbounding, and the events over a predefined threshold are identified. The characterization of the observed nominal accuracy is addressed in Section 4.5, where the mean value and 68th and 95th percentiles of error distribution are derived. The detected Galileo satellite faults are identified in Section 4.6 and, based on the observation results, the averaged P_{sat} and P_{const} are estimated.

4.2 Anomaly Monitoring

The methodology to identify potential satellite failures is described next, which involves three steps: Data Cleansing, Anomaly Detection, and Anomaly Verification, see layout in Figure 12.

4.2.1 Data Cleansing

The broadcast RINEX navigation files collected by the International GNSS Service (IGS) may contain errors or inconsistencies from different sources, such as data login errors due to accidental bad receiver data and/or hardware/software bugs, losses of navigation messages, different transmission time recording, among others.

Data Cleansing is a complex algorithm that builds a consolidated RINEX broadcast navigation file from a wide set of RINEX files of individual receivers distributed worldwide by exploiting the redundancies between them.

The following steps are defined in [33] for processing GPS broadcast navigation data:

1. Least-Significant Bit (LSB) recovery to remove potential errors in the decoding of navigation messages and to convert the values to double-precision floating-point numbers.

2. Classify the GPS URA values to cope with the different URAs appearing in the RINEX files (e.g. some receivers use URA indices instead of URA values, and the same URA index may correspond to three possible values in meters).

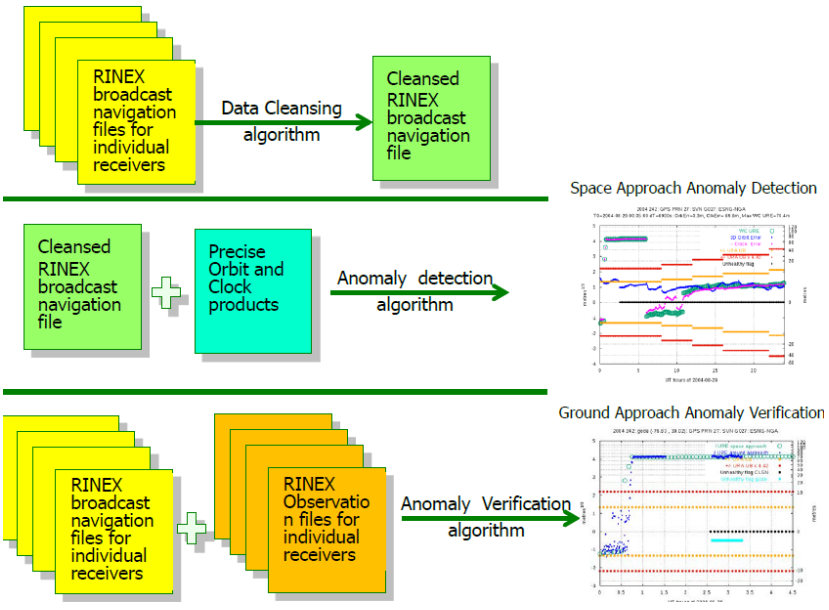

Figure 12. Layout summarising the three main steps involved in the GPS/Galileo anomaly monitoring.

3. Duplication removal and majority voting to select the most likely message as the one shared by the largest number of stations, after removing duplicates. In this step, the navigation data are classified as *robust parameters* (most ephemeris and clock parameters) and *fragile parameters* (Transmission Time of Message (TTOM), PRN, URA, Issue of Data Clock (IODC)). The robust parameters are used to identify the candidates of navigation messages. Their associated fragile parameters are then selected as those shared by the largest number of stations.

4. TTOM recovering. The TTOM is not a parameter broadcast in the navigation message. The record given in RINEX navigation files is not the TTOM but the first reception time of the message by the receiver collecting data. The correct TTOM cannot be determined by the oldest one because some IGS receivers may provide an incorrect TTOM older than the actual one. Furthermore, since the IGS stations are not evenly distributed, neither can it be determined simply by the most frequent one. A procedure is then defined to retrieve the TTOM.

5. Minority discard. After the previous steps, few navigation messages can still have errors in their robust parameters, and a uniqueness criterion is applied to select the final candidates.

4.2.1.1 Upgrading the Cleansing Algorithm to Galileo Broadcast Navigation Data

The Galileo broadcast messages have some particular features that must be taken into account to upgrade the algorithm given in [33] for GPS to process Galileo data. In short [5]:

- There is only a single Issue of Data Navigation (IOD) to identify the ephemeris, satellite clock correction parameters and SISA, instead of the two IODC and Issue of Data Ephemeris (IODE) of GPS navigation data.

- The following parameters are not linked to the IOD:
  - The Broadcast Group Delay (BGD) values;
  - The navigation Data Validity Status (DVS);
  - The signal Health Status (HS).

  In RINEX navigation files [34], DVS and HS are embedded in the 8 bits of the Satellite Vehicle (SV) health flag for the different signals E1B, E5a, and E5b. Thus, SV health = 0 means that DVS and HS are OK.
  Note: in the GPS, the Total Group Delay (TGD) and SV health are linked to the IODC.

- Galileo broadcast navigation message update [5]:
  - The typical refresh rate of navigation data ranges from 10 min to 3 h, and each message must be associated with a different IOD;
  - The maximum nominal broadcast period of a healthy navigation message data set is currently 4 h;
  - The message Validity Duration (VD) is 4 h.

Note: the GPS navigation message is, typically, updated every 2 h, with a different IODC, being the validity time given by the Fit Interval (FI), typically 4 h (it can also depend on the IODC value [35]). The validity of the Galileo message is up to 4 h after the Time of Ephemeris (Toe) [5].

- Minority discard step:
  In the case of GPS satellites, candidates are selected according to a uniqueness criterion based on PRN—IODC, i.e. the one confirmed by the larger number of stations having the same PRN—IODC. As the IODC may be occasionally reused by a satellite within the same day, a backup uniqueness criterion based on PRN and Time-of-Clock (Toc) is also applied, i.e. PRN—Toc.

  In the case of Galileo satellites, the previous uniqueness criterion, based on checking the PRN—IODC, cannot be applied. This is because the IOD may be repeated within the same day. Thence, with Galileo satellites, for each Data Source value in the RINEX file, the uniqueness is based only on the PRN—Toc criterion. This criterion is applied to all robust parameters, except SV health (i.e. DVS, HS) and BGDs, as they are not linked to the IOD.

Finally, all messages containing the selected robust parameters by the previous uniqueness criteria, appearing with any combination of SV health and BGD parameters, are approved and saved in the consolidated broadcast navigation RINEX file.

4.2.2 Anomaly Detection: Space Approach

Anomaly detection follows the "Space Approach" defined in [33], which uses the consolidated broadcast navigation files from the previous Data Cleansing step and precise orbit and clock products provided by IGS and other sources, as well.

The satellite coordinates and clock offsets are computed from the consolidated broadcast navigation files according to the Galileo OS SDD [5]. The discrepancy between coordinates and clock regarding the precise products is calculated. The orbit error is then projected to the user location on the Earth surface and combined with the clock error to represent the orbit and clock error at the user level. The Worst-Case User Range Error (WC URE) is calculated, which corresponds to the user location where URE takes the greatest absolute value. The geometric method described in Section 3.5 of [33] has been implemented for the WC URE computation. Anomalies are detected by comparing the WC URE with a threshold defined for a given level of probability (see Section 4.1).

Following [33], adapted to Galileo data, a potential anomaly is declared when all the following conditions are fulfilled simultaneously:

- The WC URE exceeds the NTE threshold;
- The most recent navigation data set broadcast on a Healthy SIS by the Galileo satellite is used, where Healthy SIS, means:

  The RINEX field SV health [34] is 0, i.e. DVS = "Navigation Data Valid" and HS = "Signal OK," and SISA ≠ NAPA (NAPA = No Accuracy Prediction Available);

- The Age of Ephemeris (AoE) is smaller than or equal to 4 h Toe, ($AoE = t - Toe \leq 4\text{h}$);
- The precise orbits and clocks are available and healthy.

  Note: in GPS the validity period is given from TTOM and Fit Interval (FI) by $\Delta t = t - TTOM \leq FI$, where FI is typically 4 h.

A configurable Sampling Rate (SR) of 300 s has been used. Precise orbits at 900 s SR have been interpolated. No interpolation is needed for clocks, as they are available at 300 or 30 s SR. Maximum data holes of 1800 s have been allowed for IGS orbits and 600 s for clocks.

4.2.3 Anomaly Verification: Ground Approach

The anomaly verification follows the "Ground Approach" defined in [33], which uses the RINEX Observation and Navigation files of individual receivers of permanent stations to validate the potential anomalies detected with the Space Approach. The algorithm is based on the following steps:

1. Select a set of 10 or more active stations having the satellite in view during the whole anomaly event, or as long as possible. These stations should experience as large anomalous UREs as possible. The algorithm for station selection presented in Section 4.2 of [33] has been implemented.

2. For each selected station (rec), the Instantaneous SIS URE (IURE) is computed from the prefit residual ($prefit_{rec}^{j}$) of the Ionosphere-Free (IF) combination of Galileo C1 and C5 code measurements [7]. That is, for each satellite, *j = 1,…,N* in view from the receiver (*rec*):

$$prefit_{rec}^{j} = \hat{\rho}_{rec}^{j} - c \cdot \hat{T}^{j} + Trop_{rec}^{j} - P_{IF,rec}^{j}$$

   where $\hat{\rho}_{rec}^{j}$ and $\hat{T}$ are the geometric range and the satellite clock offset computed with the broadcast ephemeris, $Trop_{rec}^{j}$ is the tropospheric delay estimated using the UNB-3 nominal model and the simple mapping function implemented in the gLAB tool [36], and ${P_{IF}}_{rec}^{j}$ is the IF combination of unsmoothed code measurements. Satellites below 5° of elevation are excluded.

   The IURE for the anomalous satellite (*sat*) is then computed as:

$$IURE = prefit_{rec}^{sat} + c \cdot \hat{T}_{rec}$$

   where $\hat{T}_{rec}$ is the receiver clock offset estimated as the weighted average of the prefit residuals of all satellites in view, excluding the anomalous satellite (*sat*) (see Equation (4.7) in [33]).

   As already mentioned, a configurable sampling rate of 300 s has been used.

3. Following [33], the Galileo satellite is set as "anomalous" when all the following conditions are fulfilled simultaneously:

- The IURE exceeds the NTE threshold;
- The most recent navigation data broadcast on a Healthy SIS by the Galileo satellite are used, where Healthy SIS means:
  The RINEX field SV health is 0, i.e. DVS = "Navigation Data Valid" and HS = "Signal OK" and SISA ≠ NAPA.
- The broadcast navigation message is within its validity time, $AoE = t - Toe \leq 4$ h;
- The signal was tracked with an acceptable SNR, i.e. the RINEX SNR flag value ≥4.

Figure 13 shows an example of Anomaly Detection, with the Space Approach in the left plot and Anomaly Verification with the Ground Approach in the right plot. This example corresponds to the event experienced by the Galileo satellite E101 on 26 December 2017. An NTE threshold of 4.42 × SISA is used. As depicted in the left plot, due to a large clock error (in pink), the WC URE (green circles) exceeds the NTE at 07:40 of 26 December 2017, with the satellite set as healthy. This anomalous condition ends when a new navigation message with an unhealthy condition (black line) is received at 15:00. The orbit error (in blue) is kept under the NTE threshold. This potential event is confirmed by the Ground Approach shown in the right plot, using measurements from the station SEYG (in Seychelles islands). The IURE values computed from Space and Ground approaches are shown in green and blue, respectively. The unhealthy condition from the RINEX flag shown in black corresponds to the consolidated (cleansed) RINEX file.

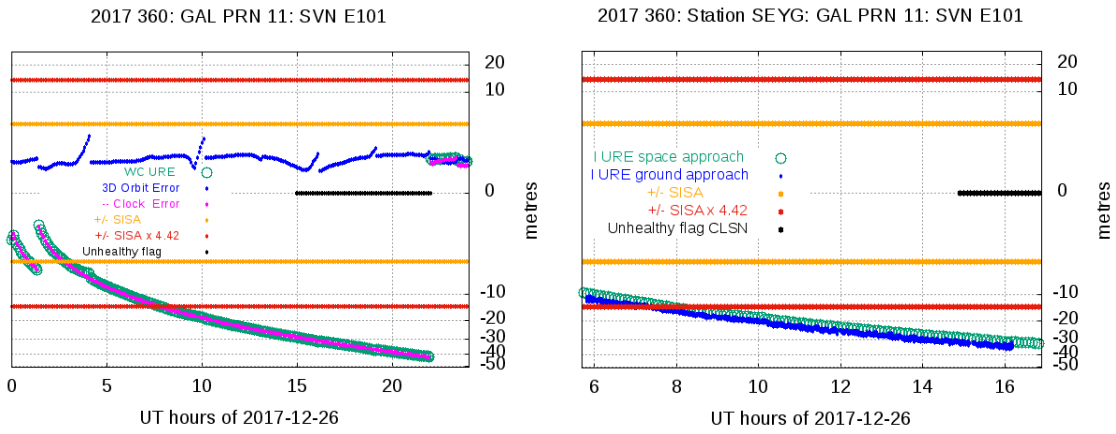

Figure 13. Example of anomaly detection and verification for the Galileo satellite E101 on 26 December 2017, using the Not-to-Exceed (NTE) = 4.42 × SISA threshold. The left plot illustrates the Anomaly Detection from the Space Approach, and the 3D orbit and clock errors are shown in blue and pink, respectively. The green circles correspond to the Worst-Case User Range Error (WC URE). The Signal-in-Space Accuracy (SISA) value is depicted in yellow, and the NTE threshold in red. The unhealthy flag from the cleansed Receiver Independent Exchange (RINEX) navigation file is shown in black. The right plot illustrates the Anomaly Verification from the Ground Approach, using measurements from the station SEYG. The Instantaneous SIS URE (IURE) values computed from the station SEYG measurements are shown in blue, and the IUREs from the Space Approach are in green. The unhealthy flag from the cleansed RINEX navigation file is shown in black. The SISA values and the NTE threshold are shown in yellow and in red, respectively. The y-axis is in a cubic root scale.

4.2.4 Decision Criterion

The potential SIS anomaly is considered "true" when none of the selected receivers show a nominal IURE, at least one receiver from the selected set shows an anomalous IURE, and the rest are unable to track the satellite during the anomalous event. On the contrary, an anomaly is considered "false" when none of the selected IGS receivers shows anomalous IURE, at least one of the receivers from the selected set shows nominal IURE, and the rest do not track the satellite. The case where, at the same time, there are receivers that present anomalous IURE and receivers that present nominal IURE is considered "paradoxical" and requires manual intervention. The satellite is considered "untracked" when the selected receivers with the anomalous satellite in view cannot track it. Then, the anomaly is very likely to be false [33].

4.3 Data Sets

The previous data cleansing, anomaly detection, and verification procedures have been applied over 67 months of F/NAV Galileo navigation data, from 1 January 2017 to 31 July 2022.

Worldwide RINEX-2/3 Navigation files have been gathered from several public domain servers, such as CDDISA, EUREF and ESNG, avoiding repetitions of stations. The already-compiled RINEX navigation files named "brdc, brdm or auto" are not used to guarantee "one station one vote." Dual-frequency RINEX-2/3 Observation files at a 1 Hz sampling rate have also been gathered from IGS servers.

Precise orbit and clock products from the Multi-GNSS Experiment (MGEX) (CODE products) [37] have been used to check the broadcast navigation data (with orbits at 900 s until 5 August 2017and at 300 s later, and clocks at 300 s until 11 August 2017and at 30 s later).

The Antenna Phase Centers (APCs) and the System Time used in the IGS products is different from those used in the broadcast navigation data. Thence, the Antenna Exchange Format (ANTEX) file provided by the European GNSS Service Center [38] has been used, which has the same APCs as in the broadcast Galileo ephemeris. Some update has been necessary for the ANTEX reading, as these files use a different reference than IGS ANTEX files.

To align the IGS clocks to the Galileo system time, the IGS clocks have been corrected first for the difference (ΔAPC) between Galileo broadcast and IGS APCs. The epoch-wise trimmed mean of the difference between the IGS (ΔAPC corrected) and broadcast clocks has been computed to estimate the difference between Galileo and IGS reference times (ΔT). This trimmed mean is calculated after removing the 20% of data above and below the epoch-wise median. Finally, the IGS (ΔAPC corrected) clocks are aligned with the Galileo system time by correcting with ΔT.

Figure 14 depicts the discrepancy between the IGS and GPS time as a function of time on 2007. The left hand plot is for 10 days (DoYs 50-60 of 2007). The right hand plot is for the whole 2007.

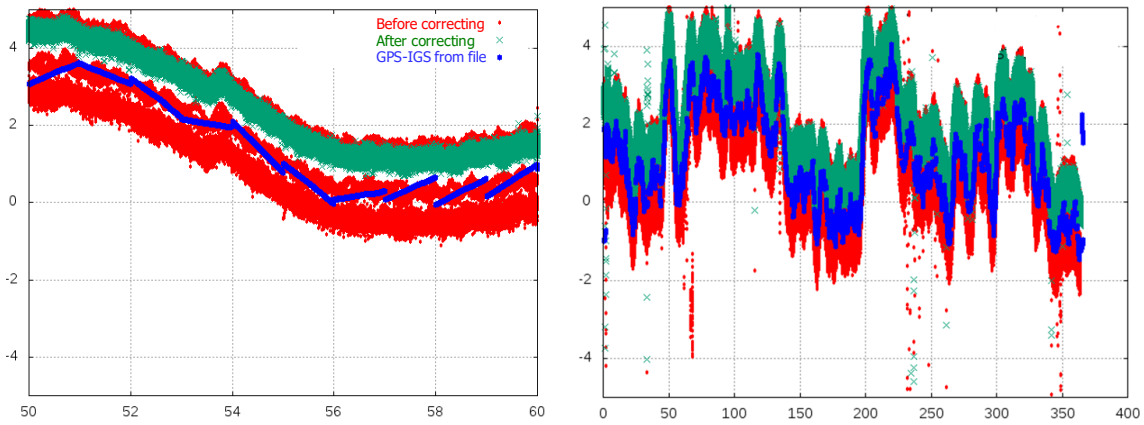

Figure 14. Discrepancy between the IGS and GPS time as a function of time on 2007. Vertical axis in in metres. Horizontal axis is in days of year 2017. The left hand plot is for 10 days (DoYs 50-60 de 2007). The right hand plot is for the whole 2007. The vertical axis in given in meters. Red colour is for the clocks of different GPS satellites before correcting by the difference between IGS and GPS APCs. Green colour is after correction by the differential APCs. In blue it is shown the estimate of GPS-IGS time correction given in the IGS files.

Although this trimmed mean can protect against clock outliers due to one or few faulty satellites, the estimation of ΔT with the previous approach can be affected by simultaneous satellite events, as experienced on 14 May 2017 (see Figure 15).

For the GPS satellites, the National Geospatial-Intelligence Agency (NGA) precise products [39] have been used, which requires neither any APC correction nor time alignment. The sampling rate of these products is 900 s until 27 February 2012 and 300 s afterwards.

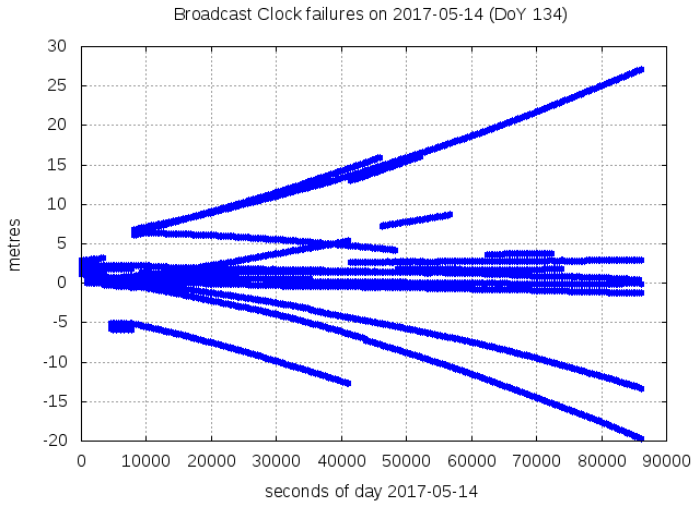

Figure 15. Simultaneous events occurring in Galileo broadcast clocks on 14 May 2017. Several satellites experience large broadcast clock errors with respect to the precise clock determinations because the navigation messages were not refreshed.

4.4 Observed Error Distribution

This section analyses the observed error distribution in the coordinates and clocks of Galileo and GPS satellites, computed from the F/NAV and LNAV broadcast navigation messages, respectively.

The plots of Figure 16 show the relative frequency histogram for the aggregate total radial (red), along-track (green), cross-track (blue), clock (pink), and IURE (cyan) errors. In the case of IURE, the values have been estimated over 20 points spread evenly on the Earth, derived from the vertices of a regular dodecahedron [33]. The plots in the left column involve more than 5.5 years of Galileo F/NAV navigation data, i.e. from 1 January 2017 to 31 July 2022. The plots in the right column are for the GPS satellites and LNAV message and contain more than 10 years of data, i.e. from 1 January 2012 to 31 July 2022. Although larger periods are also available for GPS, it is unclear if they would represent the current state of the system [32]. The bottom plots are a zoom of top plots to better see the distribution peaks.

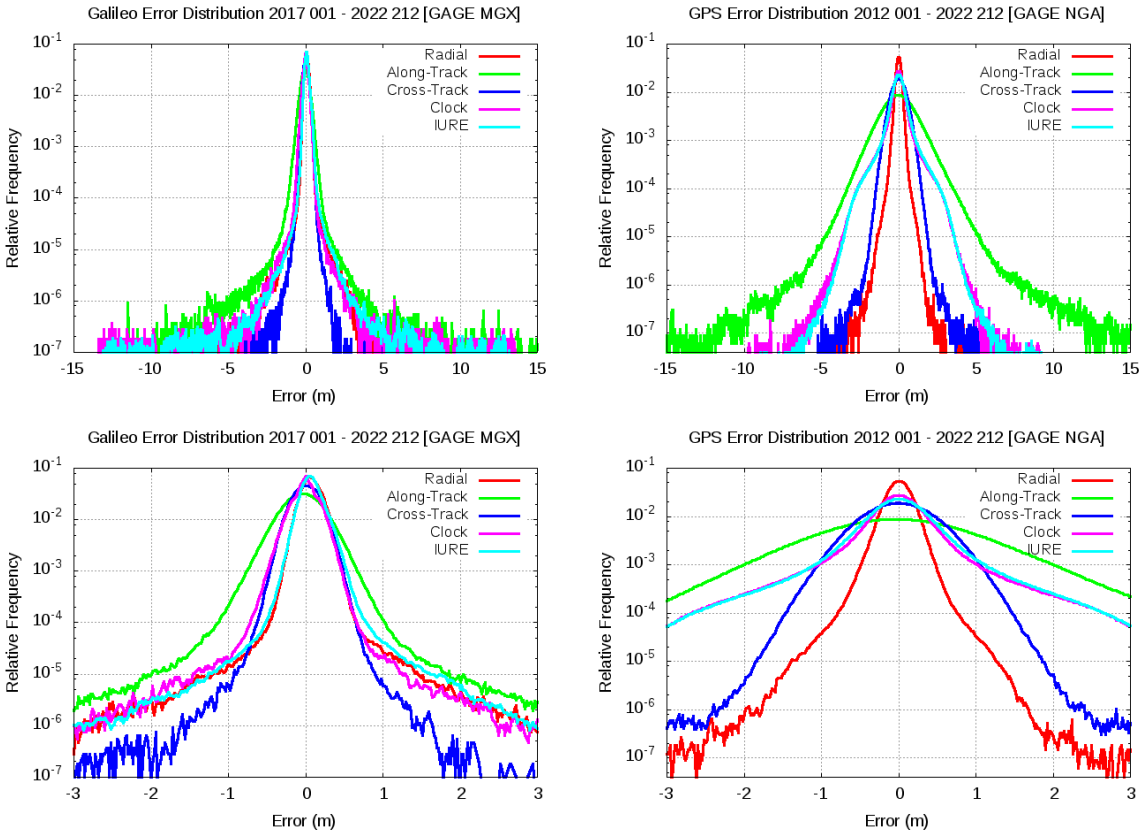

Figure 16. Relative frequency histogram for the observed error distribution of broadcast navigation data from aggregated data of all satellites (bin size: 2 cm). The plots in the left column are for Galileo F/NAV from 1 January 2017 to 31 July 2022. The plots in the right column are for GPS LNAV data from 1 January 2012 to 31 July 2022. The plots show the radial (red), along-track (green), cross-track (blue), clock (pink), and IURE (cyan) errors. Bottom plots are an x-range zoom of top plots. The eccentric satellites E201 and E202 are excluded.

A sharper distribution is found for Galileo satellites compared with the GPS histogram. The radial and cross-track errors are the error components more tightly distributed in both Galileo and GPS. Similar distributions are found for Galileo radial and clock errors, leading to a similar pattern for IURE. Moreover, a small bias appears in the radial error and IURE (see left column, bottom plot). This bias is quantified in Section 4.5, when analysing the observed nominal accuracy. No bias is observed in the clock error, although it may have been absorbed, in some way, by the clock alignment process. In the GPS, the IURE is clearly dominated by clock error, with fairly overlapping patterns. Cross-track error is sharper in the Galileo than in the GPS, whereas along-track exhibits a larger spread in both Galileo and GPS data. No remarkable biases are found in the GPS error distributions.

4.4.1 Identification of Potential Signal-in-Space Events

The Signal-in-Space Error (SISE) values, measured as the instantaneous maximum projected ranging errors at the worst user location, i.e. WC URE, are analysed this section and the next. The algorithm starts identifying first potential events having anomalous SISE values and then it will analyse the SISE overbounding by a Gaussian distribution.

As stated in the Galileo OS SIS ICD [40], the "SISA is a prediction of the minimum standard deviation (1σ) of the unbiased Gaussian distribution, which overbounds the SISE predictable distribution for all possible user locations within the satellite coverage area."

Figure 17 depicts the relative frequency of the different broadcast SISA values for the IOV and FOC satellites and across the whole constellation, excluding the eccentric satellites E201 and E202. As depicted, the most frequent SISA value (more than 97%) is 3.12 m in these three satellite sets, and NAPA is broadcast in less than 0.8% of cases.

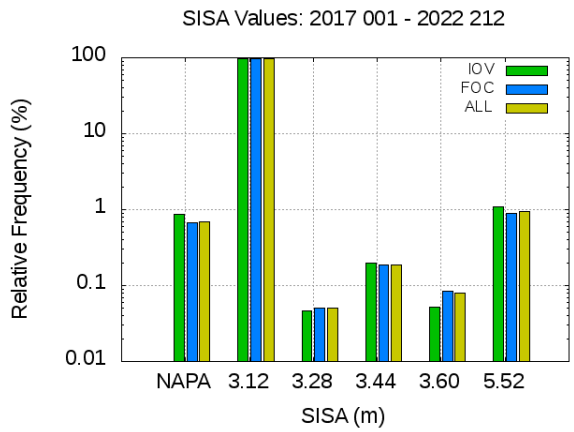

Figure 17. Relative frequencies of the Broadcast SISA values for In-Orbit Validation (IOV), Full Operational Capability (FOC), and Aggregate All satellites (ALL). More than one order of magnitude of difference is found between the most frequent SISA value, 3.12 m, and the other broadcast values. No Accuracy Prediction Available (NAPA) is broadcast in less than 1% of cases. The eccentric satellites E201 and E202 are excluded.

The methodology of Anomaly Monitoring presented in Section 4.2 is used next to identify anomalous behaviours in Galileo and GPS satellites. The same threshold as GPS with IAURA is used for Galileo with SISA to identify potential events, i.e. NTE = 4.42 × SISA.

A summary of the identified Galileo F/NAV events is given in Table 6 and Figure 18. Regarding Table 6, the detections with the Space Approach are shown on the top and the verification results with the Ground Approach on the bottom. The Satellite Vehicle Numbers (SVNs) E1XX corresponds to the IOV satellites and E2XX to the FOC satellites (see Figure 18).

Ten different Galileo satellite events exceeding the NTE = 4.42 × SISA threshold were found in 2017 (involving the satellites E101, E102, E203, E205, E206, E208, and E211), only one satellite event was identified in 2018 (E206), two more satellite events in 2019 (E101 and E103), another event on 2021 (E102) and the last two events in 2022 (E210 and E103). These detections have been confirmed by the Ground Approach algorithm (Algorithm Decision column) or set as Paradox. The last column of Table 6, shows the Final Decision based on further analysis. Multiple satellite detections appear on 14–15 May 2017.

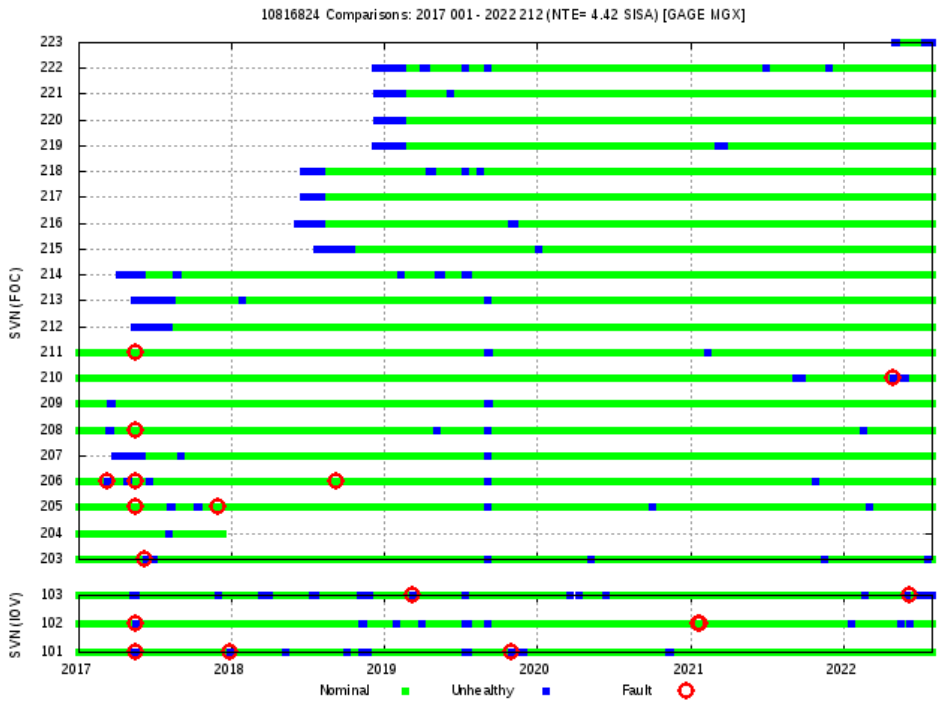

Figure 18. Galileo F/NAV, from 1 January 2017 to 31 July 2022. Summary of observations for each Galileo satellite. Green indicates valid observations, blue indicates the satellite was unhealthy, and red circles indicate events exceeding the 4.42 × SISA threshold. Consolidated broadcast RINEX files from the group of Astronomy and Geomatics (gAGE) and MGEX precise products have been used. The Galileo eccentric satellites E201 and E202 are excluded.

Table 6. Galileo F/NAV, from 1 January 2017 to 31 July 2022. Summary of events exceeding the NTE = 4.42 × SISA threshold. Events detected with the Space Approach are on the table at top, and verification results with the Ground Approach are on the table at the bottom. The "Duration" column indicates the elapsed time having WC URE over the 4.42 × SISA threshold.

Potential anomalies found with Space Approach (NTE= 4.42 × SISA)										
YYYY	DOY	SVN	PRN	Start Time		Duration (min.)	Anomaly		WC URE (m)	SISA (m)
							Type	Max. Value (m)		
2017	066	E206	30	7 March 2017	03:15	45	clock	340.9	341.9	3.12
2017	134	E101	11	14 May 2017	13:30	60	clock	14.9	15.0	3.12
2017	134	E102	12	14 May 2017	12:20	25	clock	14.4	14.4	3.12
2017	134	E205	24	14 May 2017	17:35	380	clock	20.3	20.3	3.12
2017	134	E206	30	14 May 2017	13:30	625	clock	26.6	26.9	3.12
2017	134	E208	08	14 May 2017	23:35	25	clock	13.8	14.2	3.12
2017	134	E211	02	14 May 2017	10:55	30	clock	14.6	14.9	3.12
2017	135	E205	24	15 May 2017	00:00	70	clock	20.6	20.6	3.12
2017	135	E206	30	15 May 2017	00:00	190	clock	31.4	36.7	3.12
2017	135	E208	08	15 May 2017	00:00	105	clock	15.1	15.1	3.12
2017	157	E203	26	6 June 2017	05:50	1085	clock	491.3	491.9	3.12
2017	158	E203	26	7 June 2017	00:00	435	clock	460.4	472.8	3.12
2017	332	E205	24	28 November 2017	06:45	185	clock	16.2	16.6	3.12
2017	360	E101	11	26 December 2017	07:45	385	clock	28.4	28.4	3.12
2018	248	E206	30	5 September 2018	02:20	10	eph.	18.8	17,8	3.12
2019	066	E103	19	7 March 2019	12:15	125	eph.	22.2	18.8	3.12
2019	302	E101	11	29 October 2019	18.10	30	clock	431.9	432.1	3.12
2021	021	E102	12	21 January 2021	01:40	25	clock	29.4	29.5	3.12
2022	119	E210	01	29 April 2022	01:00	15	clock	51.0	51.1	3.12
2022	159	E103	19	8 June 2022	18:25	5	clock	16.9	17.0	3.12

Potential anomalies found with Ground Approach											
YYYY	DOY	SVN	PRN	Start Time	Duration (min.)	WC URE (m)	Ref. station	Num. of stations that decide			Algorithm Decision	Final Decision
								Anom.	Nominal	Untrack		
2017	066	E206	30	03:21	38.5	341.9	SEYG	11	0	39	TRUE	TRUE
2017	134	E101	11	11:42	287.5	17.6	WGTN	10	1	39	PARADOX	TRUE
2017	134	E102	12	10:25	144.5	14.4	WGTN	13	0	37	TRUE	TRUE
2017	134	E205	24	15:38	309.5	16.9	YEL2	24	3	23	PARADOX	TRUE
2017	134	E206	30	20:17	222.0	26.9	YEL2	22	0	28	TRUE	TRUE
2017	134	E208	08	23:45	9.5	14.1	RGDG	1	7	42	PARADOX	TRUE
2017	134	E211	02	08:59	150.5	14.3	MAYG	9	6	35	PARADOX	TRUE
2017	135	E205	24	00:03	66.5	20.6	RGDG	11	1	38	PARADOX	TRUE
2017	135	E206	30	00:03	157.0	33.3	YEL2	9	0	41	TRUE	TRUE
2017	135	E208	08	01:02	47.5	15.1	AREG	5	7	38	PARADOX	TRUE
2017	157	E203	26	12:27	163.5	491.9	YEL2	31	0	19	TRUE	TRUE
2017	158	E203	26	01:09	360.5	472.8	YEL2	21	0	29	TRUE	TRUE
2017	332	E205	24	07:27	144.5	16.6	YEL2	17	1	32	PARADOX	TRUE
2017	360	E101	11	05.48	140.5	14.7	VIGO	28	7	15	PARADOX	TRUE
2018	248	E206	30	02:08	21.5	17.8	TLSE	20	7	23	PARADOX	TRUE
2019	066	E103	19	14:03	17.5	18.8	KIRU	8	0	42	TRUE	TRUE
2019	302	E101	11	18:08	36.0	432.1	STHL	18	0	32	TRUE	TRUE
2021	021	E102	12	01:42	19.0	29.5	YEL2	8	0	32	TRUE	TRUE
2022	119	E210	01	00:59	12.0	51.1	THTG	6	0	13	TRUE	TRUE
2022	159	E103	19	18:22	9.5	17.0	USUD	14	0	5	TRUE	TRUE

It is worth mentioning that the detection was found with the space approach for SVN E208 at the end of 14 May 2017 (see Table 6). The Ground Approach algorithm declares this event as "Paradoxical" because only one station, the RGDC, Rio Grande (Argentina), in the selected set of 50 stations, exhibits abnormal behaviour during the analysed time interval, while seven stations are in nominal mode. The other analysed 42 stations untracked the signal. Figure 19 shows, at the left, the plot of space approach with the WC URE over the threshold at the end of the day. The right plot shows the Ground Approach plot for the station RGDG, where the ground IURE, blue dots, reaches the 4.42 × SISA threshold, indicated by red dots. Although the other seven stations tracking the satellite are in a nominal condition on this day, many of them detect the anomalous condition a few minutes after on the next day. In fact, this is the same event involving both 14 and 15 May 2017.

The multi-satellite events detected on 14–15 May were produced by hardware equipment failure in the ground segment of Galileo. As a result, the navigation message for all satellites was not refreshed. The root cause of this failure was identified, the equipment was replaced, and the services were recovered to their nominal levels at 12:44 of 16 May 2017 (see NAGU2017015 [41]). Figure 15 depicts the large error experienced by several of these satellites during this event on 14 May 2017.

As the consolidated (cleansed) RINEX navigation files are a critical input for the Space Approach anomaly detection, and in order to improve the reliability, a double-check has been performed using the consolidated Galileo RINEX navigation files provided by Centre National D'Etudes Spatiales (CNES), cleansed with the "Galileo Ephemeris Consolidation and Control Analysis" (GECCO) software (CNES, Toulouse, France) [42]. The GECCO cleansed RINEX files are available at the CNES server [43].

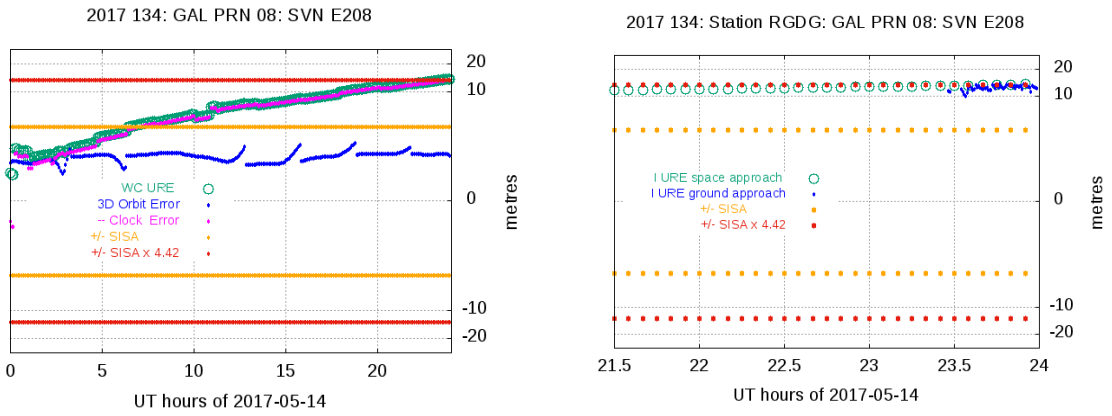

Figure 19. Space (left plot) and ground (right plot) analysis of the Satellite Vehicle Number (SVN) E208 event on 14 May 2017. The left plot shows the space approach with a WC URE reaching the detection threshold of 4.42 × SISA. The right plot shows the Ground Approach results for the only station of Table 6, RGDG, detecting the anomaly. As depicted, the WC URE values are reaching the threshold at the end of the day. The *y*-axis is in a cubic root scale.

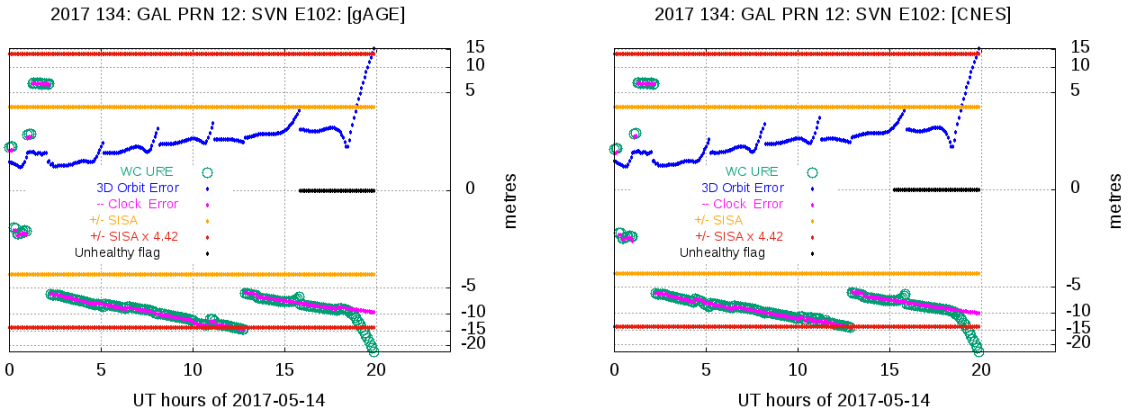

Figure 20. Example of anomaly detection using the consolidated RINEX navigation files from gAGE (left plot) and from Galileo Ephemeris Consolidation and Control Analysis (GECCO) (*Centre National D'Etudes Spatiales* (CNES)) (right plot). The *y*-axis is in a cubic root scale.

All true events detected with the gAGE cleansed RINEX navigation files were also detected with the GECCO cleansed files. Figure 20 shows an example of anomaly detection with the Space Approach using RINEX cleansed files from gAGE (left plot) and from GECCO (CNES) (right plot), with similar results.

The 29 October 2019 event detected in the Galileo IOV E101 satellite (see Table 6) is described next in detail, as it will be relevant in Section 6 when estimating the observed satellite fault probability. The other detected events are depicted in annex F.

4.4.1.1 Galileo IOV E101 Satellite Event on 29 October 2019

A major service failure was experienced by the IOV satellite E101 on 29 October 2019. A brief description of this event and its detection is depicted in Figure 21.

At 17:31:30 29 October 2019, a F/NAV message with IOD = 8 is received, indicating that the satellite was Healthy SIS, i.e. DVS = "Nav. Data Valid" and HS = "Signal OK" and SISA = 3.12 m. The next message is not received until 18:43:30 on the same day.

At approximately 18:00, the satellite clock begins to experience a large drift. This is depicted by the precise clock determination shown by the left plot in the first row of Figure 21. This behaviour cannot be reproduced by the broadcast clock that follows a linear drift (see the blue line in the same plot). The precise clocks estimated with the gAGE Processing Facility [44] have been used in this plot, but the same drift is found in the precise clocks from Centre for Orbit Determination in Europe (CODE), Deutsches GeoForschungs Zentrum (GFZ) or CNES.

About 12 min later, the WC URE exceeds the threshold NTE = 39.78 m considered in the Milestone 3 report [3] to declare a major service failure (see, for instance, the right plot in the first row of Figure 21). The anomalous condition ends 30 min later, at 18:43:30 after the reception of a new message with IOD = 15, with DVS = "Navigation Data Valid" and HS = "Signal OK," but SISA = NAPA, which means that OS SIS status was set to MARGINAL. The satellite was not declared as Healthy SIS up to several days after.

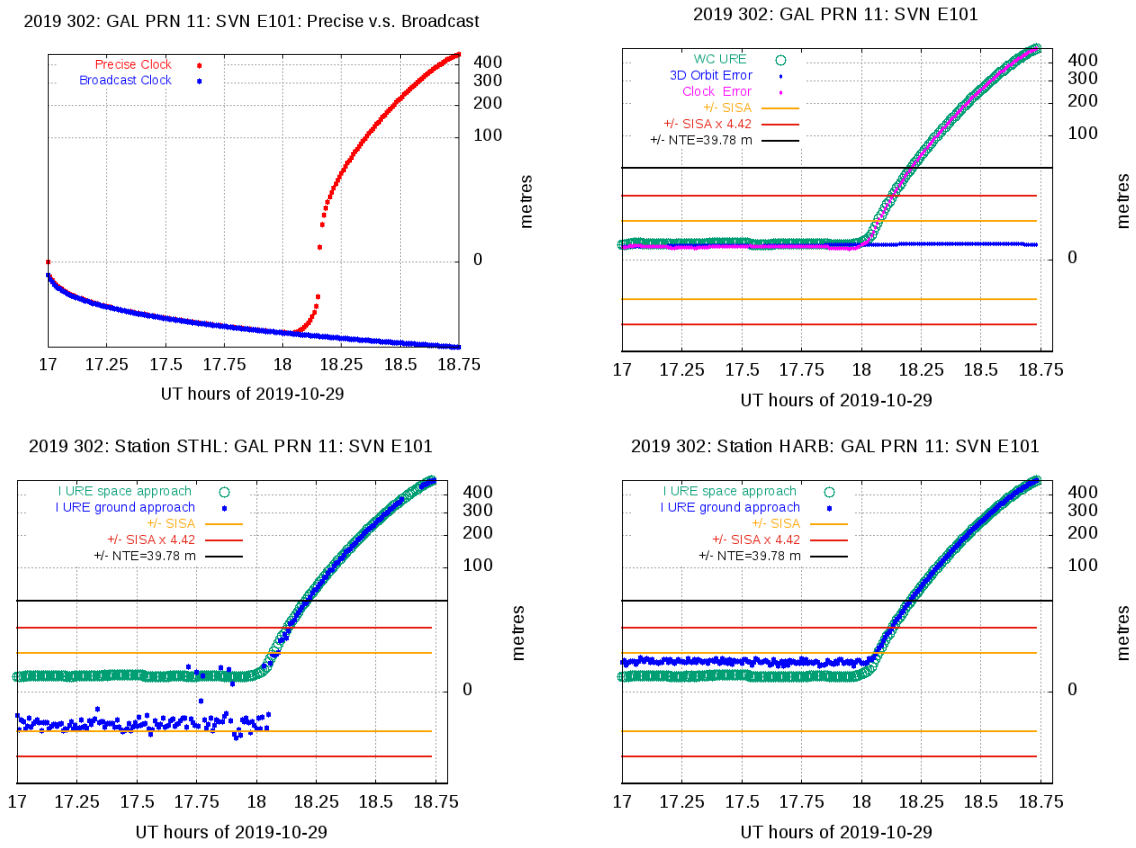

Figure 21. View of the IOV E101 satellite fault on 29 October 2019. The left plot in the first row depicts, in red, the precise clock values estimated by the gAGE processing facility and, in blue, the broadcast clock (values shifted to zero at 17:00 h). The right plot in the first row shows the anomaly detection by the Space Approach. A satellite fault is declared when WC URE reaches the NTE = 39.78 m threshold. The plots in the second row show the anomaly verification by the Ground Approach, using the station STHL (left plot) and HARB (right plot). Horizontal lines indicate +/- SISA, yellow; +/- 4.42 × SISA, red; and NTE, black. The *y*-axis is in a cubic root scale.

This anomaly detection by the Space Approach is illustrated in the right plot at the first row of Figure 21. The clock error drift dominates the WC URE, reaching the NTE threshold at about 18:12. The orbit error is well maintained at its nominal value. The second row of Figure 21 illustrates the verification of this anomaly by the Ground Approach, using the station STHL, Santa Helena island (UK) (left plot) and station HARB, Hartebeesthoek (South Africa), (right plot). A total of 50 stations have been used to verify this anomaly (see Table 6), with the anomaly being confirmed by 18 of them. The other 32 were not tracking the satellite at that time.

4.4.2 GPS Satellites: Events Exceeding the 4.42 × IAURA Threshold

Figure 22 and Table 7 summarize the analysis performed on GPS satellites for the period dating from 1 January 2012 to 31 July 2022, strictly applying the methodology given in [33]. In this period of more than 10 years, only one event is recorded (SVN G059) where the WC URE exceeds the threshold NTE = 4.42 × IAURA, totalling 20 min of failure. This satellite failure occurred on 17 June 2012. No more failures until 31 July 2022 have been detected. The analysis and validation of this failure, and other GPS satellite failures before 2012, are detailed in [32], and are not further addressed here for brevity.

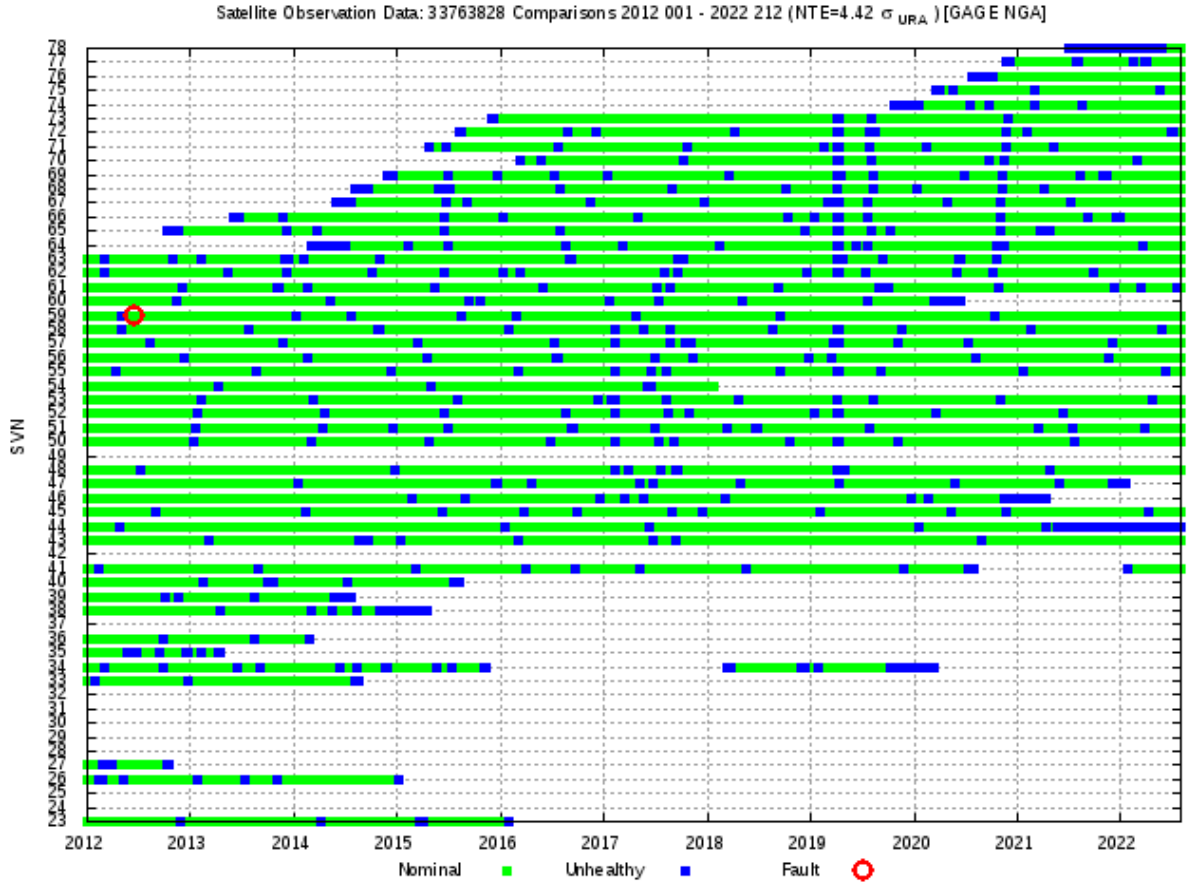

Figure 22. GPS LNAV, from 1 January 2012 to 31 July 2022. Summary of observations for each GPS satellite. Green indicates good observations, blue indicates the satellite was unhealthy, and red circles indicate events exceeding the NTE = 4.42 × IAURA threshold. Consolidated broadcast RINEX files from gAGE are used together with and NGA precise orbits and clocks.

Table 7. GPS LNAV, from 1 January 2012 to 31 July 2022. Summary of events detected based on NTE = 4.42 × IAURA. The same content as Table 6 for the Space Approach. The Ground Approach also confirmed all these events.

Events found with Space Approach (NTE= 4.42 × IAURA)								
YYYY DOY	SVN	PRN	Start Time	Duration (min.)	Anomaly		WC URE (m)	IAURA (m)
					Type	Value (m)		
2012 169	G059	19	17 June 2012 00:15	20	eph.	1899.0	451.5	2.40

4.4.3 Signal-in-Space Error Overbounding

The nominal satellite ranging accuracy is typically characterized by a Gaussian distribution that overbounds the true error distribution out to some probability level [45,46]. It is assumed that much larger errors can be experienced than would be expected according to the Gaussian distribution, but with a very low probability. This small probability corresponds to the fault likelihood [32].

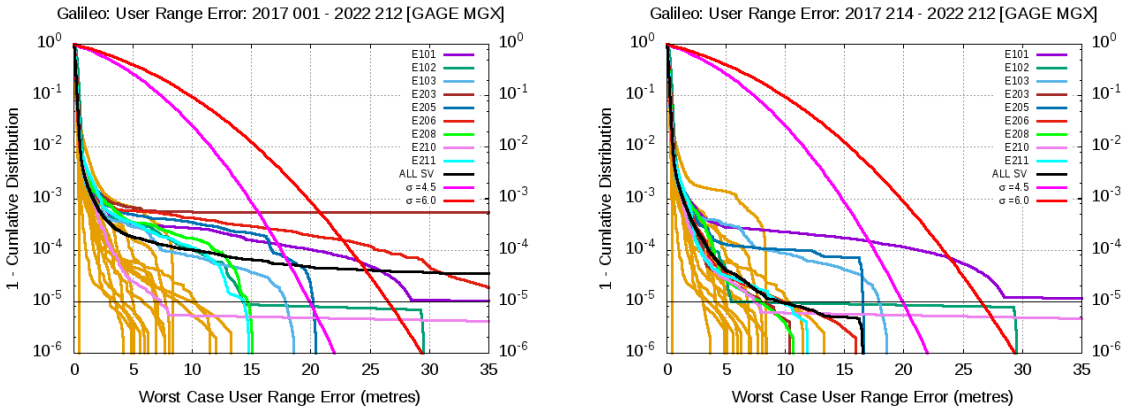

Figure 23. One minus the empirical Cumulative Distribution Function (1-CDF) of the maximum projected ranging errors of Galileo F/NAV broadcast navigation data. The left plot shows the aggregated values from 1 January 2017 to 31 July 2022. The right plot excludes the first six months of data, comprising the period from 1 August 2017 to 31 July 2022. The zero mean Gaussian distributions with σ_{URA} = 4.5 and σ_{URA} = 6.0 m are shown in pink and red, respectively.

An overbound of SISE by a zero-mean Gaussian distribution with σ_{URA} = 4.5 m for the aggregated distribution from all satellites was found in [47], after extrapolation to what is expected when the Galileo constellation reaches the FOC. A slightly higher value of σ_{URA} = 6.0 m was proposed by ICAO NSP [6] as a conservative overbound of the actual SISE to have some additional margin for Horizontal ARAIM (H-ARAIM) Galileo dual-frequency users. These two sigma values are assessed in Figure 23 for the observed SISE overbounding over two time intervals, the full period of 67 months and the last five-year window, i.e. excluding the first six-month period. This analysis is based solely on the experimental error distribution, without any extrapolation to the FOC.

The plots of Figure 23 show the One-minus empirical Cumulative Distribution Function (1-CDF) of the WC URE. The pink and red lines indicate the expected values for a Gaussian distribution with a zero mean and standard deviations σ_{URA} = 4.5 and σ_{URA} = 6 m, respectively. The left plot comprises the full period, from 1 January 2017 to 31 July 2022. Satellites that experienced failures are indicated by different colours, i.e. E101, E102, E103, E203, E205, E206, E208, E210 and E211, see Table 6. The aggregated 1-CDF for all satellites is shown in black. Several of these satellites experienced anomalous events only during the firsts six months of operation after the IS OS was declared, affecting the CDF behaviour. The root cause of these events has been analysed in detail by the CSP, and most of them are not considered representative of the FOC of Galileo [47]. In fact, according to the Galileo Project Office, only the events of E203, on 6 June 2017, and E101, on 29 October 2019, are considered

representative of the FOC [2] (see Section 6.3). Two additional events occurred Two additional events occurred after the time this paper was written: E102, on 21 January 2021, and E210, on 29 April 2022. The first one has been also confirmed by [48].

The right plot of Figure 23 shows the same 1-CDF, excluding the first six months of data, where many of the abovementioned events occurred, i.e. from 1 August 2017 to 31 July 2022. This time-window eliminates most, but not all, of the abovementioned events that occurred. As depicted, the two Gaussian distributions with σ = 4.5 and σ = 6 m overbound all satellites down to 1×10^{-5} probability level, except E101. Moreover, the aggregated 1-CDF, incorporating all satellites, in black, is well bounded below 1×10^{-5}.

It is worth to say that, although the GNSS constellation (the Galileo system in this case) is assumed to be stationary, this hypothesis is not entirely true. In fact, the ground segment software is updated and improved over time, and the satellite designs are refined with enhanced capabilities. Therefore, the GNSS constellations are expected to evolve toward a better performance along time, and stationarity can be assumed as a conservative hypothesis. It should be also noted that, whether or not a satellite exceeds the Gaussian distribution, at a given probability level, depends on the magnitude of the fault and on the total amount of data available to the satellite, regarding to the fault duration. For instance, in the case of the E206 event of the Galileo satellite (5 September 2018, see Table 6), the amount exceeding the threshold and duration of the event was not long enough, compared with the total amount of data, to strongly affect the 1-CDF overbounding (see Figure 23, right plot, Table 6 and Figure 18).

Figure 24 shows the same plots as Figure 23 but for the GPS satellites over 67 months of data period ending on the same date as the Galileo analysis (31 July 2022), from 1 January 2012 to 31 July 2022, at the left plot, and about over a 10-year period, from 1 January 2017 to 31 July 2022, in the right plot. In the plot at the left side, only the GPS satellite G059 exceeds the red line, but bellow the 1×10^{-5} probability level. As shown in Table 7 and Figure 22, although this satellite experienced a fault event (17 June 2012) of about 20 min of duration, and with a WC URE reaching up to 451.5 m, it falls below the 1×10^{-5} level, due to the large amount of valid data available of this satellite. In the right plot, all satellites largely fall under the Gaussian distributions depicted by the red, pink and even blue lines associated to σ = 6.0, 4.5 and 2.5 m, respectively.

Having in mind the previous considerations, it is important to point out that the Galileo results are based on a reduced amount of data, about five years and a half, and some of the events experienced (identified in the previous section 4.1) do not reflect the FOC configuration of the system. The results must then be consolidated with large observational data.

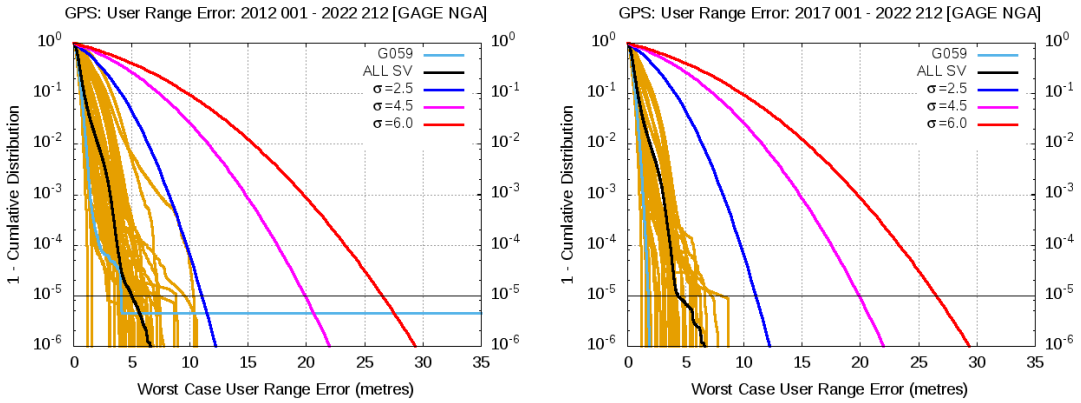

Figure 24. The same plots as in Figure 23, but for GPS LNAV broadcast navigation data in the periods 1 January 2012 to 31 July 2022, in the left plot, and 1 January 2017 to 31 July 2022, in the right plot.

4.5 Observed Nominal Accuracy

The observed nominal accuracy of Galileo data is derived by excluding the tails of the SISE distribution analysed in Section 4.3. Thence, a Galileo satellite is assumed to be in Nominal Condition when the following conditions are met simultaneously:

- The WC URE is under the 4.42 × SISA threshold;
- The most recent navigation data set broadcast on a Healthy SIS by the Galileo satellite is used, where Healthy SIS means:
  The RINEX field SV health is 0, i.e. DVS = ”Navigation Data Valid” and HS = ”Signal OK” and SISA ≠ NAPA;
- Broadcast navigation message is within its validity time, i.e. $AoE = t - Toe \leq 4$ h;
- The precise orbits and clocks are available and healthy.

Table 41, in Annex H, shows, for the Galileo F/NAV navigation data, the overall mean value, 68th and 95th percentiles, and the sigma value for the Galileo radial, along-track, cross-track, clock, WC URE, and IURE. The values are given for each individual satellite, grouped by block and aggregate total. In the case of IURE, the values have been estimated over 20 points spread evenly on the Earth, derived from the vertices of a regular dodecahedron [33]. The analysed period comprises from 1 January 2017 to 31 July 2022. The GPS nominal accuracy from LNAV navigation message over the same period is given in Table 42 (in Annex H) for comparison.

Figure 25 and Figure 26 show a compact view of the mean value and 68th and 95th percentiles associated with Table 41 and Table 42. The plots in the left column are for Galileo satellites, whereas plots in the right column are for GPS satellites. From top to bottom, plots in Figure 25 are for radial, along-track, cross-track values, and plots in Figure 26 are for clock, WC URE and IURE values. The consolidated gAGE RINEX navigation files for Galileo and GPS have been used in this assessment.

As it can be seen in Figure 25, Figure 26 and Table 41, except perhaps for the radial component, the Galileo satellites show much smaller percentile values than the GPS satellites. Nevertheless, the mean bias appearing in the radial component of IOV and FOC Galileo satellites, of 4.3 and 7.8 cm, respectively, is significant. The largest biases are found in the FOC satellites, mainly on E203 to E214, reaching up to more than 10 cm. It is worth mentioning that the ANTEX files igs14_2194.atx from IGS and GSAT_2023.atx (with its associated Antenna Reference Points) from the European GNSS Service Center [38] have been used, and only discrepancies in their APCs were identified on satellites E215 to E222, which are those experiencing the smaller biases in the FOC satellites. No discrepancies are found in the APCs for the IOV satellites. Thence, as the larger biases are associated with satellites having the same APCs in both ANTEX files, the abovementioned biases are not due to any mismatch between the APCs used in the IGS products and Galileo broadcast orbits for these satellites. In spite of these biases, the 68th and 95th percentiles and the standard deviation in the radial component error are of the same order as those of GPS, or even slightly smaller (see Table 41 and Table 42). This positive bias in the radial component could be partially linked to the accuracy of the MGEX (CODE) reference products for Galileo satellites at the level of 5 cm [49], but it deserves further studies.

The clock alignment applied for Galileo satellites can absorb a global bias in the clock error, and this is probably the reason for having only −0.2 cm of total mean clock error in the last row of Table 41. Satellites E102 and E204 experience clock biases over 10 cm. In spite of these biases, again, the 68th and 95th percentiles and standard deviation is much smaller, than in GPS. The combined bias in the radial component and clocks is translated to the WC URE, exhibiting global values of 19.4 and 9.3 cm for IOV and FOC Galileo satellites, respectively. Again, the 68th and 95th percentiles and standard deviation of Galileo are much smaller than those of GPS.

The along-track error component of Galileo satellites is several times smaller than the GPS, as depicted by the four statistics shown in Table 41 compared with Table 42. The cross-track component also shows smaller error figures than those of the GPS.

On the other hand, and as expected from the previous results, the Galileo IURE values, in the right of Table 41, shows a mean bias highly correlated with the WC URE values, while the 68th and 95th percentiles and standard deviation are, again, smaller than in GPS.

Finally, in order to have a more robust estimation of GPS nominal accuracy, Table 43 shows the values computed over the more than the ten-year period considered before, from 1 January 2012 to 31 July 2022. As it is shown, values quite similar to those in Table 42 are obtained.

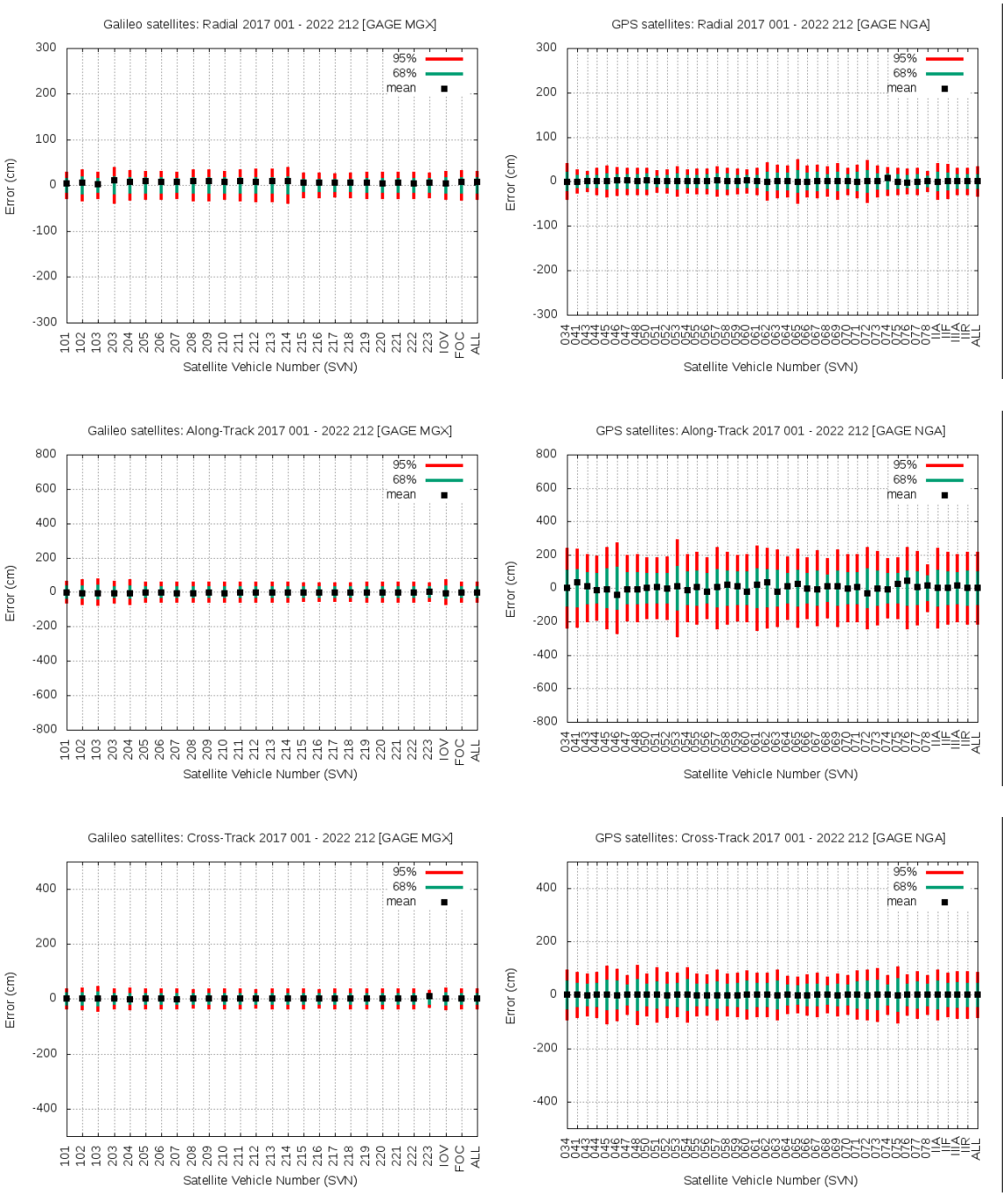

Figure 25. From top to bottom the plots are for Radial, Along-track and Cross-track, from 1 Januray 2017 to 31 July 2022. Left column plots are for Galileo F/NAV and right column plots for GPS LNAV navigation data. The same vertical range is used for Galileo and GPS satellites. The SVNs are in the horizontal axis. Each plot shows the mean value and 68th and 95th percentiles associated to Table 41 and Table 42 in Annex H.

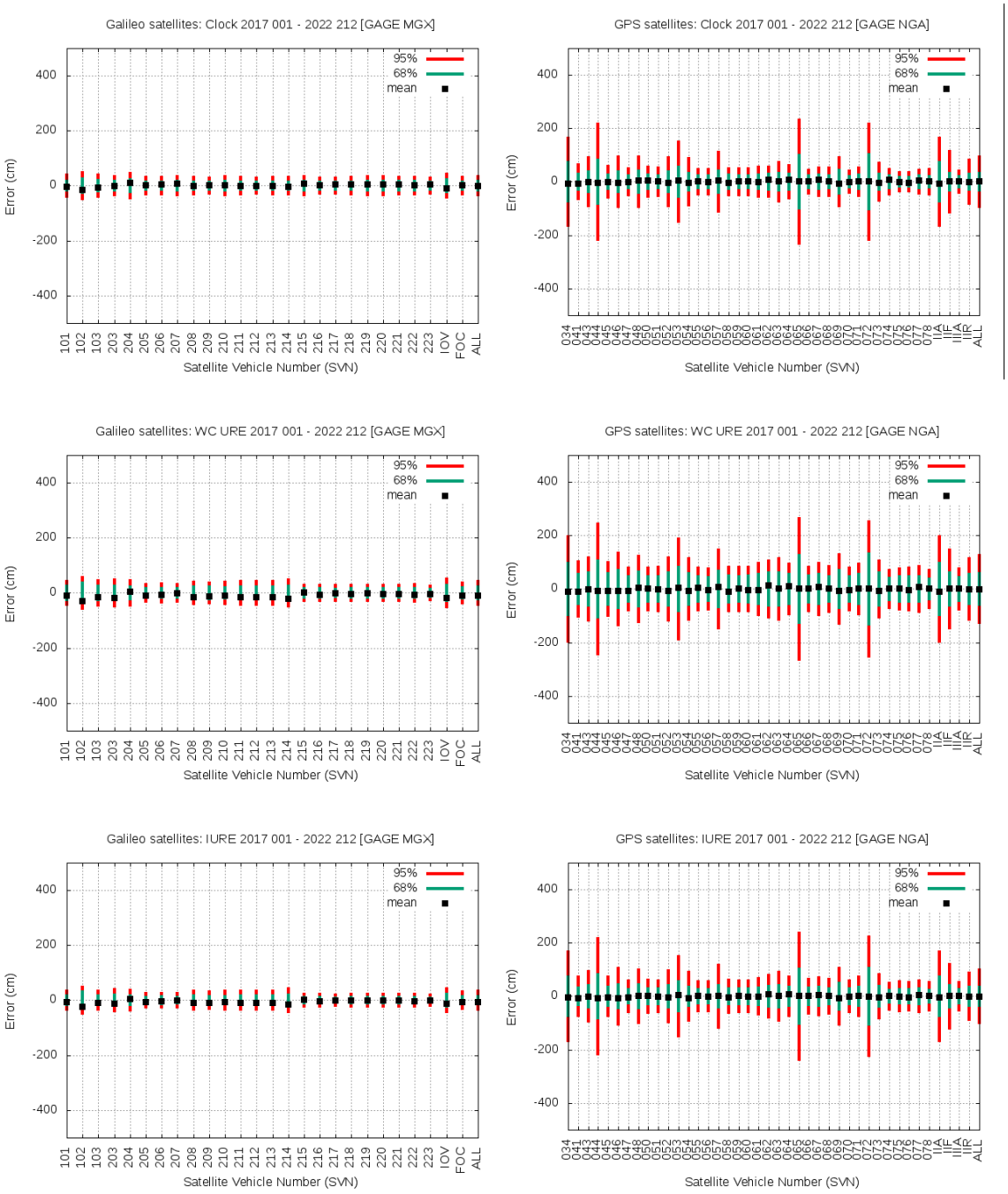

Figure 26. From top to bottom the plots are for Clock, WC URE and IURE, from 1 Januray 2017 to 31 July 2022. Left column plots are for Galileo F/NAV and right column plots for GPS LNAV navigation data. The same vertical range is used for Galileo and GPS satellites. The SVNs are in the horizontal axis. Each plot shows the mean value and 68th and 95th percentiles associated to Table 41 and Table 42 in Annex H.

4.6 Observed Fault Probabilities

The observed probabilities of satellite, P_{sat}, and constellation, P_{const}, failures have been estimated following the definitions of [1]. The expected satellite Fault Rate (R), given by k events over the interval T, can be estimated by the expression:

$$E(R|k) = \frac{k + 1/2}{T} \quad (1)$$

where T is the aggregated total signal of valid hours, i.e. with signals indicating that they were healthy (aggregated for all satellites). The probability of a satellite fault, P_{sat}, is the fault rate multiplied by the Mean Time to Notify (MTTN) the user, i.e. the delay between the event onset and the average time for the system to notify such event to the user:

$$P_{sat} = E(R|k) \times \text{MTTN} \quad (2)$$

Derivation of these formulae can be found in [1], where it is assumed that the probability of faults follows a Poisson distribution and the a priori probability of R is approximated by a distribution $f(R) \propto 1/\sqrt{R}$ between 0 and R_{max}.

A methodology to estimate the MTTN in Galileo is summarized in [47], where 60 min are expected for the future configuration of the Galileo system in the FOC. Further results from ICAO NSP [6] expect to reduce this value, considering improved monitoring capabilities on the ground and tuning performances.

The satellite fault events and their duration have been identified applying, again, the methodology of Section 2, but considering the two aforementioned NTE thresholds:

1) NTE = 4.42 × 9 = 39.78 m threshold, according to the Galileo commitments [3,5];
2) NTE = 4.17 × 6 = 25.04 m threshold recently proposed to the ICAO NSP on April 2020 [6].

In the last subsection, the results are extrapolated to the FOC of the Galileo program.

4.6.1 Observed Fault Probabilities Based on NTE = 39.78 m

According to the Milestone 3 report [3], the target H-ARAIM service level can be established based on GPS and Galileo with the following contribution from Galileo:

- σ_{URA} (overbound of SISE) lower than 9 m;
- P_{sat} lower than 1×10^{-5}/sat;
- P_{const} lower than 1×10^{-4}.

A fixed NTE = 4.42 × σ_{URA} = 39.78 m has been used for Fault Detection.

The events found using NTE = 39.78 m for all Galileo satellites are given in Table 8 and depicted in Figure 27. Two satellite failures occurred in 2017, the E206 (on 7th March) and E203 (on 6th and 7th June), one satellite failure in 2019, the E101 (on 29th October), see details of this event in Section 4.4.1.1, and one satellite failure in 2022, the E210 (on 29th April).

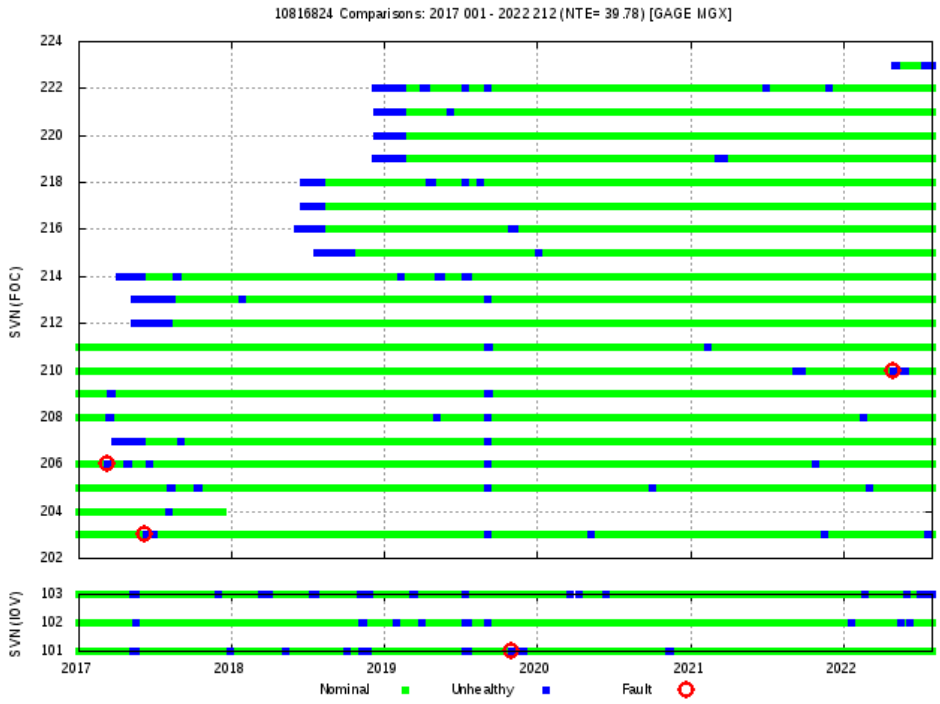

Figure 27. The same plot as in Figure 18, but considering the NTE = 39.78 m threshold.

Table 8. The same as Table 6 for the Space Approach, but considering the NTE= 39.78 m threshold. The "Duration" column indicates the elapsed time having WC URE over the NTE threshold. The Ground Approach also confirmed all these events.

Events found with Space Approach using NTE= 39.78 m									
YYYY DOY	SVN	PRN	Start Time		Duration (min.)	Anomaly		WC URE (m)	SISA (m)
						Type	Maximum Value (m)		
2017 066	E206	30	7 March 2017	03:20	40	clock	340.9	341.9	3.12
2017 157	E203	26	6 June 2017	06:00	1080	clock	491.3	491.9	3.12
2017 158			7 June 2017	00:00	435	clock	460.4	472.8	3.12
2019 302	E101	11	29 October 2019	18:15	30	clock	431.9	432.1	3.12
2022 119	E210	01	29 April 2022	01:00	15	clock	51.0	51.1	3.12

Table 9. Summary of faults detected using NTE = 39.78 m. The "Duration" column indicates the elapsed time having WC URE over the NTE threshold.

Period	Number Satellite Fault Events			Faults Duration (h)			Total Signal Valid Hours
	IOV	FOC	Total	IOV	FOC	Total	
1 January 2017–31 July 2017	0	2	2	0	25.9	25.9	58,369
1 August 2017–31 December 2017	0	0	0	0	0	0	54,006
Full 2018	0	0	0	0	0	0	133,852
Full 2019	1	0	1	0.5	0	0.5	175,729
Full 2020	0	0	0	0	0	0	186,207
Full 2021	0	0	0	0	0	0	188,410
1 January 2022–31 July 2022	0	1	1	0	0.25	0.25	104,829

Table 10. Fault Rate and Probability of Galileo Satellite Fault, estimated with NTE = 39.78 m. The "Duration" column indicates the elapsed time having WC URE over the NTE threshold.

Period	Total Satellite Fault Events			Total Valid (h)	Estimated Mean Fault Rate (/sat/hour)	Average Fault Duration (hours)	MTTN (hours)	*Psat* (/sat)
	IOV	FOC	Total					
1 January 2017–31 July 2022	1	3	4	9.01×10^5	5.0×10^{-6}	6.66	6.66	3.3×10^{-5}
1 August 2017–31 July 2022	1	1	2	8.43×10^5	3.0×10^{-6}	0.38	1.00	3.0×10^{-6}

Table 9 summarizes the number of satellite faults, the cumulative duration of detected faults, and total of signal valid hours in each year from 2017 to 2022. The first row, after the header, specifies the values from 1 August to 31 December 2017. The last row indicates the values from 1 January to 31 July 2022. Results are shown for the IOV and FOC satellites and across the whole constellation. These values are taken from the fault duration column in Table 8.

Table 10 shows the cumulative results from Table 9 for the two previously considered periods, from 1 January 2017 to 31 July 2022 (first row after the header) and for the last five-year time window, from 1 August 2017 to 31 July 2022 (in the last row). It is worth mentioning that in this last period, i.e. excluding the firsts six months of data, only two satellite faults are found, which were experienced by the IOV satellite E101 on 29 October 2019 and FOC satellite E210 on 29 April 2022.

A simple experimental estimation of MTTN can be made from the observed averaged duration of faults, but it is worth mentioning that this can only be seen as a rough estimate of this value. To be conservative, in the numerical application, MTTN is used as the highest value between this averaged duration of faults and the 60 min given in [47], see Table 10.

As shown, the obtained results for the observed fault probability over the last five-year time window are very promising, as the estimated value of P_{sat} = 3.0×10^{-6}/sat given in Table 10 is well below the previous commitment of 1×10^{-5}. This value increases to 3.3×10^{-5}/sat when considering the full period of 67 months, but as already commented, most of the faults experienced during the first half of 2017, and even others detected after this period, are considered not representative of what is expected in the FOC configuration [47].

No Wide Faults, i.e. affecting more than one satellite simultaneously, appear when considering the NTE = 39.78 m threshold. Nevertheless, taking into account the reduced size of data, a conservative value of P_{const} = 1×10^{-4} can be used [32].

4.6.2 Observed Fault Probabilities Based on NTE = 25.04 m

The Galileo program established a dedicated process involving the main actors (EC, ESA, and GSA), which analyses the Galileo performance to support the definition of the ARAIM concept and relative standards. The conclusions presented in the ICAO NSP on April 2020 consider the following values for Galileo [6]:

- σ_{URA} (overbound of SISE) lower than 6 m;
- P_{sat} lower than 3×10^{-5}/sat;
- P_{const} lower than 1×10^{-4}.

The analysis of previous subsection has been re-executed with NTE= $4.17 \times \sigma_{URA}$ = 25.04 m as the threshold for Fault Detection.

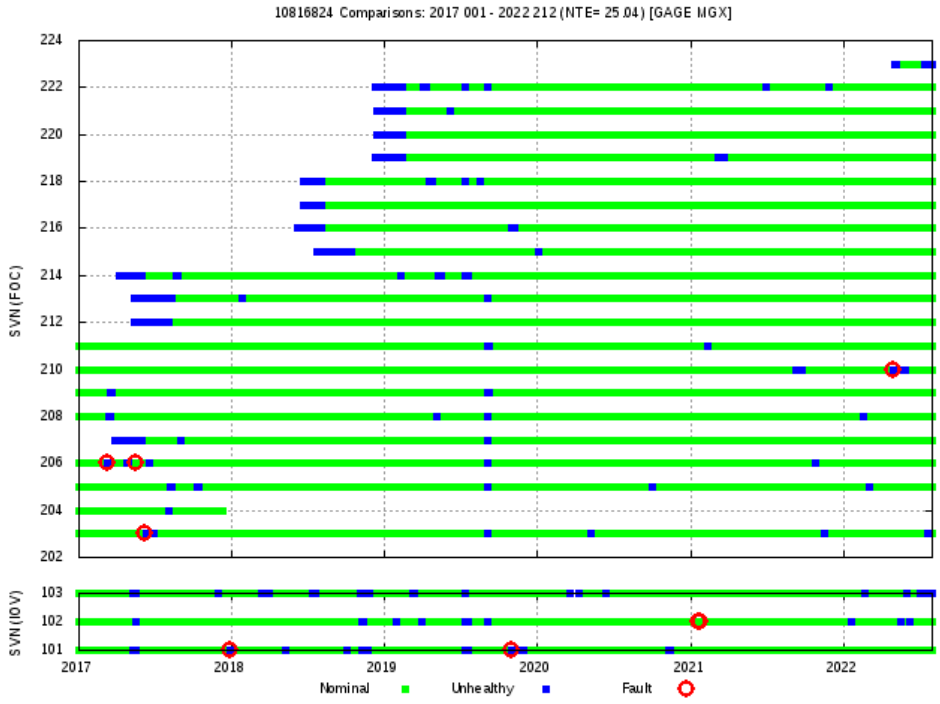

Figure 28. The same plot as in Figure 18, but considering the NTE = 25.4 m threshold.

As it is shown in Table 11, there are three additional events out of those of Table 8 having WC URE over the NTE = 25.04 m. The FOC satellite E206 on 14-15 of May 2017, the IOV satellites E101 on 26 December 2017 and E102 on 21 January 2021.

The estimated mean conditional fault rate $E(R|k)$ and P_{sat} for this more stringent threshold can be found in Table 13. As shown, P_{sat} = 5.3 × 10^{-6}/sat is estimated when considering the last five-year time window, and MTTN = 60 min, which is again below the 3 × 10^{-5}/sat value. When including in the statistics the initial period, from 1 January 2017 to 31 July 2017, the P_{sat} increases to 4.0 × 10^{-5}/sat. It must be recalled that no Wide Faults appear when considering this NTE = 25.04 m threshold, and the conservative value of P_{const} = 1×10^{-4} can be used [32].

Table 11. The same as Table 6 for the Space Approach, but considering the NTE= 25.04 m threshold. The "Duration" column indicates the elapsed time having WC URE over the NTE threshold. The Ground Approach also confirmed all these events.

Events found with Space Approach using NTE= 25.04 m									
YYYY DOY	SVN	PRN	Start Time		Duration (min.)	Anomaly		WC URE (m)	SISA (m)
						Type	Maximum Value (m)		
2017 066	E206	30	7 March 2017	03:15	45	clock	340.9	341.9	3.12
2017 134	E206	30	14 May 2017	22:45	75	clock	26.6	26.9	3.12
2017 135			15 May 2017	00:00	195	clock	31.4	36.7	3.12
2017 157	E203	26	6 June 2017	5:55	1085	clock	491.3	491.9	3.12
2017 158			7 June 2017	0:00	435	clock	460.4	472.8	3.12
2017 360	E101	11	26 December 2017	13:05	110	clock	28.4	28.4	3.12
2019 302	E101	11	29 October 2019	18:15	30	clock	431.9	432.1	3.12
2021 021	E102	12	21 January 2021	01:40	25	clock	29.4	29.5	3.12
2022 119	E210	01	29 April 2022	01:00	15	clock	51.0	51.1	3.12

Table 12. Summary of faults detected using NTE = 25.04 m. The "Duration" column indicates the elapsed time having WC URE over the NTE threshold.

Period	Number Satellite Fault Events			Faults Duration (h)			Total Signal Valid Hours
	IOV	FOC	Total	IOV	FOC	Total	
1 January 2017–31 July 2017	0	3	3	0	30.58	30.58	58,369
1 August 2017–31 December 2017	1	0	1	0	1.83	1.83	54,006
Full 2018	0	0	0	0	0	0	133,852
Full 2019	1	0	1	0.50	0	0.50	175,729
Full 2020	0	0	0	0	0	0	186,207
Full 2021	1	0	1	0.42	0	0.42	188,410
1 January 2022–31 July 2022	0	1	1	0	0.25	0.25	104,829

Table 13. Fault Rate and Probability of Galileo Satellite Fault, estimated with NTE = 25.04 m. The "Duration" column indicates the elapsed time having WC URE over the NTE threshold.

Period	Total Satellite Fault Events			Total Valid (h)	Estimated mean Fault Rate	Average Fault Duration	MTTN (hours)	*Psat* (/sat)
	IOV	FOC	Total		(/sat/hour)	(hours)		
1 January 2017–31 July 2022	3	4	7	9.01×10^5	8.3×10^{-6}	4.80	4.80	4.0×10^{-5}
1 August 2017–31 July 2022	3	1	4	8.43×10^5	5.3×10^{-6}	0.75	1.0	5.3×10^{-6}

4.6.3 Extrapolation to Galileo Full Operational Capability

As discussed above, the root cause of each one of the different events experienced by Galileo satellites was investigated in detail by the Galileo Project Office to identify whether it could continue to occur when Galileo reaches the future FOC or will be eliminated thanks to the system configuration updates during this consolidation process. Table 14 provides the list of events identified as representative of the FOC [2]. The event on 29 of April 2022 has been added to this list, as it occurred after this paper was written.

From the extrapolation to FOC, it follows that the three satellite events listed in Table 14, having been observed over a total of 9.01×10^5 valid hours on the 67 months of data (see Table 9), imply an average Fault Rate of 3.9×10^{-6}/sat/hour.

Since the averaged fault duration resulting from the exposure time, i.e. fault duration, in Table 14 is only 33.3 min, it will take, again, 60 min for the MTTN to calculate P_{sat}. It should be noted that such an averaged duration value 33.3 min is close to the 45 min considered by ICAO NSP [6] as the MTTN value that is expected to be achieved for the Narrow Faults in the future configuration of the Galileo system.

Taking MTTN equal to 60 min, it results in a P_{sat} value of 3.9×10^{-6}/sat. This value, estimated for the whole analysed period, i.e. from 1 January 2017 to 31 July 2022, is much smaller than the value $P_{sat} = 4.0 \times 10^{-5}$/sat given in Table 13 for the same time interval, and closer to the $P_{sat} = 5.3 \times 10^{-6}$/sat value found when excluding the first six-month period.

Table 14. List of retained events after FOC extrapolation and associated exposure time (also extrapolated) between 1 January 2017 and 31 July 2022.

Date	SVN	PRN	Extrapolated to FOC	
			Exposure Time (min)	WC URE (m)
6 June 2017	E203	26	50	>40
29 October 2019	E101	11	35	>40
29 April 2022	E210	01	15	>40

5 Advanced RAIM Performance Evaluation

With the new context of multiple GNSS constellations and multiple frequencies, ARAIM is meant to support service levels from RNP-03 up to the most challenging LPV-200. The Working Group C- ARAIM Technical Subgroup (ARAIM TSG) [50] is developing GPS-Galileo based Safety-of-life services. The goal of ARAIM TSG is to stablish whether ARAIM can be the basis for a multi-constellation concept to support air navigation worldwide.

As already indicated, ARAIM can detect and flag faults in single satellites (narrow faults) or concurrent failures in two or more satellites (wide faults or constellation faults). The number of fault modes to monitor by the user algorithm depends on the probabilities P_{sat} and P_{cons}. Among these probabilities, the algorithm performance depends on the nominal error model, where the contribution of the satellite to the pseudorange error is characterized by a Gaussian distribution $N(\mu, \sigma)$ such that:

- $\sigma \leq \sigma_{URA,i}$ and $|\mu| \leq b_{nom,i}$ for integrity purposes.
- $\sigma \leq \sigma_{URE,i}$ and $\mu = 0$ for continuity (false alert or failed exclusion) purposes.

These five parameters ($P_{cons}, P_{sat}, \sigma_{URA}$, σ_{URE} and b_{nom}) will be broadcast in the Integrity Support Message (ISM), see Table 16. There are other contributors to the variance of pseudorange error: the residual tropospheric delay, the code noise and multipath, and the residual ionospheric delay for single frequency users, which are given in Annex A.

Three main architectures are being considered for the GPS and Galileo constellations. Its performance evaluation is described in [50] and [28]:

- Horizontal ARAIM (H-ARAIM):
  - For single constellation P_{cons} can be set to 10^{-8} or even zero (like CRAIM).
  - For multi-constellation, only GPS P_{cons} can be set to zero, but not for other GNSSs (Annex-B assertation 1 in [50]).

  An σ_{URA} value of 2.5 metres can be used.

- Vertical ARAIM (V-ARAIM) (online): P_{cons} can be set at 10^{-7} or to 10^{-8}, assuming wide constellation faults are verified externally by an independent ground system, which will also estimate and provide ephemeris and clock corrections in an extended online V-ARAIM message (online). Low σ_{URA} values are expected, e.g. 0.5 to 2 metres, see [50] for more details.

- Vertical ARAIM (V-ARAIM) (offline): P_{cons} can be set from 10^{-4} up to almost 10^{-7}, being the constellation wide-fault check by the algorithm. As it is shown in next sections, σ_{URA} values of 2.0 metres and below can support V-ARAIM.

Before proceeding to the characterization of the ARAIM performance based on the experimental results of previous Chapter 4, the performances of H-ARAIM and V-ARAIM is illustrated, showing the sensitivity of the global coverage to the ISM parameters (considered as static parameters). The results are based in a *baseline constellation* of GPS and Galileo with 24 satellites per constellation. An extensive study of performance results using also a degraded-constellation (depleted-constellation of 23 satellites per constellation) and optimistic-constellation (27 satellites per constellation) can be found in [28].

5.1 Simulation settings

The software tool and simulation settings used are as follows, most of them from [3]:

- Software: the gNAV tool upgraded with ARAIM.
- Geographical grid and time steps:
  - 5 by 5-degree user grid.
  - 10 sidereal days. Note that GPS satellites repeat geometry every sidereal day and Galileo satellites repeat geometry every 10 sidereal days.
  - 600 seconds time steps.
- Elevation masking angle of 5 degrees for both GPS and Galileo satellites.
- Evaluation criteria:
  - Global coverage of 99.5%, between -90 and 90 degrees of latitude.
  - For coverage, user grid points are weighted by the cosine of the latitude to account for the relative area they represent.
- Satellite configuration:
  - Baseline: GPS 24, Galileo 24 (i.e. 24-slot nominal constellations). This corresponds to the almanacs: `almmops.txt` (for GPS) and `almanc_Galileo_24_Week_703.alm.txt` (for Galileo) [50].
- Navigation Modes:
  - Vertical-ARAIM (V-ARAIM): LPV-200, LPV-250.
  - Horizontal-ARAIM (H-ARAIM): RNP-0.1, RNP-0.3.

Table 15. Availability criteria

Navigation Mode	HAL	VAL	EMT	$\sigma_{acc_{max},Vert}$
LPV-200	40 m	35 m	15 m	1.87 m
LPV-250 / LPV1	40 m	50 m		
RNP-0.1	185 m			
RNP-0.3	556 m			

These navigation modes are assessed for different values of the ISM taken as constant parameters: P_{sat}, P_{const}, URA and b_{nom}, see Table 16.

Besides the protection levels, Table 15 shows the two additional conditions already introduced in section 3.2.2.8 for the LPV-200 navigation mode:

- The Effective Monitor Threshold (EMT) is defined as the maximum of the detection thresholds that have a prior probability equal or above $P_{EMT} = 10^{-5}$. This test prevents against faults that are not large enough to ensure detection, but can create vertical position errors greater than 15 m more often than 0.00001% of the time. It is worth to say that ARAIM does not use differential corrections, then its accuracy is likely to be worse than the SBAS. Furthermore, its method of error detection may allow fault modes to create larger position errors before they are identified and removed [27].

- **The accuracy threshold test, $\sigma_{acc_{max},Vert}$,** is defined to assure 10 metres of fault-free accuracy in the vertical component the 99.99999% of time. That is, assuming a Gaussian distribution, the k-factor that corresponds to the 99.99999th percentile is 5.33, and thence $\sigma_{acc,Vert} \leq 10 \text{ m} / 5.33 = 1.87 \text{ m}$.

Table 16. List of parameters derived from the ISM

Description	
$\sigma_{URA,i}$	Standard deviation of the clock and ephemeris error of satellite *i* used for integrity.
$\sigma_{URE,i}$	Standard deviation of the clock and ephemeris error of satellite *i* used for accuracy and continuity.
$b_{nom,i}$	Maximum nominal bias for satellite *i* used for integrity.
$P_{sat,i}$	Prior probability of fault in satellite *i* per approach.
$P_{const,j}$	Prior probability of a fault affecting more than one satellite in constellation *j* per approach.

Note: the same value for all satellites is taken for each ISM parameter, in the simulations.

5.2 ARAIM global performance sensitivity analysis

Using the settings defined in previous section 5.1, I have done a sensitivity analysis that involves single- (GPS or Galileo) and dual-constellation (GPS plus Galileo), with single- (L1, L5, E1 or E5) and dual-frequency (L1/L5, E1/E5).

To easy a first glance view of performances, results are summarised in a set of tables coloured following the next criterion, taken from [28]:

- **Green** colour indicates **High performance**, with availability coverage of 90% or higher.
- **Yellow** colour indicates **Medium performance**, with availability coverage from 80% to 90%.
- **Red** colour indicates **Low performance**, with availability coverage under 80%.

5.2.1 Vertical ARAIM with dual frequency GPS and Galileo

The results of simulations for V-ARAIM with a dual constellation (GPS plus Galileo) and dual frequency (L1/L5 and E1/E5) are given in this section, where the sensitivity of the Vertical Guidance Availability Coverage is assessed as a function of different ISM parameters.

For V-ARAIM, the ISM parameters are set to (for GPS and Galileo, in line with [3]):

- $\sigma_{URA} = 0.75$ m, 1 m, 1.5 m, 2 m (larger URA values do not allow LPV coverage).
- $\sigma_{URE} = 2/3\ \sigma_{URA}$.
- $b_{nom} = 0$ m, 0.75 m (0.75 m is the value suggested by [51]).
- $P_{sat} = 10^{-4}$, 10^{-5}, 10^{-6}.
- $P_{cons} = 10^{-4}$, 10^{-5}, 10^{-6}, 10^{-7} (according to the Annex-B assertation 1 in [50], for V-ARAIM it is not acceptable to assume $P_{cons} = 0$ for any constellation, including GPS).

Note. As it was already shown in Table 5, no constellation fault is monitored when $P_{cons} = 10^{-8}$.

Figure 29 depicts the coverage map for LPV-200 of 99.5th with dual frequency L1/L5 V-ARAIM with GPS and Galileo where the 98.59% of coverage area is achieved. The ISM parameters used are $\sigma_{URA} = 1\ m$, $\sigma_{URE} = 2/3\ \sigma_{URA}$, $b_{nom} = 0.75\ m$; $P_{const;GPS} = P_{const;Galileo} = 10^{-4}$; $P_{sat;GPS} = P_{sat;Galileo} = 10^{-5}$. This mode has been highlighted in blue in Table 17 to easily identify in the global context of such table.

The effect of the σ_{URA} value in the availability coverage maps is depicted in Figure 30. The ISM parameters are the same as in Figure 29, except σ_{URA} (for GPS and Galileo satellites), which is taken as 2 m. Vertical protection levels are now over 35 m, and σ_{Vacc} and EMT over 1.9 m and 15 m respectively, dramatically degrading the availability coverage down to the 3.26%. This mode has been highlighted in pink in Table 17.

Table 17 and Table 18 summarises the results of simulations for V-ARAIM with a dual constellation (GPS plus Galileo) and dual frequency (L1/L5 and E1/E5) for LPV-200. Table 19 and Table 20 summarises the results for LPV-250 navigation mode.

The next conclusions arose from these tables:

- σ_{URA} value is the dominant parameter for the availability coverage.
- The bias b_{nom} (taken as 0 m or 0.75 m) has a low impact on the availability performances, having a slightly greater coverage when this parameter is set to zero.
- The P_{cons} has a higher impact on the availability coverage than the P_{sat}.
- Global APV-200 coverage can be achieved when $\sigma_{URA} = 1\ m$ (GPS plus Galileo) and $b_{nom} = 0.75$ m, with availability coverage of 97.15% for the highest probabilities of P_{sat} and P_{cons} and 100% for the lowest probabilities in Table 17. Still global APV-200 of 99.95% or greater could be achieved with $P_{cons} = 10^{-6}$, but this low probability level would be difficult to guarantee for LPV-200.
- Results are quite similar for $P_{sat} = 10^{-5}$ to $P_{sat} = 10^{-7}$. Then, $P_{sat} = 10^{-5}$ can be enough.
- Global APV-200 coverage over 98% of can be achieved with $P_{cons} = 10^{-4}$, and $P_{sat} = 10^{-5}$ or lower, when $\sigma_{URA} = 1\ m$ and $b_{nom} = 0.75$ m.
- Global APV-250 over 95% is achieved with $P_{cons} = 10^{-4}$, and $P_{sat} = 10^{-5}$ or lower, when $\sigma_{URA} = 2\ m$ and $b_{nom} = 0.75$ m.

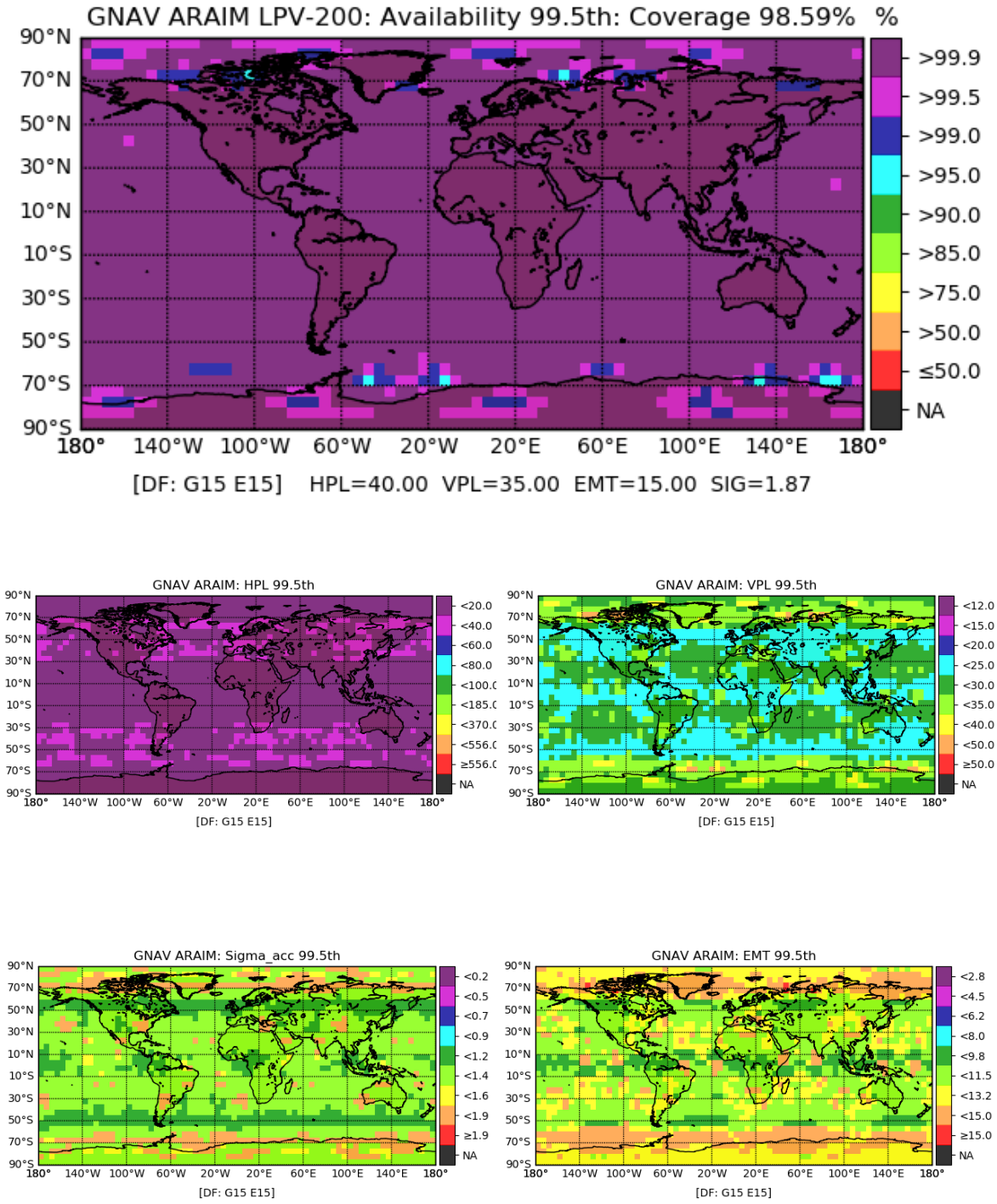

Figure 29. LPV-200 V-ARAIM analysis with Dual-frequency L1/L5 with GPS and Galileo: coverage (top), horizontal and vertical protection levels (middle), accuracy threshold test and Effective Monitor Threshold (bottom). $\sigma_{URA} = 1\ m,\ \sigma_{URE} = 2/3\ \sigma_{URA}, b_{nom} = 0.75\ m;$ $P_{const;GPS} = P_{const;Galileo} = 10^{-4};\ \ P_{sat;GPS} = P_{sat;Galileo} = 10^{-5}.$

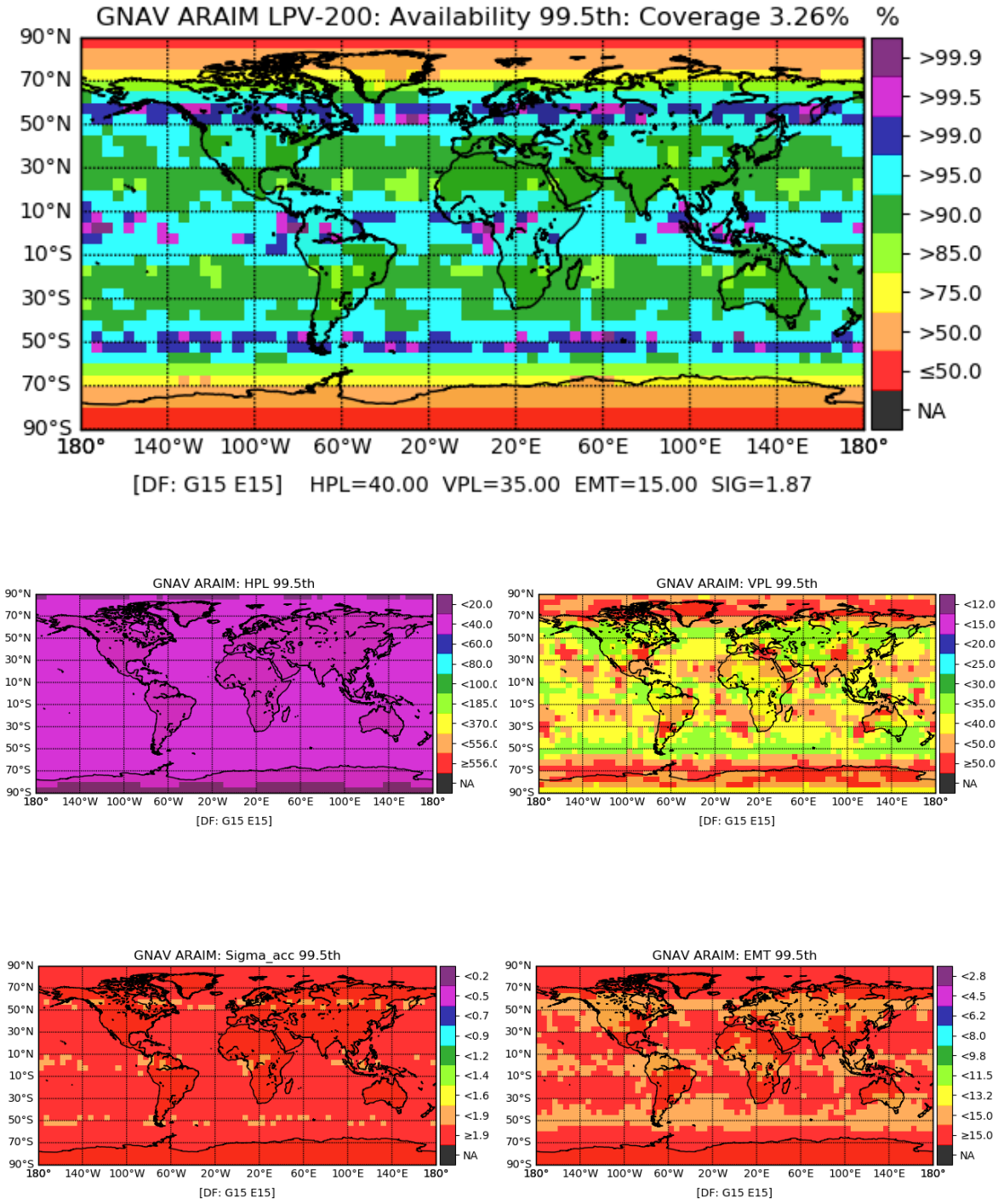

Figure 30. LPV-200 V-ARAIM analysis with Dual-frequency L1/L5 with GPS and Galileo: coverage (top), horizontal and vertical protection levels (middle), accuracy threshold test and Effective Monitor Threshold (bottom). $\sigma_{URA} = 2\ m,\ \sigma_{URE} = 2/3\ \sigma_{URA}, b_{nom} = 0.75\ m;$ $P_{const;GPS} = P_{const;Galileo} = 10^{-4};\ P_{sat;GPS} = P_{sat;Galileo} = 10^{-5}.$

Summary of V-ARAIM Results with Dual Frequency and Two constellations:

Table 17. V-ARAIM Dual-frequency L1/L5 and two constellations (GPS and Galileo).
$\sigma_{URE} = 2/3\ \sigma_{URA}$, $b_{nom} = 0.75\ m$; $P_{const;GPS} = P_{const;Galileo}$; $P_{sat;GPS} = P_{sat;Galileo}$

LPV-200: 99.5% Availability coverage												
b_{nom}=0.75m	URA=SISA=0.75 m			URA=SISA=1 m			URA=SISA=1.5 m			URA=SISA=2 m		
P_{sat}/P_{const}	10^{-4}	10^{-5}	10^{-6}	10^{-4}	10^{-5}	10^{-6}	10^{-4}	10^{-5}	10^{-6}	10^{-4}	10^{-5}	10^{-6}
10^{-4}	99.27%	99.83%	100%	97.15%	98.93%	99.95%	79.07%	87.76%	92.94%	0.98%	4.15%	4.54%
10^{-5}	99.85%	99.54%	100%	98.59%	99.54%	100%	84.99%	91.02%	96.84%	3.26%	4.48%	4.64%
10^{-6}	99.97%	99.63%	100%	98.67%	99.63%	100%	86.00%	91.21%	97.09%	3.74%	4.54%	4.64%
10^{-7}	99.97%	99.63%	100%	98.67%	99.63%	100%	86.03%	91.21%	97.09%	3.74%	4.54%	4.64%

Table 18. V-ARAIM Dual-frequency L1/L5 and two constellations (GPS and Galileo).
$\sigma_{URE} = 2/3\ \sigma_{URA}$, $b_{nom} = 0\ m$; $P_{const;GPS} = P_{const;Galileo}$; $P_{sat;GPS} = P_{sat;Galileo}$

LPV-200: 99.5% Availability coverage												
b_{nom}= 0m	URA=SISA=0.75 m			URA=SISA=1 m			URA=SISA=1.5 m			URA=SISA=2 m		
P_{sat}/P_{const}	10^{-4}	10^{-5}	10^{-6}	10^{-4}	10^{-5}	10^{-6}	10^{-4}	10^{-5}	10^{-6}	10^{-4}	10^{-5}	10^{-6}
10^{-4}	100%	100%	100%	99.43%	100%	100%	87.58%	93.85%	97.33%	2.28%	4.54%	4.64%
10^{-5}	100%	100%	100%	99.88%	100%	100%	90.42%	96.73%	98.66%	4.10%	4.57%	4.71%
10^{-6}	100%	100%	100%	99.88%	100%	100%	90.52%	96.97%	98.67%	4.10%	4.57%	4.71%
10^{-7}	100%	100%	100%	99.88%	100%	100%	90.52%	96.99%	98.67%	4.10%	4.57%	4.71%

Table 19. V-ARAIM Dual-frequency L1/L5 and two constellations (GPS and Galileo).
$\sigma_{URE} = 2/3\ \sigma_{URA}$, $b_{nom} = 0.75\ m$; $P_{const;GPS} = P_{const;Galileo}$; $P_{sat;GPS} = P_{sat;Galileo}$

LPV-250: 99.5% Availability coverage												
b_{nom}=0.75m	URA=SISA=0.75 m			URA=SISA=1 m			URA=SISA=1.5 m			URA=SISA=2 m		
P_{sat}/P_{const}	10^{-4}	10^{-5}	10^{-6}	10^{-4}	10^{-5}	10^{-6}	10^{-4}	10^{-5}	10^{-6}	10^{-4}	10^{-5}	10^{-6}
10^{-4}	100%	100%	100%	100%	100%	100%	97.61%	99.91%	99.91%	69.33%	94.88%	95.30%
10^{-5}	100%	100%	100%	100%	100%	100%	99.97%	100%	100%	95.44%	95.76%	98.96%
10^{-6}	100%	100%	100%	100%	100%	100%	100%	100%	100%	95.66%	95.79%	99.08%
10^{-7}	100%	100%	100%	100%	100%	100%	100%	100%	100%	95.75%	95.79%	99.08%

Table 20. V-ARAIM Dual-frequency L1/L5 and two constellations (GPS and Galileo).
$\sigma_{URE} = 2/3\ \sigma_{URA}$, $b_{nom} = 0\ m$; $P_{const;GPS} = P_{const;Galileo}$; $P_{sat;GPS} = P_{sat;Galileo}$

LPV-250: 99.5% Availability coverage												
b_{nom}=0 m	URA=SISA=0.75 m			URA=SISA=1 m			URA=SISA=1.5 m			URA=SISA=2 m		
P_{sat}/P_{const}	10^{-4}	10^{-5}	10^{-6}	10^{-4}	10^{-5}	10^{-6}	10^{-4}	10^{-5}	10^{-6}	10^{-4}	10^{-5}	10^{-6}
10^{-4}	100%	100%	100%	100%	100%	100%	99.67%	100%	100%	87.02%	98.96%	98.96%
10^{-5}	100%	100%	100%	100%	100%	100%	100%	100%	100%	99.03%	99.35%	100%
10^{-6}	100%	100%	100%	100%	100%	100%	100%	100%	100%	99.29%	99.35%	100%
10^{-7}	100%	100%	100%	100%	100%	100%	100%	100%	100%	99.31%	99.35%	100%

5.2.2 Horizontal ARAIM

The performance of H-ARAIM is evaluated in this section for dual- and single-frequency navigation and with one or two constellations.

For H-ARAIM, the ISM parameters have been set to:

- σ_{URA} = 2.5 m, 6 m and 9 m.
- $\sigma_{URE} = 2/3\ \sigma_{URA}$.
- b_{nom} = 0 m, 0.75 m (0.75 m is the value suggested by [51]).
- $P_{sat} = 10^{-4}$, 10^{-5} , 10^{-6}.
- $P_{cons} = 10^{-4}$, 10^{-8}.

In the case of single constellation, GPS or Galileo, P_{cons} is taken as 10^{-8}, like in the classical RAIM, to avoid monitoring that single constellation failure mode.

The results for dual constellation (GPS plus Galileo) have been calculated by considering the next two cases:

1) $P_{const;GPS} = 10^{-8}$, $P_{const;Galileo} = 10^{-4}$.
2) $P_{const;GPS} = P_{const;Galileo} = 10^{-4}$.

Note: according to the already commented Annex-B assertation 1 in [50], $P_{cons} = 10^{-8}$ can be assumed for GPS in lateral guidance in a dual constellation processing.

5.2.2.1 Horizontal ARAIM with Dual frequency

The results of simulation for H-ARAIM with dual frequency signals (L1/L5 and E1/E5) and with one or two constellations (GPS and/or Galileo) are given in this section.

The H-RAIM Dual frequency RNP-01 Availability (95.5th) coverage and HPL (95.5th) are depicted in Figure 31 for GPS alone constellation (top), Galileo alone constellation (middle) and Dual constellation GPS and Galileo. These modes correspond to those highlighted in Table 21. The ISM parameters used are $\sigma_{URA} = 9\ m$, $\sigma_{URE} = 2/3\ \sigma_{URA}$, $b_{nom} = 0.75\ m$; $P_{const;GPS} = P_{const;Galileo} = 10^{-4}$; $P_{sat;GPS} = P_{sat;Galileo} = 10^{-5}$. As it is shown, the Galileo single constellation and the dual constellation with GPS and Galileo reach the 100% of availability coverage, while the single constellation of GPS only reaches the 75.37%. As already commented the baseline constellations with 24 satellites are used for both GPS and Galileo. The root of this different coverage level between GPS and Galileo, using the same number of satellites, is due to the satellite constellations geometry as it is shown in Figure 32 and Figure 33.

Figure 32 compares the performance for GPS constellation using the GPS receiver noise model (top plots) and using the Galileo receiver noise model (bottom plots). The same ISM parameters as in Figure 31 are used in both cases. As depicted the results are basically the same. Notice that the plots at top of this Figure 32 correspond to the plots at top of Figure 31. The same comparison is done in Figure 33 for the Galileo constellation. Then, it is concluded that Galileo satellite constellation geometry is the key factor in this performance improvement.

A summary of the simulation results for H-ARAIM with dual frequency signals (L1/L5 and E1/E5) and with one or two constellations (GPS and/or Galileo) is shown in Table 21 and Table 22 for RNP-0.1, and in Table 23 and Table 24 for RNP-0.3. These tables analyse the sensitivity of the Horizontal Guidance Availability 95.5th coverage as a function of the ISM parameters.

From these tables, the next conclusions arose:

- URA value is the dominant parameter for the availability coverage.
- Again, results confirm that bias b_{nom} (taken as 0 m or 0.75 m) has a low impact on performances, having a slightly greater coverage when this parameter is set as zero.
- 100% global RNP-01 coverage (and thence RNP-0.3) is achieved for the dual constellation (GPS plus Galileo), with $\sigma_{URA} = 9$ m or lower, even with $P_{const;GPS} = P_{const;Galileo} = 10^{-4}$. It is worth to say that $\sigma_{URA} = 9\ m$ is the highest value.
- Simulated performance results for the single constellation Galileo are somewhat better than for GPS, achieving 100% of RNP-01 coverage (and thence RNP-0.3), even with $\sigma_{URA} = 9$ m when $P_{sat} = 10^{-5}$ or lower.
- 100% global RNP-03 coverage is always achieved for both single constellations (GPS or Galileo).

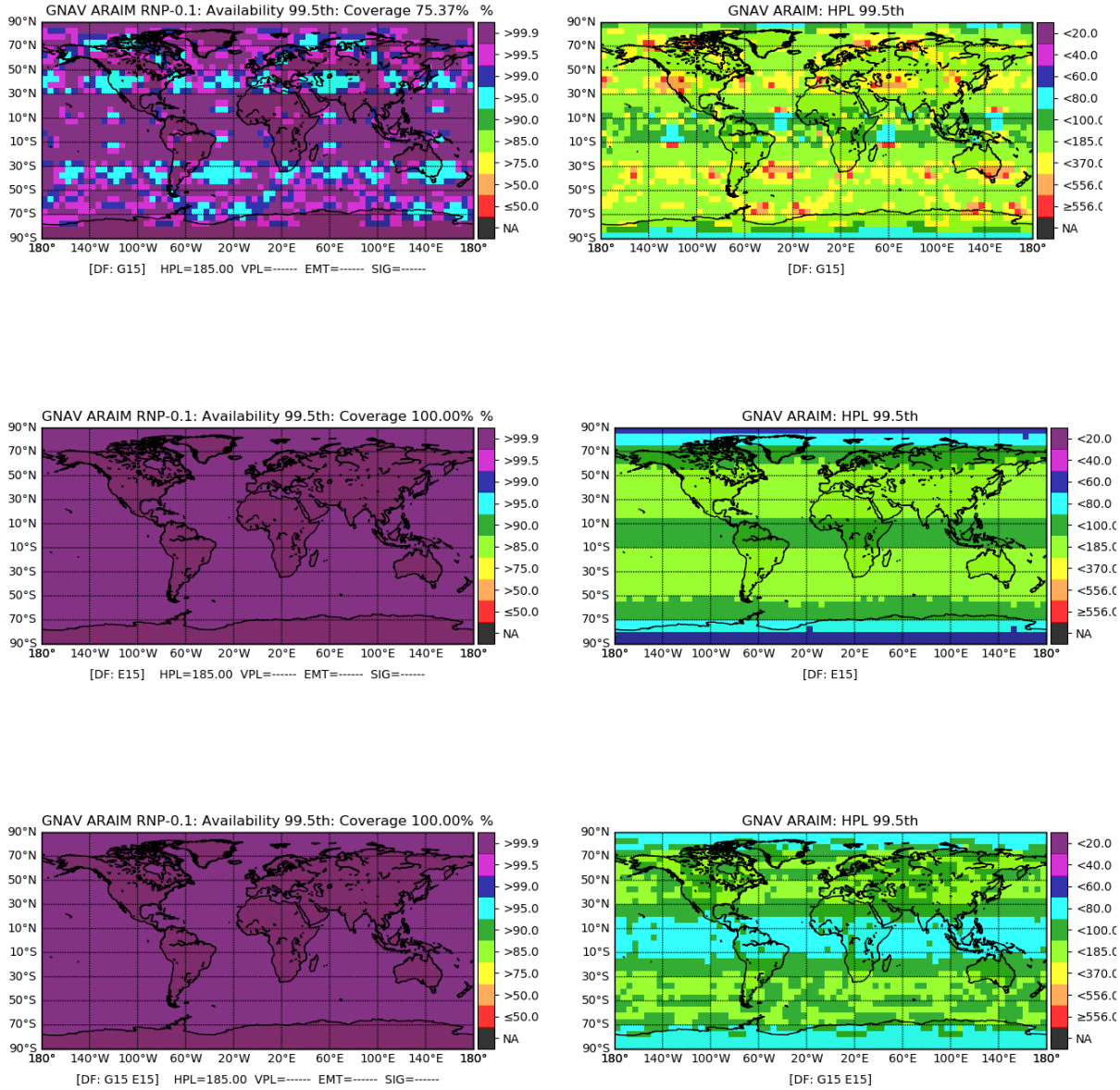

Figure 31. Examples of H-ARAIM RNP-0.1 with dual-frequency: $b_{nom} = 0.75\ m;\ \sigma_{URA} = 9\ m$; $\sigma_{URE} = 2/3\ \sigma_{URA}$; $P_{sat;GPS} = P_{sat;Galileo} = 10^{-5}$. Top row is for GPS L1/L5 with $P_{const;GPS} = 10^{-8}$. Middle row for Galileo E1/E5 with $P_{const;Galileo} = 10^{-8}$. Bottom row for dual constellation (GPS L1/L5 and Galileo E1/E5) with $P_{const;GPS} = P_{const;Galileo} = 10^{-4}$. See highlighted cells in Table 22. The left hand plots are for Availability (99.5th) and the right hand plots for the HPL (99.5th)

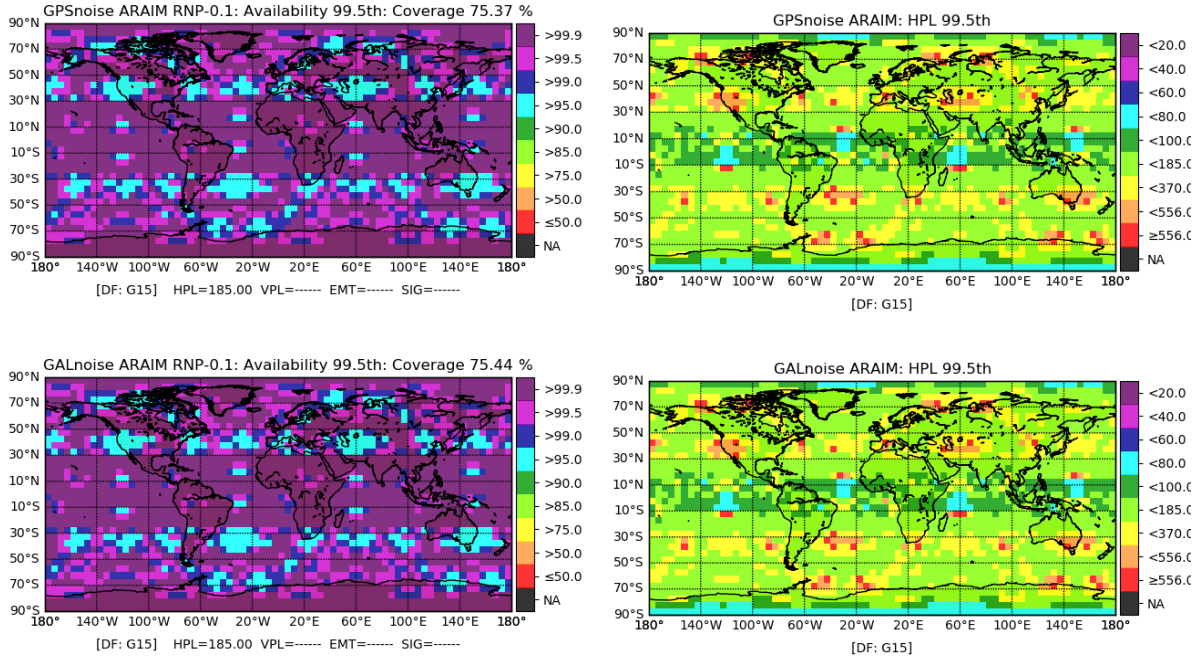

Figure 32. Comparison of H-ARAIM RNP-0.1 performance using the GPS constellation and using the GPS receiver noise model (top plots) and the Galileo receiver noise model (bottom plots). The same parameters as in Figure 31 have been used.

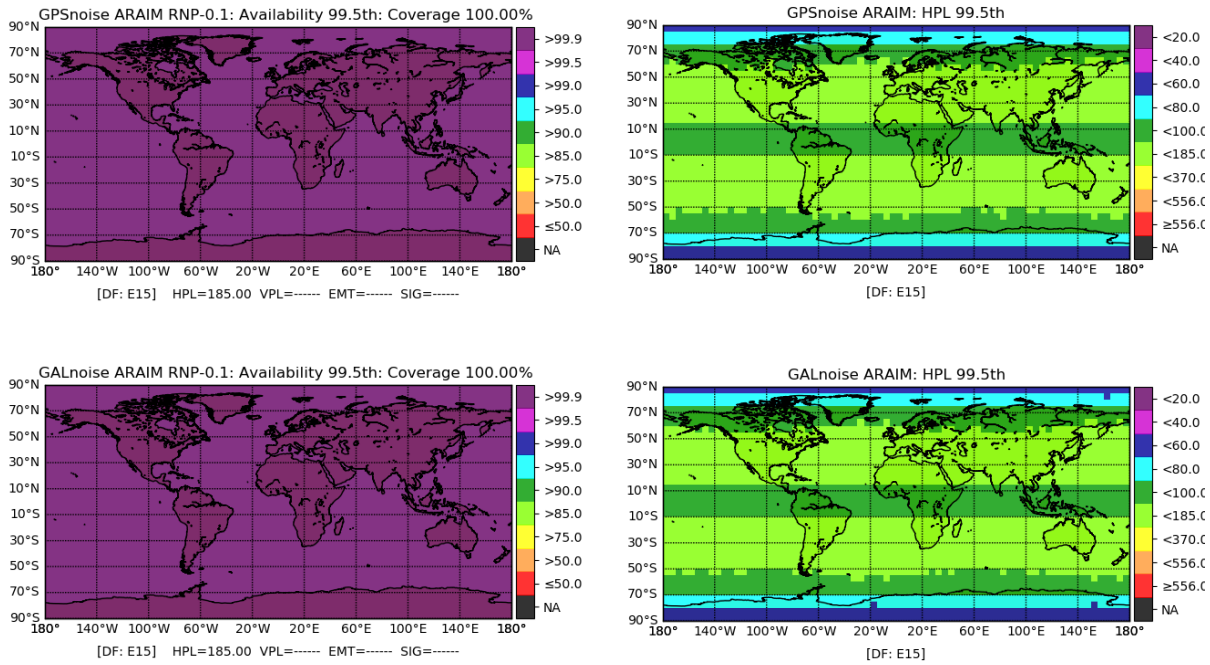

Figure 33. The same comparison as in previous Figure 32, but using the Galileo constellation.

Summary H-ARAIM Results with Dual Frequency and One or Two constellations:

Table 21. H-ARAIM Dual frequency L1/L5 (GPS or/and Galileo).
$\sigma_{URE} = 2/3\ \sigma_{URA}$, $b_{nom} = 0.75\ m$; $P_{sat;GPS} = P_{sat;Galileo}$.
(Single-constellation: $P_{const;GPS} = P_{const;Galileo} = 10^{-8}$. Two constellations: 1st column: $P_{const;GPS} = 10^{-8}$, $P_{const;Galileo} = 10^{-4}$; 2nd column: $P_{const;GPS} = P_{const;Galileo} = 10^{-4}$)

RNP-0.1: 99.5% Availability coverage												
b_{nom}=0.75m	URA=SISA=2.5 m				URA=SISA=6 m				URA=SISA=9 m			
P_{sat}	GPS	GAL	GPS+GAL	GPS+GAL	GPS	GAL	GPS+GAL	GPS+GAL	GPS	GAL	GPS+GAL	GPS+GAL
10^{-4}	97.58%	100%	100%	100%	90.82%	97.11%	100%	100%	57.27%	59.00%	100%	100%
10^{-5}	98.67%	100%	100%	100%	92.03%	100%	100%	100%	75.37%	100%	100%	100%
10^{-6}	98.88%	100%	100%	100%	93.14%	100%	100%	100%	86.58%	100%	100%	100%
10^{-7}	99.53%	100%	100%	100%	95.86%	100%	100%	100%	91.43%	100%	100%	100%

Table 22. H-ARAIM Dual frequency L1/L5 (GPS or/and Galileo).
$\sigma_{URE} = 2/3\ \sigma_{URA}$, $b_{nom} = 0\ m$; $P_{sat;GPS} = P_{sat;Galileo}$.
(Single-constellation: $P_{const;GPS} = P_{const;Galileo} = 10^{-8}$. Two constellations: 1st column: $P_{const;GPS} = 10^{-8}$, $P_{const;Galileo} = 10^{-4}$; 2nd column: $P_{const;GPS} = P_{const;Galileo} = 10^{-4}$)

RNP-0.1: 99.5% Availability coverage												
b_{nom}=0m	URA=SISA=2.5 m				URA=SISA=6 m				URA=SISA=9 m			
P_{sat}	GPS	GAL	GPS+GAL	GPS+GAL	GPS	GAL	GPS+GAL	GPS+GAL	GPS	GAL	GPS+GAL	GPS+GAL
10^{-4}	97.95%	100%	100%	100%	91.56%	98.89%	100%	100%	60.24%	59.44%	100%	100%
10^{-5}	99.17%	100%	100%	100%	92.82%	100%	100%	100%	78.30%	100%	100%	100%
10^{-6}	99.31%	100%	100%	100%	94.22%	100%	100%	100%	88.71%	100%	100%	100%
10^{-7}	99.62%	100%	100%	100%	96.32%	100%	100%	100%	91.98%	100%	100%	100%

Table 23. H-ARAIM Dual frequency L1/L5 (GPS or/and Galileo).
$\sigma_{URE} = 2/3\ \sigma_{URA}$, $b_{nom} = 0.75\ m$; $P_{sat;GPS} = P_{sat;Galileo}$.
(Single-constellation: $P_{const;GPS} = P_{const;Galileo} = 10^{-8}$. Two constellations: 1st column: $P_{const;GPS} = 10^{-8}$, $P_{const;Galileo} = 10^{-4}$; 2nd column: $P_{const;GPS} = P_{const;Galileo} = 10^{-4}$)

RNP-0.3: 99.5% Availability coverage												
b_{nom}=0.75m	URA=SISA=2.5 m				URA=SISA=6 m				URA=SISA=9 m			
P_{sat}	GPS	GAL	GPS+GAL	GPS+GAL	GPS	GAL	GPS+GAL	GPS+GAL	GPS	GAL	GPS+GAL	GPS+GAL
10^{-4}	98.21%	100%	100%	100%	98.04%	100%	100%	100%	96.62%	100%	100%	100%
10^{-5}	100%	100%	100%	100%	99.53%	100%	100%	100%	98.29%	100%	100%	100%
10^{-6}	100%	100%	100%	100%	99.76%	100%	100%	100%	98.79%	100%	100%	100%
10^{-7}	100%	100%	100%	100%	99.95%	100%	100%	100%	99.53%	100%	100%	100%

Table 24. H-ARAIM Dual frequency L1/L5 (GPS or/and Galileo).
$\sigma_{URE} = 2/3\ \sigma_{URA}$, $b_{nom} = 0\ m$; $P_{sat;GPS} = P_{sat;Galileo}$.
(Single-constellation: $P_{const;GPS} = P_{const;Galileo} = 10^{-8}$. Two constellations: 1st column: $P_{const;GPS} = 10^{-8}$, $P_{const;Galileo} = 10^{-4}$; 2nd column: $P_{const;GPS} = P_{const;Galileo} = 10^{-4}$)

RNP-0.3: 99.5% Availability coverage												
b_{nom}=0m	URA=SISA=2.5 m				URA=SISA=6 m				URA=SISA=9 m			
P_{sat}	GPS	GAL	GPS+GAL	GPS+GAL	GPS	GAL	GPS+GAL	GPS+GAL	GPS	GAL	GPS+GAL	GPS+GAL
10^{-4}	98.21%	100%	100%	100%	99.12%	100%	100%	100%	96.69%	99.96%	100%	100%
10^{-5}	100%	100%	100%	100%	99.57%	100%	100%	100%	98.38%	100%	100%	100%
10^{-6}	100%	100%	100%	100%	99.76%	100%	100%	100%	98.89%	100%	100%	100%
10^{-7}	100%	100%	100%	100%	99.95%	100%	100%	100%	99.53%	100%	100%	100%

5.2.2.2 Horizontal ARAIM with Single frequency

The results of simulations for H-ARAIM with single-frequency signals (L1 or L5 and E1 or E5) and with one or two constellations (GPS and or Galileo) are given in this section.

Figure 34 shows the H-ARAIM RNP-0.1 availability (95th) coverage and HPL (95th) with single frequency and single constellation for GPS and Galileo. The ISM parameters used are: $b_{nom} = 0.75\ m,\quad \sigma_{URA} = 6\ m,\quad \sigma_{URE} = 2/3\ \sigma_{URA},\quad P_{sat;GPS} = P_{sat;Galileo} = 10^{-6},\quad P_{const;GPS} = P_{const;Galileo} = 10^{-8}$. The top plots are for GPS L1 and the bottom plots for Galileo E1. These cases correspond to the highlighted cells in Table 25. As it is shown, GPS coverage is only of about 41.07% while in Galileo it reaches up to 85.12%. Moreover, in Galileo the availability worsening is clearly located in the equatorial regain, i.e. associated to the noise model for the ionosphere. It is worth to say that, Galileo availability (99.5^{th}) is achieved almost world-wide, except in these well-defined areas in the equatorial region. In the case of GPS, among the ionosphere noise model, the satellite constellation geometry strongly contributes to degrade the availability coverage up to the 41%.

Figure 35 shows the same results as in Figure 34, but using the GPS L5 or Galileo E5 signals. As depicted the availability coverage is highly degraded, fooling down to 1% in GPS and 7.32% in Galileo. As expected, the worse availability values appear around the geomagnetic equator, as it can be clearly seen in both GPS and Galileo.

A summary of the simulation results for H-ARAIM with single-frequency signals (L1 or L5 and E1 or E5) and with one or two constellations (GPS and or Galileo) is shown in Table 25 and Table 26 for RNP-0.1 with L1 (or E1) or L5 (or E5) signals, and in Table 27 and Table 28 for RNP-0.3 with L1 (or E1) or L5 (or E5) signals. As in the previous cases, these tables analyse the sensitivity of the Horizontal Guidance Availability Coverage as a function of the ISM parameters. The sigmas of ionospheric model from MOPS [19] (for Klobuchar) are used for both GPS and Galileo satellites.

From these tables, the next conclusions arose:

- Dual constellation GPS and Galileo, with single frequency L1 (E1) signals allows to achieve about 100% RNP-01 availability coverage even with $\sigma_{URA} = 9$ m.
- L5 (or E5) signal shows strongly worse coverage than L1 (or E1) signals, in both single or dual constellations. Noticeably, RNP-01 cannot be achieved with L5 (or E5) signals neither with dual constellation (GPS plus Galileo) and $\sigma_{URA} = 2.5$ m.
- The availability coverage for single constellation Galileo shows better results than for single constellation GPS for both E1 (L1) and E5 (L5) signals. As shown in the previous section, when analysing this effect using dual-frequency signals, it is related with the geometry of satellite constellation.
- With L1 (E1), RNP-03 global coverage over 90% is achieved by both, GPS and Galileo, with $\sigma_{URA} = 9$ m, with somewhat better results with Galileo.
- With L5 (E5), RNP-03 global coverage over 90% is always achieved for Galileo with $\sigma_{URA} = 9$ m, but not for GPS. In the case of GPS, it is nearly achieved with $\sigma_{URA} = 2.5$ m and with $P_{sat} = 10^{-6}$.

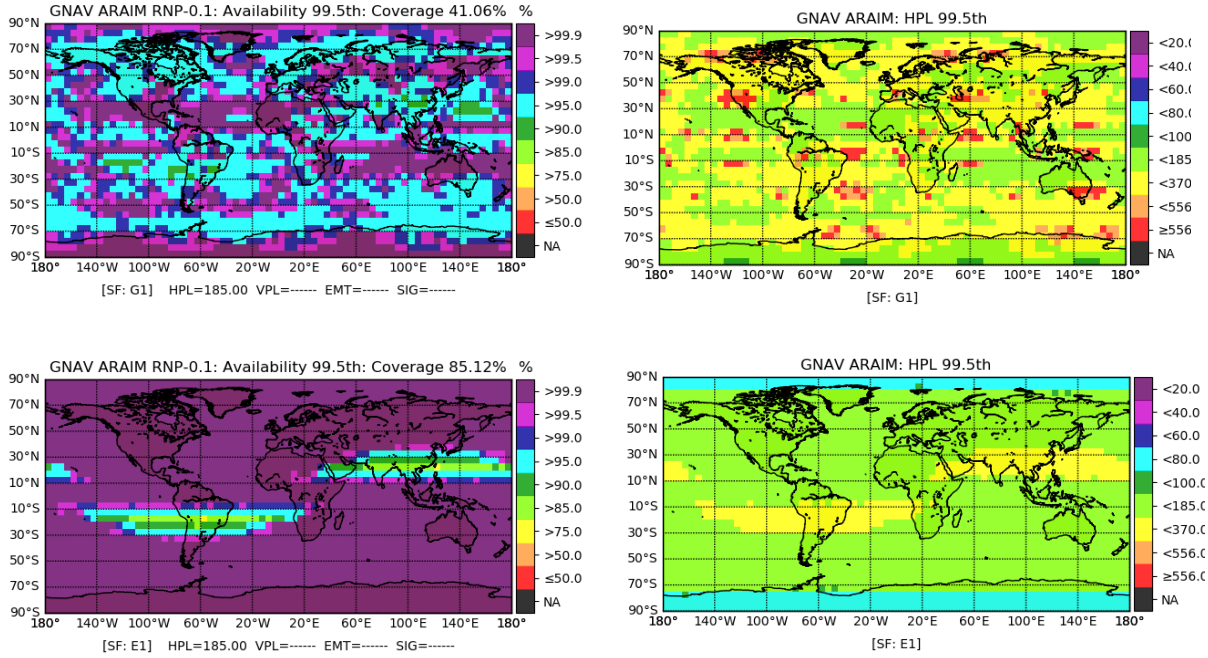

Figure 34. L1, E1: H-ARAIM RNP-0.1 with single-frequency and single-constellation: $b_{nom} = 0.75\ m;\ \ \sigma_{URA} = 6m\ ;\ \ \sigma_{URE} = 2/3\ \sigma_{URA}\ ;\ \ P_{sat;GPS} = P_{sat;Galileo} = 10^{-6};$ $P_{const;GPS} = P_{const;Galileo} = 10^{-8}$. Top row is for GPS L1, bottom row for Galileo E1. See highlighted cells in Table 25.

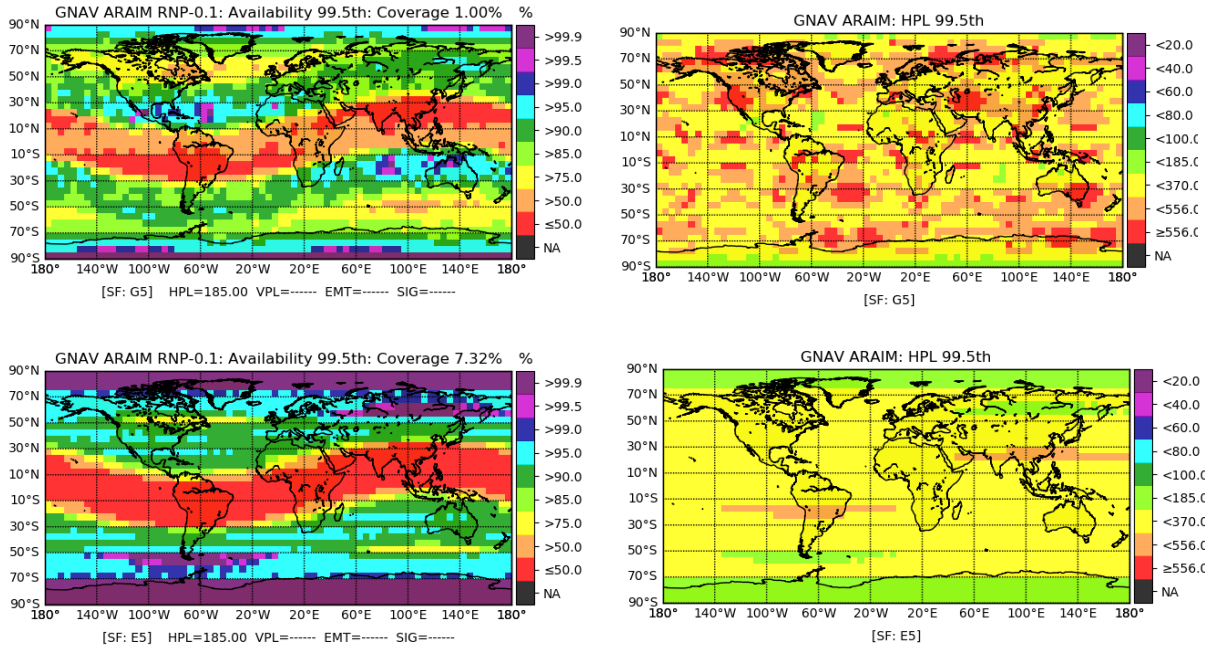

Figure 35. L5, E5: H-ARAIM RNP-0.1 with single-frequency and single-constellation: $b_{nom} = 0.75\ m;\ \ \sigma_{URA} = 6m\ ;\ \ \sigma_{URE} = 2/3\ \sigma_{URA}\ ;\ \ P_{sat;GPS} = P_{sat;Galileo} = 10^{-6};$ $P_{const;GPS} = P_{const;Galileo} = 10^{-8}$. Top row is for GPS L5, bottom row for Galileo E5. See highlighted cells in Table 26.

Summary H-ARAIM Results with Single Frequency and One or Two constellations:

Table 25. H-ARAIM Single frequency L1 (GPS or/and Galileo).
$\sigma_{URE} = 2/3\ \sigma_{URA}$, $b_{nom} = 0.75\ m$; $P_{sat;GPS} = P_{sat;Galileo}$.
(Single-constellation: $P_{const;GPS} = P_{const;Galileo} = 10^{-8}$. Two constellations: 1st column: $P_{const;GPS} = 10^{-8}$, $P_{const;Galileo} = 10^{-4}$; 2nd column: $P_{const;GPS} = P_{const;Galileo} = 10^{-4}$)

L1: RNP-0.1: 99.5% Availability coverage												
b_{nom}=0.75m	URA=SISA=2.5 m				URA=SISA=6 m				URA=SISA=9 m			
P_{sat}	GPS	GAL	GPS+GAL	GPS+GAL	GPS	GAL	GPS+GAL	GPS+GAL	GPS	GAL	GPS+GAL	GPS+GAL
10^{-4}	14.19%	28.93%	100%	100%	7.77%	24.03%	100%	99.79%	3.08%	14.41%	99.84%	98.51%
10^{-5}	32.43%	79.31%	100%	100%	18.39%	75.69%	100%	99.84%	10.03%	47.09%	99.95%	99.58%
10^{-6}	56.02%	89.45%	100%	100%	41.06%	85.12%	100%	99.89%	25.88%	78.15%	100%	99.58%
10^{-7}	76.10%	99.56%	100%	100%	70.89%	99.96%	100%	99.89%	61.51%	98.25%	100%	99.58%

Table 26. H-ARAIM Single frequency L5 (GPS or/and Galileo).
$\sigma_{URE} = 2/3\ \sigma_{URA}$, $b_{nom} = 0.75\ m$; $P_{sat;GPS} = P_{sat;Galileo}$.
(Single-constellation: $P_{const;GPS} = P_{const;Galileo} = 10^{-8}$. Two constellations: 1st column: $P_{const;GPS} = 10^{-8}$, $P_{const;Galileo} = 10^{-4}$; 2nd column: $P_{const;GPS} = P_{const;Galileo} = 10^{-4}$)

L5: RNP-0.1: 99.5% Availability coverage												
b_{nom}=0.75m	URA=SISA=2.5 m				URA=SISA=6 m				URA=SISA=9 m			
P_{sat}	GPS	GAL	GPS+GAL	GPS+GAL	GPS	GAL	GPS+GAL	GPS+GAL	GPS	GAL	GPS+GAL	GPS+GAL
10^{-4}	0.00%	2.28%	51.46%	38.76%	0.00%	2.28%	46.96%	29.24%	0.00%	0.76%	36.74%	16.63%
10^{-5}	0.00%	2.70%	57.74%	43.94%	0.00%	2.28%	54.61%	36.54%	0.00%	2.28%	47.83%	22.96%
10^{-6}	1.99%	11.56%	58.37%	45.76%	1.00%	7.32%	55.76%	39.53%	0.15%	6.40%	49.38%	27.18%
10^{-7}	10.25%	59.69%	58.43%	45.81%	9.59%	56.76%	55.92%	39.58%	8.41%	52.68%	49.46%	27.18%

Table 27. H-ARAIM Single frequency L1 (GPS or/and Galileo).
$\sigma_{URE} = 2/3\ \sigma_{URA}$, $b_{nom} = 0.75\ m$; $P_{sat;GPS} = P_{sat;Galileo}$.
(Single-constellation: $P_{const;GPS} = P_{const;Galileo} = 10^{-8}$. Two constellations: 1st column: $P_{const;GPS} = 10^{-8}$, $P_{const;Galileo} = 10^{-4}$; 2nd column: $P_{const;GPS} = P_{const;Galileo} = 10^{-4}$)

L1: RNP-0.3: 99.5% Availability coverage												
b_{nom}=0.75m	URA=SISA=2.5 m				URA=SISA=6 m				URA=SISA=9 m			
P_{sat}	GPS	GAL	GPS+GAL	GPS+GAL	GPS	GAL	GPS+GAL	GPS+GAL	GPS	GAL	GPS+GAL	GPS+GAL
10^{-4}	93.36%	100%	100%	100%	92.10%	99.84%	100%	100%	90.33%	99.51%	100%	100%
10^{-5}	95.36%	100%	100%	100%	95.20%	100%	100%	100%	92.49%	100%	100%	100%
10^{-6}	96.58%	100%	100%	100%	95.32%	100%	100%	100%	93.83%	100%	100%	100%
10^{-7}	98.05%	100%	100%	100%	97.52%	100%	100%	100%	96.52%	100%	100%	100%

Table 28. H-ARAIM Single frequency L5 (GPS or/and Galileo).
$\sigma_{URE} = 2/3\ \sigma_{URA}$, $b_{nom} = 0.75\ m$; $P_{sat;GPS} = P_{sat;Galileo}$.
(Single-constellation: $P_{const;GPS} = P_{const;Galileo} = 10^{-8}$. Two constellations: 1st column: $P_{const;GPS} = 10^{-8}$, $P_{const;Galileo} = 10^{-4}$; 2nd column: $P_{const;GPS} = P_{const;Galileo} = 10^{-4}$)

L5: RNP-0.3: 99.5% Availability coverage												
b_{nom}=0.75m	URA=SISA=2.5 m				URA=SISA=6 m				URA=SISA=9 m			
P_{sat}	GPS	GAL	GPS+GAL	GPS+GAL	GPS	GAL	GPS+GAL	GPS+GAL	GPS	GAL	GPS+GAL	GPS+GAL
10^{-4}	73.69%	95.00%	100%	100%	71.65%	93.92%	100%	100%	66.33%	89.96%	100%	100%
10^{-5}	85.58%	100%	100%	100%	84.29%	100%	100%	100%	81.98%	100%	100%	100%
10^{-6}	89.58%	100%	100%	100%	88.97%	100%	100%	100%	88.13%	100%	100%	100%
10^{-7}	93.17%	100%	100%	100%	92.95%	100%	100%	100%	92.19%	100%	100%	100%

5.3 Evaluation of ARAIM with the experimental results

The Galileo F/NAV broadcast orbit and clock error have been characterized in previous Chapter 4. Based in these experimental results, the present section demonstrates that Galileo system widely fulfils the assumptions adopted in the two considered scenarios:

1. **Scenario 1: Based on NTE= 39.78 m:**

   As indicated in previous Chapter 4, according to the Milestone 3 report [3], the target H-ARAIM service level can be established based on GPS and Galileo with the following contribution from Galileo:

   - σ_{URA} (overbound of SISE) lower than 9 m;
   - P_{sat} lower than 1×10^{-5}/sat;
   - P_{const} lower than 1×10^{-4}.

   Note: NTE = $4.42 \times \sigma_{URA}$= 39.78 m.

2. **Scenario 2: Based on NTE= 25.04 m:**

   The conclusions presented in the ICAO NSP on April 2020 consider the following values for Galileo system [6]:

   - σ_{URA} (overbound of SISE) lower than 6 m;
   - P_{sat} lower than 3×10^{-5}/sat;
   - P_{const} lower than 1×10^{-4}.

   Note: NTE = $4.17 \times \sigma_{URA}$= 25.04 m.

In the case of GPS constellation, the following values will be used when assessing the H-ARAIM for GPS and Galileo, in both scenarios [32]. The fulfilment of these values for GPS have been also confirmed in the characterization of GPS orbits and clocks done in previous Chapter 4.

- $\sigma_{URA} = 2.5\ m$;
- P_{sat} lower than 1×10^{-5}/sat;
- P_{const} lower than 1×10^{-4}.

Finally, as suggested in [51] the b_{nom} is taken as 0.75 m for both constellations GPS and Galileo.

The next sections calculate and validate the H-ARAIM global coverage for these two scenarios. As the satellite geometry plays an important role in ARAIM performance, the three reference constellations considered in [3] will be used: depleted, baseline and optimistic (see [31]):

- **Depleted**: GPS 24-1 slots and Galileo 24-1 slots. This corresponds to the almanacs: almmops-1.txt (GPS) and almanc_Galileo_24-1_Week_703.alm.txt (Galileo).
- **Baseline**: GPS 24 slots and Galileo 24 slots. This corresponds to the almanacs: `almmops.txt` (GPS) and `almanc_Galileo_24_Week_703.alm.txt` (Galileo).
- **Optimistic**: GPS 24+3 slots and Galileo 24+3 slots. This corresponds to the almanacs: `almmops24+3.txt` (GPS) and `almanc_Galileo_24+3_Week_703.alm.txt` (Galileo).

5.2.3 H-ARAIM performance for scenarios 1 and 2

The global coverage for scenario 1 has been computed using the three reference constellations: depleted, baseline and optimistic. Table 29 to Table 31 summarize the results for five different configurations including single- and double-constellation with single- and dual-frequency.

Table 29. Scenario 1. H-ARAIM Availability (99.5th) coverage. Depleted constellation

$\sigma_{URA,GPS} = 2.5\ m,\ \sigma_{URA,Galileo} = 9\ m, \sigma_{URE} = 2/3\ \sigma_{URA},$
$b_{nom} = 0.75\ m;\ P_{sat;GPS} = 1 \times 10^{-5}, P_{sat;Galileo} = 1 \times 10^{-5};$
Single-constellation: $P_{const} = 10^{-8}$. Two constellations: $P_{const;GPS} = P_{const;Galileo} = 10^{-4}$.

	RNP-0.1	RNP-0.3
GPS L1/L5 + Galileo E1/E5	99.95%	100%
GPS L1 + Galileo E1	46.58%	99.36%
GPS L5 + Galileo E5	0.91%	97.09%
Galileo E1/E5	39.45%	51.13%
Galileo E1	4.44%	48.09%
Galileo E5	0.00%	17.15%

Table 30. Scenario 1. H-ARAIM Availability (99.5th) coverage. Baseline constellation

$\sigma_{URA,GPS} = 2.5\ m,\ \sigma_{URA,Galileo} = 9\ m, \sigma_{URE} = 2/3\ \sigma_{URA},$
$b_{nom} = 0.75\ m;\ P_{sat;GPS} = 1 \times 10^{-5}, P_{sat;Galileo} = 1 \times 10^{-5};$
Single-constellation: $P_{const} = 10^{-8}$. Two constellations: $P_{const;GPS} = P_{const;Galileo} = 10^{-4}$.

	RNP-0.1	RNP-0.3
GPS L1/L5 + Galileo E1/E5	100%	100%
GPS L1 + Galileo E1	99.63%	100%
GPS L5 + Galileo E5	21.29%	100%
Galileo E1/E5	100%	100%
Galileo E1	47.09%	100%
Galileo E5	2.28%	100%

Table 31. Scenario 1. H-ARAIM Availability (99.5th) coverage. Optimistic constellation

$\sigma_{URA,GPS} = 2.5\ m,\ \sigma_{URA,Galileo} = 9\ m, \sigma_{URE} = 2/3\ \sigma_{URA},$
$b_{nom} = 0.75\ m;\ P_{sat;GPS} = 1 \times 10^{-5}, P_{sat;Galileo} = 1 \times 10^{-5};$
Single-constellation: $P_{const} = 10^{-8}$. Two constellations: $P_{const;GPS} = P_{const;Galileo} = 10^{-4}$.

	RNP-0.1	RNP-0.3
GPS L1/L5 + Galileo E1/E5	100%	100%
GPS L1 + Galileo E1	99.28%	100%
GPS L5 + Galileo E5	31.65%	100%
Galileo E1/E5	100%	100%
Galileo E1	57.09%	100%
Galileo E5	2.39%	100%

As with scenario 1, the global coverage for scenario 2 has been computed using the three reference constellations: depleted, baseline and optimistic. Table 32 to Table 34 summarize the results for five different configurations including single- and double-constellation with single- and dual-frequency.

Table 32. Scenario 2. H-ARAIM Availability (99.5th) coverage. Depleted Constellation

$\sigma_{URA,GPS} = 2.5\ m,\ \sigma_{URA,Galileo} = 6\ m, \sigma_{URE} = 2/3\ \sigma_{URA},$
$b_{nom} = 0.75\ m;\ P_{sat;GPS} = 1 \times 10^{-5}, P_{sat;Galileo} = 3 \times 10^{-5};$
Single-constellation: $P_{const} = 10^{-8}$. Two constellations: $P_{const;GPS} = P_{const;Galileo} = 10^{-4}$.

	RNP-0.1	RNP-0.3
GPS L1/L5 + Galileo E1/E5	99.95%	100%
GPS L1 + Galileo E1	57.95%	99.65%
GPS L5 + Galileo E5	1.21%	97.11%
Galileo E1/E5	49.28%	52.05%
Galileo E1	4.52%	47.87%
Galileo E5	0.00%	15.92%

Table 33. Scenario 2. H-ARAIM Availability (99.5th) coverage. Baseline Constellation

$\sigma_{URA,GPS} = 2.5\ m,\ \sigma_{URA,Galileo} = 6\ m, \sigma_{URE} = 2/3\ \sigma_{URA},$
$b_{nom} = 0.75\ m;\ P_{sat;GPS} = 1 \times 10^{-5}, P_{sat;Galileo} = 3 \times 10^{-5};$
Single-constellation: $P_{const} = 10^{-8}$. Two constellations: $P_{const;GPS} = P_{const;Galileo} = 10^{-4}$.

	RNP-0.1	RNP-0.3
GPS L1/L5 + Galileo E1/E5	100%	100%
GPS L1 + Galileo E1	99.79%	100%
GPS L5 + Galileo E5	29.02%	100%
Galileo E1/E5	100%	100%
Galileo E1	60.29%	100%
Galileo E5	2.28%	100%

Table 34. Scenario 2. H-ARAIM Availability (99.5th) coverage. Optimistic Constellation

$\sigma_{URA,GPS} = 2.5\ m,\ \sigma_{URA,Galileo} = 6\ m, \sigma_{URE} = 2/3\ \sigma_{URA},$
$b_{nom} = 0.75\ m;\ P_{sat;GPS} = 1 \times 10^{-5}, P_{sat;Galileo} = 3 \times 10^{-5};$
Single-constellation: $P_{const} = 10^{-8}$. Two constellations: $P_{const;GPS} = P_{const;Galileo} = 10^{-4}$.

	RNP-0.1	RNP-0.3
GPS L1/L5 + Galileo E1/E5	100%	100%
GPS L1 + Galileo E1	99.95%	100%
GPS L5 + Galileo E5	37.18%	100%
Galileo E1/E5	100%	100%
Galileo E1	62.87%	100%
Galileo E5	2.28%	100%

Results for the scenario 1, are shown in Table 29 for the depleted constellations (24-1 GPS, 24-1 Galileo), Table 30 for the baseline constellations (24 GPS, 24 Galileo) and in Table 31 for the optimistic constellations (24+3 GPS, 24+3 Galileo). Significant differences on RNP-0.1 and RNP-0.3 appear when comparing results computed with the depleted constellations and baseline constellations, while results using the optimistic constellations are almost similar to those with the baseline constellation.

With the depleted constellation, the almost full Availability (99.5th) coverage RNP-01 is only achieved (99.95%) with dual-constellation and double-frequency GPS L1/L5 and Galileo E1/E5, while with the baseline constellations RNP-0.1 is achieved, also, with the single frequency dual constellation (GPS L1 and Galileo E1), and even with the single constellation Galileo using double-frequency (Galileo E1/E5).

As expected, results with the single frequency L5 or E5, are strongly degraded even with the dual constellation GPS plus Galileo. Nevertheless, a significant improvement is found with the baseline constellation, regarding to the depleted constellation.

When considering the RNP-0.3, results show that 100% Availability coverage (99.5th) is achieved for all modes considered in the tables, when using the baseline or the optimistic constellation, even when navigating with the single-constellation Galileo and with the single-frequency E5 signal (Galileo E5). This is not the case when using the depleted constellation where the coverage drops to about 50% or less when considering the single-constellation Galileo, whatever with dual- or single-frequency.

Table 32 to Table 34 show the results for the scenario 2, where $\sigma_{URA,Galileo} = 6\,m$ and $P_{sat;Galileo} = 3 \times 10^{-5}$ have been used in the computations, instead of the $\sigma_{URA,Galileo} = 9$ m and $P_{sat;Galileo} = 10^{-5}$ values considered in the previous scenario 1.

From the sensitivity analysis done in previous section 5.2, this small change on the P_{sat} probability is expected to have an almost negligible impact on performance, while the change of $\sigma_{URA,Galileo}$ from 9 m to 6 m may affect the performance somewhat more. This is confirmed when comparing results from both scenarios, where a little improvement in the global coverage is found, although results do not vary significantly.

Thence, the main conclusion from this study is that results confirm that even in the worst case assumption from the experimental results (of $\sigma_{URA,Galileo} = 9\,m$ and $P_{sat;Galileo} = 1 \times 10^{-5}$), with the baseline constellation, RNP-03 is achieved for all analysed configurations, including the constellation Galileo with single frequency E5. Moreover, RNP-0.1 is also achieved except for the single constellation Galileo (with E1 or E5), or the dual constellation with single frequency (GPS L5, Galileo E5).

The maps for Availability (95.5th) coverage and HPL (95.5th) associated to the different modes considered in these scenarios 1 and 2 (i.e. Table 29 to Table 34) can be found in Annex H.

6 Conclusions and Future Work

6.1 Main conclusions

A characterization of Galileo F/NAV broadcast orbit and clock errors has been made in this PhD dissertation based on five and a half years of data since the Galileo Initial Service Open Service declaration, from 1 January 2017 to 31 July 2022. Results for GPS LNAV broadcast messages on the same data period and over the last 10 years, from 1 January 2012 to 31 July 2022, have also been determined to compare Galileo performances with the fully deployed and consolidated GPS constellation. Using these experimental results, the global performance of H-ARAIM has been assessed for multi- and single-constellation with (Galileo plus GPS or Galileo alone) and with single- and dual-frequency signals.

The methodology used in the broadcast navigation data characterization is based on the works [33, 34] by Stanford University, which involve complex algorithms for data cleansing and a procedure for anomaly detection and verification. This approach has been directly implemented and applied to GPS and extended to Galileo data.

The observed orbit and clock errors in Galileo satellites are more tightly distributed than in the GPS, mainly for the along-track and cross-track errors. Events exceeding the 4.42 × SISA threshold have been identified, and their impact over the CDF analysed. It is worth mentioning that most of the detected events have been labelled as unrepresentative of the future Galileo Full Operational Capability, being many of them experienced during the first six-month period after the Galileo IS OS. When excluding this six-month period, the aggregated 1-CDF, incorporating all satellites, is well bounded beyond the probability level 1×10^{-5} by a Gaussian distribution with $\sigma_{URA} = 4$ m.

The observed nominal accuracy of Galileo satellites has been also characterized over more than 5 years of data (67 months) and compared with the GPS determinations for the same period of time and over a longer period of more than 10 years. Results show smaller 68th and 95th Galileo percentiles for the along-track and cross-track errors than those in the GPS. Similar percentiles as in the GPS are found for the radial error component and IURE, although a bias of several centimetres appears. The Galileo satellite clocks perform better than the GPS clock, with smaller error percentiles, but some global bias could have been absorbed by the clock alignment procedure applied to align the IGS time to the Galileo system time.

Finally, the NTE = 39.78 m threshold from Galileo commitments has been used to detect the satellite faults and to estimate the observed fault probability P_{sat}. When excluding the first six-month period of Galileo IS OS, the analysis over the last five-year window, from 1 August 2017 to 31 July 2022, shows very promising results. Only two satellite faults have been found, the IOV satellite E101 on 29 October 2019, lasting for 30 min, and the FOC E210 on 29 April 2022, lasting for 10 minutes. These two Galileo faults over this five-year period result in a fault probability $P_{sat} = 3.0 \times 10^{-6}$/sat, which is far below the 1×10^{-5}/sat commitment. Moreover, P_{sat} has been also estimated using the NTE = 25.04 m threshold, from the ICAO NSP of April 2020. In this case, two additional satellite faults are included in the statistics, the ones experienced

by the IOV satellites E101 on 26 December 2017 and E102 on 21 January 2021, which leads to P_{sat} = 5.3 × 10^{-6}/sat when considering the last five-year time window, being, again, a very good result. My research ends with the extrapolation to the Galileo FOC, where only three events are thought to be representative of this future configuration. In this case, a value of P_{sat}= 3.9 × 10^{-6}/sat is estimated over the whole period of 67 months, i.e. from 1 January 2017 to 31 July 2022, which broadly meets the 1 × 10^{-5}/sat requirement.

The characterization of Clock and Ephemeris error of the GNSSs is a key element to validate the assumptions for the integrity analysis of GNSS SoL systems. Specifically, the performance metrics of SoL applications require the characterization of the nominal UREs as well as the knowledge of the probability of a satellite or a constellation fault (P_{sat}, P_{const}). These values are the key parameters of the Integrity Support Message (ISM) that will be broadcast for ARAIM users.

The obtained experimental values for the satellite and constellation fault probabilities and σ_{URA} have been applied to assess the ARAIM performance in different navigation modes, with a dual constellation with Galileo and GPS and with Galileo alone.

The Classical and Advanced ARAIM algorithms have been implemented in the in home multi-frequency and multi-constellations gNAV software in order to have an independent tool, with a full knowledge and tracking of the internal computations. This tool has been coded in FORTRAN and optimised for fast data processing. In the case of ARAIM, performance results of gNAV have been crosschecked with MAAST and ISTAR tools, from Stanford and ISTA, respectively, obtaining quite identical results.

In order to have a view of the ARAIM behaviour for this assessment, a detailed analysis of its global performance sensibility against the ISM parameters have been done. This analysis involved Vertical and Horizontal ARAIM in multi- (Galileo and GPS) and single-constellation (Galileo). Similar studies, and even wider, have done in previous works ([28] , [3]) but, this part was included to have a self-contained dissertation. As in these works, simulations used a 5 by 5-degree user grid, 10 sidereal day period and masking angle of 5 degrees. The evaluation criteria considered global coverage of 99.5%, between -90 and 90 degrees of latitude, being the user grid points weighted by the cosine of the latitude to account for the relative area they represent.

Results of this sensitivity analysis fully agree with those of previous authors. In short, it is found that the σ_{URA} value is the dominant parameter, while the bias b_{nom} has a low impact on performances. The P_{cons} has a higher impact on the availability coverage than the P_{sat}, being, in general, the results quite similar for $P_{sat} = 10^{-5}/sat$ to $P_{sat} = 10^{-7}/sat$. Then, $P_{sat} = 10^{-5}/sat$ can be enough to use. On the other hand, as expected, performances are strongly degraded when considering only the single frequency L5 (GPS) and/or E5 (Galileo).

The H-ARAIM has been assessed based in the experimental results of the two scenarios defined in the characterization of Clock and Ephemeris: Scenario 1, based on NTE=39.78 m, and scenario 2, with NTE=25.4 m. Indeed, $P_{sat} = 10^{-5}$/sat and $P_{const} = 10^{-4}$/sat with σ_{URA} = 9 m have been used for Galileo in the scenario 1; and $P_{sat} = 3 \times 10^{-5}$/sat and P_{const} =

10^{-4}/sat with $\sigma_{URA} = 6$ m for the scenario 2. For the GPS constellation, $P_{sat} = 10^{-5}$/sat and $P_{const} = 10^{-4}$/sat with $\sigma_{URA} = 2.5$ m are taken, as conservative values, according to the experimental GPS characterization. Finally, b_{nom} is taken as 0.75 m according to [51], for both, GPS and Galileo satellites.

Availability (99.5th) coverage maps for RNP-0.1 and RNP-0.3 together with HPL(95th) maps have been generated for multi-constellation in three different modes, [Galileo E1/E5 plus GPS L1/L5], [Galileo E1 plus GPS L1] and [Galileo E5 plus GPS L5], and for single constellation [Galileo E1/E5], [Galileo E1] and [Galileo E5]. Three levels of constellation strength have been considered: depleted constellations with 23 satellites per constellation, baseline constellations of 24 satellites per constellation and optimistic constellations with 27 satellites each constellation.

Results of scenario 1, and scenario 2, are quite similar, with a little improvement in scenario 2, basically due to the smaller σ_{URA} used. Similar results are also found with the optimistic and baseline constellations, with a quite slight improvement with the depleted (degraded) constellations. The results with the degraded constellations show a significant worsening.

The RNP-0.3 H-ARAIM Availability (99.5th) maps achieve the coverage level of 100% for all analysed configurations, with multi- and single-constellation, including the single-constellation Galileo with the single frequency E5, when using the baseline or optimistic constellations. With the degraded constellation, RNP-03 H-ARAIM Availability is only achieved with multi-constellation (GPS plus Galileo), in single- or double-frequency; but it cannot be reached with Galileo single constellation, even with the double-frequency E1/E5.

RNP-0.1 H-ARAIM Availability (99.5th) coverage of almost 100% is achieved for all analysed configurations, except with the single-frequency L5 or E5, when using the baseline or optimistic constellation. With the degraded constellation, RNP-01 is only achieved with multi-constellation and dual-frequency [GPS L1/L5 plus Galileo E1/E5].

It is worth to note that the Galileo system is still under the deployment phase, and the results of the present PhD dissertation are based on only about five and a half years of data. Therefore, the results do not necessarily reflect the expected performance of the Galileo system once it is fully deployed. Thus, further studies should be performed in the future with larger historical data records to consolidate results.

6.2 Future work

The present study shall be extended with the upgrade of the tools and algorithms that I contributed to develop for the Ephemeris and Clock monitoring of the GLONASS and BeiDou constellations. This is not a trivial task, mainly in the case of GLONASS, where σ_{URA} values are not broadcast in the navigation messages. In the case of GLONASS, this algorithm extension can be found in [34].

It is worth to say that, the algorithms implemented in gNAV for Classical RAIM and Advanced RAIM are able to support single and multi-constellation for all GNSS constellations and signals, being ready to be used for further studies with GLONASS and BeiDou, as well.

Bibliography

1. Walter, T.; Joerger, M.; Pervan, B. Determination of Fault Probabilities for ARAIM. In Proceedings of 2016 IEEE/ION Position, Location and Navigation Symposium (PLANS), Savannah, GA, USA, 11–16 April 2016; pp. 451–461, Corrected Version.
2. Galluzo, G., Wallner, S.; Pericacho, J.G.; Criado, O.; García, C.; Sobrero, F.J.; Brieden, P.; Binder, K.; Battista, G.; Odriozola, M.; et al. Prototyping of Galileo URA Determination with TGVF and Extended Galileo Performance Characterisation for SoL Applications. In Proceedings of the 33rd International Technical Meeting of the Satellite Division of The Institute of Navigation (ION GNSS+ 2020), Online Conference, 21–25 September 2020; pp. 1462–1475.
3. Working Group C-ARAIM Technical Subgroup. EU-U.S. *Cooperation on Satellite Navigation*; Milestone 3 Report; 2016. Available online: https://insidegnss.com/wp-content/uploads/2016/11/ARAIM-milestone-3-report.pdf (accessed on 25 November 2020).
4. United States Department of Defense. Global Positioning System Standard Positioning Service Performance Standard. Available online: https://www.gps.gov/technical/ps/2020-SPS-performance-standard.pdf (accessed on 25 November 2020).
5. European GNSS (Galileo) Open Service—Service Definition Document, Issue 1.1, May 2019. Available online: https://www.gsc-europa.eu/sites/default/files/sites/all/files/Galileo-OS-SDD_v1.1.pdf (accessed on 20 August 2022).
6. Chatre, E.; Boyero, J.P.; Martini, I.; Sgammini, M.; Wallner, S.; Cosson, F.; Brieden, P.; Laura, D.; Canestri, D. Galileo Performance Characterization for Horizontal ARAIM. In Proceedings of the ICAO Navigation System Panel (NSP), Online Conference, 20-24 April 2020; Information paper.
7. Sanz, J.; Juan Zornoza, J.M.; Hernández-Pajares, M. *GNSS Data Processing, Volume 1: Fundamentals and Algorithms*; ESA TM-23/1; ESA Communications: Noordwijk, The Netherlands, 2013; ISBN 9789292217.
   Book available at https://gage.upc.edu/gnss_book (accessed on 25 July 2022).
8. Handbook of Global Navigation Satellite Systems, P. J. Teunissen and O. Montenbruck, Eds. Springer International Publishing, 2017.
9. European Union Agency for the Space Programme (EUSPA). (2022) European GNSS Service Centre: Constellation Information. https://www.gsc-europa.eu/system-service-status/constellation-information (accessed on 24 August 2022).
10. Federal Aviation Authority. GNSS. Phase II of the GNSS Evolutionary Architecture Study; Panel Report; 2010. Available online: http://www.faa.gov/about/office_org/headquarters_offices/ato/service_units/techops/navservices/gnss/library/documents/media/GEASPhaseII_Final.pdf . (accessed on 25 July 2022).
11. Duarte Sampaio. Integrity. Navipedia, 2011. https://gssc.esa.int/navipedia/index.php/Integrity
12. International Civil Aviation Organization, "International Standards and Recommended Practices (SARPs). Annex 10 to the Convention of International Civil Aviation. Volume I –Radio Navigation Aids," Tech. Rep., 2017.
13. US Department of Transport FAA. GPS Wide Area Augmentation System (WAAS) Performance Standard, 1st edition., Dec 2008.
14. Giuseppe, M. (2016). Processing and integrity of DC/DF GBAS for CAT II/III operations (Doctoral dissertation). Toulouse, France: University of Toulouse.
15. Meng, Q ; Liu, J, Zeng, Q, Feng S.; Xu, R.. Improved ARAIM fault modes determination scheme based on feedback structure with probability accumulation. GPS Solutions 2019; 23(1): 16. DOI 10.1007/s10291-018-0809-8
16. Walter, T.; Blanch, J.; Enge, P., "Reduced Subset Analysis for Multi-Constellation ARAIM,"Proceedings of the 2014 International Technical Meeting of The Institute of Navigation, San Diego, California, January 2014, pp. 89-98.
17. Ibañez, D.; Rovira-Garcia, A., Sanz, J.;, Juan, J.; González-Casado, G.; Jimenez-Baños, D.; López, C.; Lapin, I. (2018) , "The GNSS Laboratory Tool Suite (gLAB) updates: SBAS, DGNSS and Global Monitoring System," 2018 9th ESA Workshop on Satellite Navigation Technologies and European Workshop on GNSS Signals and Signal Processing (NAVITEC), 2018, pp. 1-11, doi: 10.1109/NAVITEC.2018.8642707.

18. gLAB-SUM "GNSS-Lab tool Software User Manual", issue 2.00, Date 29th May 2020.
19. Minimum Operational Performance Standard (MOPS) for Global Positioning System (GPS)/Wide Area Augmentation System (WAAS) Airborne Equipment. RTCA-DO229D, December 13 2006.
20. European Union Agency for the Space Program (EUSPA) https://egnos-user-support.essp-sas.eu/new_egnos_ops/egnos-system/about-egnos (accessed on 21 March 2022).
21. Caamaño, M. (2022), Network-Based Ionospheric Gradient Monitoring to support Ground Based Augmentation Systems. PhD Dissertation. Universitat Politècnica de Catalunya, Spain. https://www.tdx.cat/handle/10803/674794
22. Lee, Y., Example Fault Detection and Exclusion Algorithm, RTCA Paper No. 595-95/SC159-683.
23. K. L. Van Dyke, "The world after SA: benefits to GPS integrity," IEEE 2000. Position Location and Navigation Symposium (Cat. No.00CH37062), 2000, pp. 387-394, doi: 10.1109/PLANS.2000.838329. Integrity.
24. Brown. R. G., GPS RAIM: Calculation of Thresholds and Horizontal Integrity Limit Using Chi-Square Methods – A Geometric Approach. RTCA Paper No. 491-94/SC159-584, November 7, 1994.
25. Walter, T. and Enge, P. Weighted RAIM for Precision Approach, Proceedings of the 8th International Technical Meeting of the Satellite Division of The Institute of Navigation (ION GPS 1995), Palm Springs, CA, September 1995, pp. 1995-2004.
26. Blanch, J.; Walter, T.; Enge, P. Fixed Subset Selection to Reduce Advanced RAIM Complexity; Proceedings of the 2018 International Technical Meeting of The Institute of Navigation; Reston, VA, USA. 1–29 January 2018; pp. 88–98 (accessed on 6 November 2021).
27. Blanch, J.; Walter, T.; Enge, P.; Lee, Y.; Pervan, B.; Rippl, M.; Spletter, A.; Kropp, V., " Baseline advanced RAIM user algorithm and possible improvements. *IEEE Trans. Aerosp. Electron. Syst.* 2015, *51*, 713–732, doi:10.1109/taes.2014.130739.
28. Kropp, V. Advanced Receiver Autonomous Integrity Monitoring for Aircraft Guidance Using GNSS. PhD dissertation, Institut für Raumfahrttchnik un Weltraumnutzung, Germany, 26 March 2018.
29. MAAST-Matlab Algorithm Availability Simulation Tool for ARAIM, Stanford University http://web.stanford.edu/group/scpnt/gpslab/website_files/maast/maast_araimpb0.4.zip (accessed on 2 April 2021).
30. Walter, T.; Blanch, J.; Choi, M.J.; Reid; T., Enge, P. Incorporating GLONASS into Aviation RAIM Receivers. In Proceedings of the ION International Technical Meeting, San Diego, CA, USA, 3 January 2013; pp. 239–249.
31. "WG-C Advanced RAIM Technical Subgroup Reference Airborne Algorithm Description Document Version 3.1, June 20, 2019.
32. Walter, T.; Blanch, J. KEYNOTE—Characterization of GNSS Clock and Ephemeris Errors to Support ARAIM. In Proceedings of the ION 2015 Pacific PNT Meeting, Honolulu, HI, USA, 20–23 April 2015; pp. 920–931.
33. Heng, L. Safe Satellite Navigation with Multiple Constellations: Global Monitoring of GPS and GLONASS Signal-in-Space Anomalies. Ph.D. Dissertation, Stanford University, Stanford, CA, USA, 2012.
34. Gurtner, W. *RINEX: The Receiver Independent Exchange Format*; version 2.11; Astronomical Institute, University of Berne: Bern, Switzerland, 2012. Available online: ftp://igs.org/pub/data/format/rinex211.txt (accessed on 21 October 2020).
35. Global Positioning System Wing (GPSW). *Interface Specification IS-GPS-200E*; 2010. https://www.navcen.uscg.gov/pdf/gps/IS-GPS-200E_Final_08Jun10.pdf (accessed on 25 November 2020).
36. Ibáñez, D.; Rovira-Garcia, A.; Alonso, M.T.; Sanz, J.; Juan, J.M.; González-Casado, G.; Lopez-Martínez, M. EGNOS 1046 Maritime Service Assessment. *Sensors* 2020, *20*, 276, doi:10.3390/s20010276.
37. Montenbruck, O.; Steigenberger, P.; Prange, L.; Deng, Z.; Zhao, Q.; Perosanz, F.; Romero, I.; Noll, C.; Stürze, A.; Weber, G.; et al. The Multi-GNSS Experiment (MGEX) of the International GNSS Service (IGS)—Achievements, prospects and challenges. *Adv. Space Res.* 2017, *59*, 1671–1697, doi:10.1016/ j.asr.2017.01.011.
38. ANTEX Files Server. European GNSS Service Centre, April 2019. Available online: https://www.gsc-europa.eu/sites/default/files/sites/all/files/GSAT_2023.atx.txt (accessed on 21 October 2020).
39. National Geospatial Agency server ftp://ftp.nga.mil/pub2/gps/apcpe (accessed on 25 November 2020).
40. European GNSS (Galileo) Open Service—Signal-In-Space Interface Control Document, Issue 1.3, December 2016. Available online: https://www.gsc-europa.eu/sites/default/files/sites/all/files/Galileo-OS-SIS-ICD.pdf (accessed on).
41. NAGU: https://www.gsc-europa.eu/system-status/user-notifications-archive (accessed on 25 November 2020).

42. Cedric, R.; Bonhoure, B.; Suard, N.; Mabilleau, M.; Vuillaume, J.; Dulery, C.; Lapeyre, D.; Sauce, C. Galileo ephemeris consolidation and control analysis—GECCO. In Proceedings of the 28th International Technical Meeting of the Satellite Division of The Institute of Navigation (ION GNSS+ 2015), Tampa, FL, USA, 14–18 September 2015.
43. Serenad server from CNES: ftp://serenad-public.cnes.fr/SERENAD0/FROM_NTMFV2 (accessed on 25 November 2020).
44. Juan, J.M.; Sanz, J.; Rovira-Garcia, A.; González-Casado, G.; Ventura-Traveset, J.; Cacciapuoti, L.; Schoenemann, E. A New Approach to Improve Satellite Clock Estimates, Removing the Inter-day Jumps. In Proceedings of the 51st Annual Precise Time and Time Interval Systems and Applications Meeting, San Diego, CA, USA, 21–24 January 2020; pp. 279–301, doi:10.33012/2020.17306.
45. Walter, T.; Rife, J.; Blanch, J. Treatment of Biased Error Distributions in SBAS. In Proceedings of the 2004. International Symposium on GNSS/GPS, Sydney, Australia, 6–8 December 2004.
46. DeCleene, B. Defining pseudorange integrity—Overbounding. In Proceedings of the 13th International Technical Meeting of the Satellite Division of The Institute of Navigation (ION GPS 2000), Salt Lake City, UT, USA, 19–22 September 2000; pp. 1916–1924.
47. Brieden, P.; Wallner, S.; Canestri, E.; Joly, D.; Sanz, J.; Martini, I.; Nuckelt, A.; Battista, G.; Lauria, D.; Luongo, F.; et al. Galileo Characterization as Input to H-ARAIM and SBAS DFMC. In Proceedings of the 32nd International Technical Meeting of the Satellite Division of The Institute of Navigation (ION GNSS+ 2019), Miami, FL, USA, 16–20 September 2019; pp. 2819–2841.
48. Pericacho, J. G.;, Celada, J.;Sánchez, D.; Janicki, K. W.; Díaz, F.; Quiles, X.; Arribas, V.;, Andrés, J.;, de Echazarreta, C. L., "PROARAIM: Towards the Early Adoption of ARAIM Air Navigation Services," Proceedings of the 34th International Technical Meeting of the Satellite Division of The Institute of Navigation (ION GNSS+ 2021), St. Louis, Missouri, September 2021, pp. 1160-1175. https://doi.org/10.33012/2021.18050.
49. Guo, F.; Li, X.; Zhang, X.; Wang, J. Assessment of precise orbits and clock products for Galileo, Beidou and QZSS from IGS Multi-GNSS Experiment (MGEX). *GPS Solut.* 2017, *21*, 279–290, doi:10.1007/s10291-016-0523-3.
50. "WG-C Advanced RAIM Technical Subgroup Reference Airborne Algorithm Description Document Version 3, February 25, 2016.
51. Macabiau, C.; Milner, C.; Tesier, Q.; Mabilleau, M.; Vuillaume, J.; Suard, N.; Rodriguez, C., « Impact of Nominal Bias Bounding Techniques on Final ARAIM User Performance", Proceedings of the ION, San Diego, California, January 2014.
52. Blanch, J.; Walter, T.; Enge, P.; Kropp, V., A Simple Position Estimator that improves RAIM Performance, "IEEE Transactions in Aerospace Electronic Systems, Vol.51, No. 3, July 2015.

ANNEX A: Error models for GPS and Galileo

A. 1 Error model for dual frequency users

A.1.1 Classical RAIM

When a satellite is not faulted, the contribution of the satellite to the pseudorange error is characterized by a normal Gaussian $N(0, \sigma_{URA})$.

The diagonal elements of covariance matrices are defined as:

$$C(i,i) = \sigma^2_{URA,i} + \sigma^2_{tropo,i} + \sigma^2_{user,i}$$

The first term σ_{URA} is broadcast in the navigation message for GPS, Galileo and BeiDou. As GLONASS has no σ_{URA} in its navigation message, the conservative value of $\sigma_{URA} = 9.65\ m$ can be used (which corresponds to GPS IURA UB=4).

For availability of FDE tests (without SA), the value $\sigma_{URA} = 5.7\ m$ given in ANNEX-A of [19] for GPS satellites, can be taken for all constellations. An inflation factor can be applied over $C(i,i)$ for GLONASS and BeiDou constellations.

There are two other contributors to the variance of the pseudorange error: the code noise and multipath and the residual tropospheric delay. They are characterized by a zero mean Gaussian distributions $N(0, \sigma)$ with the variances specified in equations (A.1) to (A.4).

A.1.2 Advanced RAIM

When a satellite is not faulted, the contribution of the satellite to the pseudorange error is characterized by a normal Gaussian $N(\mu, \sigma)$ such that [31]:

$\sigma \leq \sigma_{URA,i}$, and $|\mu| \leq b_{nom,i}$ for integrity purposes

$\sigma \leq \sigma_{URE,i}$, and $\mu = 0$ for continuity (false alert or failed exclusion) purposes

As in the previous case, the diagonal elements of covariance matrices are defined as:

$$C_{int}(i,i) = \sigma^2_{URA,i} + \sigma^2_{tropo,i} + \sigma^2_{user,i}$$

$$C_{acc}(i,i) = \sigma^2_{URE,i} + \sigma^2_{tropo,i} + \sigma^2_{user,i}$$

where $\sigma_{URA,i}$ and $\sigma_{URE,i}$ are broadcast in the Integrity Support message (ISM), together with other parameters.

According to [31], the error models that will be used for Advanced RAIM have not yet been fully determined. The final values will need to be consistent with the values developed for dual frequency SBAS. The error budgets that are included here reflect the best estimate.

Two error budgets for GPS and Galileo have been used to allow for a performance prediction in the frame of ARAIM. A preliminary Galileo user contribution to the error budget is described in tabular form, detailed next.

Table 35. Galileo Elevation Dependent SIS user error [31]

Galileo SIS user error: $\boldsymbol{\sigma_{n,user}^{Galileo}(\theta)}$ (in metres)			
5°	0.4529	50°	0.2359
10°	0.3553	55°	0.2339
15°	0.3063	60°	0.2302
20°	0.2638	65°	0.2295
25°	0.2593	70°	0.2278
30°	0.2555	75°	0.2297
35°	0.2504	80°	0.2310
40°	0.2438	85°	0.2274
45°	0.2396	90°	0.2277

However, at the moment, it is more likely that the error bound for Galileo will be the one used for GPS, which is specified below (in metres).

$$\sigma_{n,user}^{GPS}(\theta) = \sqrt{\frac{f_{L1}^4 + f_{L5}^4}{(f_{L1}^2 - f_{L5}^2)^2}} \sqrt{\sigma_{MP}^2(\theta) + \sigma_{noise}^2(\theta)}$$

$$\sigma_{MP}(\theta) = 0.13 + 0.53\, e^{-\frac{\theta}{10^\circ}}, \quad \sigma_{noise}(\theta) = 0.11 + 0.13\, e^{-\frac{\theta}{6.9^\circ}} \tag{A.1}$$

where θ is the elevation angle in degrees. This represents an overbound of the error after carrier smoothing.

The tropospheric delay $\sigma_{n,tropo}$ can be modelled according to [31] as (in metres):

$$\sigma_{n,tropo}(\theta) = 0.12 \frac{1.001}{\sqrt{0.002001 + \left(sin(\pi\theta/180^\circ)\right)^2}} \tag{A.2}$$

A.2 Error model for single frequency users

The diagonal elements of covariance matrices are defined as:

$$C_{int}(i,i) = \sigma^2_{URA,i} + \sigma^2_{tropo,i} + \sigma^2_{iono,i} + \sigma^2_{SF\ user,i}$$
$$C_{acc}(i,i) = \sigma^2_{URE,i} + \sigma^2_{tropo,i} + \sigma^2_{iono,i} + \sigma^2_{SF\ user,i} \quad \text{(A.3)}$$

with

$$\sigma_{SF\ user,i} = \sqrt{\frac{(f_{L1}^2 - f_{L5}^2)^2}{f_{L1}^4 + f_{L5}^4}}\,\sigma_{user,i} \quad \text{(A.4)}$$

$$\sigma^2_{iono,i} = \sigma^2_{UIRE,i} \quad (for\ L1)$$
$$\sigma^2_{iono,i} = \frac{f_{L1}^4}{f_{L5}^4}\sigma^2_{UIRE,i} \quad (for\ L5)$$

where $\sigma^2_{UIRE,i}$ for GPS is defined in MOPS, Appendix J of RTCA-Do229D [19]. That is:

$$\sigma^2_{UIRE,i} = max\left\{\left(\frac{c\ T_{iono}}{5}\right)^2, \left(F_{pp}\ \tau_{vert}\right)^2\right\}$$

where:

c = the speed of light in a vacuum.

T_{iono} = ionospheric correction (see Section 20.3.3.5.2.6 of ICD-GPS-200) "Navstar GPS Space Segment / Navigation User Interfaces").

and:

$$F_{pp} = \frac{1}{\sqrt{1 - \left(\frac{R_e \cos E}{R_e + h_I}\right)^2}}$$

$R_e = 6378{,}1363\ km$; $h_I = 350\ km$; E =satellite elevation.

$$\tau_{vert} = \begin{cases} 9\ m; & 0 \le |\emptyset_m| \le 20 \\ 4.5\ m; & 20 < |\emptyset_m| \le 55 \\ 6\ m; & |\emptyset_m| > 55 \end{cases}$$

being $\emptyset_m$ the geomagnetic latitude.

Note: For FDE availability tests $\sigma_{UIRE,i} = F_{pp}\ \tau_{vert}$

A.3 Error models for other GNSSs

By default, the GPS error model will be applied to the GLONASS and BeiDou satellites, using conversion factors for the frequencies, and applying an inflation factor, if needed.

ANNEX B: ARAIM Integrity Support Message and Design Parameters

In order to have a self-contained dissertation, this appendix reproduces the section 3 of [31], describing the Integrity Support Message (ISM) and its relation to the navigation requirements, together with the design parameters.

Note that the parameters included in Table 36 might be dependent on the frequency combination (single- or dual-frequency), or on the mode of operation (horizontal guidance or vertical guidance).

Table 36. List of parameters derived from the ISM

Description		Source
$\sigma_{URA,i}$	Standard deviation of the clock and ephemeris error of satellite i used for integrity.	ISM + Nav. data
$\sigma_{URE,i}$	Standard deviation of the clock and ephemeris error of satellite i used for accuracy and continuity.	ISM + Nav. data
$b_{nom,i}$	Maximum nominal bias for satellite *i* used for integrity.	ISM
$P_{sat,i}$	Prior probability of fault in satellite *i* per approach.	ISM
$P_{const,j}$	Prior probability of a fault affecting more than one satellite in constellation *j* per approach.	ISM

Table 37. Navigation requirement parameters for LPV-200 and LPV-250

Name	Description	Value for LPV-200 (preliminary)	Value for LPV-250 (preliminary)
$PHMI$	Total Integrity budget.	10^{-7}/app.	10^{-7}/app.
P_{FA}	Continuity budget allocated to disruptions due to false alert. The total continuity budget is $8 \times 10^{-6}/15\ s$ (because of the temporal correlation of the error, it is adequate to use this value per 150 s).	4×10^{-6}/app (*)	4×10^{-6}/app (*)
P_{EMT}	Probability used for the calculation of the Effective Monitor Threshold.	10^{-5}/app.	NA
VAL	Vertical Alert Limit.	35 m	50 m
HAL	Horizontal Alert Limit.	40 m	40 m
$EMTL$	Effective Monitor Threshold Limit.	15 m	N/A

(*) This value is set to $5 \times 10^{-7}/app$ in [31], but according to [50] and [28] it is assumed $4 \times 10^{-6}/app$.

Table 38. Navigation requirement parameters for RNP-X

Name	Description	Value for RNP-X (preliminary)
$PHMI$	Total Integrity budget.	10^{-7}/h (*)
P_{Alert}	Continuity budget allocated to disruptions due to false alert and failed exclusions.	4×10^{-6}/h
HAL	Horizontal Alert Limit.	X * 1852 m

(*) This value is set to $5 \times 10^{-7}/h$ in [31], but according to [50] and [28] it is assumed $4 \times 10^{-6}/h$.

Table 39. Constants derived from navigation requirements

Name	Description	Value for LPV-200 or LPV-250 if applicable (preliminary)	Value for RNP (preliminary)
K_{ACC}	Number of standard deviations used for the accuracy formula.	1.96	N/A
K_{FF}	Number of standard deviations used for the 10^{-7} fault free vertical position error.	5.33	N/A

Table 40. Design parameters (tuneable)

Name	Description	Value for LPV-200 and LPV-250	Value for RNP
$PHMI_{VERT}$	Integrity budget for the vertical component.	9.8×10^{-8}/app	0
$PHMI_{HOR}$	Integrity budget for the horizontal component.	2×10^{-9}/app	$1 \times 10^{-7}/h$
P_{FA_VERT}	Probability of false alert allocated to the vertical mode.	3.9×10^{-6}/app	0
P_{FA_HOR}	Probability of false alert allocated to the horizontal mode.	9×10^{-8}/app	$3.99 \times 10^{-6}/h$ (*)
P_{THRES}	Threshold for the integrity risk coming from unmonitored faults.	8×10^{-8}/app	$4 \times 10^{-8}/h$
σ_{V,acc_max}	Required vertical (V) accuracy	1.87 m	20 m
σ_{H1,acc_max}	Required horizontal (H1) accuracy	20 m	20 m
σ_{H2,acc_max}	Required horizontal (H2) accuracy	20 m	20 m
F_C	Threshold used for fault consolidation.	0.01	0.01
$N_{ITER,MAX}$	Maximum number of iterations to compute the PL.	10	10
TOL_{PL}	Tolerance for the computation of the Protection Level.	$5 \times 10^{-2}\ m$	$5 \times 10^{-2}\ m$

(*) This value is set to $5 \times 10^{-7}/h$ in [31], but according to [50] and [28] it is assumed $P_{FA\_VERT} + P_{FA\_HOR} = 3.99 \times 10^{-6}$

Note: $PHMI_{HOR} = PHMI - HMI_{VERT}$; $P_{THRES} < PHMI$

ANNEX C: Adjust Projection Matrix for weak geometries

Next equations from [3], describes de computation of an optimized estimator of projection matrix $\boldsymbol{A}$ to minimise the Protection Levels. Because it degrades accuracy, this approach should only be applied when a target protection level is not achieved, for instance, for LPV-200 in the VPL exceeds 35 m or the EMT exceeds 15 m, being $\sigma_{acc,Vert} \leq 1.87\ m$).

The optimised estimator is as follows:

$$\left[\boldsymbol{A}^{(\boldsymbol{0})^{\boldsymbol{adj}}}\right]_{\boldsymbol{q}} = \left[\boldsymbol{A}^{(\boldsymbol{0})}\right]_{\boldsymbol{q}} + \boldsymbol{t}_{\boldsymbol{q}}\left(\left[\boldsymbol{A}^{(\boldsymbol{mx})}\right]_{\boldsymbol{q}} - \left[\boldsymbol{A}^{(\boldsymbol{0})}\right]_{\boldsymbol{q}}\right) \quad ;\ q = 1,2,3$$

where $\left[\boldsymbol{A}^{(\boldsymbol{0})}\right]_q$ indicates the row q of matrix $\boldsymbol{A}^{(\boldsymbol{0})}$

For each component $q = 1,2,3$

1. Find the fault mode ($k = mx$) with the largest contribution to the integrity risk $PHMI_q$. That is, find the largest σ_q with a prior probability $P_{ap\ subset}$ that exceeds the available integrity budget.

$$mx = \{\max_{k=0,\ldots,Nfaut\ modes} \left\{\sigma_q^{(k)}\right\} \mid P_{ap\ subset}(mk) > PHMI_q\}$$

2. Define coefficients a, b and c

$$a_q = \left[\boldsymbol{\Delta A}^{(\boldsymbol{mx})}\right]_q \boldsymbol{C_{acc}} \left[\boldsymbol{\Delta A}^{(\boldsymbol{mx})}\right]_q^T = \left(\sigma_{ssq}^{(mx)}\right)^2$$
$$b_q = 2\left[\boldsymbol{A}^{(\boldsymbol{0})}\right]_{\boldsymbol{q}} \boldsymbol{C_{acc}} \left[\boldsymbol{\Delta A}^{(\boldsymbol{mx})}\right]_q^T$$
$$c_q = \left[\boldsymbol{A}^{(\boldsymbol{0})}\right]_q \boldsymbol{C_{acc}} \left[\boldsymbol{A}^{(\boldsymbol{mx})}\right]_q^T - \left(\sigma_{acc_{max},q}\right)^2$$

where $\sigma_{acc_{max},q}$ is the accuracy requirement for the navigation mode. For instance, for LPV-200, $\sigma_{acc_{max},Hor1} = \sigma_{acc_{max},Hor2} = 3\ m$ and $\sigma_{acc_{max},Vert} = 1.87\ m$

3. Calculate t_q

$$t_q = \begin{cases} \dfrac{-b_q + \sqrt{b_q^2 - a_q\, c_q}}{a_q}, & c_q < 0 \\ 0, & otherwise \end{cases}$$

4. Calculate $\left[\boldsymbol{A}^{(\boldsymbol{0})^{\boldsymbol{adj}}}\right]_{\boldsymbol{q}}$

$$\left[\boldsymbol{A}^{(\boldsymbol{0})^{\boldsymbol{adj}}}\right]_{\boldsymbol{q}} = \left[\boldsymbol{A}^{(\boldsymbol{0})}\right]_{\boldsymbol{q}} + \boldsymbol{t}_{\boldsymbol{q}}\left(\left[\boldsymbol{A}^{(\boldsymbol{mx})}\right]_{\boldsymbol{q}} - \left[\boldsymbol{A}^{(\boldsymbol{0})}\right]_{\boldsymbol{q}}\right) \quad ;\ q = 1,2,3$$

5. Calculate:

$$\sigma_q^{(0)^{adj}} = \sqrt{\left[\boldsymbol{A}^{(\boldsymbol{0})^{\boldsymbol{adj}}}\right]_q \boldsymbol{C_{int}} \left[\boldsymbol{A}^{(\boldsymbol{0})^{\boldsymbol{adj}}}\right]_{\boldsymbol{q}}^T}$$

$$b_q^{(0)^{adj}} = \sum_{\boldsymbol{i=1}}^{\boldsymbol{Nsat}} \left|\left[\boldsymbol{A}^{(\boldsymbol{0})^{\boldsymbol{adj}}}\right]_{q_i}\right| b_{nom_i}$$

Note: only $\sigma_q^{(0)}$ and $b_q^{(0)}$ are updated.

$$\sigma_{ss,q}^{(k)\,adj} = \sqrt{\left[\Delta \boldsymbol{A}^{(k)\boldsymbol{adj}}\right]_q \; \boldsymbol{C_{acc}} \; \left[\Delta \boldsymbol{A}^{(k)\boldsymbol{adj}}\right]_{\boldsymbol{q}}^{T}}$$

where $\left[\Delta \boldsymbol{A}^{(k)\boldsymbol{adj}}\right]_q = \left[\boldsymbol{A}^{(k)\boldsymbol{adj}}\right]_q - \left[\boldsymbol{A}^{(\boldsymbol{0})\boldsymbol{adj}}\right]_q$

Finally;

$$\widehat{\boldsymbol{x}}^{(0)\,adj} = \boldsymbol{A}^{*\,adj}\,\boldsymbol{y_w}$$

where $[\boldsymbol{A}^{*\,adj}]_q = \begin{cases} \left[\boldsymbol{A}^{(\boldsymbol{0})\boldsymbol{adj}}\right]_q \;, & q = 1,2,3 \\ \left[\boldsymbol{A}^{(\boldsymbol{0})}\right]_q \;, & q = 4, \dots, N_{par} \end{cases}$

Notice that only the first 3 rows of matrix $\boldsymbol{A}^{(\boldsymbol{0})}$ are adjusted,

$$\boldsymbol{r_w}^{(0)\,adj} = \boldsymbol{y_w} - \boldsymbol{G_w}^{(\boldsymbol{0})}\,\widehat{\boldsymbol{x}}^{(0)\,adj}$$

$$Chi2^{(0)\,adj} = (\boldsymbol{r_w}^{(0)\,adj})^T\;\boldsymbol{r_w}^{(0)\,adj}$$

Comment:

These updated values impact on the solution separation test, as the differences are referred to $\widehat{\boldsymbol{x}}_{\boldsymbol{q}}^{(\boldsymbol{0})}$*. i.e.* $\left|\widehat{\boldsymbol{x}}_{\boldsymbol{q}}^{(\boldsymbol{k})} - \widehat{\boldsymbol{x}}_{\boldsymbol{q}}^{(\boldsymbol{0})}\right| \leq \boldsymbol{T}_{\boldsymbol{q}}^{(\boldsymbol{k})}$*, as the updated value* $\widehat{\boldsymbol{x}}^{(0)\,adj}$ *must be used, see Annex E.*

Note:

In the FORTRAN implementation, the Projection Matrix Adjustment is inserted after Filtering out the modes that cannot be monitored (if any) and after applying the exclusion of double counted modes (if any). Then, in case of having any fault mode exclusion (as a result of applying these filters), it can affect the results when comparing with the MATLAB code, as the MATLAB code applies the Projection Matrix Adjustment without excluding such modes.

In fact, the algorithm for the Projection matrix Adjustment uses the Projection matrix for the all-in-view, $\left[\boldsymbol{A}^{(\boldsymbol{0})}\right]_q$, and also the projection matrix for the fault mode with the larger contribution to the integrity risk, $\left[\boldsymbol{A}^{(\boldsymbol{mx})}\right]_q$. Then, if this mode has been excluded, the results will change. From my point of view, although it does not seem critical, is better to apply the Adjustment after filtering such modes.

Comments:

Baseline Projection matrix adjustment is only required when next conditions are meet:

$$\begin{cases} \sigma_{acc,Vert} < \sigma_{acc_{max},Vert} \\ and \\ (EMT > EMT_{TOL})\; or\; (HPL > HAL_{TOL})\; or\; (VPL > VAL_{TOL}) \end{cases}$$

where EMT_{TOL}, HAL_{TOL} and VAL_{TOL} are thresholds defined for the given navigation mode. For example, for LPV-200, $EMT_{TOL} = 15\ m$, $HAL_{TOL} = 40\ m$ and $VAL_{TOL} = 35\ m$.

C.1 Rational

This section reproduces some of the content of [52], which is added here for a self-containing explanation. The notation has been changed to be updated to this report.

The WLS all-in-view linear estimator $\boldsymbol{A^{(0)}}$ is unbiased and, as an unbiased estimator, can have an arbitrarily large nominal estimation error. Thus the algorithm introduces the next constrain on accuracy:

$$\sigma^2_{acc,q} = \left[\boldsymbol{A^{(0)}}\right]_q \boldsymbol{C_{acc}} \left[\boldsymbol{A^{(0)}}\right]^T_{\boldsymbol{q}} \leq \sigma^2_{acc_{max},q}$$

Then, the idea is find, for each error component $q = 1,2,3$, the vector $\left[\boldsymbol{A^{(0)}}\right]_q$ that minimises the Protection Levels PL_q.

The protection levels $HPL_1 \equiv PL_1$, $HPL_2 \equiv PL_2$ and $VPL \equiv PL_3$ are calculated by solving the implicit equation, where $PHMI_q$ is integrity budget allocated to each position component ($q = 1,2,3$) and K_{fa_q} is a factor set to the probability of false alert under fault-free condition.

$$2\,Q\left(\frac{PL_q - b_q^{(0)}}{\sigma_q^{(0)}}\right) + \sum_{k=1}^{Nfaut\ modes} P_{fault,k}\, Q\left(\frac{PL_q - K_{fa_q}\sqrt{\left(\left[\boldsymbol{A^{(k)}}\right]_q - \left[\boldsymbol{A^{(0)}}\right]_q\right)\boldsymbol{C_{acc}}\left(\left[\boldsymbol{A^{(k)}}\right]_q - \left[\boldsymbol{A^{(0)}}\right]_q\right)^T} - b_q^{(k)}}{\sigma_q^{(k)}}\right) = PHMI_q$$

where $Q^{-1}(p)$ is the $(1-p)$ quantile of a zero-mean unit-variance Gaussian distribution.

To reduce complexity, the previous equation is simplified by only taking into account the fault mode with the largest contribution to the integrity risk, because it is the one most likely to drive the protection level PL_q. This simplification is only done to search for the all-in-view estimator coefficients of $\left[\boldsymbol{A^{(0)}}\right]_q$, not to compute the final PL_q.

This fault mode is, typically, the one with the largest deviation σ_q with a prior probability $P_{ap\ subset}$ that exceeds the available integrity budget $PHMI_q$.

By considering, only, the corresponding term in previous equation, it follows

$$P_{fault,max}\, Q\left(\frac{PL_q - K_{fa_q}\sqrt{\left(\left[\boldsymbol{A^{(mx)}}\right]_q - \left[\boldsymbol{A^{(0)}}\right]_q\right)\boldsymbol{C_{acc}}\left(\left[\boldsymbol{A^{(mx)}}\right]_q - \left[\boldsymbol{A^{(0)}}\right]_q\right)^T} - b_q^{(mx)}}{\sigma_q^{(mx)}}\right) = PHMI_q$$

Thence, solving for PL_q (now labelled PL_{approx_q}) it follows:

$$PL_{\text{approx}_q} = \frac{K_{fa_q}\sqrt{\left(\left[\boldsymbol{A^{(mx)}}\right]_q - \left[\boldsymbol{A^{*(0)}}\right]_q\right)\boldsymbol{C_{acc}}\left(\left[\boldsymbol{A^{(mx)}}\right]_q - \left[\boldsymbol{A^{*(0)}}\right]_q\right)^T} - b_q^{(mx)}}{\sigma_q^{(mx)}} + Q^{-1}\left(\frac{PHMI_q}{P_{fault,max}}\right)$$

The previous equation shows that to minimise this approximate PL, the solution separation term must be minimised:

$$\sigma^{*(mx)}_{SS,q} = \sqrt{\left(\left[\boldsymbol{A^{(mx)}}\right]_q - \left[\boldsymbol{A^{*(0)}}\right]_q\right)\boldsymbol{C_{acc}}\left(\left[\boldsymbol{A^{(mx)}}\right]_q - \left[\boldsymbol{A^{*(0)}}\right]_q\right)^T}$$

One can see that, as $\left[\boldsymbol{A}^{*(0)}\right]_q$ moves towards $\left[\boldsymbol{A}^{(mx)}\right]_q$, the $\sigma^*_{ss,q}(max)$ decreases. To simplify the search of the estimator $\left[\boldsymbol{A}^{*(0)}\right]_q$, an affine combination of the all-in-view least squares estimator $[\boldsymbol{A}(1)]_q$ and the fault tolerant $[\boldsymbol{A}(max)]_q$ is considered:

$$\left[\boldsymbol{A}^{*(0)}\right]_q = \left[\boldsymbol{A}^{(\mathbf{0})}\right]_q + t_q\left(\left[\boldsymbol{A}^{(mx)}\right]_q - \left[\boldsymbol{A}^{(\mathbf{0})}\right]_q\right)$$

Then,

$$\sigma^{*(mx)}_{ss,q} = \sqrt{\left(t_q - 1\right)^2 \left(\left[\boldsymbol{A}^{(mx)}\right]_q - \left[\boldsymbol{A}^{*(0)}\right]_q\right) \boldsymbol{c_{acc}} \left(\left[\boldsymbol{A}^{(mx)}\right]_q - \left[\boldsymbol{A}^{*(0)}\right]_q\right)^T}$$

However, as $\left[\boldsymbol{A}^{*(0)}\right]_q$ moves towards $\left[\boldsymbol{A}^{(mx)}\right]_q$, the accuracy degrades.

After replacing $\left[\boldsymbol{A}^{*(0)}\right]_q$ in $\sigma^{*(mx)}_{ss,q}$, it follows:

$$\left[\left[\boldsymbol{A}^{(\mathbf{0})}\right]_q + t_q\left(\left[\boldsymbol{A}^{(mx)}\right]_q - \left[\boldsymbol{A}^{(\mathbf{0})}\right]_q\right)\right] \boldsymbol{C_{acc}} \left[\left[\boldsymbol{A}^{(\mathbf{0})}\right]_q + t_q\left(\left[\boldsymbol{A}^{(mx)}\right]_q - \left[\boldsymbol{A}^{(\mathbf{0})}\right]_q\right)\right]^T \leq \sigma^2_{acc_{max},q}$$

This expression is equivalent to

$$a_q\, t_q^2 + b_q\, t_q + c_q \leq 0$$

where the parameters are defined as:

$$a_q = \left[\boldsymbol{\Delta A^{(mx)}}\right]_q \boldsymbol{C_{acc}} \left[\boldsymbol{\Delta A^{(mx)}}\right]_q^T = \left(\sigma^{(mx)}_{ssq}\right)^2$$
$$b_q = 2\left[\boldsymbol{A^{(\mathbf{0})}}\right]_{\boldsymbol{q}} \boldsymbol{C_{acc}} \left[\boldsymbol{\Delta A^{(mx)}}\right]_q^T$$
$$c_q = \left[\boldsymbol{A^{(\mathbf{0})}}\right]_q \boldsymbol{C_{acc}} \left[\boldsymbol{A^{(mx)}}\right]_q^T - \left(\sigma_{acc_{max},q}\right)^2$$

The accuracy constrain therefore imposes:

$$t_q \in \left[\frac{-b_q - \sqrt{b_q^2 - a_q\, c_q}}{a_q} \quad , \quad \frac{-b_q + \sqrt{b_q^2 - a_q\, c_q}}{a_q}\right]$$

By noticing that $a_q \geq 0$ and $c_q \leq 0$ (if c_q is positive, the optimization cannot be performed, because the accuracy requirement cannot be met), it can be seen that the lower limit is negative and the upper limit is positive.

As the coefficients aim to be as close to 1 as possible to minimise $\sigma^{*(mx)}_{ss,q}$, there are two possible cases: Either the upper limit is above 1 or below. If it is above, then $t_q = 1$ is feasible and should be chosen. If not, choose the upper limit. Therefore:

$$t_q = min\left(1\,, \frac{-b_q + \sqrt{b_q^2 - a_q\, c_q}}{a_q}\right)$$

		Initial Projection matrix (first row) [All-in-view]																				
		G										E						R	C			
	k/sat	1	2	3	4	5	6	7	8	9	10	11	12	13	14	15	16	17	18	19	20	21
$[A^{(0)}]_1$	0	-0,005	-0,06	0,2307	0,0428	-0,083	-0,123	0,0785	-0,107	0,0591	-0,033	-0,275	0,3435	-0,005	0,1822	-0,176	-0,07	-5,2E-17	-0,021	0,0092	0,039	-0,027
$[A^{(0)}]_2$	0	-0,0788	0,0697	0,0179	0,0342	0,1421	0,0895	-0,142	-0,056	0,069	-0,146	-0,246	0,1722	0,0034	-0,191	0,1847	0,0764	8,25E-18	-0,013	0,0007	0,0269	-0,014
$[A^{(0)}]_3$	0	-0,1490	-0,311	0,0724	0,0982	-0,092	0,0982	0,0842	-0,211	0,1492	0,2614	0,2351	0,1385	-0,377	0,2912	0,1987	-0,486	1,2E-17	0,1477	-0,089	-0,225	0,1663

		Adjusted Projection matrix (first row) [All-in-view]																				
		G										E						R	C			
	k/sat	1	2	3	4	5	6	7	8	9	10	11	12	13	14	15	16	17	18	19	20	21
$[A^{(0)}]_1$	0	-0,011	-0,098	0,5931	0,1055	-0,17	-0,311	0,1601	-0,263	0,1487	-0,154	0	0	0	0	0	0	-5,6E-17	-0,077	0,0362	0,1384	-0,097
$[A^{(0)}]_2$	0	0	0	0	0	0	0	0	0	0	0	-0,446	0,2995	-0,021	-0,432	0,4568	0,1436	6,09E-18	-0,012	-0,008	0,031	-0,011
$[A^{(0)}]_3$	0	0	0	0	0	0	0	0	0	0	0	0,3135	0,4111	-0,704	0,6201	0,294	-0,935	-1,6E-16	0,2655	-0,161	-0,402	0,2972

Figure 36. Example of first three rows of the all-in-view matrix $\left[\boldsymbol{A}^{(\mathbf{0})}\right]_q$, before and after its adjustment.

	All-in-view solution							Chi2	
	ΔE	ΔN	ΔU	dt_G	dt_E	dt_R	dt_C		
$\hat{x}^{(0)}$	-0,349	-0,160	-2,335	-9,442	-8,571	-2,564	13,376	100,79	$Chi2^{(0)}$
$\hat{x}^{(0)\,adj}$	0,047	-0,456	-3,092	-9,442	-8,571	-2,564	13,376	109,61	$Chi2^{(0)\,adj}$

Figure 37. Example of all-in-view solution before and after adjusting the first three rows of the all-in-view Projection matrix $\left[\boldsymbol{A}^{(\mathbf{0})}\right]_q$ (i.e. subset $k = 0$).

Comment: As commented before, projection matrix adjustment is only required when next conditions are meet:

$$\begin{cases} \sigma_{acc,Vert} < \sigma_{acc_{max},Vert} \\ and \\ (EMT > EMT_{TOL})\ or\ (HPL > HAL_{TOL})\ or\ (VPL > VAL_{TOL}) \end{cases}$$

Nevertheless, in the driving example, this adjusting has been applied here (i.e. before completing the full chain needed to calculate the Projection Levels, EMT and sigma accuracy and check these conditions, see Annex E, to not to extend excessively this example steps (iterations), as the target is to illustrate how this adjustment affects to the matrix and vectors involved, i.e. $\hat{\boldsymbol{x}}^{(\mathbf{0})\boldsymbol{adj}}$, $Chi2^{(0)^{adj}}$, $\sigma_q^{(0)^{adj}}$, $b_q^{(0)^{adj}}$, $\sigma_{ss,\,q}^{(k)\ adj}$, $\boldsymbol{A}^{(\mathbf{0})\boldsymbol{adj}}$ and $\boldsymbol{\Delta A}^{(\boldsymbol{k})\boldsymbol{adj}}$

ANNEX D: Protection Levels Computation

Protection Levels are determined by the integrity requirement. For each PL, the integrity risk (which is the sum of the contributions of each fault mode) must be below the integrity risk allocated in the associated position component.

The solutions of the following equations provide the protection levels that meets the required integrity allocation:

For the horizontal components $q = 1,2$:

$$2\bar{Q}\left(\frac{PL_q - b_q^{(0)})}{\sigma_q^{(0)}}\right) + \sum_{k=1}^{N_{fault\,modes}} P_{fault_k}\,\bar{Q}\left(\frac{PL_q - b_q^{(k)} - T_{k,q})}{\sigma_q^{(k)}}\right) = \rho_j\,\frac{PHMI_{HOR}}{2}\left(1 - \frac{P_{not\,monitored}}{PHMI_{HOR} + PHI_{VER}}\right)$$

For the vertical component: $q = 3$

$$2\bar{Q}\left(\frac{PL_3 - b_3^{(0)}}{\sigma_3^{(0)}}\right) + \sum_{k=1}^{N_{fault\,modes}} P_{fault_k}\,\bar{Q}\left(\frac{PL_3 - b_3^{(k)} - T_{k,3})}{\sigma_3^{(k)}}\right) = \rho_j\,PHMI_{VER}\left(1 - \frac{P_{not\,monitored}}{PHMI_{HOR} + PHMI_{VER}}\right)$$

where ρ_j is the fraction of the integrity budget given to exclusion mode and Q is the right-hand side cumulative distribution function of a zero-mean Gaussian.

Each term of the left-hand side of previous equations is an upper bound of the contribution of each fault to the integrity risk.

Procedure (from [29])

1. Define the fraction of the integrity budget given to exclusion mode ρ_j
   Non exclusion mode: $\rho_j = 1$
   Exclusion mode: $\rho_j = \frac{1}{N_{excl}+1}$, being N_{excl} number of exclusion trials to attempt.

2. Calculate $PHMI_q$, $q = 1,2,3$:

$$PHMI_1 = PHMI_2 = \rho_j\,\frac{PHMI_{HOR}}{2}\left(1 - \frac{P_{not\,monitored}}{PHMI_{HOR} + PHMI_{VER}}\right)$$

$$PHMI_3 = \rho_j\,PHMI_{VER}\left(1 - \frac{P_{not\,monitored}}{PHMI_{HOR} + PHMI_{VER}}\right)$$

3. Calculate Protection Levels
   a. Exclude modes not monitored, i.e. having $\sigma_q^{(k)} = 0$, and update $PHMI_q$ by adding their associated $P_{fault,k}$.

   b. $if\ \left(PHMI_q \geq 0\right)\ then$

      i. Determine $PL_{q\ low}$:

         1.- For each valid subset $k = 0, \dots, N_{faut\ modes}$ calculate

$$p(k) = \frac{PHMI_q}{P_{fault,\ k}}$$
$$if\ \ (p(k) > 1)\ then\ \ p(k) = 1$$

$$K_{q\ low}(k) = Q^{-1}(p(k))$$

$$v_{low}(k) = T_{k,q} + K_{q\ low}(k)\ \sigma_q^{(k)} + b_q^{(k)}$$

         2.- Select the maximum value.

$$PL_{q\ low} = \max_{k=0,\dots,N_{faut\ modes}} \{v_{low}(k)\}$$

      ii. Determine $PL_{q\ high}$:

         1.- For each valid subset $k = 0, \dots, N_{faut\ modes}$ calculate

$$p(k) = \frac{PHMI_q}{\left(N_{faut\ modes} + 1\right) P_{fault,k}}$$

$$K_{q\ high}(k) = \max\left\{0\ ,\ Q^{-1}\left(p(k)\right)\right\}$$

$$v_{high}(k) = T_{k,q} + K_{high}(k)\ \sigma_q^{(k)} + b_q^{(k)}$$

         2.- Select the maximum value.

$$PL_{q\ high} = \max_{k=0,\dots,N_{faut\ modes}} \left\{v_{high}(k)\right\}$$

      iii. Solve PL_q equation by half-interval search

$$n_{iter} = 0$$
$$sum = 0$$
$$while\ \left(PL_{q\ high} - PL_{q\ low} > P_{TOL}\right).and.\left(n_{iter} < n_{iter_{max}}\right)$$

$$n_{iter} = n_{iter} + 1$$

$$PL_{q\ half} = \frac{PL_{q\ low} + PL_{q\ high}}{2}$$

$foreach\ (k = 0, \dots, N_{faut\ modes})$

$z = \frac{PL_{q\ half} - T_{k,q} - b_q^{(k)}}{\sigma_q^{(k)}}$

$p(k) = = \begin{cases} Q(z);\ z > 0 \\ 1 \quad ;\ z \leq 0 \end{cases}$

$alloc_q^{(k)} = p(k)$

$sum = sum + p(k)\ \ P_{ap\ subset,k}$

$endfor$

$if\ \left(\log(sum) > \log\left(PHMI_q\right)\right)\ then$

$PL_{q\ low} = PL_{q\ half}$

$else$

$PL_{q\ high} = PL_{q\ half}$

$endif$

$endwhile$

$PL_q = PL_{q\ high}$

$endif$

c. $if\ \left(PHMI_q < 0\right)\ then$

$PL_q = 0$

$alloc_q^{(k)} = 0,\ k = 0, \dots, N_{faut\ modes}$

$endif$

$HPL = \sqrt{PL_1^2 + PL_2^2}$

$VPL = PL_3$

Note: $alloc_q^{(k)}$ is the cumulative $N(0,1)$ probability density for the different subsets .

$alloc_q^{(0)} = Q\left(\frac{PL_q - b_q^0}{\sigma_q^{(0)}}\right)$

$alloc_q^{(k)} = Q\left(\frac{PL_q - b_q^{(k)} - T_{k,q})}{\sigma_q^{(k)}}\right)$

ANNEX E: ARAIM Driving example

Let us consider $N_{sat} = 21$ satellites in view from $N_{const} = 4$ different constellations (GLONASS, GPS, Galileo, BeiDou), with the associated data given in Figure 38.

PRN	Prefit	DE	DN	DU	Receiver clocks				Cint	Cacc	bnom	Psat	Pconst
R24	-1,0321	0,5546	-0,4351	-0,7093	1	0	0	0	1,8383	1,2828	0,75	1,00E-05	1,00E-04
G01	-8,6832	0,0682	-0,4273	-0,9015	0	1	0	0	1,3693	0,8137	0,75	1,00E-05	1,00E-04
G03	-8,3550	-0,1509	0,1561	-0,9761	0	1	0	0	1,3651	0,8096	0,75	1,00E-05	1,00E-04
G04	-8,6761	0,7267	-0,0403	-0,6857	0	1	0	0	1,3987	0,8432	0,75	1,00E-05	1,00E-04
G14	-8,9353	0,3967	0,9135	-0,0904	0	1	0	0	5,2824	4,7269	0,75	1,00E-05	1,00E-04
G17	-9,5199	-0,3734	0,6342	-0,6770	0	1	0	0	1,4009	0,8454	0,75	1,00E-05	1,00E-04
G19	-5,4742	-0,6410	0,6353	-0,4308	0	1	0	0	1,5662	1,0106	0,75	1,00E-05	1,00E-04
G21	10,437	0,3078	-0,6372	-0,7066	0	1	0	0	1,3939	0,8383	0,75	1,00E-05	1,00E-04
G22	-5,5399	-0,2630	-0,2954	-0,9185	0	1	0	0	1,3682	0,8126	0,75	1,00E-05	1,00E-04
G28	-8,3878	0,2305	0,9584	-0,1682	0	1	0	0	3,0290	2,4734	0,75	1,00E-05	1,00E-04
G31	-10,5530	-0,2590	-0,9394	-0,2247	0	1	0	0	2,3556	1,8001	0,75	1,00E-05	1,00E-04
E04	-6,2814	-0,5734	-0,6455	-0,5046	0	0	1	0	1,1214	0,5658	0,75	1,00E-05	1,00E-04
E05	-7,3463	0,7427	0,3235	-0,5863	0	0	1	0	1,1038	0,5483	0,75	1,00E-05	1,00E-04
E09	-6,9453	0,1320	-0,2383	-0,9622	0	0	1	0	1,0682	0,5126	0,75	1,00E-05	1,00E-04
E11	-6,9421	0,4923	-0,6597	-0,5679	0	0	1	0	1,1074	0,5518	0,75	1,00E-05	1,00E-04
E18	-7,4358	-0,5891	0,7279	-0,3510	0	0	1	0	1,1846	0,6290	0,75	1,00E-05	1,00E-04
E36	-7,0523	-0,0177	-0,0385	-0,9991	0	0	1	0	1,0662	0,5107	0,75	1,00E-05	1,00E-04
C06	17,5230	-0,8395	-0,5305	-0,1177	0	0	0	1	4,0658	3,5102	0,75	1,00E-05	1,00E-04
C09	13,1918	-0,5817	-0,6474	-0,4924	0	0	0	1	1,4723	0,9167	0,75	1,00E-05	1,00E-04
C14	19,0078	-0,4866	-0,6366	-0,5983	0	0	0	1	1,4071	0,8516	0,75	1,00E-05	1,00E-04
C16	6,7818	-0,8325	-0,5329	-0,1516	0	0	0	1	3,2340	2,6785	0,75	1,00E-05	1,00E-04

Figure 38. Driving example: Dual-frequency prefit-residuals, in blue, design matrix, in green, diagonal elements of covariance matrices, in yellow, nominal bias, in pink, and satellite and constellation fault probabilities, in grey. An error of 17 metres has been added to GPS satellite PRN21 prefit (in red) to simulate a fault. The configuration parameters for LPV-200 are used, see Annex B.

a) Determine the probability of No Fault

$$P_{no\_fault} = \prod_{k=1}^{21+4} \left(1 - P_{event,k}\right) = 0.999390164973674$$

where $P_{event,k} \equiv p(k)$ are the probabilities of the independent fault events k.
This example uses:
p(k)= Psat= 1e-5 ; k=1,..., $Nsat$
p(k)= Pcon= 1e-4 ; k= $Nsat$ +1,..., $Nsat + Nconst$

b) Generate the subsets and select subsets until having $P_{not\ monitored} < P\_THRES$.

The next algorithm is applied:

$n = 1$

$P_{not\ monitored} = 1$

while ($P_{not\ monitored} < P_{THRES}$ && $n < Nsat + Nconst$)

1. All possible subsets (combinations) with n failures in an array of $Nsat + Nconst$ elements, with n ones and $Nsat + Nconst - n$ zeroes are generated.

2. The prior (a priori) probability $P_{fault,n}$ of each individual subset is determined:

$$P_{fault,n} = P_{no\_fault} \prod_{s=1,\ldots,n} \frac{P_{event,\, i_s}}{1 - P_{event,\, i_s}}$$

3. The subsets are sorted by decreasing the prior probability $P_{fault,n}$.

4. Thence, being subsets sorted by decreasing probability, selecting subsets while $P_{not\ monitored} < P_{THRES}$.

5. When select a subset " n ", reduce the $P_{not\ monitored}$ by the amount

$$P_{not\ monitored} = P_{not\ monitored} - P_{fault,n}$$

$n = n + 1$

end while

$N_{faults\ max} = n$

Given the previous probabilities and number of satellite and constellations, the number of the faults that need to be monitored, in the example results: $N_{faults\ max} = 2$ (satellite or constellation events).

	Satellites																				Systems				
k	R	G										E						C				R	G	E	C	$P_{ap\ subset,k}$
0	0	0	0	0	0	0	0	0	0	0	0	0	0	0	0	0	0	0	0	0	0	0	0	0	0	9,99390164973673E-01
1	**0**	**0**	**0**	**0**	**0**	**0**	**0**	**0**	**0**	**0**	**0**	**0**	**0**	**0**	**0**	**0**	**0**	**0**	**0**	**0**	**0**	**1**	**0**	**0**	**0**	**9,99490113985072E-05**
2	**0**	**0**	**0**	**0**	**0**	**0**	**0**	**0**	**0**	**0**	**0**	**0**	**0**	**0**	**0**	**0**	**0**	**0**	**0**	**0**	**0**	**0**	**1**	**0**	**0**	**9,99490113985072E-05**
3	0	0	0	0	0	0	0	0	0	0	0	0	0	0	0	0	0	0	0	0	0	0	0	1	0	9,99490113985072E-05
4	0	0	0	0	0	0	0	0	0	0	0	0	0	0	0	0	0	0	0	0	0	0	0	0	1	9,99490113985072E-05
5	1	0	0	0	0	0	0	0	0	0	0	0	0	0	0	0	0	0	0	0	0	0	0	0	0	9,99400158975263E-06
6	0	1	0	0	0	0	0	0	0	0	0	0	0	0	0	0	0	0	0	0	0	0	0	0	0	9,99400158975263E-06
7	0	0	1	0	0	0	0	0	0	0	0	0	0	0	0	0	0	0	0	0	0	0	0	0	0	9,99400158975263E-06
8	0	0	0	1	0	0	0	0	0	0	0	0	0	0	0	0	0	0	0	0	0	0	0	0	0	9,99400158975263E-06
9	0	0	0	0	1	0	0	0	0	0	0	0	0	0	0	0	0	0	0	0	0	0	0	0	0	9,99400158975263E-06
10	0	0	0	0	0	1	0	0	0	0	0	0	0	0	0	0	0	0	0	0	0	0	0	0	0	9,99400158975263E-06
11	0	0	0	0	0	0	1	0	0	0	0	0	0	0	0	0	0	0	0	0	0	0	0	0	0	9,99400158975263E-06
12	0	0	0	0	0	0	0	1	0	0	0	0	0	0	0	0	0	0	0	0	0	0	0	0	0	9,99400158975263E-06
13	0	0	0	0	0	0	0	0	1	0	0	0	0	0	0	0	0	0	0	0	0	0	0	0	0	9,99400158975263E-06
14	0	0	0	0	0	0	0	0	0	1	0	0	0	0	0	0	0	0	0	0	0	0	0	0	0	9,99400158975263E-06
15	0	0	0	0	0	0	0	0	0	0	1	0	0	0	0	0	0	0	0	0	0	0	0	0	0	9,99400158975263E-06
16	0	0	0	0	0	0	0	0	0	0	0	1	0	0	0	0	0	0	0	0	0	0	0	0	0	9,99400158975263E-06
17	0	0	0	0	0	0	0	0	0	0	0	0	1	0	0	0	0	0	0	0	0	0	0	0	0	9,99400158975263E-06
18	0	0	0	0	0	0	0	0	0	0	0	0	0	1	0	0	0	0	0	0	0	0	0	0	0	9,99400158975263E-06
19	0	0	0	0	0	0	0	0	0	0	0	0	0	0	1	0	0	0	0	0	0	0	0	0	0	9,99400158975263E-06
20	0	0	0	0	0	0	0	0	0	0	0	0	0	0	0	1	0	0	0	0	0	0	0	0	0	9,99400158975263E-06
21	0	0	0	0	0	0	0	0	0	0	0	0	0	0	0	0	1	0	0	0	0	0	0	0	0	9,99400158975263E-06
22	0	0	0	0	0	0	0	0	0	0	0	0	0	0	0	0	0	1	0	0	0	0	0	0	0	9,99400158975263E-06
23	0	0	0	0	0	0	0	0	0	0	0	0	0	0	0	0	0	0	1	0	0	0	0	0	0	9,99400158975263E-06
24	0	0	0	0	0	0	0	0	0	0	0	0	0	0	0	0	0	0	0	1	0	0	0	0	0	9,99400158975263E-06
25	0	0	0	0	0	0	0	0	0	0	0	0	0	0	0	0	0	0	0	0	1	0	0	0	0	9,99400158975263E-06
26	**0**	**0**	**0**	**0**	**0**	**0**	**0**	**0**	**0**	**0**	**0**	**0**	**0**	**0**	**0**	**0**	**0**	**0**	**0**	**0**	**0**	**1**	**1**	**0**	**0**	**9,99590072992371E-09**
27	**0**	**0**	**0**	**0**	**0**	**0**	**0**	**0**	**0**	**0**	**0**	**0**	**0**	**0**	**0**	**0**	**0**	**0**	**0**	**0**	**0**	**1**	**0**	**1**	**0**	**9,99590072992371E-09**
28	**0**	**0**	**0**	**0**	**0**	**0**	**0**	**0**	**0**	**0**	**0**	**0**	**0**	**0**	**0**	**0**	**0**	**0**	**0**	**0**	**0**	**1**	**0**	**0**	**1**	**9,99590072992371E-09**
29	0	0	0	0	0	0	0	0	0	0	0	0	0	0	0	0	0	0	0	0	0	0	1	1	0	9,99590072992371E-09
30	0	0	0	0	0	0	0	0	0	0	0	0	0	0	0	0	0	0	0	0	0	0	1	0	1	9,99590072992371E-09
31	0	0	0	0	0	0	0	0	0	0	0	0	0	0	0	0	0	0	0	0	0	0	0	1	1	9,99590072992371E-09
32	1	0	0	0	0	0	0	0	0	0	0	0	0	0	0	0	0	0	0	0	0	1	0	0	0	9,99500108986162E-10
33	1	0	0	0	0	0	0	0	0	0	0	0	0	0	0	0	0	0	0	0	0	0	1	0	0	9,99500108986162E-10
34	1	0	0	0	0	0	0	0	0	0	0	0	0	0	0	0	0	0	0	0	0	0	0	1	0	9,99500108986162E-10
35	1	0	0	0	0	0	0	0	0	0	0	0	0	0	0	0	0	0	0	0	0	0	0	0	1	9,99500108986162E-10
36	0	1	0	0	0	0	0	0	0	0	0	0	0	0	0	0	0	0	0	0	0	1	0	0	0	9,99500108986162E-10
37	0	1	0	0	0	0	0	0	0	0	0	0	0	0	0	0	0	0	0	0	0	0	1	0	0	9,99500108986162E-10
38	0	1	0	0	0	0	0	0	0	0	0	0	0	0	0	0	0	0	0	0	0	0	0	1	0	9,99500108986162E-10
39	0	1	0	0	0	0	0	0	0	0	0	0	0	0	0	0	0	0	0	0	0	0	0	0	1	9,99500108986162E-10
40	0	0	1	0	0	0	0	0	0	0	0	0	0	0	0	0	0	0	0	0	0	1	0	0	0	9,99500108986162E-10
41	0	0	1	0	0	0	0	0	0	0	0	0	0	0	0	0	0	0	0	0	0	0	1	0	0	9,99500108986162E-10
42	0	0	1	0	0	0	0	0	0	0	0	0	0	0	0	0	0	0	0	0	0	0	0	1	0	9,99500108986162E-10
43	0	0	1	0	0	0	0	0	0	0	0	0	0	0	0	0	0	0	0	0	0	0	0	0	1	9,99500108986162E-10
44	0	0	0	1	0	0	0	0	0	0	0	0	0	0	0	0	0	0	0	0	0	1	0	0	0	9,99500108986162E-10
45	0	0	0	1	0	0	0	0	0	0	0	0	0	0	0	0	0	0	0	0	0	0	1	0	0	9,99500108986162E-10
46	0	0	0	1	0	0	0	0	0	0	0	0	0	0	0	0	0	0	0	0	0	0	0	1	0	9,99500108986162E-10
47	0	0	0	1	0	0	0	0	0	0	0	0	0	0	0	0	0	0	0	0	0	0	0	0	1	9,99500108986162E-10
48	0	0	0	0	1	0	0	0	0	0	0	0	0	0	0	0	0	0	0	0	0	1	0	0	0	9,99500108986162E-10
49	0	0	0	0	1	0	0	0	0	0	0	0	0	0	0	0	0	0	0	0	0	0	1	0	0	9,99500108986162E-10
50	0	0	0	0	1	0	0	0	0	0	0	0	0	0	0	0	0	0	0	0	0	0	0	1	0	9,99500108986162E-10
51	0	0	0	0	1	0	0	0	0	0	0	0	0	0	0	0	0	0	0	0	0	0	0	0	1	9,99500108986162E-10
52	0	0	0	0	0	1	0	0	0	0	0	0	0	0	0	0	0	0	0	0	0	1	0	0	0	9,99500108986162E-10
53	0	0	0	0	0	1	0	0	0	0	0	0	0	0	0	0	0	0	0	0	0	0	1	0	0	9,99500108986162E-10
54	0	0	0	0	0	1	0	0	0	0	0	0	0	0	0	0	0	0	0	0	0	0	0	1	0	9,99500108986162E-10
55	0	0	0	0	0	1	0	0	0	0	0	0	0	0	0	0	0	0	0	0	0	0	0	0	1	9,99500108986162E-10
56	0	0	0	0	0	0	1	0	0	0	0	0	0	0	0	0	0	0	0	0	0	1	0	0	0	9,99500108986162E-10

Figure 39. Initially selected fault modes and associated a priori probability of each subset $P_{ap\ subset,k}$. The total probability of unmonitored subsets is $P_{not\ monitored}$ = 7.99844E-08.

	Satellites																					Systems				Satellites																				
k	R	G										E						C				R	G	E	C	R	G										E						C			
0	0	0	0	0	0	0	0	0	0	0	0	0	0	0	0	0	0	0	0	0	0	0	0	0	0	0	0	0	0	0	0	0	0	0	0	0	0	0	0	0	0	0	0	0	0	0
1	0	0	0	0	0	0	0	0	0	0	0	0	0	0	0	0	0	0	0	0	0	1	0	0	0	1	0	0	0	0	0	0	0	0	0	0	0	0	0	0	0	0	0	0	0	0
2	0	0	0	0	0	0	0	0	0	0	0	0	0	0	0	0	0	0	0	0	0	0	1	0	0	0	1	1	1	1	1	1	1	1	1	1	0	0	0	0	0	0	0	0	0	0
3	0	0	0	0	0	0	0	0	0	0	0	0	0	0	0	0	0	0	0	0	0	0	0	1	0	0	0	0	0	0	0	0	0	0	0	0	1	1	1	1	1	1	0	0	0	0
4	0	0	0	0	0	0	0	0	0	0	0	0	0	0	0	0	0	0	0	0	0	0	0	0	1	0	0	0	0	0	0	0	0	0	0	0	0	0	0	0	0	0	1	1	1	1
5	1	0	0	0	0	0	0	0	0	0	0	0	0	0	0	0	0	0	0	0	0	0	0	0	0	0	0	0	0	0	0	0	0	0	0	0	0	0	0	0	0	0	0	0	0	0
6	0	1	0	0	0	0	0	0	0	0	0	0	0	0	0	0	0	0	0	0	0	0	0	0	0	0	0	0	0	0	0	0	0	0	0	0	0	0	0	0	0	0	0	0	0	0
7	0	0	1	0	0	0	0	0	0	0	0	0	0	0	0	0	0	0	0	0	0	0	0	0	0	0	0	0	0	0	0	0	0	0	0	0	0	0	0	0	0	0	0	0	0	0
8	0	0	0	1	0	0	0	0	0	0	0	0	0	0	0	0	0	0	0	0	0	0	0	0	0	0	0	0	0	0	0	0	0	0	0	0	0	0	0	0	0	0	0	0	0	0
9	0	0	0	0	1	0	0	0	0	0	0	0	0	0	0	0	0	0	0	0	0	0	0	0	0	0	0	0	0	0	0	0	0	0	0	0	0	0	0	0	0	0	0	0	0	0
10	0	0	0	0	0	1	0	0	0	0	0	0	0	0	0	0	0	0	0	0	0	0	0	0	0	0	0	0	0	0	0	0	0	0	0	0	0	0	0	0	0	0	0	0	0	0
11	0	0	0	0	0	0	1	0	0	0	0	0	0	0	0	0	0	0	0	0	0	0	0	0	0	0	0	0	0	0	0	0	0	0	0	0	0	0	0	0	0	0	0	0	0	0
12	0	0	0	0	0	0	0	1	0	0	0	0	0	0	0	0	0	0	0	0	0	0	0	0	0	0	0	0	0	0	0	0	0	0	0	0	0	0	0	0	0	0	0	0	0	0
13	0	0	0	0	0	0	0	0	1	0	0	0	0	0	0	0	0	0	0	0	0	0	0	0	0	0	0	0	0	0	0	0	0	0	0	0	0	0	0	0	0	0	0	0	0	0
14	0	0	0	0	0	0	0	0	0	1	0	0	0	0	0	0	0	0	0	0	0	0	0	0	0	0	0	0	0	0	0	0	0	0	0	0	0	0	0	0	0	0	0	0	0	0
15	0	0	0	0	0	0	0	0	0	0	1	0	0	0	0	0	0	0	0	0	0	0	0	0	0	0	0	0	0	0	0	0	0	0	0	0	0	0	0	0	0	0	0	0	0	0
16	0	0	0	0	0	0	0	0	0	0	0	1	0	0	0	0	0	0	0	0	0	0	0	0	0	0	0	0	0	0	0	0	0	0	0	0	0	0	0	0	0	0	0	0	0	0
17	0	0	0	0	0	0	0	0	0	0	0	0	1	0	0	0	0	0	0	0	0	0	0	0	0	0	0	0	0	0	0	0	0	0	0	0	0	0	0	0	0	0	0	0	0	0
18	0	0	0	0	0	0	0	0	0	0	0	0	0	1	0	0	0	0	0	0	0	0	0	0	0	0	0	0	0	0	0	0	0	0	0	0	0	0	0	0	0	0	0	0	0	0
19	0	0	0	0	0	0	0	0	0	0	0	0	0	0	1	0	0	0	0	0	0	0	0	0	0	0	0	0	0	0	0	0	0	0	0	0	0	0	0	0	0	0	0	0	0	0
20	0	0	0	0	0	0	0	0	0	0	0	0	0	0	0	1	0	0	0	0	0	0	0	0	0	0	0	0	0	0	0	0	0	0	0	0	0	0	0	0	0	0	0	0	0	0
21	0	0	0	0	0	0	0	0	0	0	0	0	0	0	0	0	1	0	0	0	0	0	0	0	0	0	0	0	0	0	0	0	0	0	0	0	0	0	0	0	0	0	0	0	0	0
22	0	0	0	0	0	0	0	0	0	0	0	0	0	0	0	0	0	1	0	0	0	0	0	0	0	0	0	0	0	0	0	0	0	0	0	0	0	0	0	0	0	0	0	0	0	0
23	0	0	0	0	0	0	0	0	0	0	0	0	0	0	0	0	0	0	1	0	0	0	0	0	0	0	0	0	0	0	0	0	0	0	0	0	0	0	0	0	0	0	0	0	0	0
24	0	0	0	0	0	0	0	0	0	0	0	0	0	0	0	0	0	0	0	1	0	0	0	0	0	0	0	0	0	0	0	0	0	0	0	0	0	0	0	0	0	0	0	0	0	0
25	0	0	0	0	0	0	0	0	0	0	0	0	0	0	0	0	0	0	0	0	1	0	0	0	0	0	0	0	0	0	0	0	0	0	0	0	0	0	0	0	0	0	0	0	0	0
26	0	0	0	0	0	0	0	0	0	0	0	0	0	0	0	0	0	0	0	0	0	1	1	0	0	1	1	1	1	1	1	1	1	1	1	1	0	0	0	0	0	0	0	0	0	0
27	0	0	0	0	0	0	0	0	0	0	0	0	0	0	0	0	0	0	0	0	0	1	0	1	0	1	0	0	0	0	0	0	0	0	0	0	1	1	1	1	1	1	0	0	0	0
28	0	0	0	0	0	0	0	0	0	0	0	0	0	0	0	0	0	0	0	0	0	1	0	0	1	1	0	0	0	0	0	0	0	0	0	0	0	0	0	0	0	0	1	1	1	1
29	0	0	0	0	0	0	0	0	0	0	0	0	0	0	0	0	0	0	0	0	0	0	1	1	0	0	1	1	1	1	1	1	1	1	1	1	1	1	1	1	1	1	0	0	0	0
30	0	0	0	0	0	0	0	0	0	0	0	0	0	0	0	0	0	0	0	0	0	0	1	0	1	0	1	1	1	1	1	1	1	1	1	1	0	0	0	0	0	0	1	1	1	1
31	0	0	0	0	0	0	0	0	0	0	0	0	0	0	0	0	0	0	0	0	0	0	0	1	1	0	0	0	0	0	0	0	0	0	0	0	1	1	1	1	1	1	1	1	1	1
32	1	0	0	0	0	0	0	0	0	0	0	0	0	0	0	0	0	0	0	0	0	1	0	0	0	1	0	0	0	0	0	0	0	0	0	0	0	0	0	0	0	0	0	0	0	0
33	1	0	0	0	0	0	0	0	0	0	0	0	0	0	0	0	0	0	0	0	0	0	1	0	0	0	1	1	1	1	1	1	1	1	1	1	0	0	0	0	0	0	0	0	0	0
34	1	0	0	0	0	0	0	0	0	0	0	0	0	0	0	0	0	0	0	0	0	0	0	1	0	0	0	0	0	0	0	0	0	0	0	0	1	1	1	1	1	1	0	0	0	0
35	1	0	0	0	0	0	0	0	0	0	0	0	0	0	0	0	0	0	0	0	0	0	0	0	1	0	0	0	0	0	0	0	0	0	0	0	0	0	0	0	0	0	1	1	1	1
36	0	1	0	0	0	0	0	0	0	0	0	0	0	0	0	0	0	0	0	0	0	1	0	0	0	1	0	0	0	0	0	0	0	0	0	0	0	0	0	0	0	0	0	0	0	0
37	0	1	0	0	0	0	0	0	0	0	0	0	0	0	0	0	0	0	0	0	0	0	1	0	0	0	1	1	1	1	1	1	1	1	1	1	0	0	0	0	0	0	0	0	0	0
38	0	1	0	0	0	0	0	0	0	0	0	0	0	0	0	0	0	0	0	0	0	0	0	1	0	0	0	0	0	0	0	0	0	0	0	0	1	1	1	1	1	1	0	0	0	0
39	0	1	0	0	0	0	0	0	0	0	0	0	0	0	0	0	0	0	0	0	0	0	0	0	1	0	0	0	0	0	0	0	0	0	0	0	0	0	0	0	0	0	1	1	1	1
40	0	0	1	0	0	0	0	0	0	0	0	0	0	0	0	0	0	0	0	0	0	1	0	0	0	1	0	0	0	0	0	0	0	0	0	0	0	0	0	0	0	0	0	0	0	0
41	0	0	1	0	0	0	0	0	0	0	0	0	0	0	0	0	0	0	0	0	0	0	1	0	0	0	1	1	1	1	1	1	1	1	1	1	0	0	0	0	0	0	0	0	0	0
42	0	0	1	0	0	0	0	0	0	0	0	0	0	0	0	0	0	0	0	0	0	0	0	1	0	0	0	0	0	0	0	0	0	0	0	0	1	1	1	1	1	1	0	0	0	0
43	0	0	1	0	0	0	0	0	0	0	0	0	0	0	0	0	0	0	0	0	0	0	0	0	1	0	0	0	0	0	0	0	0	0	0	0	0	0	0	0	0	0	1	1	1	1
44	0	0	0	1	0	0	0	0	0	0	0	0	0	0	0	0	0	0	0	0	0	1	0	0	0	1	0	0	0	0	0	0	0	0	0	0	0	0	0	0	0	0	0	0	0	0
45	0	0	0	1	0	0	0	0	0	0	0	0	0	0	0	0	0	0	0	0	0	0	1	0	0	0	1	1	1	1	1	1	1	1	1	1	0	0	0	0	0	0	0	0	0	0
46	0	0	0	1	0	0	0	0	0	0	0	0	0	0	0	0	0	0	0	0	0	0	0	1	0	0	0	0	0	0	0	0	0	0	0	0	1	1	1	1	1	1	0	0	0	0
47	0	0	0	1	0	0	0	0	0	0	0	0	0	0	0	0	0	0	0	0	0	0	0	0	1	0	0	0	0	0	0	0	0	0	0	0	0	0	0	0	0	0	1	1	1	1
48	0	0	0	0	1	0	0	0	0	0	0	0	0	0	0	0	0	0	0	0	0	1	0	0	0	1	0	0	0	0	0	0	0	0	0	0	0	0	0	0	0	0	0	0	0	0
49	0	0	0	0	1	0	0	0	0	0	0	0	0	0	0	0	0	0	0	0	0	0	1	0	0	0	1	1	1	1	1	1	1	1	1	1	0	0	0	0	0	0	0	0	0	0
50	0	0	0	0	1	0	0	0	0	0	0	0	0	0	0	0	0	0	0	0	0	0	0	1	0	0	0	0	0	0	0	0	0	0	0	0	1	1	1	1	1	1	0	0	0	0
51	0	0	0	0	1	0	0	0	0	0	0	0	0	0	0	0	0	0	0	0	0	0	0	0	1	0	0	0	0	0	0	0	0	0	0	0	0	0	0	0	0	0	1	1	1	1
52	0	0	0	0	0	1	0	0	0	0	0	0	0	0	0	0	0	0	0	0	0	1	0	0	0	1	0	0	0	0	0	0	0	0	0	0	0	0	0	0	0	0	0	0	0	0
53	0	0	0	0	0	1	0	0	0	0	0	0	0	0	0	0	0	0	0	0	0	0	1	0	0	0	1	1	1	1	1	1	1	1	1	1	0	0	0	0	0	0	0	0	0	0
54	0	0	0	0	0	1	0	0	0	0	0	0	0	0	0	0	0	0	0	0	0	0	0	1	0	0	0	0	0	0	0	0	0	0	0	0	1	1	1	1	1	1	0	0	0	0
55	0	0	0	0	0	1	0	0	0	0	0	0	0	0	0	0	0	0	0	0	0	0	0	0	1	0	0	0	0	0	0	0	0	0	0	0	0	0	0	0	0	0	1	1	1	1
56	0	0	0	0	0	0	1	0	0	0	0	0	0	0	0	0	0	0	0	0	0	1	0	0	0	1	0	0	0	0	0	0	0	0	0	0	0	0	0	0	0	0	0	0	0	0

Figure 40. Initially selected fault modes (satellite and constellation faults) translated to satellites. The combinations that will be assimilated in the consolidation are indicated in the left hand column by different colors. $P_{not\ monitored} = 7.99844\text{E-}08$.

	Satellites																					
k	R	G										E						C				$P_{ap\ subset,k}$	
0	0	0	0	0	0	0	0	0	0	0	0	0	0	0	0	0	0	0	0	0	0	9,99390164973673E-01	
1	**1**	**0**	**0**	**0**	**0**	**0**	**0**	**0**	**0**	**0**	**0**	**0**	**0**	**0**	**0**	**0**	**0**	**0**	**0**	**0**	**0**	**1,09940000000000E-04**	[1]+[5]+[32]
2	**0**	**1**	**1**	**1**	**1**	**1**	**1**	**1**	**1**	**1**	**1**	**0**	**0**	**0**	**0**	**0**	**0**	**0**	**0**	**0**	**0**	**9,99540000000000E-05**	[2]+[37][41]+[45]+[49]+[53]
3	0	0	0	0	0	0	0	0	0	0	0	1	1	1	1	1	1	0	0	0	0	9,99490000000000E-05	
4	0	0	0	0	0	0	0	0	0	0	0	0	0	0	0	0	0	1	1	1	1	9,99490000000000E-05	
5	0	1	0	0	0	0	0	0	0	0	0	0	0	0	0	0	0	0	0	0	0	9,99400000000000E-06	
6	0	0	1	0	0	0	0	0	0	0	0	0	0	0	0	0	0	0	0	0	0	9,99400000000000E-06	
7	0	0	0	1	0	0	0	0	0	0	0	0	0	0	0	0	0	0	0	0	0	9,99400000000000E-06	
8	0	0	0	0	1	0	0	0	0	0	0	0	0	0	0	0	0	0	0	0	0	9,99400000000000E-06	
9	0	0	0	0	0	1	0	0	0	0	0	0	0	0	0	0	0	0	0	0	0	9,99400000000000E-06	
10	0	0	0	0	0	0	1	0	0	0	0	0	0	0	0	0	0	0	0	0	0	9,99400000000000E-06	
11	0	0	0	0	0	0	0	1	0	0	0	0	0	0	0	0	0	0	0	0	0	9,99400000000000E-06	
12	0	0	0	0	0	0	0	0	1	0	0	0	0	0	0	0	0	0	0	0	0	9,99400000000000E-06	
13	0	0	0	0	0	0	0	0	0	1	0	0	0	0	0	0	0	0	0	0	0	9,99400000000000E-06	
14	0	0	0	0	0	0	0	0	0	0	1	0	0	0	0	0	0	0	0	0	0	9,99400000000000E-06	
15	0	0	0	0	0	0	0	0	0	0	0	1	0	0	0	0	0	0	0	0	0	9,99400000000000E-06	
16	0	0	0	0	0	0	0	0	0	0	0	0	1	0	0	0	0	0	0	0	0	9,99400000000000E-06	
17	0	0	0	0	0	0	0	0	0	0	0	0	0	1	0	0	0	0	0	0	0	9,99400000000000E-06	
18	0	0	0	0	0	0	0	0	0	0	0	0	0	0	1	0	0	0	0	0	0	9,99400000000000E-06	
19	0	0	0	0	0	0	0	0	0	0	0	0	0	0	0	1	0	0	0	0	0	9,99400000000000E-06	
20	0	0	0	0	0	0	0	0	0	0	0	0	0	0	0	0	1	0	0	0	0	9,99400000000000E-06	
21	0	0	0	0	0	0	0	0	0	0	0	0	0	0	0	0	0	1	0	0	0	9,99400000000000E-06	
22	0	0	0	0	0	0	0	0	0	0	0	0	0	0	0	0	0	0	1	0	0	9,99400000000000E-06	
23	0	0	0	0	0	0	0	0	0	0	0	0	0	0	0	0	0	0	0	1	0	9,99400000000000E-06	
24	0	0	0	0	0	0	0	0	0	0	0	0	0	0	0	0	0	0	0	0	1	9,99400000000000E-06	
25	**1**	**1**	**1**	**1**	**1**	**1**	**1**	**1**	**1**	**1**	**1**	**0**	**0**	**0**	**0**	**0**	**0**	**0**	**0**	**0**	**0**	**1,09950000000000E-08**	[26]+[33]
26	**1**	**0**	**0**	**0**	**0**	**0**	**0**	**0**	**0**	**0**	**0**	**1**	**1**	**1**	**1**	**1**	**1**	**0**	**0**	**0**	**0**	**1,09950000000000E-08**	[27]+[34]
27	**1**	**0**	**0**	**0**	**0**	**0**	**0**	**0**	**0**	**0**	**0**	**0**	**0**	**0**	**0**	**0**	**0**	**1**	**1**	**1**	**1**	**1,09950000000000E-08**	[28]+[35]
28	0	1	1	1	1	1	1	1	1	1	1	1	1	1	1	1	1	0	0	0	0	9,99590000000000E-09	
29	0	1	1	1	1	1	1	1	1	1	1	0	0	0	0	0	0	1	1	1	1	9,99590000000000E-09	
30	0	0	0	0	0	0	0	0	0	0	0	1	1	1	1	1	1	1	1	1	1	9,99590000000000E-09	
31	1	1	0	0	0	0	0	0	0	0	0	0	0	0	0	0	0	0	0	0	0	9,99500000000000E-10	
32	0	1	0	0	0	0	0	0	0	0	0	1	1	1	1	1	1	0	0	0	0	9,99500000000000E-10	
33	0	1	0	0	0	0	0	0	0	0	0	0	0	0	0	0	0	1	1	1	1	9,99500000000000E-10	
34	1	0	1	0	0	0	0	0	0	0	0	0	0	0	0	0	0	0	0	0	0	9,99500000000000E-10	
35	0	0	1	0	0	0	0	0	0	0	0	1	1	1	1	1	1	0	0	0	0	9,99500000000000E-10	
36	0	0	1	0	0	0	0	0	0	0	0	0	0	0	0	0	0	1	1	1	1	9,99500000000000E-10	
37	1	0	0	1	0	0	0	0	0	0	0	0	0	0	0	0	0	0	0	0	0	9,99500000000000E-10	
38	0	0	0	1	0	0	0	0	0	0	0	1	1	1	1	1	1	0	0	0	0	9,99500000000000E-10	
39	0	0	0	1	0	0	0	0	0	0	0	0	0	0	0	0	0	1	1	1	1	9,99500000000000E-10	
40	1	0	0	0	1	0	0	0	0	0	0	0	0	0	0	0	0	0	0	0	0	9,99500000000000E-10	
41	0	0	0	0	1	0	0	0	0	0	0	1	1	1	1	1	1	0	0	0	0	9,99500000000000E-10	
42	0	0	0	0	1	0	0	0	0	0	0	0	0	0	0	0	0	1	1	1	1	9,99500000000000E-10	
43	1	0	0	0	0	1	0	0	0	0	0	0	0	0	0	0	0	0	0	0	0	9,99500000000000E-10	
44	0	0	0	0	0	1	0	0	0	0	0	1	1	1	1	1	1	0	0	0	0	9,99500000000000E-10	
45	0	0	0	0	0	1	0	0	0	0	0	0	0	0	0	0	0	1	1	1	1	9,99500000000000E-10	
46	1	0	0	0	0	0	1	0	0	0	0	0	0	0	0	0	0	0	0	0	0	9,99500000000000E-10	

Figure 41. Consolidated subsets. The combinations assimilated in the consolidation are indicated in the left- and right-hand columns by different colors. The combination numbers in the right hand column corresponds to numbering before consolidating. $P_{not\ monitored} = 0.79984E\text{-}07$.

	Satellite combinations																				
k	R	G										E						C				$P_{ap\ subset,k}$
0	1	1	1	1	1	1	1	1	1	1	1	1	1	1	1	1	1	1	1	1	1	9,99390164973673E-01
1	0	1	1	1	1	1	1	1	1	1	1	1	1	1	1	1	1	1	1	1	1	1,09940000000000E-04
2	1	0	0	0	0	0	0	0	0	0	0	1	1	1	1	1	1	1	1	1	1	9,99540000000000E-05
3	1	1	1	1	1	1	1	1	1	1	1	0	0	0	0	0	0	1	1	1	1	9,99490000000000E-05
4	1	1	1	1	1	1	1	1	1	1	1	1	1	1	1	1	1	0	0	0	0	9,99490000000000E-05
5	1	0	1	1	1	1	1	1	1	1	1	1	1	1	1	1	1	1	1	1	1	9,99400000000000E-06
6	1	1	0	1	1	1	1	1	1	1	1	1	1	1	1	1	1	1	1	1	1	9,99400000000000E-06
7	1	1	1	0	1	1	1	1	1	1	1	1	1	1	1	1	1	1	1	1	1	9,99400000000000E-06
8	1	1	1	1	0	1	1	1	1	1	1	1	1	1	1	1	1	1	1	1	1	9,99400000000000E-06
9	1	1	1	1	1	0	1	1	1	1	1	1	1	1	1	1	1	1	1	1	1	9,99400000000000E-06
10	1	1	1	1	1	1	0	1	1	1	1	1	1	1	1	1	1	1	1	1	1	9,99400000000000E-06
11	1	1	1	1	1	1	1	0	1	1	1	1	1	1	1	1	1	1	1	1	1	9,99400000000000E-06
12	1	1	1	1	1	1	1	1	0	1	1	1	1	1	1	1	1	1	1	1	1	9,99400000000000E-06
13	1	1	1	1	1	1	1	1	1	0	1	1	1	1	1	1	1	1	1	1	1	9,99400000000000E-06
14	1	1	1	1	1	1	1	1	1	1	0	1	1	1	1	1	1	1	1	1	1	9,99400000000000E-06
15	1	1	1	1	1	1	1	1	1	1	1	0	1	1	1	1	1	1	1	1	1	9,99400000000000E-06
16	1	1	1	1	1	1	1	1	1	1	1	1	0	1	1	1	1	1	1	1	1	9,99400000000000E-06
17	1	1	1	1	1	1	1	1	1	1	1	1	1	0	1	1	1	1	1	1	1	9,99400000000000E-06
18	1	1	1	1	1	1	1	1	1	1	1	1	1	1	0	1	1	1	1	1	1	9,99400000000000E-06
19	1	1	1	1	1	1	1	1	1	1	1	1	1	1	1	0	1	1	1	1	1	9,99400000000000E-06
20	1	1	1	1	1	1	1	1	1	1	1	1	1	1	1	1	0	1	1	1	1	9,99400000000000E-06
21	1	1	1	1	1	1	1	1	1	1	1	1	1	1	1	1	1	0	1	1	1	9,99400000000000E-06
22	1	1	1	1	1	1	1	1	1	1	1	1	1	1	1	1	1	1	0	1	1	9,99400000000000E-06
23	1	1	1	1	1	1	1	1	1	1	1	1	1	1	1	1	1	1	1	0	1	9,99400000000000E-06
24	1	1	1	1	1	1	1	1	1	1	1	1	1	1	1	1	1	1	1	1	0	9,99400000000000E-06
25	0	0	0	0	0	0	0	0	0	0	0	1	1	1	1	1	1	1	1	1	1	1,09950000000000E-08
26	0	1	1	1	1	1	1	1	1	1	1	0	0	0	0	0	0	1	1	1	1	1,09950000000000E-08
27	0	1	1	1	1	1	1	1	1	1	1	1	1	1	1	1	1	0	0	0	0	1,09950000000000E-08
28	1	0	0	0	0	0	0	0	0	0	0	0	0	0	0	0	0	1	1	1	1	9,99590000000000E-09
29	1	0	0	0	0	0	0	0	0	0	0	1	1	1	1	1	1	0	0	0	0	9,99590000000000E-09
30	1	1	1	1	1	1	1	1	1	1	1	0	0	0	0	0	0	0	0	0	0	9,99590000000000E-09
31	0	0	1	1	1	1	1	1	1	1	1	1	1	1	1	1	1	1	1	1	1	9,99500000000000E-10
32	1	0	1	1	1	1	1	1	1	1	1	0	0	0	0	0	0	1	1	1	1	9,99500000000000E-10
33	1	0	1	1	1	1	1	1	1	1	1	1	1	1	1	1	1	0	0	0	0	9,99500000000000E-10
34	0	1	0	1	1	1	1	1	1	1	1	1	1	1	1	1	1	1	1	1	1	9,99500000000000E-10
35	1	1	0	1	1	1	1	1	1	1	1	0	0	0	0	0	0	1	1	1	1	9,99500000000000E-10
36	1	1	0	1	1	1	1	1	1	1	1	1	1	1	1	1	1	0	0	0	0	9,99500000000000E-10
37	0	1	1	0	1	1	1	1	1	1	1	1	1	1	1	1	1	1	1	1	1	9,99500000000000E-10
38	1	1	1	0	1	1	1	1	1	1	1	0	0	0	0	0	0	1	1	1	1	9,99500000000000E-10
39	1	1	1	0	1	1	1	1	1	1	1	1	1	1	1	1	1	0	0	0	0	9,99500000000000E-10
40	0	1	1	1	0	1	1	1	1	1	1	1	1	1	1	1	1	1	1	1	1	9,99500000000000E-10
41	1	1	1	1	0	1	1	1	1	1	1	0	0	0	0	0	0	1	1	1	1	9,99500000000000E-10
42	1	1	1	1	0	1	1	1	1	1	1	1	1	1	1	1	1	0	0	0	0	9,99500000000000E-10
43	0	1	1	1	1	0	1	1	1	1	1	1	1	1	1	1	1	1	1	1	1	9,99500000000000E-10
44	1	1	1	1	1	0	1	1	1	1	1	0	0	0	0	0	0	1	1	1	1	9,99500000000000E-10
45	1	1	1	1	1	0	1	1	1	1	1	1	1	1	1	1	1	0	0	0	0	9,99500000000000E-10
46	0	1	1	1	1	1	0	1	1	1	1	1	1	1	1	1	1	1	1	1	1	9,99500000000000E-10

Figure 42. Satellite combinations associated to subsets of Figure 41. $P_{not\ monitored}$ = 0.79984E-07. In red it is indicated a subset that will produce the largest error values in Figure 43.

	subsets solution								
k	ΔE	ΔN	ΔU	dt_R	dt_G	dt_E	dt_C	$Chi2^{(k)}$	$P_{ap\ subset,k}$
0	0,9533	-2,5113	-0,7450	-3,1819	-6,2728	-7,7766	13,5829	239,4317	9,9939E-01
1	0,9533	-2,5113	-0,7450		-6,2728	-7,7766	13,5829	239,4317	1,0994E-04
2	-0,1591	-0,4880	-2,3933	-2,8538		-8,6406	13,4210	34,0813	9,9954E-05
3	2,6060	-3,5320	-1,3719	-4,9873	-6,6432		13,7143	224,7365	9,9949E-05
4	0,7371	-2,6408	0,3318	-2,3546	-5,5556	-7,0596		205,7962	9,9949E-05
5	0,9384	-2,9112	-1,6369	-3,9802	-6,2204	-8,4117	12,9464	223,2621	9,9940E-06
6	0,7717	-2,2946	-1,7626	-3,7087	-6,5883	-8,4298	13,1656	234,4145	9,9940E-06
7	2,2341	-2,4218	-0,4934	-3,6748	-5,4330	-7,6505	14,5390	225,3742	9,9940E-06
8	1,0087	-2,4685	-0,6179	-3,1038	-6,1552	-7,6896	13,6980	239,2806	9,9940E-06
9	0,7360	-2,1738	-1,0103	-3,1027	-6,1721	-7,9130	13,5404	236,3710	9,9940E-06
10	1,4832	-2,8491	-1,1113	-3,8826	-6,9022	-8,0755	13,5476	233,0735	9,9940E-06
11	-0,5969	0,1625	-2,0644	-2,0947	-9,4895	-8,3402	13,6882	47,1623	9,9940E-06
12	0,8910	-2,5415	-0,8758	-3,2533	-6,2915	-7,8646	13,4697	239,2476	9,9940E-06
13	0,9584	-2,5055	-0,7322	-3,1731	-6,2602	-7,7677	13,5951	239,4305	9,9940E-06
14	0,4638	-4,4149	2,7165	-1,2834	-3,1760	-5,6233	13,6044	209,3736	9,9940E-06
15	0,9757	-2,4921	-0,7651	-3,2002	-6,2858	-7,8033	13,5999	239,4283	9,9940E-06
16	0,8958	-2,5384	-0,7640	-3,1753	-6,2867	-7,8200	13,5226	239,4156	9,9940E-06
17	0,9564	-2,5056	-1,0347	-3,3866	-6,4669	-7,8252	13,4639	238,9527	9,9940E-06
18	1,4135	-2,9721	-0,0449	-3,1410	-5,7884	-6,9200	13,8874	235,2449	9,9940E-06
19	1,7772	-3,2752	-1,6337	-4,6015	-6,8414	-9,1978	13,2452	229,8040	9,9940E-06
20	0,9453	-2,5009	-0,8104	-3,2193	-6,3169	-7,7934	13,5562	239,4179	9,9940E-06
21	1,0147	-2,4741	-1,1263	-3,4702	-6,5271	-8,0308	12,9804	236,2064	9,9940E-06
22	0,9700	-2,5108	-0,8913	-3,2947	-6,3704	-7,8752	14,5175	235,9208	9,9940E-06
23	0,7671	-2,6344	0,2205	-2,4474	-5,6295	-7,1347	11,4876	222,0878	9,9940E-06
24	0,7715	-2,6049	0,2456	-2,4192	-5,6128	-7,1152	15,3065	218,1368	9,9940E-06
25	-0,1591	-0,4880	-2,3933			-8,6406	13,4210	34,0813	1,0995E-08
26	2,6060	-3,5320	-1,3719		-6,6432		13,7143	224,7365	1,0995E-08
27	0,7371	-2,6408	0,3318		-5,5556	-7,0596		205,7962	1,0995E-08
28	569,6886	-128,4060	443,5751	-58,2230			479,8660	0,0000	9,9959E-09
29	-0,3225	-0,6614	0,0233	-1,1246		-7,0329		0,0788	9,9959E-09
30	1,9745	-3,8366	0,2894	-3,5912	-5,5432			193,7297	9,9959E-09
31	0,9384	-2,9112	-1,6369		-6,2204	-8,4117	12,9464	223,2621	9,9950E-10
32	2,6674	-4,3423	-3,1114	-6,6077		-6,9952	12,5105	201,0637	9,9950E-10
33	0,7390	-3,0131	-0,6111	-3,1864	-5,5670		-7,7268	191,1487	9,9950E-10
34	0,7717	-2,2946	-1,7626	-6,5883	-8,4298	13,1656		234,4145	9,9950E-10
35	2,3478	-3,1329	-3,0591		-5,8672	-7,4004	13,0733	219,9578	9,9950E-10
36	0,5919	-2,4456	-0,6223	-2,8659		-5,8767	-7,6737	202,0572	9,9950E-10
37	2,2341	-2,4218	-0,4934	-5,4330	-7,6505		14,5390	225,3742	9,9950E-10
38	8,9200	-2,5993	-1,3955	-8,0999	-5,1769	18,1845		185,1846	9,9950E-10
39	1,9727	-2,5486	0,5081		-2,8746	-4,7956	-6,9818	192,9867	9,9950E-10
40	1,0087	-2,4685	-0,6179	-6,1552		-7,6896	13,6980	239,2806	9,9950E-10
41	2,6428	-3,5070	-1,3147	-4,9562	-6,5945		13,7769	224,7237	9,9950E-10
42	0,8187	-2,5773	0,5393	-2,2251	-5,3675	-6,9178		205,4494	9,9950E-10
43	0,7360	-2,1738	-1,0103		-6,1721	-7,9130	13,5404	236,3710	9,9950E-10
44	2,4440	-3,3278	-1,5261	-4,9180		-6,6457	13,6724	224,3627	9,9950E-10
45	0,5217	-2,3055	0,0665	-2,2774	-5,4569		-7,1963	202,7801	9,9950E-10
46	1,4832	-2,8491	-1,1113	-6,9022	-8,0755	13,5476		233,0735	9,9950E-10

Figure 43. Subsets solutions $\hat{x}_q^{(k)}$ and $Chi2^{(k)}$ and $P_{pap\ subset,k}$. The largest values are indicated in red.

	$\sigma_q^{(k)}$			$b_q^{(k)}$			$\sigma_{ss,q}^{(k)}$		
k	σ_1	σ_2	σ_3	bias $_1$	bias $_2$	bias $_3$	σ_{ss_1}	σ_{ss_2}	σ_{ss_3}
0	0,6745	0,5861	1,1741	1,4670	1,2893	2,7593			
1	0,6745	0,5861	1,1741	1,4670	1,2893	2,7593	0,0000	0,0000	0,0000
2	0,9063	0,8953	1,7507	1,4334	1,3835	3,2598	0,4617	0,5211	1,0149
3	1,0377	0,7866	1,5002	1,7125	1,2754	2,5040	0,6103	0,4085	0,7125
4	0,6774	0,5873	1,2256	1,4215	1,2661	2,6547	0,0537	0,0314	0,3051
5	0,6745	0,5945	1,1948	1,4651	1,2400	2,6996	0,0029	0,0767	0,1711
6	0,6794	0,5941	1,2589	1,4583	1,2710	2,8371	0,0623	0,0744	0,3492
7	0,7561	0,5866	1,1760	1,5601	1,2776	2,7286	0,2655	0,0186	0,0522
8	0,6894	0,5964	1,2188	1,4698	1,2981	2,8833	0,1314	0,1015	0,3016
9	0,6859	0,6171	1,1838	1,4687	1,2991	2,6963	0,0967	0,1502	0,1180
10	0,7065	0,6012	1,1830	1,5294	1,2619	2,6904	0,1678	0,1070	0,1160
11	0,6837	0,6170	1,1779	1,4334	1,2906	2,7110	0,0870	0,1500	0,0740
12	0,6900	0,5903	1,2130	1,4718	1,2469	2,7413	0,1119	0,0543	0,2348
13	0,6896	0,6092	1,2294	1,4435	1,3239	2,8792	0,1259	0,1459	0,3208
14	0,6804	0,6812	1,3331	1,4442	1,5577	3,1031	0,0737	0,2867	0,5212
15	0,7738	0,6705	1,2222	1,5855	1,3734	2,7115	0,2846	0,2444	0,2549
16	0,8127	0,6239	1,1835	1,6889	1,3358	2,7383	0,3362	0,1585	0,1109
17	0,6745	0,5862	1,2464	1,4634	1,2860	2,6401	0,0032	0,0058	0,2967
18	0,7110	0,6279	1,2229	1,4606	1,2681	2,8019	0,1630	0,1632	0,2480
19	0,7249	0,6357	1,2085	1,5608	1,3498	2,7133	0,2000	0,1855	0,2158
20	0,6780	0,5927	1,2986	1,4514	1,2788	2,7383	0,0492	0,0634	0,3982
21	0,6754	0,5865	1,1931	1,4514	1,2858	2,7219	0,0312	0,0189	0,1936
22	0,6746	0,5861	1,1766	1,4634	1,2892	2,7368	0,0072	0,0002	0,0629
23	0,6760	0,5869	1,1967	1,4527	1,2813	2,7529	0,0358	0,0236	0,1854
24	0,6757	0,5865	1,1935	1,4493	1,2850	2,7041	0,0352	0,0181	0,1916
25	0,9063	0,8953	1,7507	1,4334	1,3835	3,2598	0,4617	0,5211	1,0149
26	1,0377	0,7866	1,5002	1,7125	1,2754	2,5040	0,6103	0,4085	0,7125
27	0,6774	0,5873	1,2256	1,4215	1,2661	2,6547	0,0537	0,0314	0,3051
28	129,9782	68,1527	110,3420	84,1716	64,4540	62,0094	119,4389	59,9018	101,5614
29	0,9071	0,8965	1,9152	1,3986	1,3463	3,1445	0,4635	0,5222	1,1486
30	1,0602	0,7932	1,6282	1,5823	1,1982	2,3533	0,6336	0,4175	0,8915
31	0,6745	0,5945	1,1948	1,4651	1,2400	2,6996	0,0029	0,0767	0,1711
32	1,0378	0,8040	1,5422	1,7045	1,1968	2,4515	0,6102	0,4316	0,7667
33	0,6774	0,5953	1,2502	1,4212	1,2203	2,5831	0,0537	0,0814	0,3584
34	0,6794	0,5941	1,2589	1,4583	1,2710	2,8371	0,0623	0,0744	0,3492
35	1,0444	0,8075	1,6871	1,6721	1,2104	2,6687	0,6162	0,4359	0,9523
36	0,6815	0,5959	1,3212	1,4121	1,2396	2,7324	0,0789	0,0835	0,4853
37	0,7561	0,5866	1,1760	1,5601	1,2776	2,7286	0,2655	0,0186	0,0522
38	1,4439	0,8005	1,5002	2,3005	1,2170	2,5024	1,0582	0,4342	0,7125
39	0,7603	0,5878	1,2266	1,5084	1,2526	2,6329	0,2724	0,0369	0,3081
40	0,6894	0,5964	1,2188	1,4698	1,2981	2,8833	0,1314	0,1015	0,3016
41	1,0870	0,8170	1,5826	1,7121	1,3146	2,6801	0,6647	0,4493	0,8395
42	0,6914	0,5971	1,2753	1,4234	1,2740	2,7810	0,1393	0,1047	0,4416
43	0,6859	0,6171	1,1838	1,4687	1,2991	2,6963	0,0967	0,1502	0,1180
44	1,0710	0,8546	1,5212	1,6899	1,2613	2,4020	0,6410	0,4941	0,7381
45	0,6886	0,6182	1,2351	1,4228	1,2755	2,5912	0,1108	0,1533	0,3267
46	0,7065	0,6012	1,1830	1,5294	1,2619	2,6904	0,1678	0,1070	0,1160

Figure 44. Sigma and bias for each subset $\sigma_q^{(k)}$, $b_q^{(k)}$, $\sigma_{ss,q}^{(k)}$. The largest values are indicated in red.

k	Test Thresholds T_1	T_2	T_3
0			
1	0,0000	0,0000	0,0000
2	2,8223	3,1854	5,4362
3	3,7304	2,4972	3,8167
4	0,3281	0,1916	1,6342
5	0,0175	0,4689	0,9163
6	0,3811	0,4545	1,8707
7	1,6228	0,1134	0,2794
8	0,8033	0,6202	1,6156
9	0,5911	0,9179	0,6322
10	1,0257	0,6538	0,6212
11	0,5317	0,9170	0,3965
12	0,6839	0,3317	1,2577
13	0,7698	0,8918	1,7182
14	0,4506	1,7523	2,7921
15	1,7397	1,4940	1,3655
16	2,0553	0,9690	0,5940
17	0,0193	0,0357	1,5891
18	0,9962	0,9975	1,3282
19	1,2227	1,1337	1,1558
20	0,3005	0,3874	2,1330
21	0,1904	0,1153	1,0369
22	0,0438	0,0012	0,3370
23	0,2187	0,1445	0,9933
24	0,2149	0,1106	1,0261
25	2,8223	3,1854	5,4362
26	3,7304	2,4972	3,8167
27	0,3281	0,1916	1,6342
28	730,1204	366,1747	544,0281
29	2,8332	3,1921	6,1529
30	3,8731	2,5521	4,7752
31	0,0175	0,4689	0,9163
32	3,7300	2,6386	4,1067
33	0,3281	0,4975	1,9199
34	0,3811	0,4545	1,8707
35	3,7669	2,6649	5,1014
36	0,4822	0,5102	2,5993
37	1,6228	0,1134	0,2794
38	6,4685	2,6542	3,8165
39	1,6654	0,2257	1,6503
40	0,8033	0,6202	1,6156
41	4,0635	2,7463	4,4966
42	0,8517	0,6399	2,3656
43	0,5911	0,9179	0,6322
44	3,9185	3,0204	3,9539
45	0,6772	0,9371	1,7498
46	1,0257	0,6538	0,6212

k	Allocation 1	2	3	sum
0	0,00E+00	0,00E+00	2,05E-28	2,05E-28
1	0,00E+00	0,00E+00	2,05E-28	2,05E-28
2	0,00E+00	0,00E+00	3,43E-05	3,43E-05
3	0,00E+00	0,00E+00	2,34E-10	2,34E-10
4	0,00E+00	0,00E+00	8,25E-21	8,25E-21
5	0,00E+00	0,00E+00	3,20E-24	3,20E-24
6	0,00E+00	0,00E+00	1,59E-18	1,59E-18
7	0,00E+00	0,00E+00	2,54E-27	2,54E-27
8	0,00E+00	0,00E+00	2,53E-20	2,53E-20
9	0,00E+00	0,00E+00	9,83E-26	9,83E-26
10	0,00E+00	0,00E+00	7,85E-26	7,85E-26
11	0,00E+00	0,00E+00	7,67E-27	7,67E-27
12	0,00E+00	0,00E+00	3,33E-22	3,33E-22
13	0,00E+00	0,00E+00	1,10E-19	1,10E-19
14	0,00E+00	0,00E+00	1,15E-13	1,15E-13
15	0,00E+00	0,00E+00	1,24E-21	1,24E-21
16	0,00E+00	0,00E+00	9,90E-26	9,90E-26
17	0,00E+00	0,00E+00	2,24E-20	2,24E-20
18	0,00E+00	0,00E+00	1,99E-21	1,99E-21
19	0,00E+00	0,00E+00	8,20E-23	8,20E-23
20	0,00E+00	0,00E+00	4,68E-17	4,68E-17
21	0,00E+00	0,00E+00	9,29E-24	9,29E-24
22	0,00E+00	0,00E+00	4,98E-27	4,98E-27
23	0,00E+00	0,00E+00	1,13E-23	1,13E-23
24	0,00E+00	0,00E+00	7,56E-24	7,56E-24
25	0,00E+00	0,00E+00	3,43E-05	3,43E-05
26	0,00E+00	0,00E+00	2,34E-10	2,34E-10
27	0,00E+00	0,00E+00	8,25E-21	8,25E-21
28	2,00E-02	2,00E-02	1,00E+00	**1,04E+00**
29	0,00E+00	0,00E+00	4,41E-04	4,41E-04
30	0,00E+00	0,00E+00	7,87E-08	7,87E-08
31	0,00E+00	0,00E+00	3,20E-24	3,20E-24
32	0,00E+00	0,00E+00	1,75E-09	1,75E-09
33	0,00E+00	0,00E+00	2,14E-19	2,14E-19
34	0,00E+00	0,00E+00	1,59E-18	1,59E-18
35	0,00E+00	0,00E+00	1,43E-06	1,43E-06
36	0,00E+00	0,00E+00	2,60E-15	2,60E-15
37	0,00E+00	0,00E+00	2,54E-27	2,54E-27
38	0,00E+00	0,00E+00	2,32E-10	2,32E-10
39	0,00E+00	0,00E+00	8,47E-21	8,47E-21
40	0,00E+00	0,00E+00	2,53E-20	2,53E-20
41	0,00E+00	0,00E+00	4,06E-08	4,06E-08
42	0,00E+00	0,00E+00	7,99E-17	7,99E-17
43	0,00E+00	0,00E+00	9,83E-26	9,83E-26
44	0,00E+00	0,00E+00	4,67E-10	4,67E-10
45	0,00E+00	0,00E+00	2,38E-20	2,38E-20
46	0,00E+00	0,00E+00	7,85E-26	7,85E-26

HPL	**1222,67**
VPL	**15,67**

Figure 45. Left hand table (in blue), Solution Separation threshold values for the three error components, for each subset. Tables at the middle (in orange and violet), Probabilities allocated for the different subsets when computing the Protection Levels. Right hand tables, Protection Levels. The largest values are indicated in red.

k	Alloctation (before) 1	2	3	sum	k
0	0,00E+00	0,00E+00	2,05E-28	2,05E-28	0
1	0,00E+00	0,00E+00	2,05E-28	2,05E-28	1
2	0,00E+00	0,00E+00	3,43E-05	3,43E-05	2
3	0,00E+00	0,00E+00	2,34E-10	2,34E-10	3
4	0,00E+00	0,00E+00	8,25E-21	8,25E-21	4
5	0,00E+00	0,00E+00	3,20E-24	3,20E-24	5
6	0,00E+00	0,00E+00	1,59E-18	1,59E-18	6
7	0,00E+00	0,00E+00	2,54E-27	2,54E-27	7
8	0,00E+00	0,00E+00	2,53E-20	2,53E-20	8
9	0,00E+00	0,00E+00	9,83E-26	9,83E-26	9
10	0,00E+00	0,00E+00	7,85E-26	7,85E-26	10
11	0,00E+00	0,00E+00	7,67E-27	7,67E-27	11
12	0,00E+00	0,00E+00	3,33E-22	3,33E-22	12
13	0,00E+00	0,00E+00	1,10E-19	1,10E-19	13
14	0,00E+00	0,00E+00	1,15E-13	1,15E-13	14
15	0,00E+00	0,00E+00	1,24E-21	1,24E-21	15
16	0,00E+00	0,00E+00	9,90E-26	9,90E-26	16
17	0,00E+00	0,00E+00	2,24E-20	2,24E-20	17
18	0,00E+00	0,00E+00	1,99E-21	1,99E-21	18
19	0,00E+00	0,00E+00	8,20E-23	8,20E-23	19
20	0,00E+00	0,00E+00	4,68E-17	4,68E-17	20
21	0,00E+00	0,00E+00	9,29E-24	9,29E-24	21
22	0,00E+00	0,00E+00	4,98E-27	4,98E-27	22
23	0,00E+00	0,00E+00	1,13E-23	1,13E-23	23
24	0,00E+00	0,00E+00	7,56E-24	7,56E-24	24
25	0,00E+00	0,00E+00	3,43E-05	3,43E-05	25
26	0,00E+00	0,00E+00	2,34E-10	2,34E-10	26
27	0,00E+00	0,00E+00	8,25E-21	8,25E-21	27
28	2,00E-02	2,00E-02	1,00E+00	**1,04E+00**	
29	0,00E+00	0,00E+00	0,000441	4,41E-04	28
30	0,00E+00	0,00E+00	7,87E-08	7,87E-08	29
31	0,00E+00	0,00E+00	3,2E-24	3,20E-24	30
32	0,00E+00	0,00E+00	1,75E-09	1,75E-09	31
33	0,00E+00	0,00E+00	2,14E-19	2,14E-19	32
34	0,00E+00	0,00E+00	1,59E-18	1,59E-18	33
35	0,00E+00	0,00E+00	1,43E-06	1,43E-06	34
36	0,00E+00	0,00E+00	2,60E-15	2,60E-15	35
37	0,00E+00	0,00E+00	2,54E-27	2,54E-27	36
38	0,00E+00	0,00E+00	2,32E-10	2,32E-10	37
39	0,00E+00	0,00E+00	8,47E-21	8,47E-21	38
40	0,00E+00	0,00E+00	2,53E-20	2,53E-20	39
41	0,00E+00	0,00E+00	4,06E-08	4,06E-08	40
42	0,00E+00	0,00E+00	7,99E-17	7,99E-17	41
43	0,00E+00	0,00E+00	9,83E-26	9,83E-26	42
44	0,00E+00	0,00E+00	4,67E-10	4,67E-10	43
45	0,00E+00	0,00E+00	2,38E-20	2,38E-20	44
46	0,00E+00	0,00E+00	7,85E-26	7,85E-26	45
			TOTAL=	**1,04E+00**	
			HPL	**1222,67**	
			VPL	**15,67**	

k	Alloctation (after) 1	2	3	sum	k
0	3,96E-43	1,70E-38	9,07E-27	9,07E-27	0
1	3,96E-43	1,70E-38	9,07E-27	9,07E-27	1
2	4,86E-13	8,01E-07	8,81E-05	8,89E-05	2
3	1,82E-07	4,80E-11	1,26E-09	1,83E-07	3
4	2,48E-40	9,34E-37	1,76E-19	1,76E-19	4
5	5,46E-43	1,18E-33	9,69E-23	9,69E-23	5
6	2,38E-39	1,48E-33	2,60E-17	2,60E-17	6
7	1,03E-23	1,83E-37	1,03E-25	1,04E-23	7
8	8,07E-35	1,21E-31	5,26E-19	5,26E-19	8
9	7,47E-37	2,35E-27	3,45E-24	3,45E-24	9
10	3,37E-31	3,46E-31	2,78E-24	2,78E-24	10
11	7,66E-38	1,98E-27	2,98E-25	3,00E-25	11
12	1,11E-35	2,77E-35	8,21E-21	8,21E-21	12
13	2,86E-35	5,00E-28	2,11E-18	2,11E-18	13
14	8,94E-39	1,78E-16	1,07E-12	1,07E-12	14
15	6,03E-22	1,90E-19	2,86E-20	2,19E-19	15
16	4,54E-18	3,77E-26	3,48E-24	4,54E-18	16
17	5,48E-43	3,54E-38	4,39E-19	4,39E-19	17
18	1,59E-31	3,96E-26	4,48E-20	4,48E-20	18
19	3,34E-28	5,30E-24	2,14E-21	2,15E-21	19
20	3,03E-40	3,17E-34	6,22E-16	6,22E-16	20
21	1,72E-41	2,20E-37	2,73E-22	2,73E-22	21
22	9,13E-43	1,74E-38	1,97E-25	1,97E-25	22
23	3,66E-41	4,19E-37	3,27E-22	3,27E-22	23
24	2,91E-41	1,95E-37	2,23E-22	2,23E-22	24
25	4,86E-13	8,01E-07	8,81E-05	8,89E-05	25
26	1,82E-07	4,80E-11	1,26E-09	1,83E-07	26
27	2,48E-40	9,34E-37	1,76E-19	1,76E-19	27
28	4,21E-13	6,97E-07	9,20E-04	1,40E-02	28
29	3,39E-07	5,69E-11	2,93E-07	1,40E-02	29
30	5,46E-43	1,18E-33	9,69E-23	2,48E-03	30
31	1,74E-07	1,99E-10	8,33E-09	2,86E-04	31
32	2,46E-40	1,70E-33	3,83E-18	3,39E-06	32
33	2,38E-39	1,48E-33	2,60E-17	3,78E-17	33
34	2,11E-07	3,24E-10	4,48E-06	5,14E-24	34
35	1,17E-38	3,78E-33	2,85E-14	1,31E-05	35
36	1,03E-23	1,83E-37	1,03E-25	1,42E-15	36
37	8,79E-02	2,22E-10	1,25E-09	1,72E-17	37
38	1,59E-23	1,69E-36	1,80E-19	1,79E-03	38
39	8,07E-35	1,21E-31	5,26E-19	1,18E-11	39
40	2,67E-06	2,06E-09	1,62E-07	2,01E-26	40
41	1,30E-34	1,31E-31	1,09E-15	4,27E-06	41
42	7,47E-37	2,35E-27	3,45E-24	5,91E-17	42
43	8,99E-07	4,10E-08	2,40E-09	8,21E-21	43
44	2,98E-36	2,70E-27	4,77E-19	1,08E-04	44
45	3,37E-31	3,46E-31	2,78E-24	6,05E-14	45
			TOTAL=	**3,29E-02**	
			HPL	**13,94**	
			VPL	**15,26**	

Figure 46. Allocated probabilities when computing the protection levels, before (left hand) and after (right hand) excluding double counted modes. The protection level values are also given at the bottom. The excluded mode is indicated in red.

	Solution Separation test									
k	$\lvert \hat{x}_1^{(k)} - \hat{x}_1^{(0)} \rvert$	$T_{k,1}$	*Difference*	$\lvert \hat{x}_2^{(k)} - \hat{x}_2^{(0)} \rvert$	$T_{k,2}$	*Difference*	$\lvert \hat{x}_3^{(k)} - \hat{x}_3^{(0)} \rvert$	$T_{k,3}$	*Difference*	k
0										0
1	0,0000	0,0000	0,0000	0,0000	0,0000	0,0000	0,0000	0,0000	0,0000	1
2	1,1124	2,8207	1,7083	2,0233	3,1836	1,1603	1,6483	5,4322	3,7839	2
3	1,6527	3,7283	2,0756	1,0207	2,4958	1,4750	0,6269	3,8139	3,1870	3
4	0,2162	0,3279	0,1117	0,1295	0,1915	0,0620	1,0768	1,6330	0,5562	4
5	0,0150	0,0175	0,0026	0,3999	0,4687	0,0687	0,8918	0,9156	0,0238	5
6	0,1816	0,3809	0,1992	0,2167	0,4543	0,2376	1,0176	1,8693	0,8517	6
7	1,2808	1,6218	0,3411	0,0895	0,1133	0,0238	0,2517	0,2792	0,0275	7
8	0,0554	0,8028	0,7474	0,0428	0,6198	0,5770	0,1272	1,6144	1,4872	8
9	0,2174	0,5908	0,3734	0,3375	0,9174	0,5799	0,2653	0,6318	0,3665	9
10	0,5299	1,0251	0,4952	0,3378	0,6535	0,3157	0,3663	0,6208	0,2545	10
11	1,5502	0,5314	**-1,0188**	2,6738	0,9165	**-1,7573**	1,3194	0,3962	**-0,9231**	**11**
12	0,0623	0,6835	0,6212	0,0302	0,3315	0,3012	0,1308	1,2567	1,1259	12
13	0,0050	0,7693	0,7643	0,0058	0,8913	0,8855	0,0128	1,7169	1,7040	13
14	0,4895	0,4504	**-0,0392**	1,9036	1,7513	-0,1524	3,4615	2,7900	**-0,6715**	**14**
15	0,0223	1,7387	1,7163	0,0192	1,4932	1,4740	0,0200	1,3645	1,3444	15
16	0,0575	2,0542	1,9966	0,0271	0,9685	0,9414	0,0190	0,5935	0,5746	16
17	0,0031	0,0193	0,0162	0,0057	0,0357	0,0300	0,2897	1,5880	1,2983	17
18	0,4602	0,9957	0,5355	0,4608	0,9969	0,5361	0,7002	1,3272	0,6271	18
19	0,8238	1,2220	0,3982	0,7639	1,1331	0,3692	0,8887	1,1550	0,2663	19
20	0,0081	0,3004	0,2923	0,0104	0,3872	0,3768	0,0654	2,1314	2,0660	20
21	0,0614	0,1903	0,1290	0,0372	0,1153	0,0781	0,3813	1,0361	0,6548	21
22	0,0166	0,0438	0,0271	0,0004	0,0012	0,0007	0,1462	0,3368	0,1905	22
23	0,1863	0,2186	0,0323	0,1231	0,1444	0,0213	0,9655	0,9925	0,0270	23
24	0,1818	0,2148	0,0330	0,0936	0,1106	0,0170	0,9906	1,0253	0,0347	24
25	1,1124	2,8207	1,7083	2,0233	3,1836	1,1603	1,6483	5,4322	3,7839	25
26	1,6527	3,7283	2,0756	1,0207	2,4958	1,4750	0,6269	3,8139	3,1870	26
27	0,2162	0,3279	0,1117	0,1295	0,1915	0,0620	1,0768	1,6330	0,5562	27
28	1,2758	2,8316	1,5558	1,8499	3,1903	1,3404	0,7683	6,1483	5,3800	28
29	1,0212	3,8709	2,8497	1,3253	2,5506	1,2253	1,0345	4,7717	3,7372	29
30	0,0150	0,0175	0,0026	0,3999	0,4687	0,0687	0,8918	0,9156	0,0238	30
31	1,7141	3,7279	2,0138	1,8310	2,6370	0,8061	2,3664	4,1037	1,7373	31
32	0,2143	0,3279	0,1136	0,5018	0,4972	**-0,0045**	0,1340	1,9185	1,7845	**32**
33	0,1816	0,3809	0,1992	0,2167	0,4543	0,2376	1,0176	1,8693	0,8517	33
34	1,3945	3,7647	2,3702	0,6216	2,6633	2,0417	2,3141	5,0976	2,7835	34
35	0,3614	0,4819	0,1206	0,0657	0,5099	0,4442	0,1227	2,5974	2,4746	35
36	1,2808	1,6218	0,3411	0,0895	0,1133	0,0238	0,2517	0,2792	0,0275	36
37	7,9667	6,4648	**-1,5019**	0,0880	2,6526	2,5647	0,6505	3,8137	3,1632	**37**
38	1,0194	1,6645	0,6451	0,0374	0,2255	0,1882	1,2532	1,6490	0,3959	38
39	0,0554	0,8028	0,7474	0,0428	0,6198	0,5770	0,1272	1,6144	1,4872	39
40	1,6894	4,0612	2,3718	0,9957	2,7448	1,7491	0,5697	4,4933	3,9236	40
41	0,1346	0,8512	0,7166	0,0661	0,6395	0,5735	1,2843	2,3638	1,0795	41
42	0,2174	0,5908	0,3734	0,3375	0,9174	0,5799	0,2653	0,6318	0,3665	42
43	1,4907	3,9162	2,4255	0,8165	3,0187	2,2021	0,7811	3,9510	3,1699	43
44	0,4316	0,6768	0,2452	0,2058	0,9365	0,7308	0,8115	1,7485	0,9370	44
45	0,5299	1,0251	0,4952	0,3378	0,6535	0,3157	0,3663	0,6208	0,2545	45

Figure 47. Solution Separation test results for the three error components ($q = 1,2,3$). The FAIL tests are indicated in red.

k	$Chi2^{(k)}$	$T_{\chi^2}^{(k)}$	Difference	$P_{ap\ subset,k}$
0	239,43174	66,00933	-173,4224	9,9939E-01
1	239,43174	66,00933	-173,4224	1,0994E-04
2	34,08129	45,19332	**11,1120**	9,9954E-05
3	224,73652	55,36229	-169,3742	9,9949E-05
4	205,79618	59,77465	-146,0215	9,9949E-05
5	223,26206	63,97265	-159,2894	9,9940E-06
6	234,41446	63,97265	-170,4418	9,9940E-06
7	225,3742	63,97265	-161,4016	9,9940E-06
8	239,28055	63,97265	-175,3079	9,9940E-06
9	236,37101	63,97265	-172,3984	9,9940E-06
10	233,0735	63,97265	-169,1009	9,9940E-06
11	47,16228	63,97265	**16,8104**	9,9940E-06
12	239,24759	63,97265	-175,2749	9,9940E-06
13	239,4305	63,97265	-175,4579	9,9940E-06
14	209,37363	63,97265	-145,4010	9,9940E-06
15	239,42827	63,97265	-175,4556	9,9940E-06
16	239,41562	63,97265	-175,4430	9,9940E-06
17	238,95273	63,97265	-174,9801	9,9940E-06
18	235,24489	63,97265	-171,2722	9,9940E-06
19	229,80395	63,97265	-165,8313	9,9940E-06
20	239,41787	63,97265	-175,4452	9,9940E-06
21	236,20641	63,97265	-172,2338	9,9940E-06
22	235,92082	63,97265	-171,9482	9,9940E-06
23	222,08775	63,97265	-158,1151	9,9940E-06
24	218,13683	63,97265	-154,1642	9,9940E-06
25	34,08129	45,19332	**11,1120**	1,0995E-08
26	224,73652	55,36229	-169,3742	1,0995E-08
27	205,79618	59,77465	-146,0215	1,0995E-08
28	0,07877	36,84136	**36,7626**	9,9959E-09
29	193,72973	48,04043	-145,6893	9,9959E-09
30	223,26206	63,97265	-159,2894	9,9950E-10
31	201,06374	53,04496	-148,0188	9,9950E-10
32	191,14873	57,60017	-133,5486	9,9950E-10
33	234,41446	63,97265	-170,4418	9,9950E-10
34	219,95777	53,04496	-166,9128	9,9950E-10
35	202,05723	57,60017	-144,4571	9,9950E-10
36	225,3742	63,97265	-161,4016	9,9950E-10
37	185,18455	53,04496	-132,1396	9,9950E-10
38	192,98672	57,60017	-135,3866	9,9950E-10
39	239,28055	63,97265	-175,3079	9,9950E-10
40	224,72365	53,04496	-171,6787	9,9950E-10
41	205,44944	57,60017	-147,8493	9,9950E-10
42	236,37101	63,97265	-172,3984	9,9950E-10
43	224,36266	53,04496	-171,3177	9,9950E-10
44	202,78007	57,60017	-145,1799	9,9950E-10
45	233,0735	63,97265	-169,1009	9,9950E-10

k	Satellites																								
	R	G										E						C							
0	1	1	1	1	1	1	1	1	1	1	1	1	1	1	1	1	1	1	1	1	1	1	1	1	1
1	0	1	1	1	1	1	1	1	1	1	1	1	1	1	1	1	1	1	1	1	1	1	1	1	1
2	1	0	0	0	0	0	0	0	0	0	0	1	1	1	1	1	1	1	1	1	1	1	1	1	1
3	1	1	1	1	1	1	1	1	1	1	1	0	0	0	0	0	0	1	1	1	1	1	1	1	1
4	1	1	1	1	1	1	1	1	1	1	1	1	1	1	1	1	1	0	0	0	0	1	1	1	1
5	1	0	1	1	1	1	1	1	1	1	1	1	1	1	1	1	1	1	1	1	1	1	1	1	1
6	1	1	0	1	1	1	1	1	1	1	1	1	1	1	1	1	1	1	1	1	1	1	1	1	1
7	1	1	1	0	1	1	1	1	1	1	1	1	1	1	1	1	1	1	1	1	1	1	1	1	1
8	1	1	1	1	0	1	1	1	1	1	1	1	1	1	1	1	1	1	1	1	1	1	1	1	1
9	1	1	1	1	1	0	1	1	1	1	1	1	1	1	1	1	1	1	1	1	1	1	1	1	1
10	1	1	1	1	1	1	0	1	1	1	1	1	1	1	1	1	1	1	1	1	1	1	1	1	1
11	1	1	1	1	1	1	1	0	1	1	1	1	1	1	1	1	1	1	1	1	1	1	1	1	1
12	1	1	1	1	1	1	1	1	0	1	1	1	1	1	1	1	1	1	1	1	1	1	1	1	1
13	1	1	1	1	1	1	1	1	1	0	1	1	1	1	1	1	1	1	1	1	1	1	1	1	1
14	1	1	1	1	1	1	1	1	1	1	0	1	1	1	1	1	1	1	1	1	1	1	1	1	1
15	1	1	1	1	1	1	1	1	1	1	1	0	1	1	1	1	1	1	1	1	1	1	1	1	1
16	1	1	1	1	1	1	1	1	1	1	1	1	0	1	1	1	1	1	1	1	1	1	1	1	1
17	1	1	1	1	1	1	1	1	1	1	1	1	1	0	1	1	1	1	1	1	1	1	1	1	1
18	1	1	1	1	1	1	1	1	1	1	1	1	1	1	0	1	1	1	1	1	1	1	1	1	1
19	1	1	1	1	1	1	1	1	1	1	1	1	1	1	1	0	1	1	1	1	1	1	1	1	1
20	1	1	1	1	1	1	1	1	1	1	1	1	1	1	1	1	0	1	1	1	1	1	1	1	1
21	1	1	1	1	1	1	1	1	1	1	1	1	1	1	1	1	1	0	1	1	1	1	1	1	1
22	1	1	1	1	1	1	1	1	1	1	1	1	1	1	1	1	1	1	0	1	1	1	1	1	1
23	1	1	1	1	1	1	1	1	1	1	1	1	1	1	1	1	1	1	1	0	1	1	1	1	1
24	1	1	1	1	1	1	1	1	1	1	1	1	1	1	1	1	1	1	1	1	0	1	1	1	1
25	0	0	0	0	0	0	0	0	0	0	0	1	1	1	1	1	1	1	1	1	1	1	1	1	1
26	0	1	1	1	1	1	1	1	1	1	1	0	0	0	0	0	0	1	1	1	1	1	1	1	1
27	0	1	1	1	1	1	1	1	1	1	1	1	1	1	1	1	1	0	0	0	0	1	1	1	1
28	1	0	0	0	0	0	0	0	0	0	0	1	1	1	1	1	1	0	0	0	0	1	1	1	1
29	1	1	1	1	1	1	1	1	1	1	1	0	0	0	0	0	0	0	0	0	0	1	1	1	1
30	0	0	1	1	1	1	1	1	1	1	1	1	1	1	1	1	1	1	1	1	1	1	1	1	1
31	1	0	1	1	1	1	1	1	1	1	1	0	0	0	0	0	0	1	1	1	1	1	1	1	1
32	1	0	1	1	1	1	1	1	1	1	1	1	1	1	1	1	1	0	0	0	0	1	1	1	1
33	0	1	0	1	1	1	1	1	1	1	1	1	1	1	1	1	1	1	1	1	1	1	1	1	1
34	1	1	0	1	1	1	1	1	1	1	1	0	0	0	0	0	0	1	1	1	1	1	1	1	1
35	1	1	0	1	1	1	1	1	1	1	1	1	1	1	1	1	1	0	0	0	0	1	1	1	1
36	0	1	1	0	1	1	1	1	1	1	1	1	1	1	1	1	1	1	1	1	1	1	1	1	1
37	1	1	1	0	1	1	1	1	1	1	1	0	0	0	0	0	0	1	1	1	1	1	1	1	1
38	1	1	1	0	1	1	1	1	1	1	1	1	1	1	1	1	1	0	0	0	0	1	1	1	1
39	0	1	1	1	0	1	1	1	1	1	1	1	1	1	1	1	1	1	1	1	1	1	1	1	1
40	1	1	1	1	0	1	1	1	1	1	1	0	0	0	0	0	0	1	1	1	1	1	1	1	1
41	1	1	1	1	0	1	1	1	1	1	1	1	1	1	1	1	1	0	0	0	0	1	1	1	1
42	0	1	1	1	1	0	1	1	1	1	1	1	1	1	1	1	1	1	1	1	1	1	1	1	1
43	1	1	1	1	1	0	1	1	1	1	1	0	0	0	0	0	0	1	1	1	1	1	1	1	1
44	1	1	1	1	1	0	1	1	1	1	1	1	1	1	1	1	1	0	0	0	0	1	1	1	1
45	0	1	1	1	1	1	0	1	1	1	1	1	1	1	1	1	1	1	1	1	1	1	1	1	1

Figure 48. Chi2 Test results with indication of the associated subsets and probabilities.

$$P_{not\ monitored} = 0.89980\text{E-}07.$$

Comment:

As indicated in section 3.2.2.9, the projection matrix has to be adjusted when next conditions are check:

$$\begin{cases} \sigma_{acc,Vert} < \sigma_{acc_{max},Vert} \\ and \\ (EMT > EMT_{TOL})\ or\ (HPL > HAL_{TOL})\ or\ (VPL > VAL_{TOL}) \end{cases}$$

As the driving example presents

$$\sigma_{acc,V} = 0.935 < \sigma_{acc_{max},V} = 1.87\ m$$
$$EMT = 5.432 < EMT_{TOL} = 15\ m$$
$$HPL = 13.937 < HAL = 40\ m$$
$$VPL = 15.2589 < VAL = 35\ m$$

Thence, the Projection matrix has not to be adjusted.

Fault exclusion:

The selected candidates for Fault Exclusion are the subsets that PASS the Chi2 test.

The candidate subsets are explored, starting *with the subsets with larger size* (i.e. number of satellites), and for each size, the search starts with the subset with smaller $Chi2^{(k)} < T_{\chi^2}^{(k)}$, and increasing value of Chi2. The search ends when having the first valid subset.

This example presents 4 candidate subsets, all of them with different sizes (number of satellites). Then, the search will start with the combination "11", that contains 20 satellites.

The value $\rho_j = \frac{1}{N_{excl}+1}$ with $N_{excl} = 4$ will be used when computing the Protection Levels.

						Satellites																
k	$Chi2^{(k)}$	$T_{\chi^2}^{(k)}$	**Difference**	***k***	R	G									E					C				N. sat
11	47,16228	63,97265	**16,8104**	11	**1**	**1**	**1**	**1**	**1**	**1**	**1**	**0**	**1**	**1**	**1**	**1**	**1**	**1**	**1**	**1**	**1**	**1**	**1**	**20**
2	34,08129	45,19332	**11,1120**	2	1	0	0	0	0	0	0	**0**	0	0	0	1	1	1	1	1	1	1	1	1	11
25	34,08129	45,19332	**11,1120**	25	0	0	0	0	0	0	0	**0**	0	0	0	1	1	1	1	1	1	1	1	1	10
28	0,07877	36,84136	**36,7626**	28	1	0	0	0	0	0	0	**0**	0	0	0	1	1	1	1	1	1	0	0	0	7

Figure 49. Candidate subsets for Fault-Exclusion. The zero, in red, indicates the exclusion of the GPS satellite PRN21, to which an error of 16 meters had been added to simulate a fault.

Output:

The candidate subsets for Fault Exclusion and the parameter $\rho_j = \frac{1}{5}$

ANNEX F: Analysis of the observed Galileo faults

The orbit and clock events given in Table 6 are depicted in this section from the Space Approach detection plots and Ground Approach verification plots for each particular event. When available, the Space Approach results are computed with both GAGE and CNES consolidated files to crosschecked results.

F.1 Event of 07/03/2017 (Doy 066) on Galileo Satellite E206

The Space Approach detection plots and Ground Approach verification plots for this event are shown next.

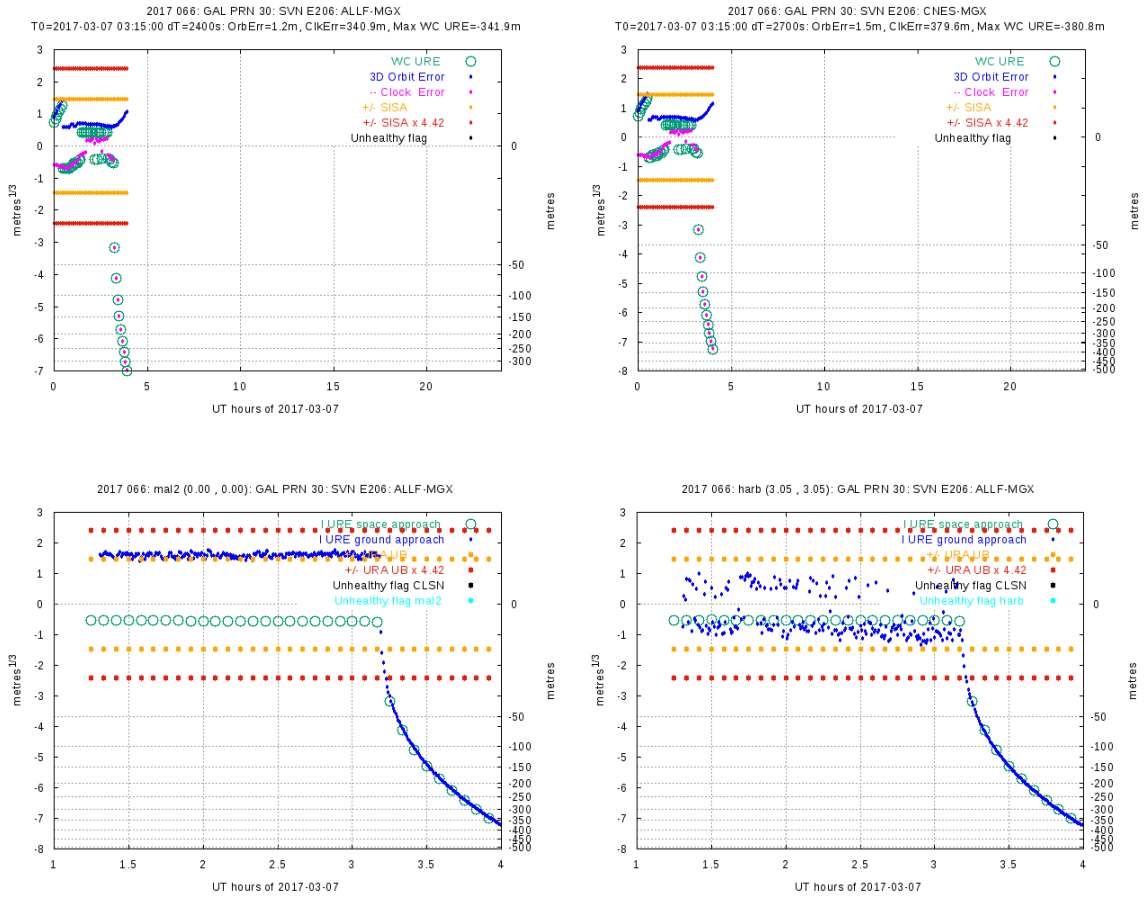

Figure 50. Top row shows the Anomaly Detection plots computed using the gAGE (left hand plot) and CNES (right hand plot) RINEX cleansed files. Bottom row shows Anomaly Verification plots for two different stations (the station name and coordinates are given in the title of each plot).

F.2 Events on 14/05/2017 (Doy 134)

Several satellites experienced events on this day. Similar results are found with the gAGE and CNES cleansed RINEX navigation files. The anomaly detections from the Space Approach are confirmed by the Ground Approach verification.

The Space Approach detection plots and Ground Approach verification plots for each detected event are shown next.

Satellite E101

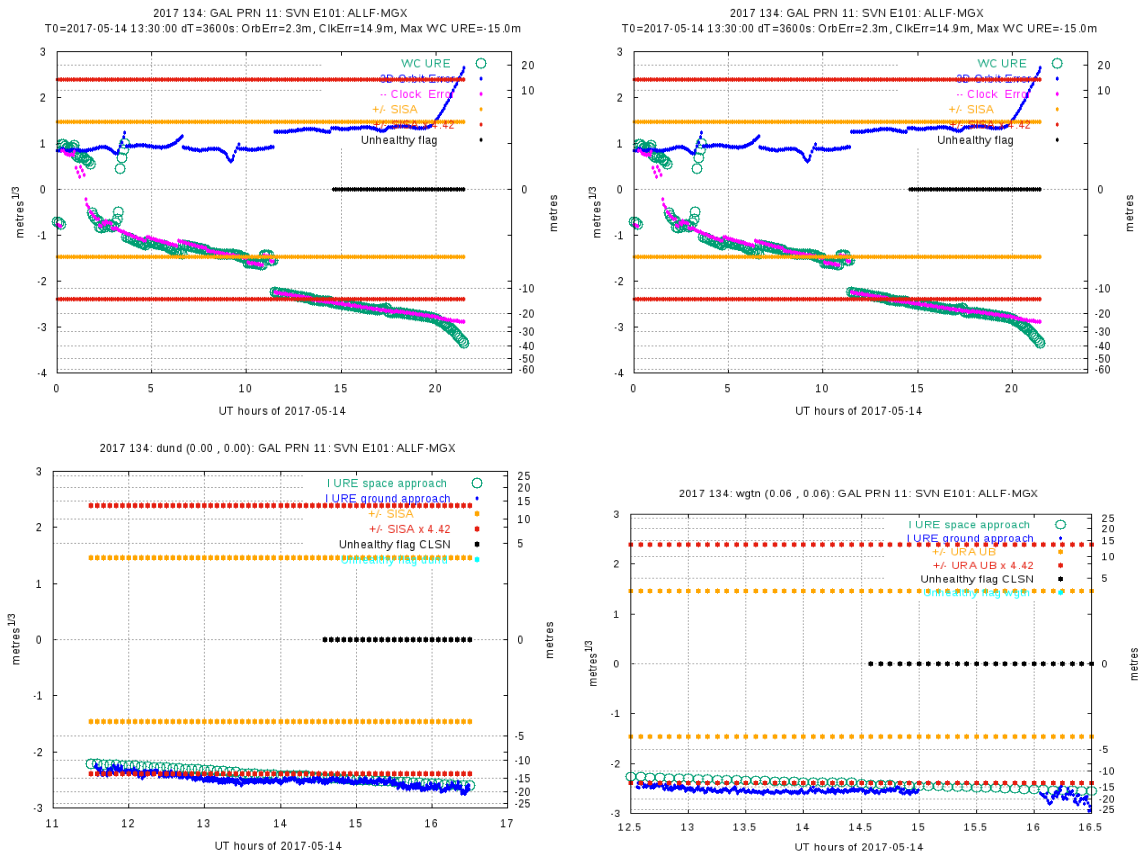

Figure 51. The same plots as in Figure 50.

Satellite E102

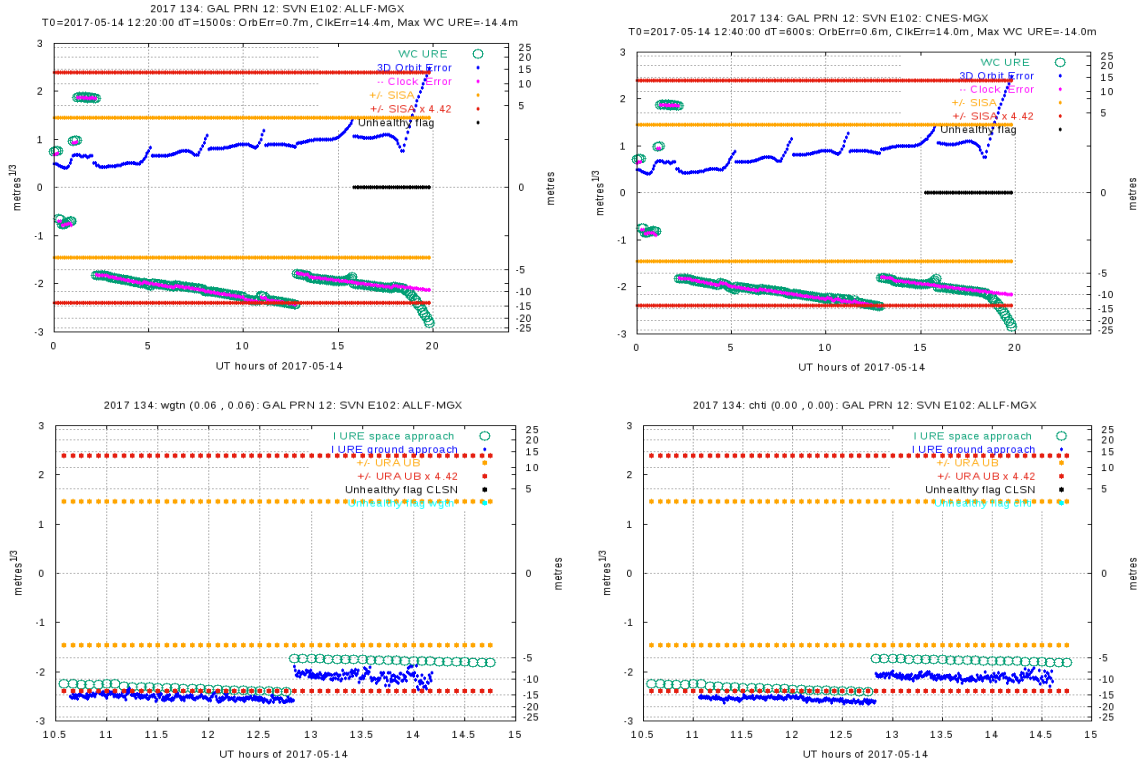

Figure 52. The same plots as in Figure 50.

Satellite E205

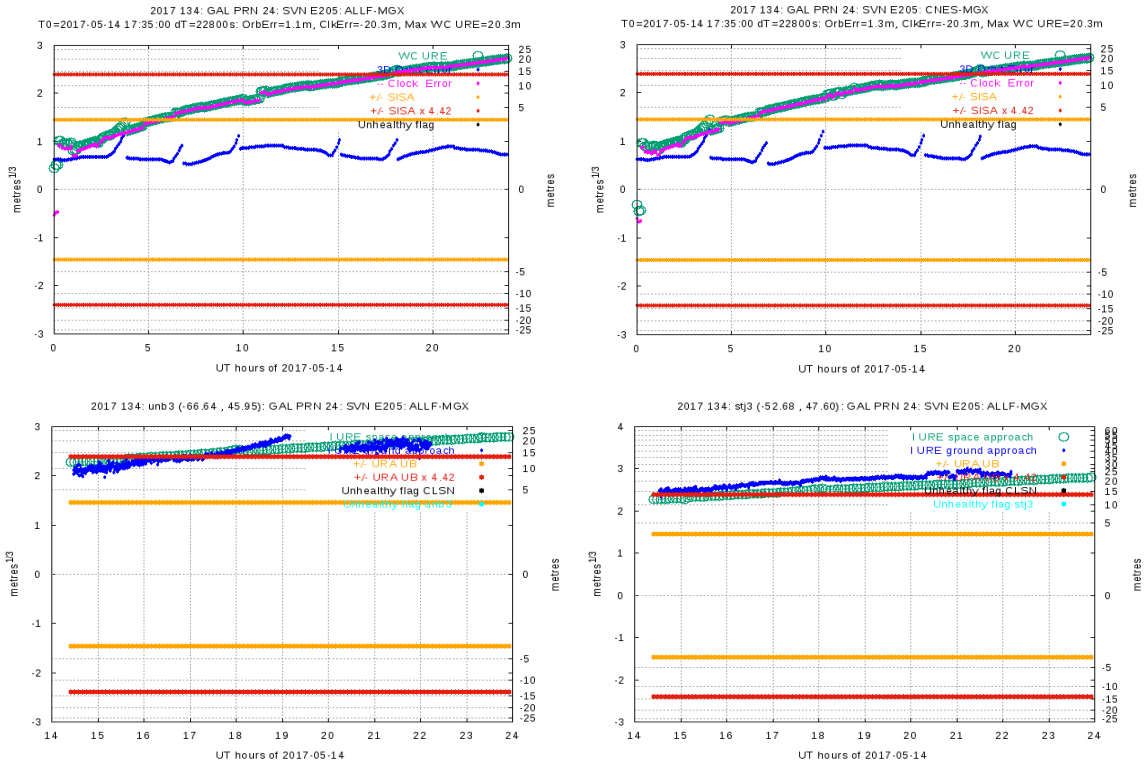

Figure 53. The same plots as in Figure 50.

Satellite E206

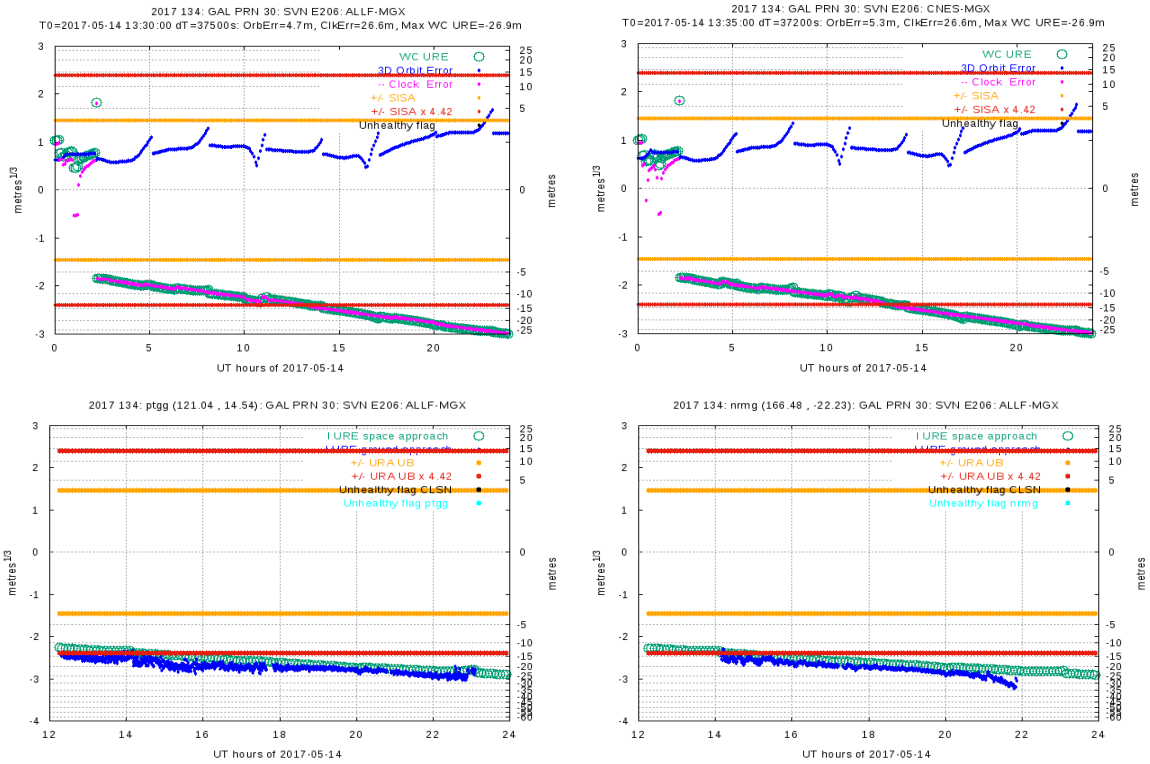

Figure 54. The same plots as in Figure 50.

Satellite E208

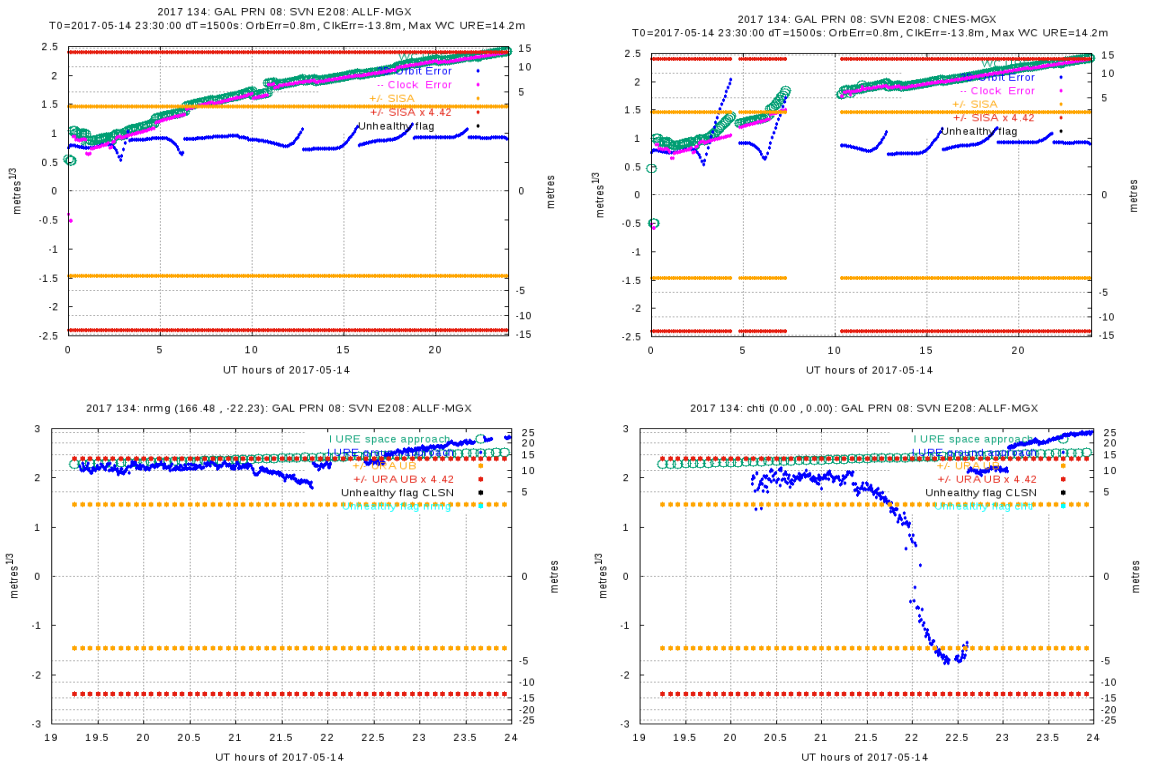

Figure 55. The same plots as in Figure 50.

Satellite E211

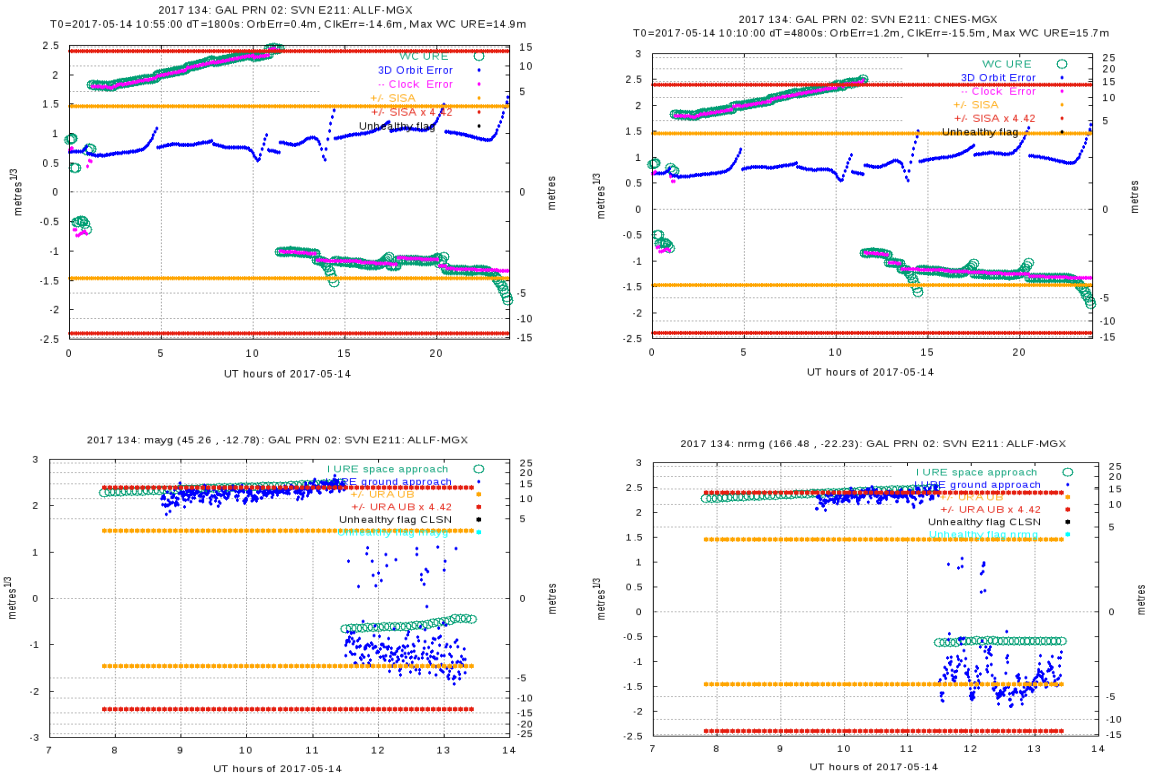

Figure 56. The same plots as in Figure 50.

F.3 Events on 15/05/2017 (Doy 135)

Several satellites experienced events on this day. Similar results are found with the gAGE and CNES cleansed RINEX navigation files. The anomaly detections from the Space Approach are confirmed by the Ground Approach verification.

The Space Approach detection plots and Ground Approach verification plots for each detected event are shown next.

Satellite E205

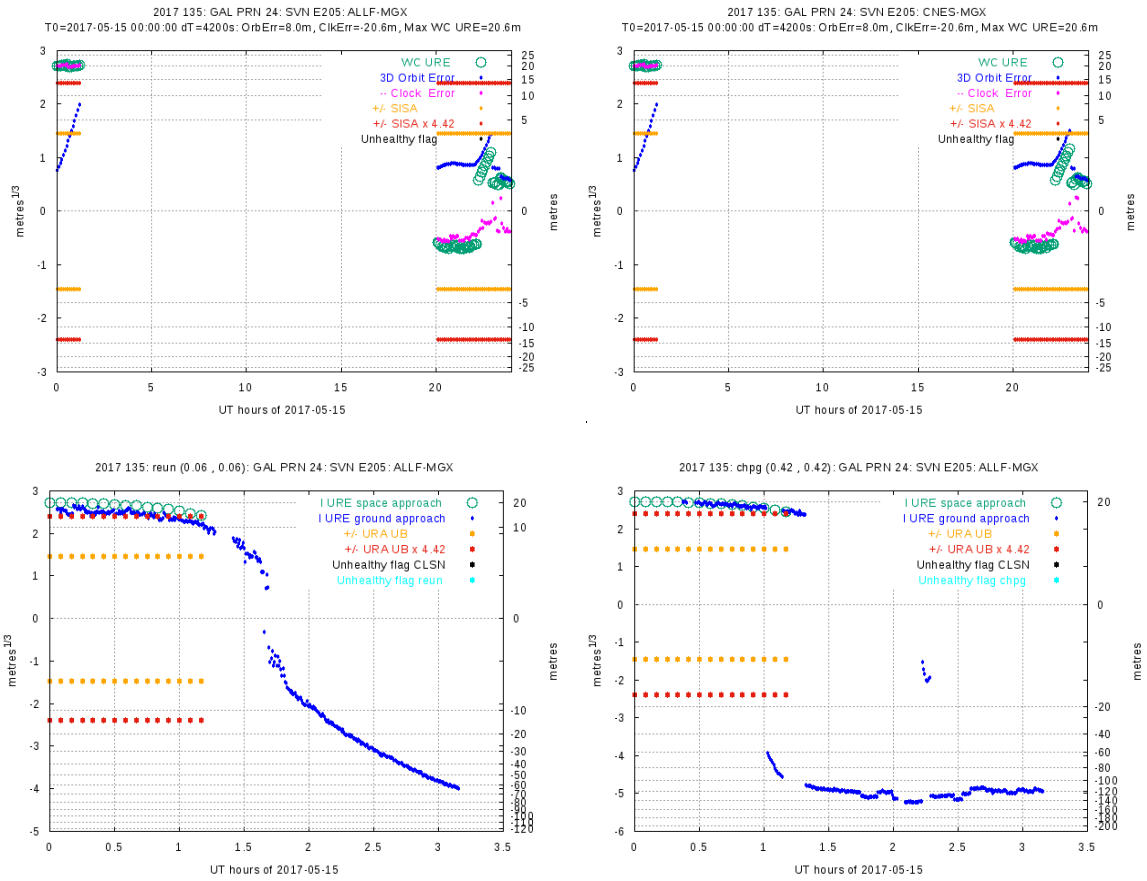

Figure 57. The same plots as in Figure 50.

Satellite E206

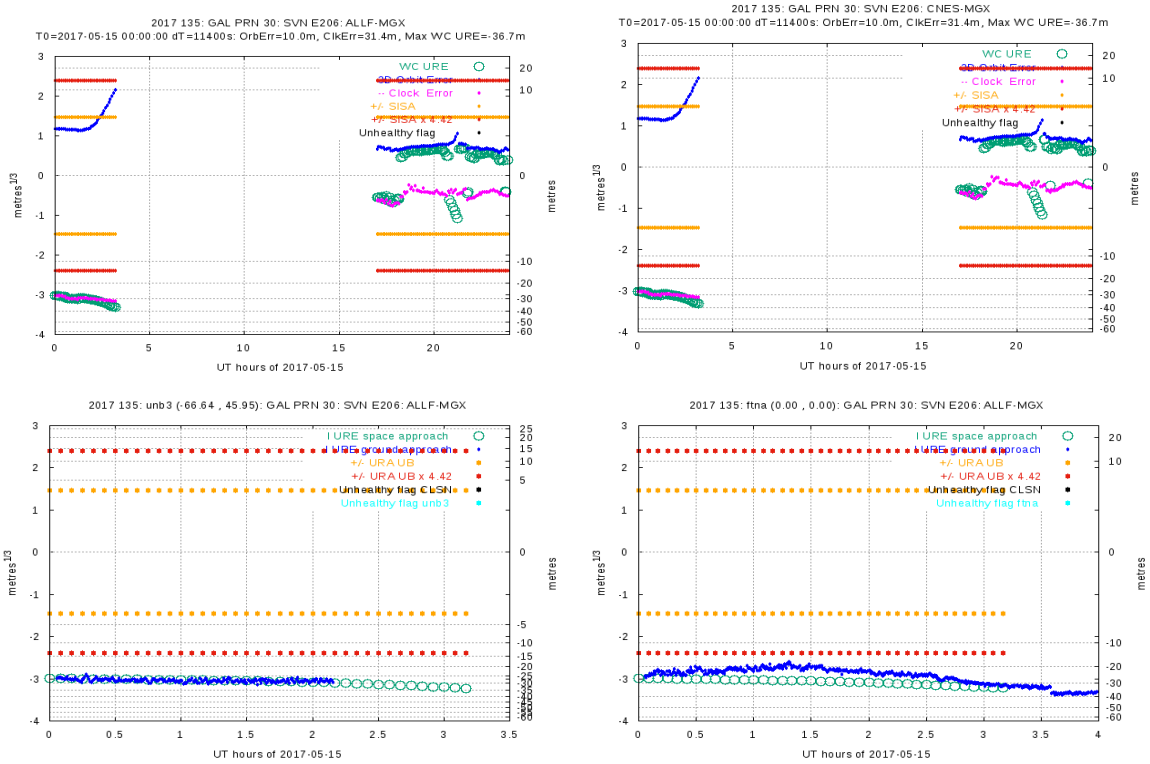

Figure 58. The same plots as in Figure 50.

Satellite E208

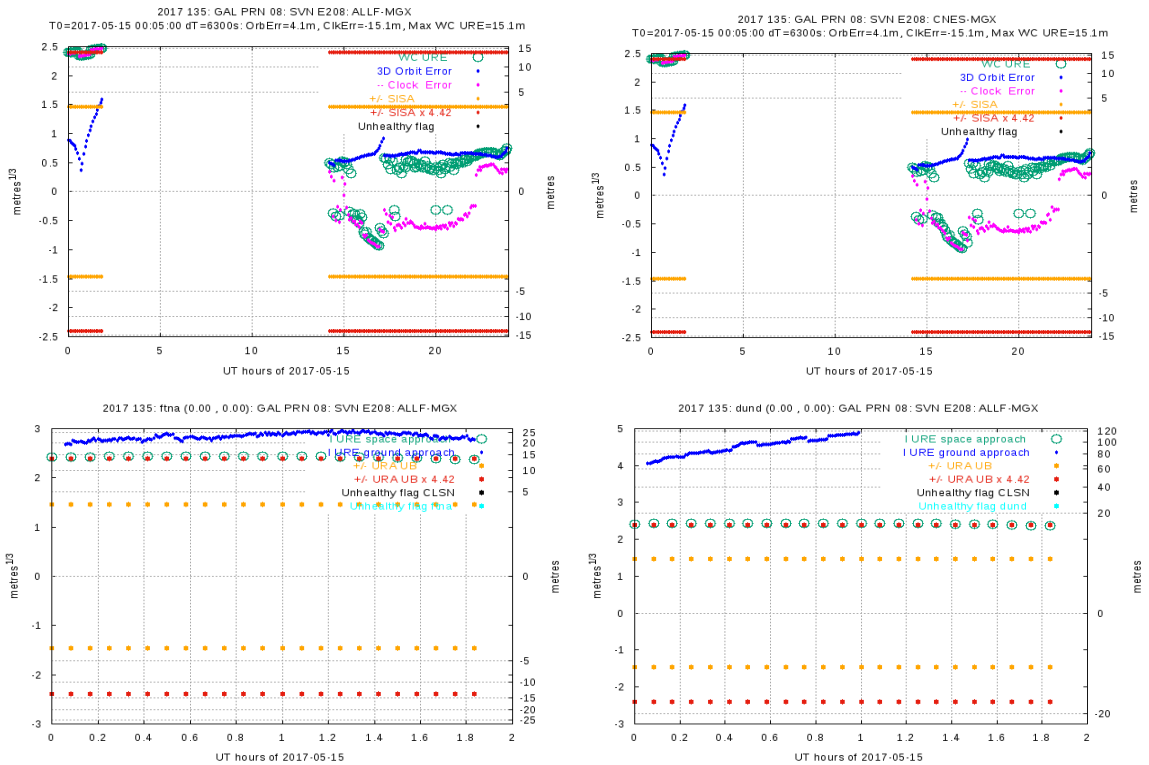

Figure 59. The same plots as in Figure 50.

F.4 Event of 06/06/2017 (Doy 157) on Galileo Satellite E203

Similar results are found with the gAGE and CNES cleansed RINEX navigation files. The Space Approach detection plots and Ground Approach verification plots for this event are shown next.

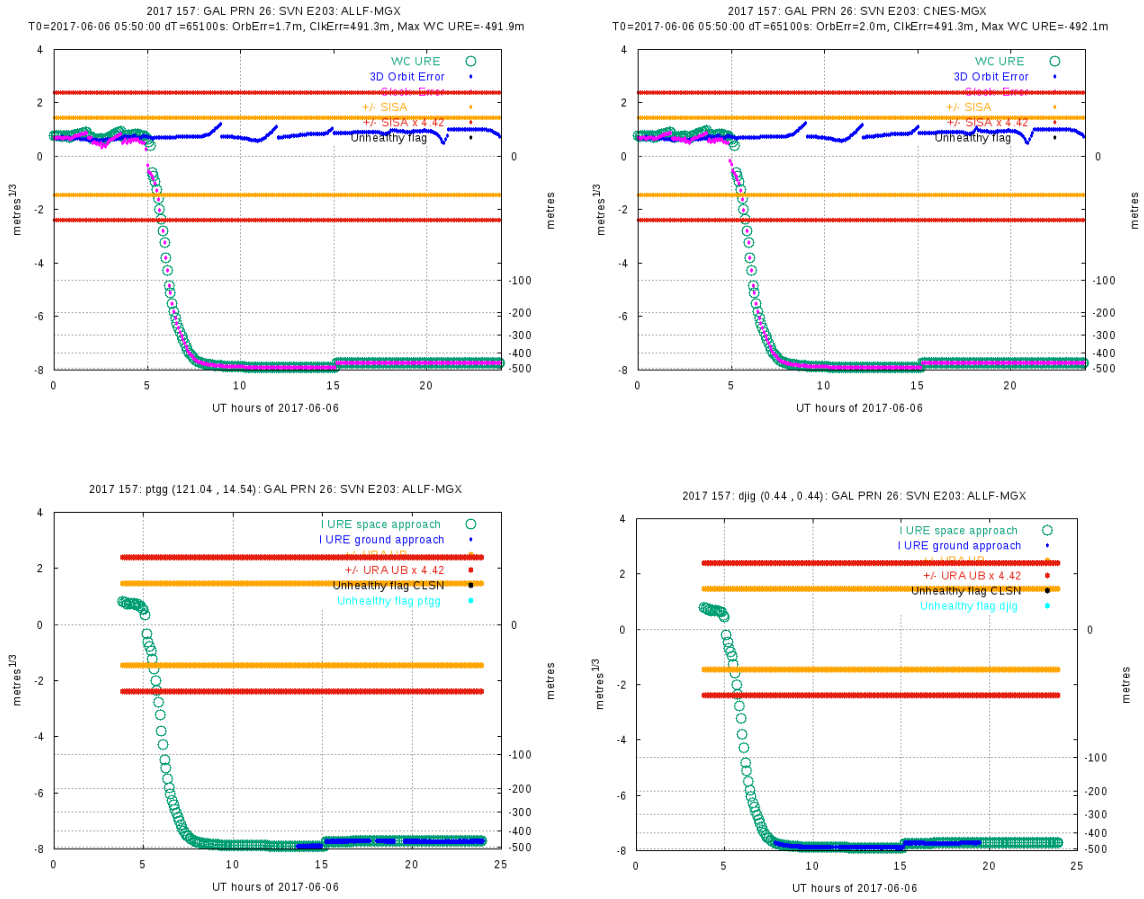

Figure 60. The same plots as in Figure 50.

F.5 Event of 07/06/2017 (Doy 158) on Galileo Satellite E203

Similar results are found with the gAGE and CNES cleansed RINEX navigation files. The Space Approach detection plots and Ground Approach verification plots for this event are shown next.

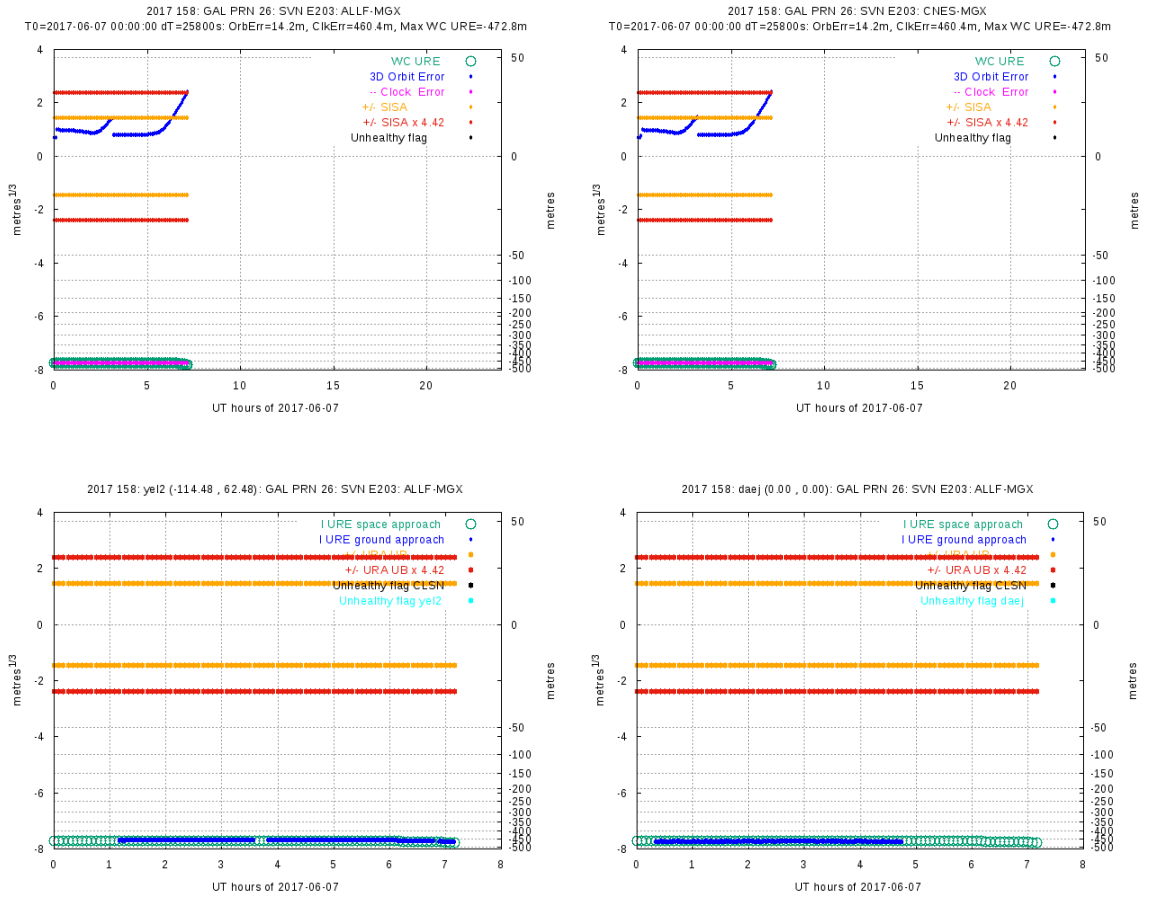

Figure 61. The same plots as in Figure 50.

F.6 Event of 28/11/2017 (Doy 332) on Galileo Satellite E205

Similar results are found with the gAGE and CNES cleansed RINEX navigation files. The Space Approach detection plots and Ground Approach verification plots for this event are shown next.

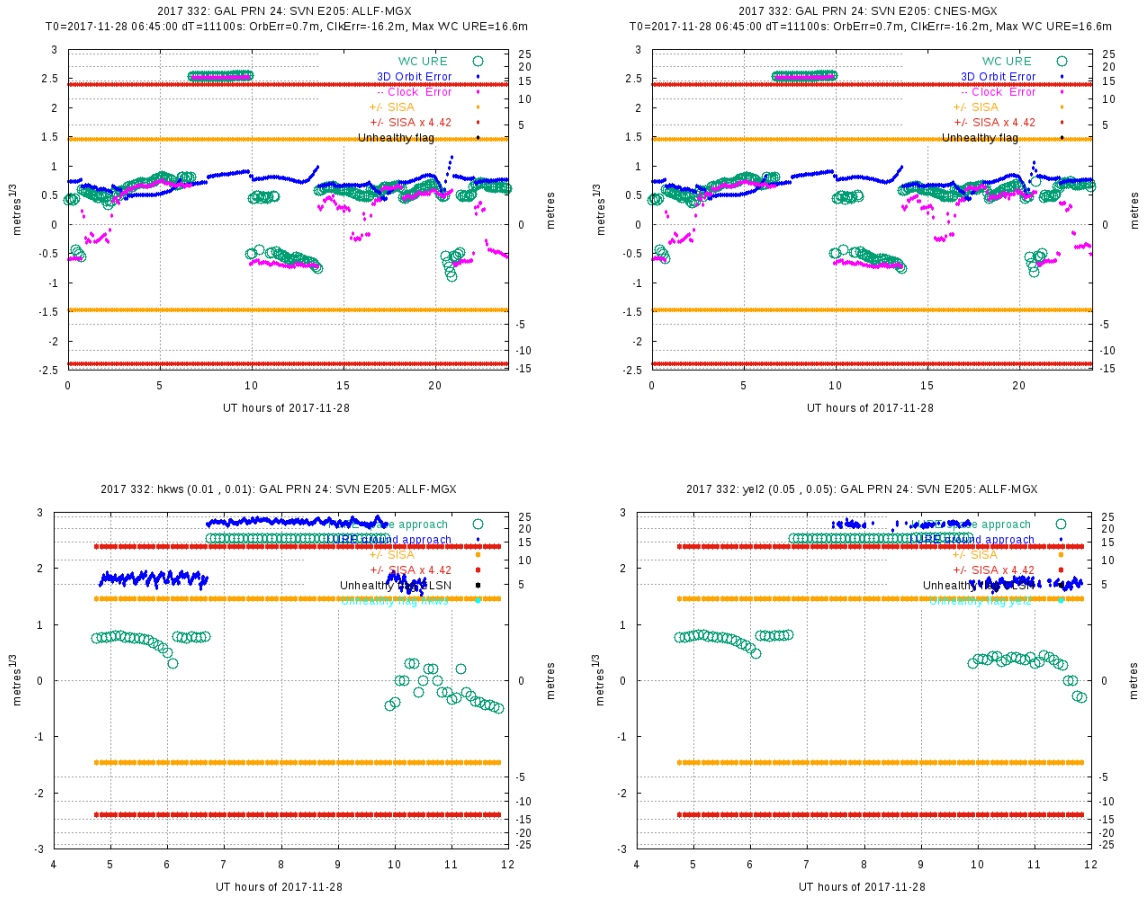

Figure 62. The same plots as in Figure 50.

F.7 Events of 26/12/2017 (Doy 360) on Galileo Satellite E101

Similar results are found with the gAGE and CNES cleansed RINEX navigation files. The Space Approach detection plots and Ground Approach verification plots for this event are shown next.

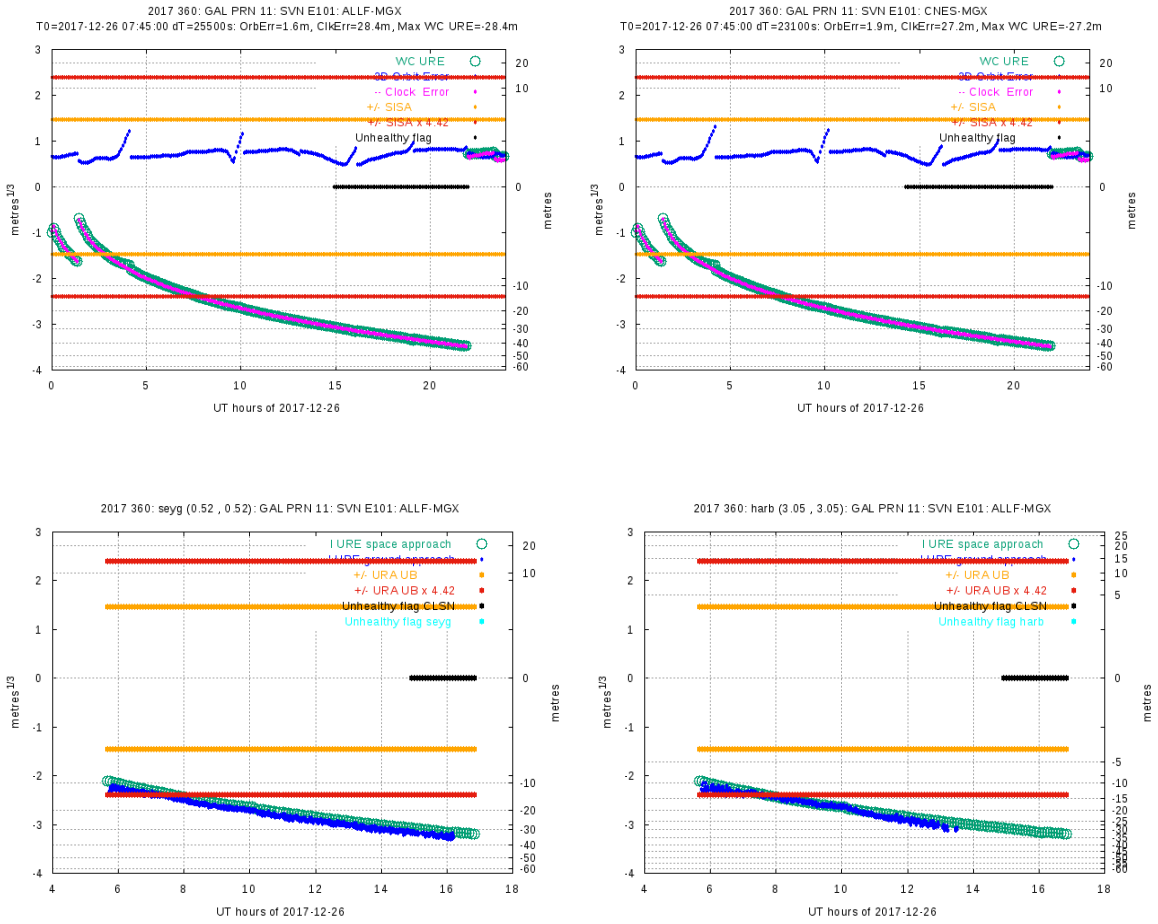

Figure 63. The same plots as in Figure 50.

F.8 Event of 5/09/2018 on Galileo Satellite E206

Similar results are found with the gAGE and CNES cleansed RINEX navigation files. The Space Approach detection plots and Ground Approach verification plots for this event are shown next.

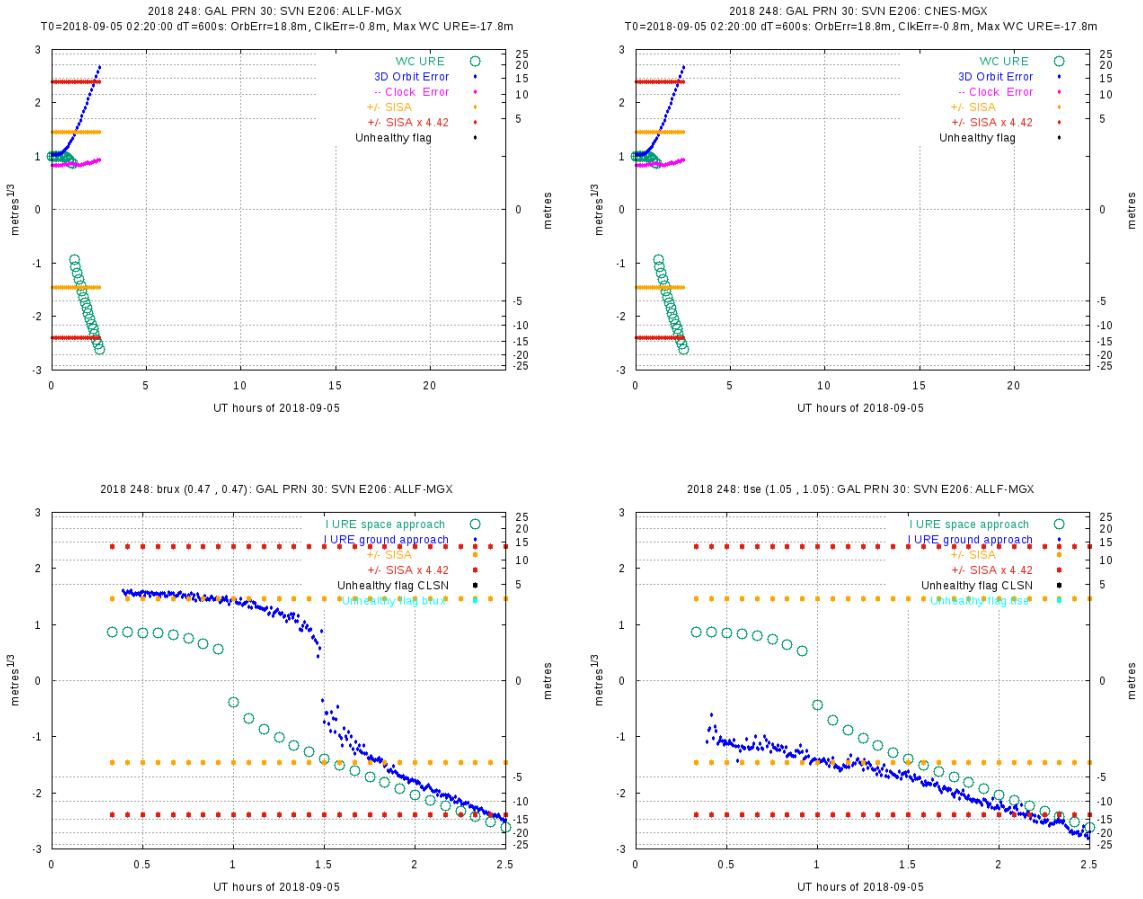

Figure 64. The same plots as in Figure 50.

F.9 Event of 7/03/2019 on Galileo Satellite E103

Similar results are found with the gAGE and CNES cleansed RINEX navigation files. The Space Approach detection plots and Ground Approach verification plots for this event are shown next.

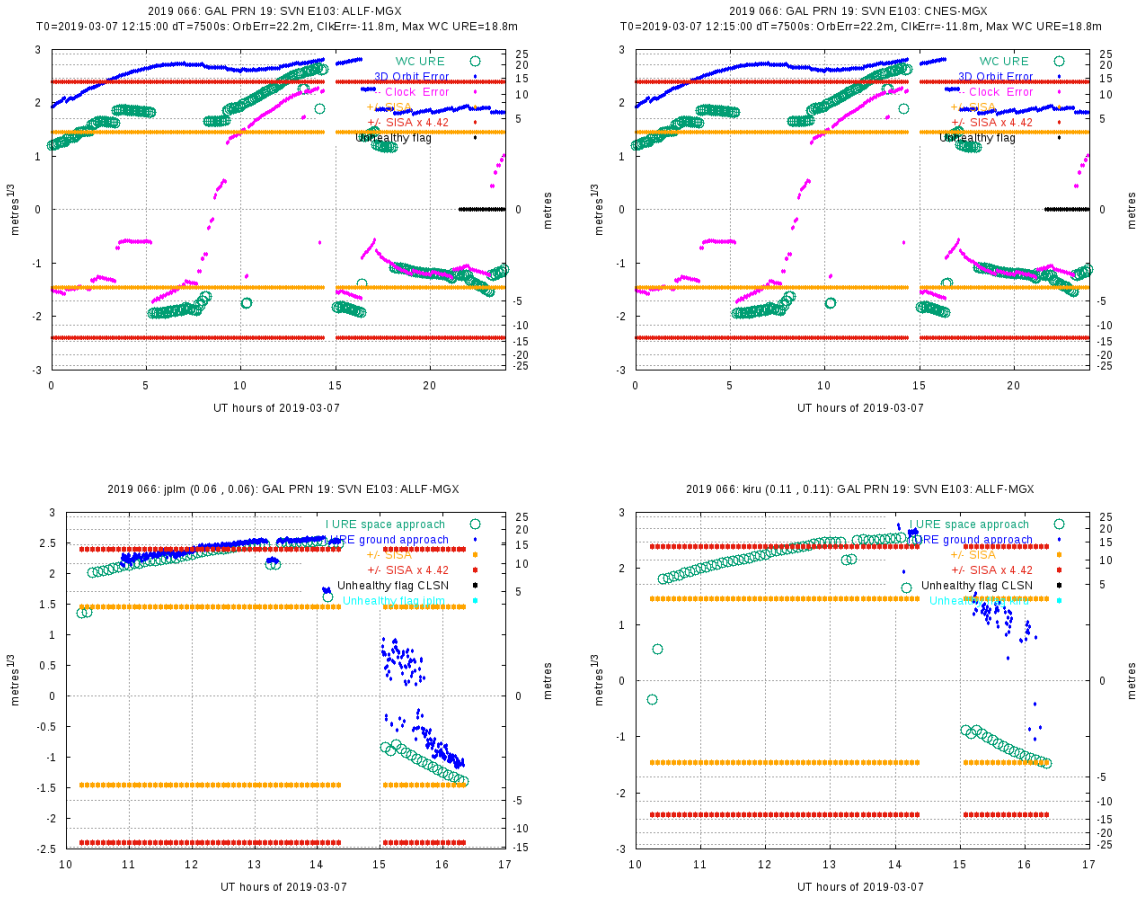

Figure 65. The same plots as in Figure 50.

F.10 Event of 29/10/2019 on Galileo Satellite E101

Similar results are found with the gAGE and CNES cleansed RINEX navigation files. The Space Approach detection plots and Ground Approach verification plots for this event are shown next.

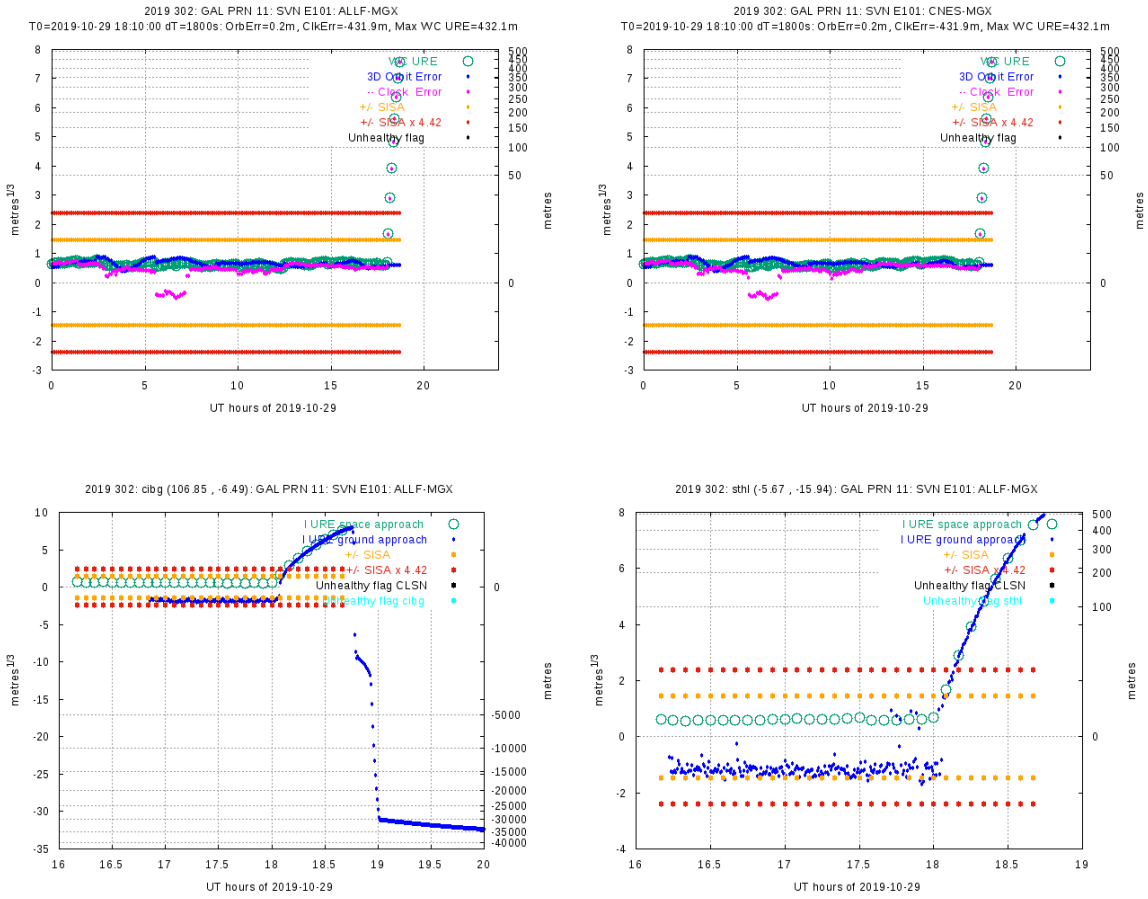

Figure 66. The same plots as in Figure 50.

F.11 Event of 21/01/2021 on Galileo Satellite E102

Similar results are found with the gAGE and CNES cleansed RINEX navigation files. The Space Approach detection plots and Ground Approach verification plots for this event are shown next.

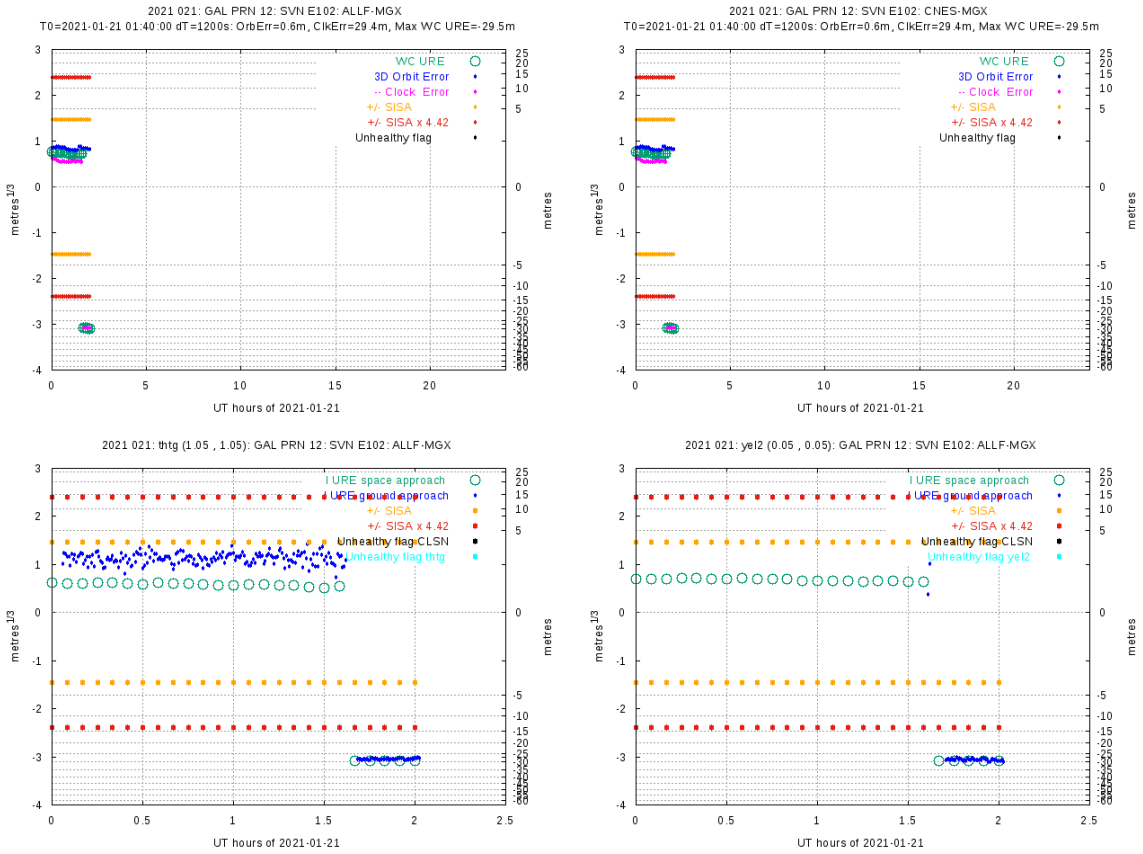

Figure 67. The same plots as in Figure 50.

F.12 Event of 29/04/2022 on Galileo Satellite E210

Similar results are found with the gAGE and CNES cleansed RINEX navigation files. The Space Approach detection plots and Ground Approach verification plots for this event are shown next.

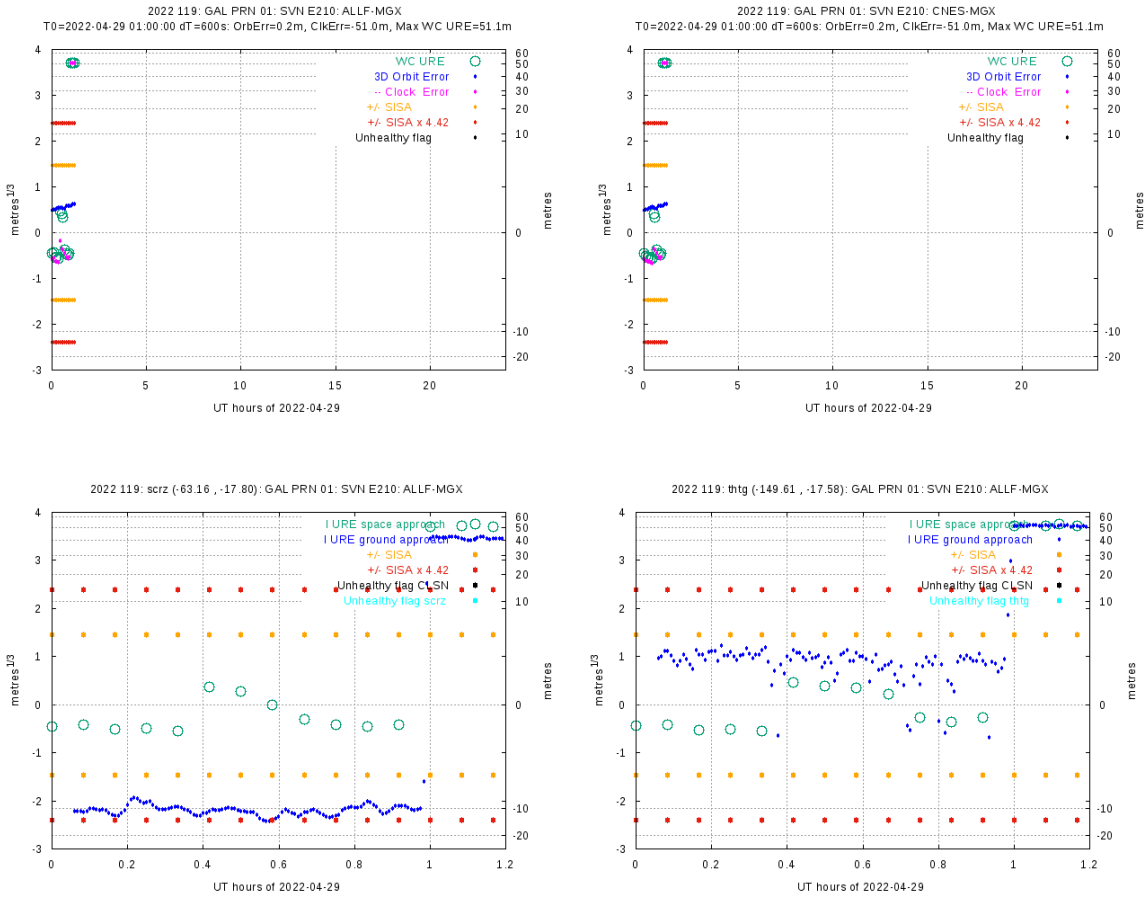

Figure 68. The same plots as in Figure 50.

F.13 Event of 8/06/2022 on Galileo Satellite E103

Similar results are found with the gAGE and CNES cleansed RINEX navigation files. The Space Approach detection plots and Ground Approach verification plots for this event are shown next.

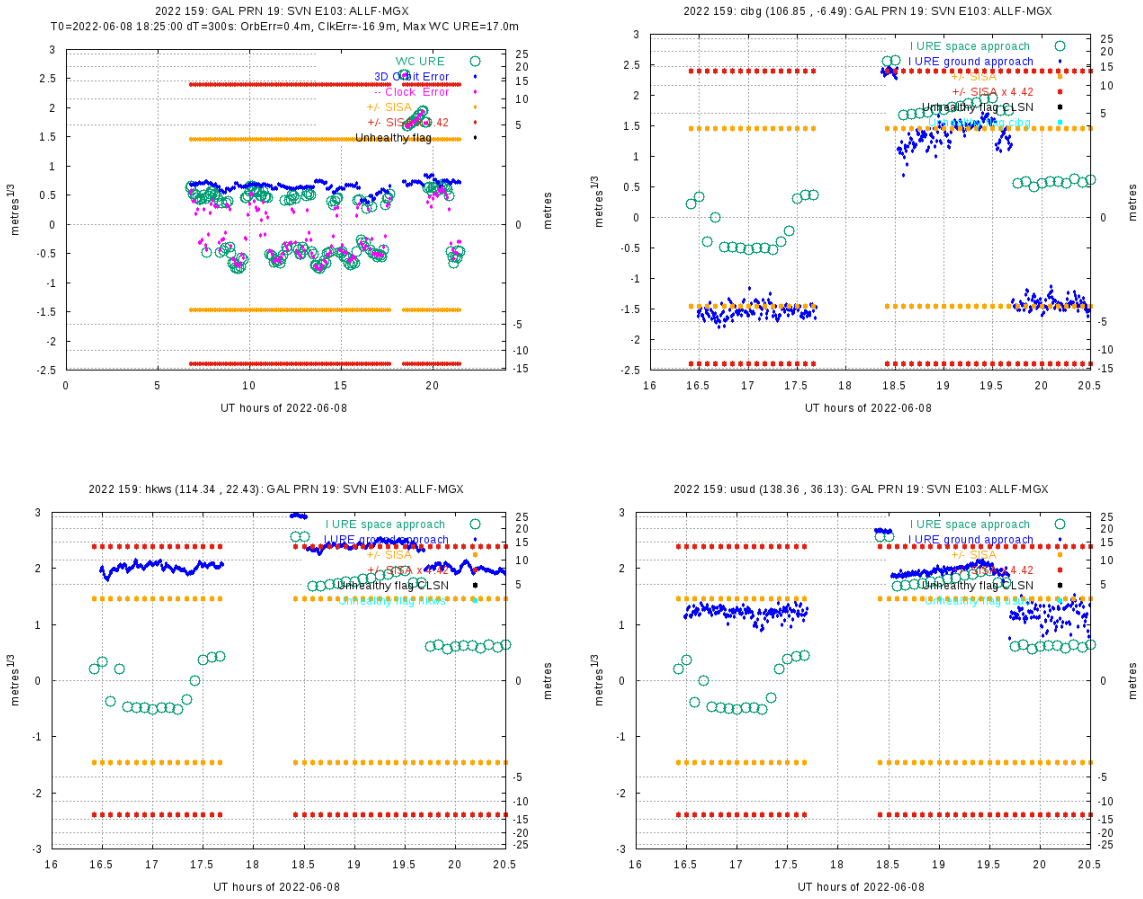

Figure 69. The same plots as in Figure 50.

ANNEX G: HARAIM performance maps for Scenarios 1 and 2

G.1 Global Maps HARAIM Scenario 1

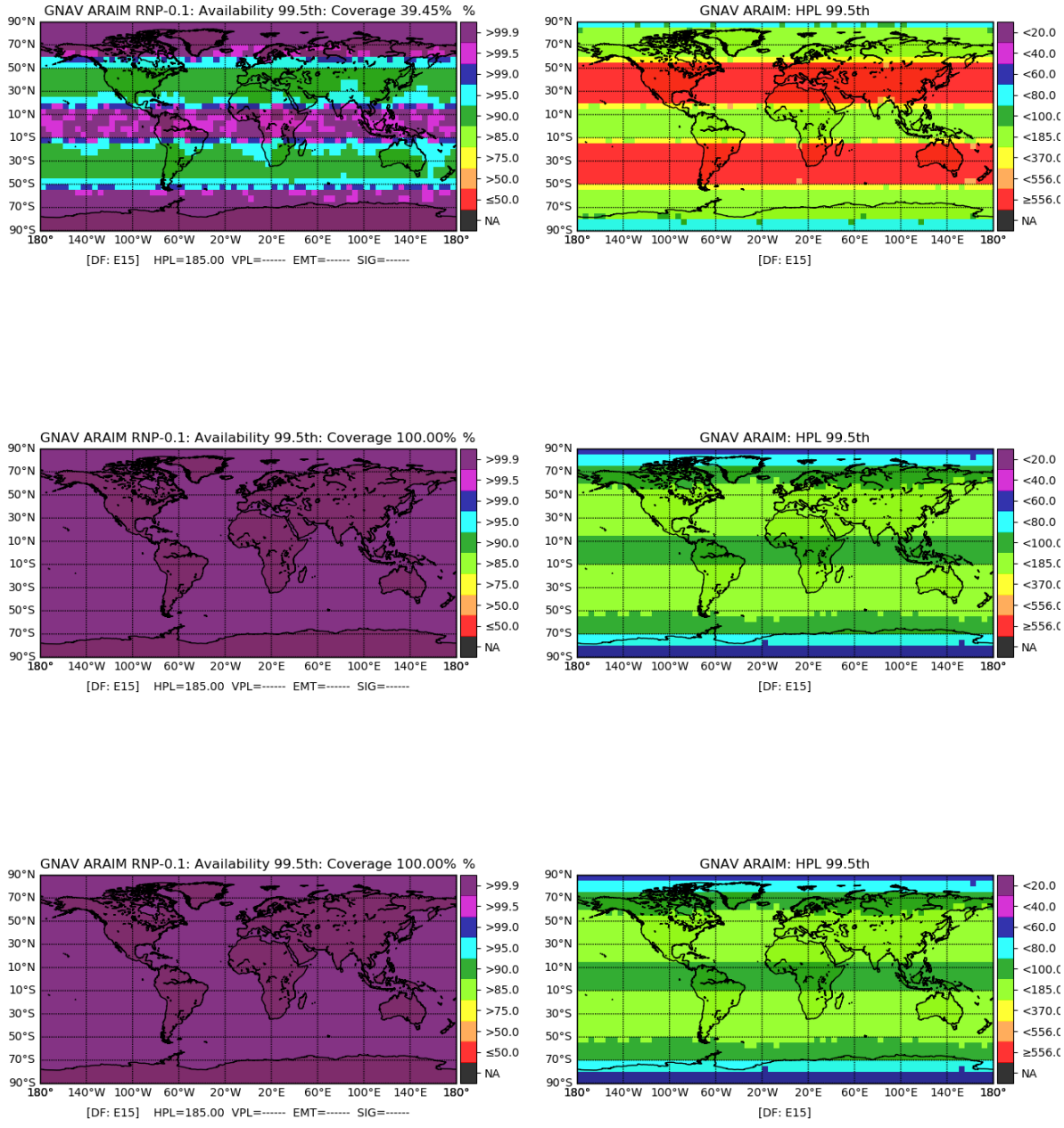

Figure 70. Scenario-1: RNP-0.1 Availability (99.5th), left hand maps, and HPL (95.5th) right hand maps, with dual frequency E15 Galileo constellation. $\sigma_{URA,GPS} = 2.5\ m,\ \sigma_{URA,Galileo} = 9\ m$, $\sigma_{URE} = 2/3\ \sigma_{URA}$, $b_{nom} = 0.75\ m;\ P_{sat;GPS} = 1 \times 10^{-5}$, $P_{sat;Galileo} = 1 \times 10^{-5}$; $P_{const} = 10^{-8}$. Depleted constellation (top), Table 29, baseline constellation (middle), Table 30, and optimistic constellation (bottom), Table 31.

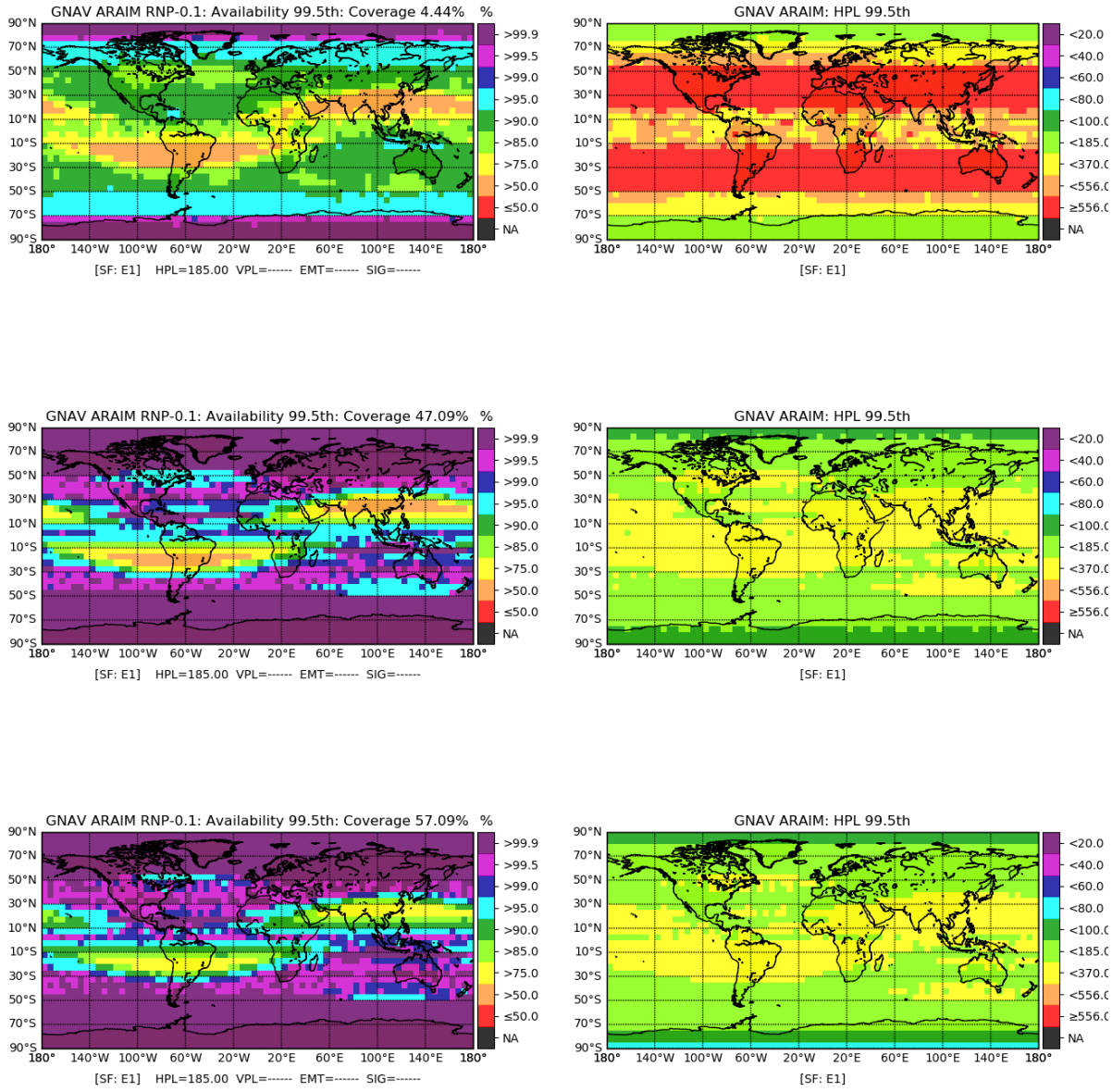

Figure 71. Scenario-1: RNP-0.1 Availability (99.5th), left hand maps, and HPL (95.5th) right hand maps, with single frequency E1 Galileo constellation. $\sigma_{URA,GPS} = 2.5\ m$, $\sigma_{URA,Galileo} = 9\ m$, $\sigma_{URE} = 2/3\ \sigma_{URA}$, $_{nom} = 0.75\ m$; $P_{sat;GPS} = 1 \times 10^{-5}$, $P_{sat;Galileo} = 1 \times 10^{-5}$; $P_{const} = 10^{-8}$. Depleted constellation (top), Table 29, baseline constellation (middle), Table 30, and optimistic constellation (bottom), Table 31.

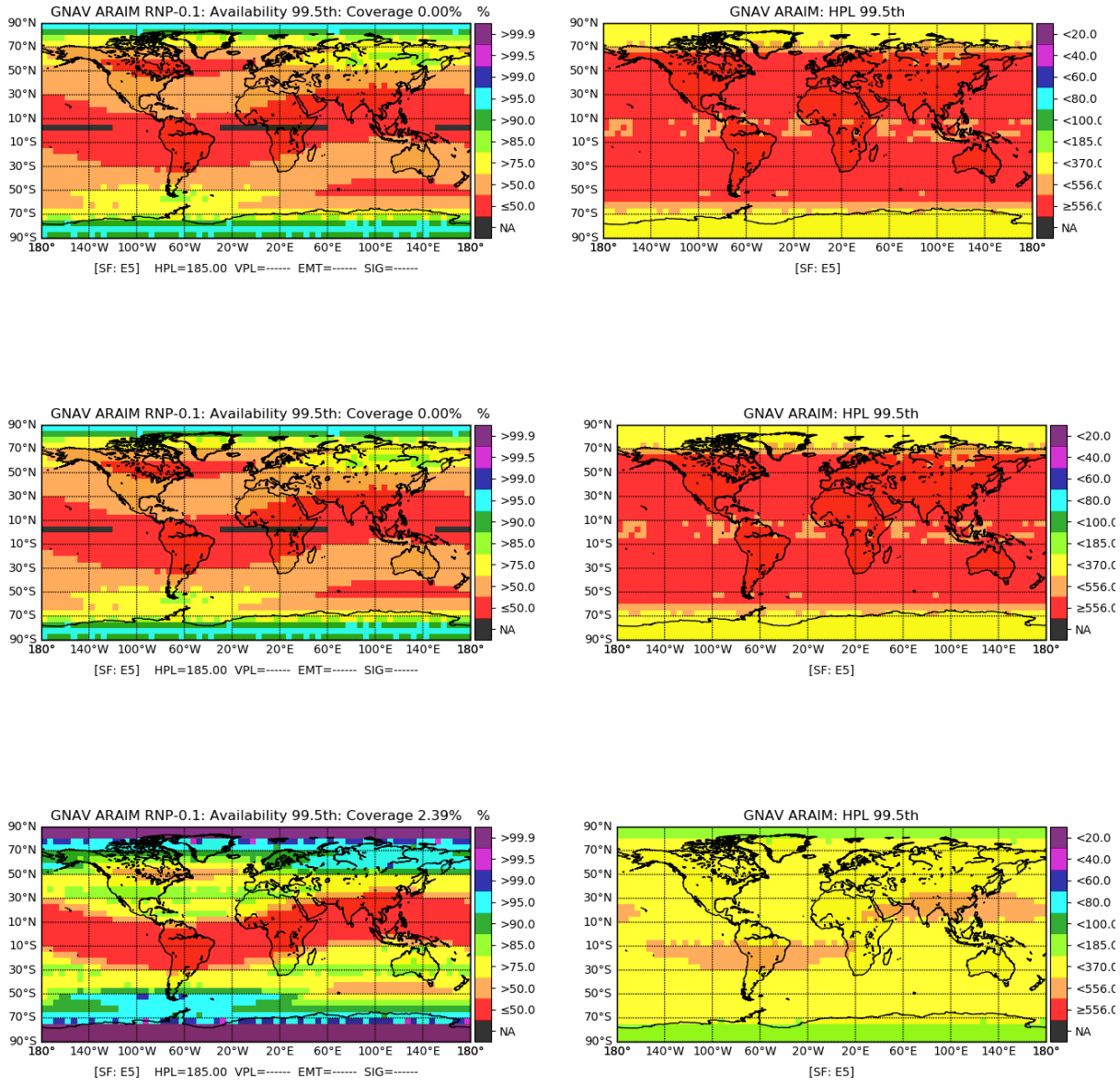

Figure 72. Scenario-1: RNP-0.1 Availability (99.5th), left hand maps, and HPL (95.5th) right hand maps, with single frequency E5 Galileo constellation. $\sigma_{URA,GPS} = 2.5\ m$, $\sigma_{URA,Galileo} = 9\ m$, $\sigma_{URE} = 2/3\ \sigma_{URA}$, $b_{nom} = 0.75\ m$; $P_{sat;GPS} = 1 \times 10^{-5}$, $P_{sat;Galileo} = 1 \times 10^{-5}$; $P_{const} = 10^{-8}$. Depleted constellation (top), Table 29, baseline constellation (middle), Table 30, and optimistic constellation (bottom), Table 31.

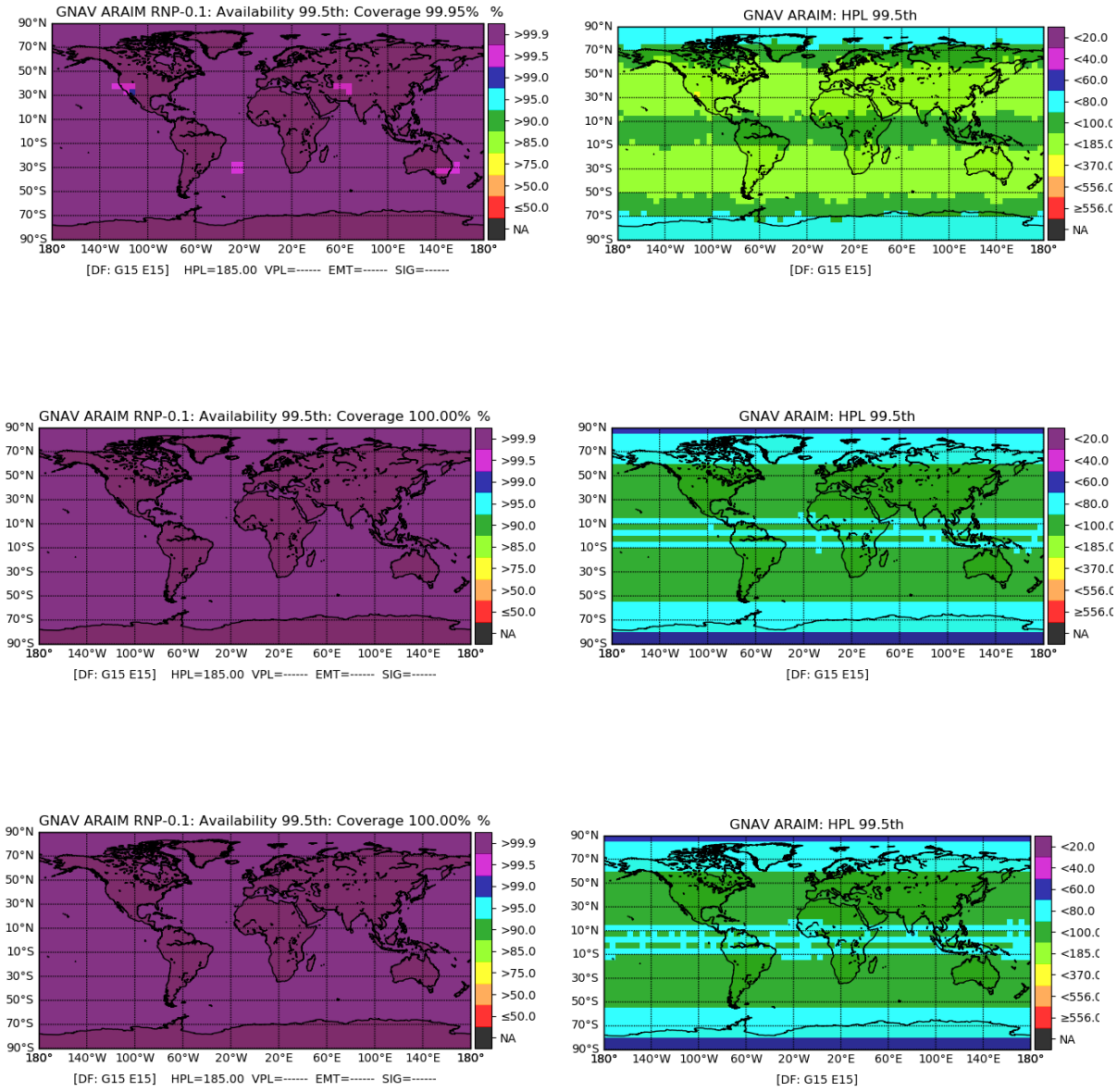

Figure 73. Scenario-1: RNP-0.1 Availability (99.5th), left hand maps, and HPL (95.5th) right hand maps, with dual frequency and dual constellation GPS L1/L5 and Galileo E1/E5. $\sigma_{URA,GPS} = 2.5\,m,\ \sigma_{URA,Galileo} = 9\,m,\ \sigma_{URE} = 2/3\,\sigma_{URA},\ b_{nom} = 0.75\,m;\ \ P_{sat;GPS} = 1 \times 10^{-5},\ P_{sat;Galileo} = 1 \times 10^{-5};\ P_{const} = 10^{-8}$. Depleted constellation (top), Table 29, baseline constellation (middle), Table 30, and optimistic constellation (bottom), Table 31.

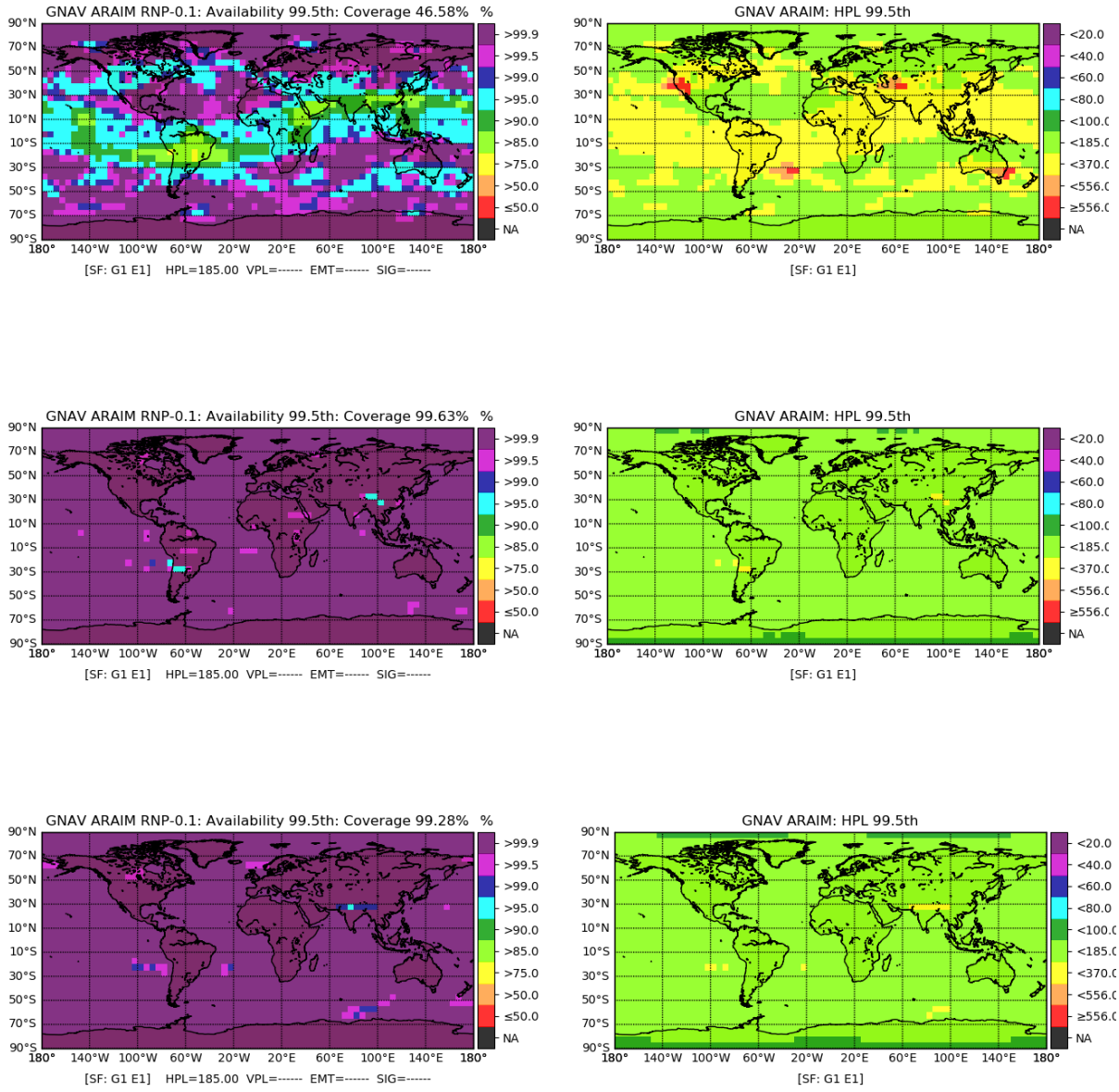

Figure 74. Scenario-1: RNP-0.1 Availability (99.5th), left hand maps, and HPL (95.5th) right hand maps, with single frequency and dual constellation GPS L1 and Galileo E1. $\sigma_{URA,GPS} = 2.5\ m$, $\sigma_{URA,Galileo} = 9\ m$, $\sigma_{URE} = 2/3\ \sigma_{URA}$, $b_{nom} = 0.75\ m$; $P_{sat;GPS} = 1 \times 10^{-5}$, $P_{sat;Galileo} = 1 \times 10^{-5}$; $P_{const} = 10^{-8}$. Depleted constellation (top), Table 29, baseline constellation (middle), Table 30, and optimistic constellation (bottom), Table 31.

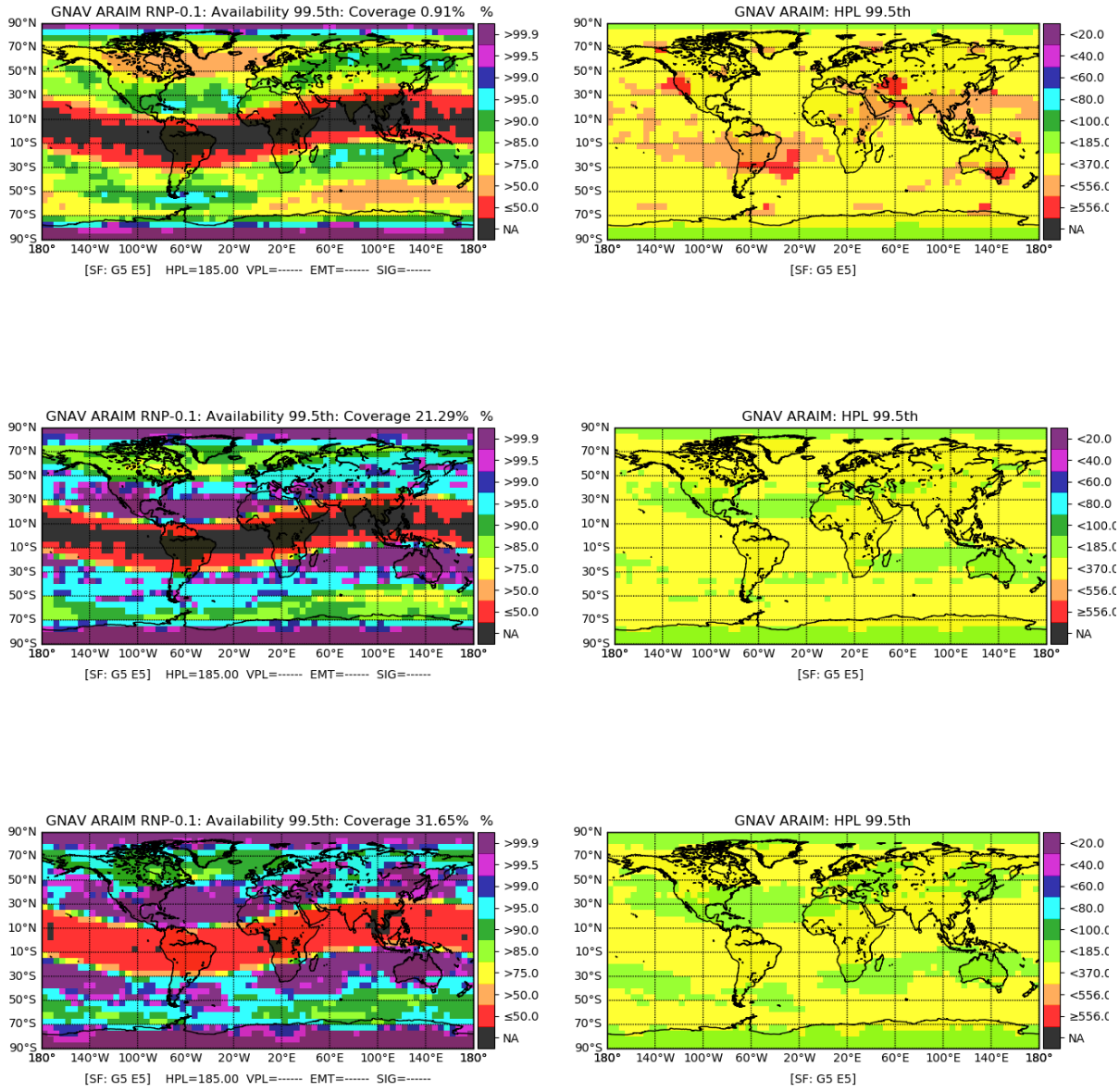

Figure 75. Scenario-1: RNP-0.1 Availability (99.5th), left hand maps, and HPL (95.5th) right hand maps, with single frequency and dual constellation GPS L5 and Galileo E5. $\sigma_{URA,GPS} = 2.5\ m$, $\sigma_{URA,Galileo} = 9\ m$, $\sigma_{URE} = 2/3\ \sigma_{URA}$, $b_{nom} = 0.75\ m$; $P_{sat;GPS} = 1 \times 10^{-5}$, $P_{sat;Galileo} = 1 \times 10^{-5}$; $P_{const} = 10^{-8}$. Depleted constellation (top), Table 29, baseline constellation (middle), Table 30, and optimistic constellation (bottom), Table 31.

G.2 Global Maps HARAIM Scenario 2

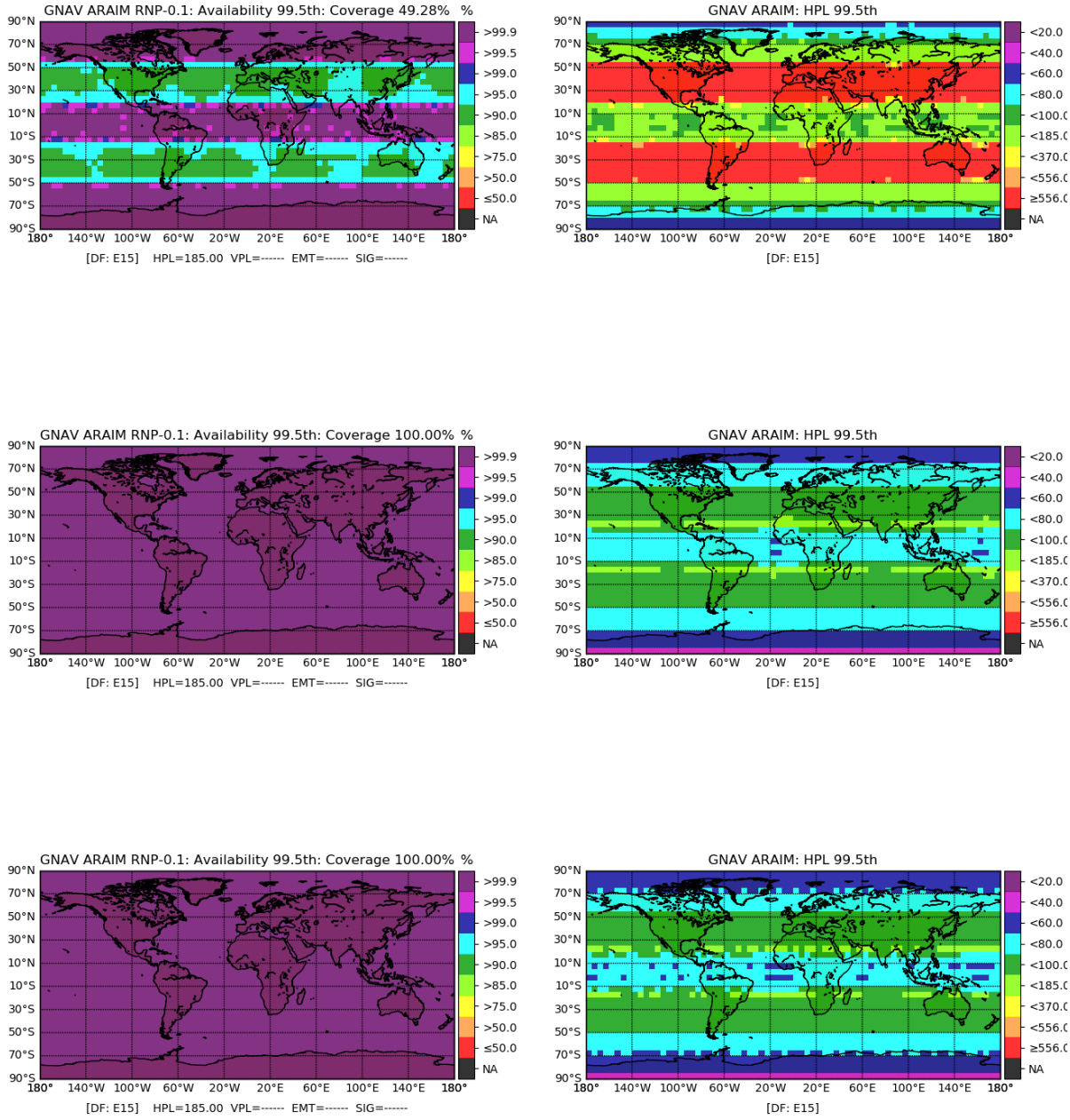

Figure 76. Scenario-2: RNP-0.1 Availability (99.5th), left hand maps, and HPL (95.5th) right hand maps, with dual frequency E15 Galileo constellation. $\sigma_{URA,GPS} = 2.5\ m,\ \sigma_{URA,Galileo} = 6\ m$, $\sigma_{URE} = 2/3\ \sigma_{URA}$, $b_{nom} = 0.75\ m$; $P_{sat;GPS} = 1 \times 10^{-5}$, $P_{sat;Galileo} = 3 \times 10^{-5}$; $P_{const} = 10^{-8}$. Depleted constellation (top), Table 32, baseline constellation (middle), Table 33, and optimistic constellation (bottom), Table 34.

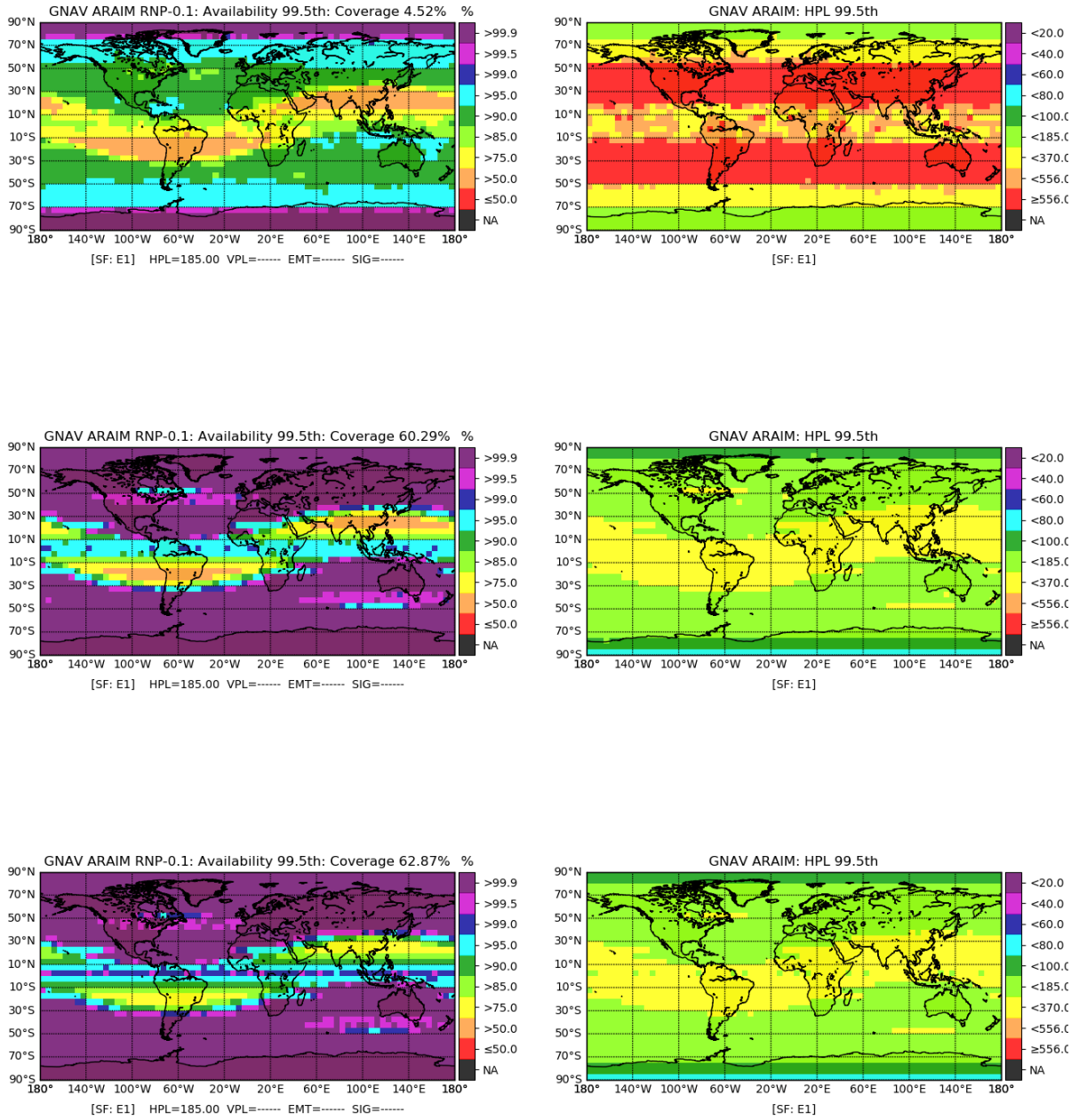

Figure 77. Scenario-2: RNP-0.1 Availability (99.5th), left hand maps, and HPL (95.5th) right hand maps, with single frequency E1 Galileo constellation. $\sigma_{URA,GPS} = 2.5\ m$, $\sigma_{URA,Galileo} = 6\ m$, $\sigma_{URE} = 2/3\ \sigma_{URA}$, $b_{nom} = 0.75\ m$; $P_{sat;GPS} = 1 \times 10^{-5}$, $P_{sat;Galileo} = 3 \times 10^{-5}$; $P_{const} = 10^{-8}$. Depleted constellation (top), Table 32, baseline constellation (middle), Table 33, and optimistic constellation (bottom), Table 34.

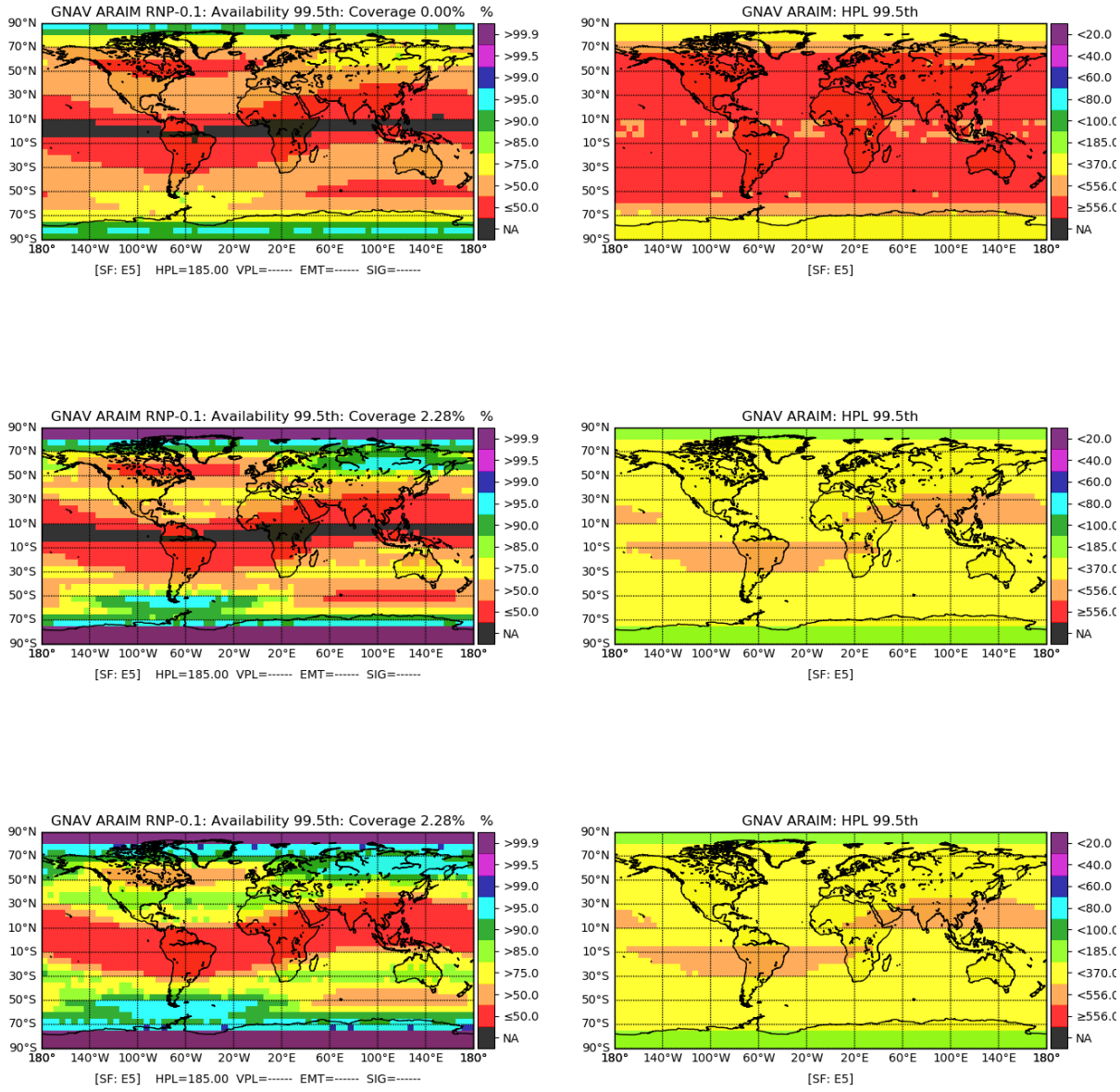

Figure 78. Scenario-2: RNP-0.1 Availability (99.5th), left hand maps, and HPL (95.5th) right hand maps, with single frequency E5 Galileo constellation. $\sigma_{URA,GPS} = 2.5\,m$, $\sigma_{URA,Galileo} = 6\,m$, $\sigma_{URE} = 2/3\,\sigma_{URA}$, $b_{nom} = 0.75\,m$; $P_{sat;GPS} = 1 \times 10^{-5}$, $P_{sat;Galileo} = 3 \times 10^{-5}$; $P_{const} = 10^{-8}$. Depleted constellation (top), Table 32, baseline constellation (middle), Table 33, and optimistic constellation (bottom), Table 34.

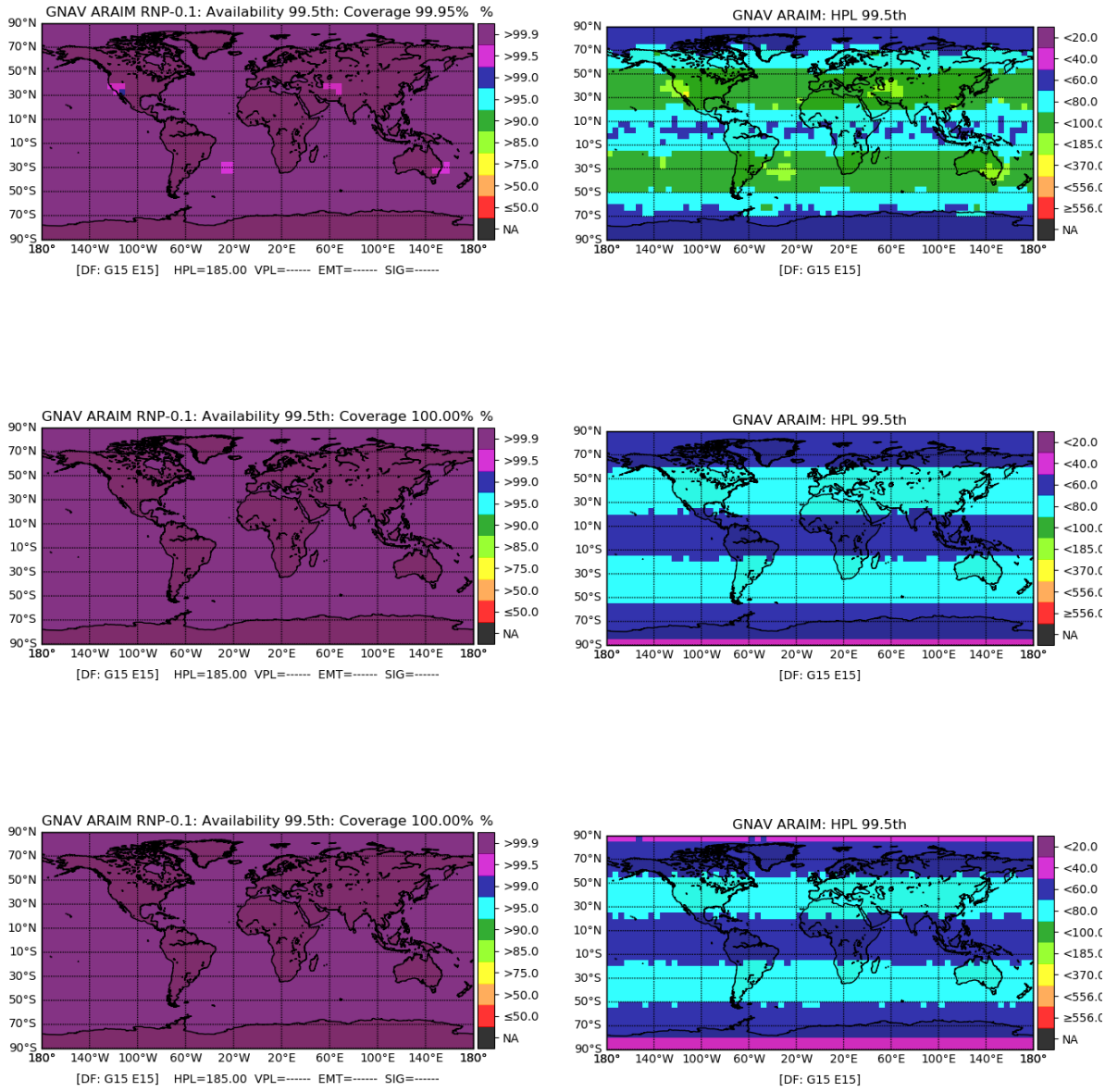

Figure 79. Scenario-2: RNP-0.1 Availability (99.5th), left hand maps, and HPL (95.5th) right hand maps, with dual frequency and dual constellation GPS L1/L5 and Galileo E1/E5. $\sigma_{URA,GPS} = 2.5\,m$, $\sigma_{URA,Galileo} = 6\,m$, $\sigma_{URE} = 2/3\,\sigma_{URA}$, $b_{nom} = 0.75\,m$; $P_{sat;GPS} = 1 \times 10^{-5}$, $P_{sat;Galileo} = 3 \times 10^{-5}$; $P_{const} = 10^{-8}$. Depleted constellation (top), Table 32, baseline constellation (middle), Table 33, and optimistic constellation (bottom), Table 34.

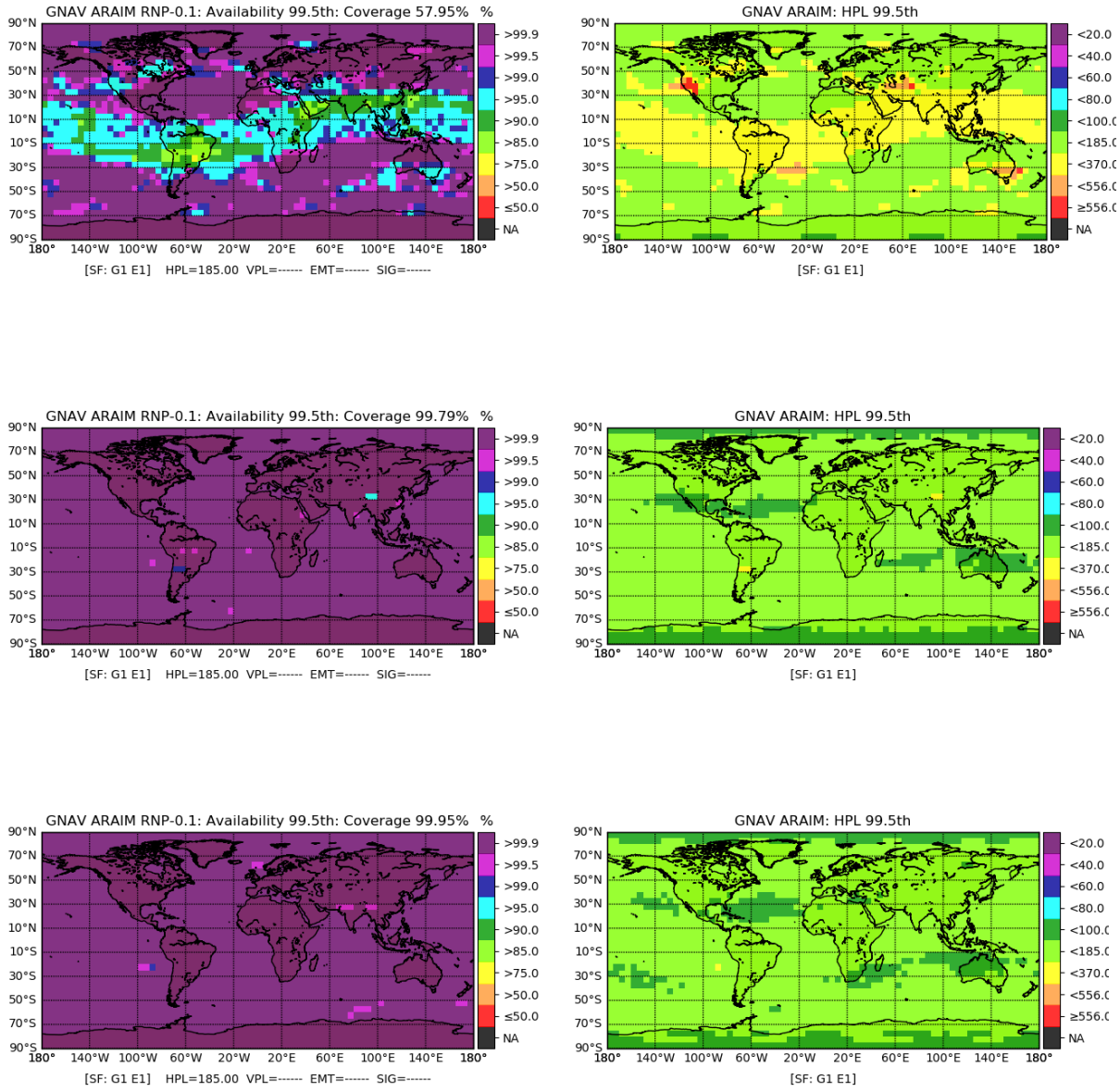

Figure 80. Scenario-2: RNP-0.1 Availability (99.5th), left hand maps, and HPL (95.5th) right hand maps, with single frequency and dual constellation GPS L1 and Galileo E1. $\sigma_{URA,GPS} = 2.5\ m$, $\sigma_{URA,Galileo} = 6\ m$, $\sigma_{URE} = 2/3\ \sigma_{URA}$, $b_{nom} = 0.75\ m$; $P_{sat;GPS} = 1 \times 10^{-5}$, $P_{sat;Galileo} = 3 \times 10^{-5}$; $P_{const} = 10^{-8}$. Depleted constellation (top), Table 32, baseline constellation (middle), Table 33, and optimistic constellation (bottom), Table 34.

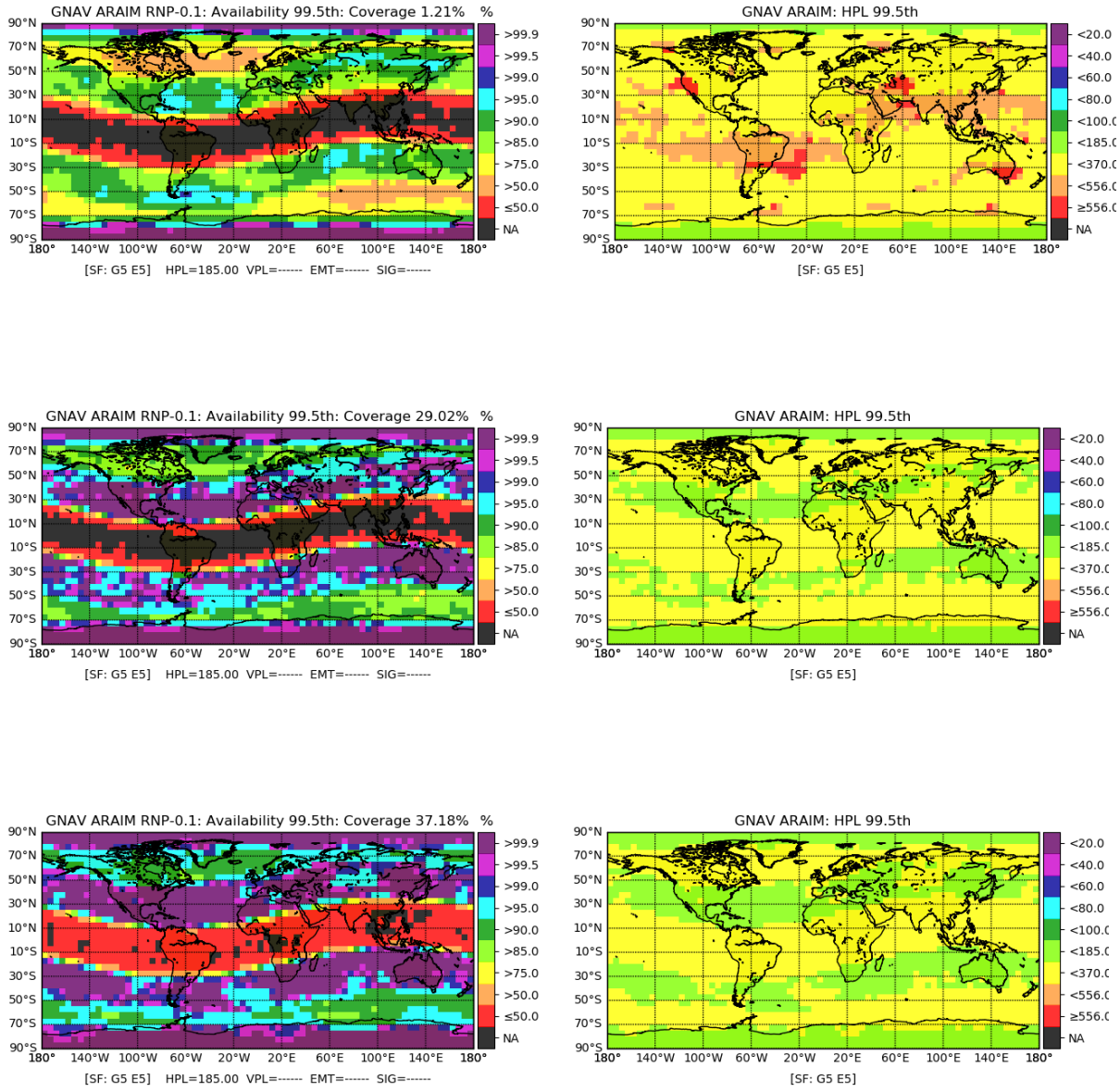

Figure 81. Scenario-2: RNP-0.1 Availability (99.5th), left hand maps, and HPL (95.5th) right hand maps, with single frequency and dual constellation GPS L5 and Galileo E5. $\sigma_{URA,GPS} = 2.5\ m$, $\sigma_{URA,Galileo} = 6\ m$, $\sigma_{URE} = 2/3\ \sigma_{URA}$, $b_{nom} = 0.75\ m$; $P_{sat;GPS} = 1 \times 10^{-5}$, $P_{sat;Galileo} = 3 \times 10^{-5}$; $P_{const} = 10^{-8}$. Depleted constellation (top), Table 32, baseline constellation (middle), Table 33, and optimistic constellation (bottom), Table 34.

ANNEX H: Galileo and GPS Nominal Accuracy Tables

Table 41. Galileo F/NAV Nominal Accuracy, from 1 January 2017 to 31 July 2022.

From 1 January 2017 to 31 July 2022: gAGE Consolidated Broadcast + MGEX Precise Orbits and Clocks

		Radial (cm)				Along-Track (cm)				Cross-Track (cm)				Clock (cm)				WC URE (cm)				N.	IURE (cm) (Acum. Dodec.)				
	SVN	$\bar{x}$	68th	95th	σ	$\bar{x}$	68th	95th	σ	$\bar{x}$	68th	95th	σ	$\bar{x}$	68th	95th	σ	$\bar{x}$	68th	95th	σ	Samples	$\bar{x}$	68th	95th	σ	N. Sampl.
IOV	E101	4,0	13	27	15	-4,3	28	59	31	0,9	18	34	18	-2,9	17	38	23	10,9	23	42	26	558.220	6,8	15	33	22	3.856.834
IOV	E102	6,7	16	31	15	-8,8	31	66	35	0,5	18	37	19	-16,6	25	46	24	31,3	37	55	23	570.153	23,2	29	46	21	3.995.580
IOV	E103	2,0	12	26	15	-5,6	33	69	47	2,7	20	40	21	-7,6	19	38	19	15,6	25	44	24	541.936	9,7	17	34	17	3.772.463
FOC	E203	10,8	17	36	17	-5,5	25	55	31	0,7	17	32	17	-2,2	16	33	19	17,7	24	46	21	562.304	12,8	18	39	18	3.939.135
FOC	E204	7,0	14	30	28	-6,5	28	64	35	-0,5	17	35	28	11,2	20	43	27	-5,2	21	45	33	97.644	-4,4	15	36	26	679.576
FOC	E205	8,6	14	29	13	-3,1	24	51	27	1,2	16	32	16	2,6	13	29	21	8,8	17	31	24	566.435	5,9	11	25	20	3.949.040
FOC	E206	8,0	14	28	13	-3,1	24	53	28	0,4	16	33	17	3,2	14	31	22	7,4	17	32	24	567.018	4,8	12	25	20	3.927.629
FOC	E207	7,8	13	27	13	-6,1	24	52	27	-0,2	15	32	16	7,3	16	34	16	1,3	16	30	18	531.669	0,4	10	23	13	3.737.247
FOC	E208	9,3	15	31	14	-6,0	24	53	32	0,7	15	31	16	-1,8	13	29	23	15,5	21	39	25	567.119	11,0	15	33	22	3.937.463
FOC	E209	9,2	15	31	13	-2,0	24	53	28	1,3	17	33	17	0,2	12	28	14	12,8	20	37	17	565.592	8,9	14	30	13	3.980.142
FOC	E210	8,5	14	29	13	-5,7	24	53	27	1,7	17	33	17	2,2	15	34	17	8,8	18	39	20	554.020	6,1	12	32	15	3.858.486
FOC	E211	9,3	15	31	15	-2,2	24	52	27	1,3	16	32	16	-1,2	13	29	22	14,5	20	40	25	566.384	10,4	15	34	22	3.943.782
FOC	E212	8,4	14	33	16	-3,6	24	53	30	0,2	15	31	16	-2,5	12	28	16	15,7	21	40	18	512.143	10,9	15	33	14	3.600.390
FOC	E213	9,1	15	33	15	-3,9	24	53	31	1,4	16	33	17	-1,6	13	30	15	15,1	21	40	19	511.129	10,6	15	33	14	3.563.727
FOC	E214	10,1	16	37	16	-2,4	24	51	30	1,5	17	33	17	-5,4	14	31	16	20,8	25	48	19	527.809	15,5	19	42	16	3.676.528
FOC	E215	5,3	11	24	12	-2,2	24	50	26	1,1	17	32	16	7,1	15	32	15	-1,9	16	28	18	384.358	-1,8	10	22	13	2.672.839
FOC	E216	5,4	11	24	11	-2,3	23	49	26	0,8	16	31	16	1,8	12	28	14	6,0	15	27	15	404.039	3,6	9	20	10	2.807.854
FOC	E217	5,2	11	23	11	-3,0	24	50	26	0,0	16	32	16	4,1	13	28	14	2,5	14	26	16	407.579	1,0	8	19	11	2.837.585
FOC	E218	5,5	11	24	12	-2,9	23	49	29	1,1	16	32	16	3,0	13	29	15	4,5	15	28	16	404.814	2,6	9	21	11	2.812.443
FOC	E219	5,8	13	27	14	-1,5	25	53	38	1,0	17	32	18	5,2	16	33	16	1,9	15	28	19	347.352	0,6	9	20	11	2.430.079
FOC	E220	5,0	13	26	12	-3,6	24	51	27	0,4	17	32	17	3,6	15	32	15	3,2	16	28	17	349.183	1,4	10	21	11	2.407.626
FOC	E221	5,5	13	26	12	-3,6	25	52	26	0,8	17	33	17	3,1	15	31	15	4,8	16	28	16	351.283	2,3	9	21	10	2.457.987
FOC	E222	4,9	13	26	14	-3,4	25	54	40	0,3	17	32	17	1,9	15	31	18	5,8	16	30	21	349.111	2,9	10	22	12	2.407.085
FOC	E223	6,2	13	25	11	2,9	23	49	24	10,2	15	28	11	3,9	13	27	13	4,0	13	25	13	18.745	2,0	8	18	8	129.009
ALL	**IOV**	**4,3**	**14**	**28**	**15**	**-6,2**	**30**	**65**	**38**	**1,4**	**19**	**37**	**19**	**-9,1**	**20**	**41**	**23**	**19,4**	**28**	**49**	**26**	**1.670.309**	**13,4**	**21**	**40**	**21**	**11.624.877**
ALL	**FOC**	**7,8**	**14**	**30**	**14**	**-3,6**	**24**	**52**	**29**	**0,9**	**16**	**32**	**17**	**1,4**	**14**	**31**	**18**	**9,3**	**18**	**37**	**21**	**9.145.730**	**6,3**	**12**	**30**	**16**	**63.755.652**
ALL	**ALL**	**7,2**	**14**	**29**	**14**	**-4,0**	**25**	**54**	**31**	**0,9**	**17**	**33**	**17**	**-0,2**	**15**	**33**	**19**	**10,9**	**20**	**40**	**22**	**10.816.039**	**7,4**	**13**	**32**	**17**	**75.380.529**

Table 42. GPS LNAV Nominal Accuracy, from 1 January 2017 to 31 July 2022.

From 1 January 2017 to 31 July 2022: gAGE Consolidated Broadcast + MGEX Precise Orbits and Clocks																					N. Samples	IURE (cm) (Acum. Dodec.)				
		Radial (cm)				Along-Track (cm)				Cross-Track (cm)				Clock (cm)				WC URE (cm)								
	SVN	$\bar{x}$	68th	95th	σ	$\bar{x}$	68th	95th	σ	$\bar{x}$	68th	95th	σ	$\bar{x}$	68th	95th	σ	$\bar{x}$	68th	95th	σ		$\bar{x}$	68th	95th	σ	N. Sampl.
IIA	G034	-0,4	19	37	19	1,5	101	233	115	0,5	49	89	47	-6,3	71	162	78	8,9	96	194	99	156.232	3,1	71	165	79	1.119.991
IIR	G041	-0,4	11	24	12	36,6	105	226	107	0,2	41	81	41	-6,6	28	64	31	11,1	54	101	55	416.307	6,5	32	72	35	3.048.203
IIR	G043	0,1	11	21	11	13,4	88	196	95	-0,2	37	76	38	-2,3	37	88	43	2,8	59	117	62	577.013	2,0	39	93	45	3.845.909
IIR	G044	1,6	12	27	13	-11,8	84	184	91	0,4	40	81	40	-4,7	81	216	96	8,7	103	241	114	465.696	6,3	82	217	97	3.074.889
IIR	G045	1,3	15	32	16	-7,0	108	236	117	1,4	50	103	51	-1,8	26	56	29	6,2	56	99	56	576.799	4,5	33	71	36	3.898.130
IIR	G046	2,1	14	29	14	-40,5	119	266	124	-0,7	47	92	47	-3,2	36	92	44	8,6	68	133	71	402.476	6,7	42	103	49	2.726.850
IIR	G047	2,2	13	27	14	-9,0	89	190	96	0,4	35	70	36	-2,7	23	48	24	8,4	45	78	44	512.233	5,5	26	56	28	3.466.822
IIR	G048	0,8	14	27	14	-5,8	89	197	97	1,1	55	106	54	3,2	39	92	44	-4,5	64	123	65	574.803	-2,6	42	97	47	3.673.970
IIR	G050	1,8	15	28	15	3,1	82	175	87	0,1	37	74	38	4,2	26	54	27	-2,9	45	79	45	576.556	-2,5	28	59	29	3.734.026
IIR	G051	0,8	10	22	11	8,3	81	175	87	0,2	45	97	47	0,8	23	50	25	0,4	46	80	46	576.727	1,0	27	58	29	3.890.960
IIR	G052	1,2	12	24	12	-1,5	82	180	89	-0,2	38	81	40	-3,4	38	90	43	6,1	59	115	61	576.550	4,0	40	94	45	3.704.349
IIR	G053	0,3	15	30	15	13,0	124	285	137	0,5	39	79	40	3,7	53	149	68	-4,1	82	186	92	576.659	-3,2	54	149	69	3.776.459
IIR	G054	1,1	12	24	12	-13,5	92	197	99	1,3	54	97	51	-4,2	31	86	41	6,9	56	114	61	110.854	6,4	35	90	43	749.849
IIR	G055	0,5	12	25	12	7,3	94	210	103	-0,2	37	74	37	2,6	21	44	22	-3,7	44	78	43	576.461	-1,6	25	53	26	3.780.842
IIR	G056	1,5	13	26	13	-20,3	83	175	85	-0,3	36	71	36	-0,5	22	46	23	3,8	43	74	42	576.866	1,7	25	53	27	3.852.260
IIR	G057	1,9	15	30	15	5,7	104	239	116	-0,1	44	88	45	3,6	39	111	53	-6,4	65	146	75	576.384	-2,2	41	115	56	3.656.224
IIR	G058	0,8	15	28	15	20,2	94	207	101	-0,4	37	75	38	-4,5	24	49	25	9,9	47	82	46	576.660	5,7	28	59	30	3.870.020
IIR	G059	0,8	12	25	12	12,6	91	191	95	-0,5	39	77	39	2,4	23	49	24	-2,5	46	80	45	577.035	-0,3	27	57	28	4.155.048
IIR	G060	2,1	12	24	12	-19,8	90	193	93	0,7	47	87	46	0,2	22	47	23	3,0	47	80	46	331.845	1,4	27	58	29	2.206.980
IIR	G061	0,3	12	27	13	21,7	108	244	118	0,7	39	77	39	-1,4	24	54	27	3,4	53	96	53	576.648	2,2	30	66	33	3.812.732
IIF	G062	-1,3	19	39	20	35,1	106	231	111	0,1	40	78	40	7,1	28	55	27	-13,7	60	104	57	576.234	-7,5	38	78	39	4.139.700
IIF	G063	1,2	17	35	18	-18,8	99	221	107	-1,0	48	89	47	2,1	32	72	37	-1,1	61	112	62	574.390	-1,0	40	88	44	3.764.867
IIF	G064	0,7	16	32	16	11,6	82	181	94	0,3	33	66	34	8,7	29	61	29	-11,1	54	92	52	576.519	-7,8	35	72	36	3.867.597
IIF	G065	-0,4	22	47	23	25,6	103	229	114	-0,5	31	64	32	1,0	99	231	109	-0,7	125	262	131	573.799	-2,0	102	236	112	3.855.657
IIF	G066	-0,2	16	32	16	-4,6	82	178	89	-0,4	38	73	37	0,4	21	43	22	-0,5	48	81	47	572.949	-0,2	31	62	31	3.859.678
IIF	G067	1,4	18	35	18	-8,0	98	220	107	0,0	38	79	39	6,8	24	52	25	-7,5	54	94	53	576.583	-4,6	34	69	35	3.656.046
IIF	G068	1,2	14	31	15	10,1	75	171	85	0,5	32	63	32	1,7	22	51	27	-0,6	45	84	47	576.646	-0,1	28	63	33	3.740.081
IIF	G069	0,2	18	37	19	9,8	98	225	111	-0,3	38	76	39	-6,3	42	90	47	8,3	69	129	71	573.054	8,6	47	103	52	3.819.585
IIF	G070	0,8	13	28	14	-2,7	85	193	97	0,4	34	69	35	-0,9	19	40	21	3,2	44	79	45	576.529	2,0	27	57	29	4.048.418

IIF	G071	-0,1	18	35	18	6,0	88	196	100	0,0	45	87	45	1,8	24	52	25	-2,6	53	93	53	576.446	-0,8	33	71	35	3.700.615
IIF	G072	1,2	22	44	22	-28,7	112	239	119	-0,1	47	88	46	2,0	101	215	105	-0,2	130	250	130	576.466	0,1	104	220	108	3.655.734
IIF	G073	0,4	15	32	16	-1,4	95	213	106	0,8	50	96	50	-3,3	29	70	34	6,2	59	105	59	576.660	5,0	38	80	40	3.891.368
IIIA	G074	7,7	15	29	13	-7,5	80	173	89	0,3	33	70	35	8,7	21	45	21	-2,0	39	69	39	261.103	-1,7	22	48	24	1.739.641
IIIA	G075	-1,5	13	27	14	24,4	81	177	93	-0,3	56	101	53	-1,3	17	35	17	-0,4	44	74	44	238.366	1,6	25	53	27	1.511.398
IIIA	G076	-2,1	12	26	12	44,0	98	237	103	0,1	38	72	37	-4,2	17	35	17	4,0	44	79	44	185.847	3,5	25	52	26	1.308.388
IIIA	G077	-0,9	13	27	13	8,6	90	213	105	0,1	45	84	46	3,8	21	43	21	-7,8	46	84	47	167.772	-3,9	27	57	29	1.126.651
IIIA	G078	0,3	10	21	10	15,7	68	134	68	0,1	38	68	36	2,3	18	44	21	-2,9	37	69	37	15.057	-1,1	23	52	25	101.580
IIA	**IIA**	**-0,4**	**19**	**37**	**19**	**1,5**	**101**	**233**	**115**	**0,5**	**49**	**89**	**47**	**-6,3**	**71**	**162**	**78**	**8,9**	**96**	**194**	**99**	**156.232**	**3,1**	**71**	**165**	**79**	**1.119.991**
IIR	**IIR**	**1,1**	**13**	**27**	**13**	**2,2**	**94**	**211**	**104**	**0,2**	**41**	**84**	**42**	**-0,4**	**29**	**82**	**41**	**2,4**	**54**	**113**	**62**	**9.734.572**	**1,8**	**33**	**87**	**44**	**64.924.522**
IIF	**IIF**	**0,4**	**17**	**36**	**18**	**2,8**	**93**	**210**	**105**	**0,0**	**39**	**79**	**40**	**1,7**	**32**	**112**	**52**	**-1,7**	**61**	**146**	**74**	**6.906.275**	**-0,7**	**40**	**118**	**56**	**45.999.346**
IIIA	**IIIA**	**1,3**	**14**	**27**	**14**	**15,8**	**85**	**195**	**98**	**0,0**	**43**	**85**	**43**	**2,1**	**19**	**40**	**20**	**-1,4**	**43**	**76**	**43**	**868.145**	**-0,1**	**25**	**52**	**26**	**5.787.658**
ALL	**ALL**	**0,8**	**14**	**31**	**16**	**3,1**	**93**	**210**	**104**	**0,1**	**40**	**82**	**41**	**0,5**	**30**	**91**	**45**	**0,6**	**56**	**125**	**66**	**17.665.224**	**0,8**	**35**	**98**	**49**	**117.831.517**

Table 43. GPS LNAV Nominal Accuracy, from 1 January 2012 to 31 July 2022.

From 1 January 2012 to 31 July 2022: gAGE Consolidated Broadcast + NGA Precise Orbits and Clocks																										
		Radial (cm)				Along-Track (cm)				Cross-Track (cm)				Clock (cm)				WC URE (cm)				N. Samples	IURE (cm) (Acum. Dodec.)				
	SVN	$\bar{x}$	68th	95th	σ	$\bar{x}$	68th	95th	σ	$\bar{x}$	68th	95th	σ	$\bar{x}$	68th	95th	σ	$\bar{x}$	68th	95th	σ		$\bar{x}$	68th	95th	σ	N. Samples
IIA	G023	-2,4	26	47	25	19,8	98	224	110	-0,2	37	73	38	-3,2	61	130	65	3,4	79	153	81	427.092	1,6	54	125	60	2.743.693
IIA	G026	-2,5	14	34	17	13,6	101	253	124	-0,8	41	82	41	3,9	39	100	50	-8,2	67	145	75	312.903	-5,8	45	112	55	2.099.362
IIA	G027	-0,8	87	129	77	-13,4	259	457	246	-1,0	43	85	43	9,9	211	370	199	-2,8	229	377	216	80.477	-11,5	165	311	161	583.716
IIA	G033	-1,6	26	51	26	-16,0	116	249	124	-0,9	42	85	43	2,0	127	254	128	-1,9	152	281	149	272.024	-2,7	124	251	126	1.816.049
IIA	G034	-1,6	18	36	18	3,7	102	232	115	0,2	38	76	39	0,1	72	168	81	-1,0	96	199	101	559.395	-2,3	72	169	80	3.813.411
IIA	G035	-0,7	20	42	21	1,4	81	173	86	-0,3	49	93	48	-6,9	143	304	154	8,8	167	330	173	127.419	6,6	145	308	155	829.326
IIA	G036	-2,3	17	37	18	10,7	116	260	128	-0,5	40	77	39	-5,7	72	166	80	5,1	100	204	104	225.284	3,2	73	173	82	1.508.996
IIA	G038	-1,4	31	59	32	-12,9	135	285	146	1,4	77	134	72	-4,7	138	269	137	6,2	168	299	162	297.403	3,5	134	263	133	1.934.474
IIA	G039	-2,4	45	77	43	14,4	155	311	160	-0,3	33	70	36	-1,7	143	276	141	3,4	169	300	163	250.147	-0,8	132	261	132	1.658.953
IIA	G040	-1,7	19	41	21	-1,7	102	231	117	-0,9	37	75	38	5,7	121	245	122	-7,7	146	275	144	372.000	-7,5	122	248	124	2.502.923
IIR	G041	-0,1	11	23	12	7,3	98	214	106	0,3	44	86	44	-4,2	28	65	32	6,9	54	99	55	940.967	4,9	32	72	36	6.558.496
IIR	G043	0,4	11	22	12	-1,6	87	193	96	-0,3	41	82	41	-2,1	35	85	41	3,2	57	113	61	1.101.298	2,6	38	91	44	7.256.533
IIR	G044	1,1	13	27	13	-13,9	89	196	96	0,3	41	84	42	-4,4	93	226	104	8,0	115	252	123	990.569	5,8	94	227	105	6.555.673
IIR	G045	0,7	14	30	15	-5,9	106	233	115	1,2	51	102	52	-2,0	26	58	30	5,5	56	100	56	1.101.551	3,9	32	72	36	7.322.243
IIR	G046	0,2	14	28	14	-21,6	111	245	119	-1,0	44	88	45	-0,7	42	113	54	1,0	71	148	77	926.444	2,1	46	119	57	6.308.818
IIR	G047	1,2	13	26	13	-12,0	91	199	99	0,6	49	104	51	2,0	33	116	54	-1,2	56	146	72	1.036.486	0,2	36	117	55	7.009.032
IIR	G048	0,5	13	27	14	-3,8	85	190	93	1,0	55	104	54	1,5	37	86	42	-2,1	61	115	63	1.099.691	-0,8	40	92	44	7.009.396
IIR	G050	0,7	14	27	14	0,1	80	169	86	0,0	35	71	36	2,3	25	52	26	-1,9	44	77	44	1.101.256	-1,9	27	57	28	7.158.763
IIR	G051	0,2	11	22	12	-3,3	86	191	95	-0,1	47	95	48	0,2	23	51	26	0,4	47	83	47	1.101.393	1,1	27	60	30	7.426.622
IIR	G052	0,8	12	25	12	-4,3	87	194	95	-0,2	40	83	42	-2,4	40	97	47	4,1	63	125	66	1.101.263	2,8	42	101	49	7.060.126
IIR	G053	0,0	14	29	15	8,2	119	266	131	0,6	46	92	46	3,6	50	143	65	-4,0	79	180	89	1.101.411	-3,2	52	144	67	7.273.031
IIR	G054	-0,1	13	26	13	0,5	95	210	104	1,7	54	99	52	-3,8	27	77	38	5,3	53	109	59	635.749	4,8	32	82	41	4.421.101
IIR	G055	0,1	12	25	12	-2,1	95	206	102	-0,2	41	82	42	2,1	21	43	21	-3,1	45	77	44	1.101.206	-1,5	25	53	26	7.190.835
IIR	G056	0,5	13	25	13	-16,1	83	175	87	-0,3	39	78	40	-0,5	22	45	23	2,2	43	73	42	1.101.564	1,4	25	53	26	7.348.908
IIR	G057	0,8	15	29	15	9,9	110	254	123	-0,3	44	90	45	2,7	39	113	54	-6,8	68	152	77	1.101.137	-1,4	42	119	57	6.984.465
IIR	G058	0,2	15	28	15	17,4	99	215	107	-0,4	38	77	39	-3,6	24	50	26	7,5	48	85	48	1.101.342	4,5	28	61	31	7.393.616
IIR	G059	0,2	11	24	12	2,0	87	185	93	-0,7	42	82	42	0,5	23	51	25	-0,2	46	82	46	1.101.722	1,0	27	59	29	7.660.388
IIR	G060	1,2	11	24	12	-10,7	86	182	90	0,6	47	92	47	-0,3	21	45	22	2,7	45	77	44	856.408	1,0	26	55	27	5.717.499
IIR	G061	0,0	11	25	12	15,0	95	216	105	0,7	41	79	40	-2,1	25	56	29	3,8	51	92	52	1.100.815	2,9	30	66	33	7.295.663
IIF	G062	-0,8	17	36	18	16,5	96	212	106	-0,1	38	75	39	3,1	23	49	24	-6,3	53	95	53	1.100.675	-3,2	33	71	35	7.943.952

IIF	G063	0,8	16	33	16	-23,2	98	217	105	-0,2	45	85	44	0,2	25	61	30	1,5	54	102	56	1.098.829	0,8	33	77	38	7.221.678
IIF	G064	0,2	16	32	17	17,3	82	182	95	0,3	35	70	36	4,8	26	58	30	-6,0	52	92	53	847.560	-4,5	34	71	36	5.670.909
IIF	G065	-0,4	22	45	23	14,5	105	232	116	-0,2	34	69	35	0,5	102	229	109	-0,1	129	260	132	1.006.950	-1,6	105	234	112	6.784.414
IIF	G066	0,1	16	32	16	-6,7	86	188	97	-0,3	35	70	35	0,4	20	42	21	-0,2	48	82	48	942.892	0,0	30	62	32	6.355.082
IIF	G067	1,2	16	34	17	-8,5	93	211	104	0,0	39	80	40	4,0	22	49	24	-3,6	51	92	51	844.543	-1,8	32	67	33	5.369.241
IIF	G068	0,8	15	32	16	9,7	78	178	89	0,4	33	66	34	0,0	22	50	26	1,5	46	86	49	816.144	1,2	29	64	33	5.289.825
IIF	G069	0,5	17	37	19	3,9	97	227	114	-0,1	37	75	38	-4,6	35	84	42	6,9	64	124	67	787.752	6,9	42	98	49	5.244.975
IIF	G070	0,7	13	31	16	-2,3	89	202	103	0,4	34	71	35	-1,2	20	44	24	3,3	46	87	50	661.091	2,2	28	62	33	4.642.447
IIF	G071	-0,3	18	36	19	7,3	91	201	103	0,2	42	84	42	1,1	24	51	25	-1,9	53	94	54	754.062	-0,7	34	71	36	4.835.846
IIF	G072	1,1	22	44	22	-31,5	112	241	119	-0,1	46	87	45	2,0	98	210	102	-0,4	127	245	128	721.243	-0,1	101	216	105	4.574.863
IIF	G073	0,4	15	33	17	-2,0	93	212	107	0,7	52	98	51	-5,0	29	69	33	8,8	59	106	59	687.520	6,6	37	81	40	4.639.197
IIIA	G074	7,7	15	29	13	-7,5	80	173	89	0,3	33	70	35	8,7	21	45	21	-2,0	39	69	39	261.103	-1,7	22	48	24	1.739.641
IIIA	G075	-1,5	13	27	14	24,4	81	177	93	-0,3	56	101	53	-1,3	17	35	17	-0,4	44	74	44	238.366	1,6	25	53	27	1.511.398
IIIA	G076	-2,1	12	26	12	44,0	98	237	103	0,1	38	72	37	-4,2	17	35	17	4,0	44	79	44	185.847	3,5	25	52	26	1.308.388
IIIA	G077	-0,9	13	27	13	8,6	90	213	105	0,1	45	84	46	3,8	21	43	21	-7,8	46	84	47	167.772	-3,9	27	57	29	1.126.651
IIIA	G078	0,3	10	21	10	15,7	68	134	68	0,1	38	68	36	2,3	18	44	21	-2,9	37	69	37	15.057	-1,1	23	52	25	101.580
IIA	**IIA**	**-1,9**	**23**	**56**	**28**	**3,8**	**113**	**264**	**130**	**-0,2**	**42**	**88**	**44**	**-0,2**	**93**	**234**	**109**	**-0,1**	**119**	**261**	**129**	**2.924.144**	**-1,6**	**90**	**227**	**106**	**19.490.903**
IIR	**IIR**	**0,5**	**13**	**26**	**13**	**-1,6**	**94**	**208**	**103**	**0,1**	**44**	**88**	**45**	**-0,5**	**30**	**89**	**44**	**1,5**	**55**	**121**	**64**	**19.702.272**	**1,5**	**34**	**94**	**47**	**130.951.208**
IIF	**IIF**	**0,3**	**17**	**36**	**18**	**-0,1**	**93**	**210**	**106**	**0,0**	**39**	**78**	**40**	**0,6**	**29**	**111**	**51**	**-0,1**	**59**	**146**	**73**	**10.269.261**	**0,2**	**39**	**118**	**56**	**68.572.429**
IIIA	**IIIA**	**1,3**	**14**	**27**	**14**	**15,8**	**85**	**195**	**98**	**0,0**	**43**	**85**	**43**	**2,1**	**19**	**40**	**20**	**-1,4**	**43**	**76**	**43**	**868.145**	**-0,1**	**25**	**52**	**26**	**5.787.658**
ALL	**ALL**	**0,2**	**15**	**32**	**17**	**-0,2**	**95**	**214**	**107**	**0,1**	**42**	**85**	**43**	**-0,1**	**32**	**119**	**54**	**0,8**	**59**	**150**	**74**	**33.763.822**	**0,8**	**38**	**121**	**57**	**224.802.198**